EURATOM-MedC Annual Report 2011

Summary of the 2011 research activities of the Association Euratom – MEdC Romania

The research on controlled thermonuclear fusion in magnetically confined plasma is organized in Europe as an effectively integrated activity with common work plan and very strong collaborations. The objective of the research is to create a clean, safe and sustainable source of energy. A major step toward this objective is in progress and consists in the construction of the International Thermonuclear Experimental Reactor (ITER), which is expected to demonstrate the generation of power by fusion reaction in plasmas.

The Association EURATOM – MEdC Romania was founded in 1999. It coordinates at the national level the activities of several research groups, from four national institutes and two universities. It has a flexible structure, which involves now around 90 professionals and 30 non-professionals, with about 34 ppy. Part of the research costs is provided by the European Commission. A series of important results have been obtained both in understanding fundamental aspects of the complex plasma processes in tokamak and in technological research.

The year 2011 has been marked by a still increasing importance of the changes related to ITER. Physics and construction of ITER have both influenced the work in the Associations. The common European work plan elaborated through the European Fusion Development Agreement (EFDA) has reflected the need for supporting ITER. The MEdC Association has responded by taking part in the European collaborations that have been set up for the investigation of the physical processes that are not completely understood and are considered important for ITER.

The 2011 research program of the MEdC Association was complex, with contributions to the main directions of EFDA Work Plan. We have participated to European Topical Groups [Transport (T), MHD, Materials (M) and Diagnostics (D)], to the European Task Forces [Plasma-Wall Interaction (PWI) and Integrated Tokamak Modeling (ITM)], to the program of JET diagnostics enhancement (JET-D) and to Fusion Technology (JET-FT). A complete alignment exists between our research activity and EFDA Work Plan in the sense that each internal project corresponds to at least one topic in the EFDA or EFDA-JET Work Plan or to a co-operative action. The PWI projects, which represents 35% of the 2011 budget, maintains the dominant position in our Association although our strong implication in the project ‘’ITER like Wall at JET’’ was completed in 2010.

The MEdC Association was composed in 2011 of groups from seven institutes:

- Institute of Atomic Physics – Management Group of the Research Unit
- National Institute of Laser, Plasma and Radiation Physics (NILPRP)
- National Institute of Cryogenic and Isotope Technology (NICIT)
- National Institute of Physics and Nuclear Engineering (NIPNE)
- National Institute of Physics of Materials (NIPM)
- University of Craiova (UCv)
- University A. I. Cuza from Iassy (UAIC)

The 2011 budget of 1,388,000 E was used for funding 35 research projects.

The work presented in this report in the section Physics of Tokamak Plasma represents our participation in the EFDA work programme on transport (WP11-TRA), magneto hydrodynamics (WP11-MHD) and integrated tokamak modelling (WP11-ITM). The main topics and results are:

- Study of the selection mechanism for the vorticity distribution in the presence of an external torque, which contributed to the understanding of the connection between the plasma rotation and the inflow/outflow of impurities.
- Study of the effects on transport of the 3d stochastic fields by analysing the linear stochastic stability of the Hamaguchi-Horton equations that describes the evolution of the electric potential fluctuations.
- Studies of the stochastic processes and transport in turbulent plasmas (simulation of charged particle trajectories in electromagnetic fields generated with TURBO code, development of a low dimensional model for describing the quasiperiodic oscillations (ELM/sawtooth, chaotic, simple/double periodic orbits) observed in ASDEX-Upgrade tokamak.
- Effects of trapping or eddying in the turbulent potential on the transport and convection of impurities in the edge plasma, on electron heat transport in small scale turbulence and on the nonlinear evolution of drift turbulence.
- The contributions to ITM concern the atomic data collaboration (ITM-AMNS, which consists this year in the calculation of fundamental and applied atomic data for Ar III ion) and in extending the ITM web portal.
- Evaluation of flow stabilization effects on ITER equilibrium states with the objective to extend the generic linear static equilibrium solutions applied to realistic ASDEX Upgrade equilibria to ITER equilibria.
- Study of the effects of non-resonant error fields and of neoclassical toroidal viscosity on tokamak plasma stability.

The participation at the PWI Work Programme spreaded on a wide subject palette:

- Recent investigations of blanket concepts from the European Power Plant Conceptual Study (PPCS) indicate that in the case of reduced activation steel as a structural material a fraction of the particle flux impinging onto the first wall of a blanket module from the plasma can diffuse through the structural material into the coolant. This will lead to tritium contamination of the coolant. For this reason, in one of our projects, it was suggested to integrate a tritium permeation barrier into the plasma-facing side of a blanket module. Since a tungsten coating is proposed as a plasma-facing material, while alumina is considered to be one of the most efficient permeation barriers, the permeation barrier performance of such combinations of thin coatings (coatings of tungsten and alumina with thicknesses in the µm range deposited on a fusion relevant material, EUROFER 97 steel) was investigated.
- The application of several materials at the first wall of ITER leads under operation to the formation of compounds. The retention mechanisms for deuterium and the influence of surface composition, structure, and temperature are essential fundamental properties which enable predictions of the behavior of multi-component first walls in e.g. JET and ITER. The MEdC Association used its broad experience in preparing and characterization of mixed films using the original thermionic vacuum arc (TVA) method.
- X-ray imaging techniques were used for investigating the CFC coating and structure. X-ray 3-D microtomography studies were performed on graphite and CFC samples for porosity network characterization. This analysis was systematically applied to several post mortem Tore Supra samples which involve Cu/Ti/NB11 CFC and to the new bonding technology that it is developed for W7-X and ITER. The thickness of tungsten layers deposited on carbon substrates was measured by a combination of non-destructive X-ray based techniques: i) high resolution X-ray absorption and ii) X-ray fluorescence mapping iii) X-ray backscattering. The thickness and the composition maps were obtained using a 2D X-ray fluorescence/backscattering scanning technique. The X-ray fluorescence mapping can be also used also for the determination of the spatial distribution of high Z materials deposited on low density matrixes. The analysis was applied for divertor marker tiles at the outer strike point of AUG in order to determine the 2-D pattern of net erosion of W and some other elements at the outer AUG strike point.
- Complex experiments were dedicated to sheath properties and related phenomena of the plasma wall interaction in magnetized plasmas. They focused on two major objectives: (i) characterization of Pilot-PSI plasma beam by electrical methods (multi-probe system and electrostatic analyzer) and (ii) plasma diagnostic and correlation measurements in the divertor region of COMPASS tokamak by arrays of electrical probes. Two original numerical codes, 2D PIC-MCC and 2D MC, were used in order two calculate the charged particle fluxes collected by a plane or cylindrical probe placed in a strongly magnetized plasma column.

Our Association has extended the research domain in 2010 by including fusion material topics. The program was continued this year, when we have five projects accepted in the WP11-MAT.

The participation at JET Enhancement and Experimental Program is structured on following main directions:

1. Development of studies related to the ILW project, focusing on the following topics:
   - Investigation of the D retention rate for W coatings. A large number of samples, made of various materials (CFC, fine grain graphite, eurofer) and coated with different W thicknesses under different conditions were analyzed. The first experiments indicated a larger D retention than bulk W. This might be associated with the nano-structure of the layer.
   - Study of the behaviour of W coatings to a cyclic thermal loading relevant for JET operation. Thermal fatigue and mainly carbidization of the tungsten due to the diffusion of the carbon from the substrate have been recognized as mechanisms for degradation of the coatings during the thermal loading at high temperatures.
   - An advanced procedure for the calibration of the measure this emissivity and to calibrate the JET KP-M1AP IR camera was developed in order to be used for temperature measurement of the W coating during JET operation.
   - Characterization of mixed materials was performed in support of the ILW project. Mixed materials, in combinations similar with those deposited during JET operations were prepared using two TVA simultaneous evaporators. Samples having different relative Be/C/W concentrations were thermal treated in vacuum and characterized using XPS technique. Structural changes had been observed with thermal treatment temperature by complex analysis (XPS, SIMS, XRD and X-Ray Fluorescence).
   - High sensitivity accelerator mass spectrometry analysis (AMS) and Full Combustion flowed by scintillator Counting (FCM) were performed for determining the tritium depth profile concentrations in divertor tiles from JET (samples from campaigns 1998-2004, 1998-2007 and 2004-2007). By both these methods, the following striking results were obtained: 1) unexpected fuel retention and migration of tritium in protection tiles, 2) first microscopic investigation of fuel removal by laser ablation.

2. Development of instruments, tools and techniques for JET diagnostics:
   - The participation of the MEdC Association to the Enhancement Project II at JET continued with the work on the two projects leaded by our Association: i) the upgrade of the Gamma-Ray Cameras (GRC) by development and construction of the KN3-NA neutron attenuators system and ii) the upgrade of the JET Tangential Gamma-Ray Spectrometer KM6T by developing a Tandem Collimators System. The tandem collimator system and several components of the KN3-NA system were installed at JET and the engineering commissioning has been successfully performed. The final collimation configurations were evaluated by Monte Carlo transport simulations using the MCNP numerical code. The preparation of the complex experiments dedicated to the commissioning of the two systems in the JET environment was also accomplished.

- In the framework of developing imaging diagnostic techniques based on video data, a recently developed optical flow image processing method has been improved and adapted in order to allow real-time evaluation of the pellets extrusion velocity, based on the image sequences provided by a CCD camera viewing the ice at the exit of the nozzles of the extrusion cryostat.

3. The Participation to JET campaigns C28-C29 was related mainly to the investigation of the behaviour of W coatings during JET operation. Monitoring of the W coatings temperature and analysis of their integrity using the JET video system was performed. Our Association also supplied staff for Diagnostic Coordinator and Video System Operator positions.

FINANCIAL INFORMATION

The details of the expenditures of the MEdC Association in 2011 are presented in the Table 1 and in the Figures 1 and 2.
The European Commission support for the 33 Baseline Projects represents 9.3% of the expenditure while the total contribution is of 28.8% of the budget. This shows that the contribution of the European Commission is mainly used for goal oriented projects.

Table 1: Association Euratom – MEdC expenditure and European Commission S

	No of Projects	Expenditure (kE)	CE Support (kE)
Baseline Support (AG)	**33**	**912.8**	**84.5**
Physics	22	649.5	
JET Notifications	8	207.4	
Power Plant Physics and Technology (PPPT)	3	55.9	
Specific Co-operative actions (8.2a and 8.2b)	**6**	**126.8**	**32,2**
JET S / T Task (EFDA Art. 6.3)	**7**	**86.3**	**86.3**
Fellowship contracts (8.2e)	**1**	**107.7**	**43,1**
Secondments to CSU (EFDA Art 9.4 + 9.5)	**1**	**75.7**	**75.7**
Mobilities		**78.3**	**78.3**
T O T A L		**1387,6**	**400.1**

Figure 1 shows the largest part of the expenditures is for the projects included in the Baseline research, with about 30% for JET Notifications. Figure 2 shows that our Association contributes to all main directions of research in the EFDA Work Plan, with the strongest implication in Plasma Wall Interaction (PWI) topics.

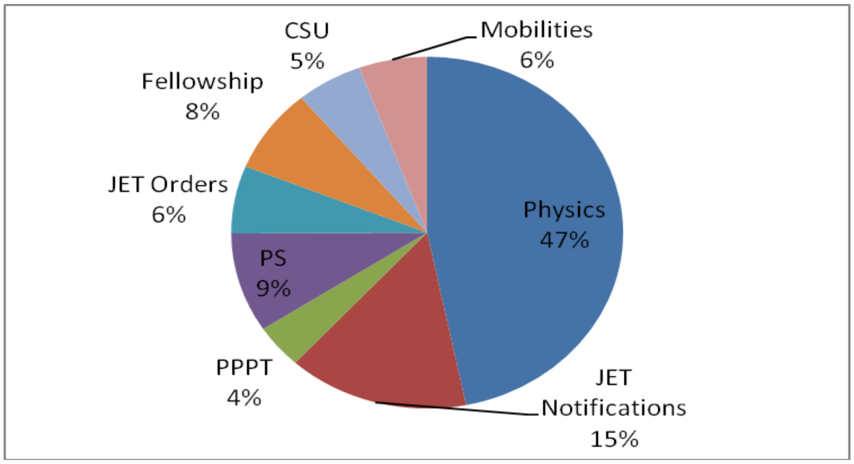

Figure 1: The repartition of the 2011 expenditure on the types of contracts

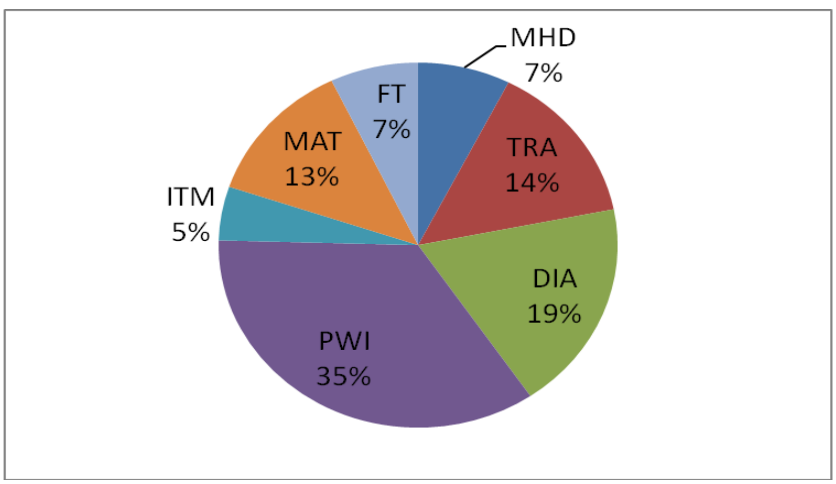

Figure 2: The repartition of the 2011 expenditure on domains of research

---

Madalina Vlad, *Head of Research Unit*
Teddy Craciunescu, *Deputy*

Physics of the Tokamak Plasma

1. **Large Scale Flows And Selection Mechanisms for Vorticity Distribution in the Presence of External Torque – Understanding of the connection between the plasma rotation and the inflow/outflow of impurities** *(Florin Spineanu, Madalina Vlad, Daniela Nendrean)*
2. **Investigation of Helical Perturbations in Tokamaks** *(C.V.Atanasiu, A.Moraru, D.Dumitru)*
3. **Efects Of The Stochasticity And Rf Heating On The Transport In Fusion Plasma** *(N. Pometescu, G. Steinbrecher)*
4. **Anomalous Transport in Plasma. Stochastic processes and transport in turbulent plasma** (*I.Petrisor, M. Negrea, Dana Constantinescu)*
5. **Nonlinear Effects of The ExB Drift on Transport and Structure Generation in Turbulent Plasmas** *(M. Vlad, F. Spineanu)*
6. **Non-resonant error fields and NTV effects on global tokamak plasma stability** *(I.G. Miron)*
7. **Fundamental and Applied Data to the Atomic, Molecular, Nuclear Surface (AMNS) Activity and to Further Development of Documentation on AMNS Codes** *(V. Stancalie, A. Mihailescu, V.F. Pais, A.O. Stancalie, O. Budriga)*
8. **Extending the ITM Web Portal** *(V.F. Pais, V. Stancalie, A. Mihailescu, A.O. Stancalie, O. Budriga)*

Plasma Wall Interaction

1. **Permeation measurements** *(C. P. Lungu, C. Porosnicu, I. Jepu, A. M. Lungu, P. Chiru, C. Ticos, C. Luculescu)*
2. **Preparation of the Be containing layers for D retention and Characterization** *(C.P Lungu, C. Porosnicu, I. Jepu, A. Anghel, A. M. Lungu, P. Chiru, C. Ticos, C. Luculescu, V. Kuncser, C. Teodorescu, M. Văleanu, N. Gheorghe, G. Schinteie, C. Valsangiacom, A. Leca, S. Sandu, G. Gheorghe, A. Stoica)*
3. ***X-ray Micro-Tomography Studies on Graphite and CFC Samples for Porosity Network Characterization*** *(I. Tiseanu, T. Craciunescu, C. Dobrea, A. Sima)*
4. **X-ray Microbeam Absorption/Fluorescence Method as a Non-Invasive Solution for Investigation of the Erosion of W Coatings on Graphite/CFC** *(I. Tiseanu, T. Craciunescu, C. Dobrea, A. Sima)*
5. **Sheath Properties and Related Phenomena of the Plasma Wall Interaction in Magnetised Plasmas. Application To ITER** *(C. Agheorghiesei, V. Anita, S. Costea, C. Costin, G. Popa, L. Sirghi, M. L. Solomon)*

Fusion Materials Development

1. **Consolidation and densification of W and SiC composites** *(A. Galatanu, J. Riesch, B. Popescu, P. Palade, M. Enculescu)*
2. **Joining W with steel using FGM and direct pulse sintering routes** *(A. Galatanu, B. Popescu, M. Valeanu, M. Enculescu)*
3. **Growth of SiC Based Composites by Laser And Radio-Frequency Discharge Methods** (M. Filipescu, F. Stokker-Cheregi, D. Colceag, V. Ion, R. Birjega, A. Nedelcea, M. Dinescu)
4. **Growth of SiC Thin Films with Closed Porosity by Laser and Plasma Methods** *(M. Filipescu, D. Colceag, V. Ion, R. Birjega, A. Nedelcea, M. Dinescu)*
5. **Microstructure and Microcomposition Characterization of W And WW-Alloys by Analytical HRTEM (X-Eds, Eels, Haadf), by SEM/FIB and by XRD** *(C. Sârbu)*

Participation at JET Enhancement and Experimental Program

1. **Deuterium and Helium Retention In W Coatings** (*C. Ruset, E. Grigore, I. Munteanu, M. Gherendi)*
2. **The Limits of the W Coatings Deposited on CFC Tiles for the ITER-like Wall at JET** (*C. Ruset, E. Grigore, I. Munteanu, M. Gherendi)*
3. **Advanced Calibration of the PIW IR Cameras** (*C. Ruset, D. Falie, I. Munteanu, M. Gherendi)*
4. **Characterization of Mixed Materials in Support of the ITER-like Wall Project** (C.P Lungu, C. Porosnicu, I. Jepu, A. M. Lungu, P. Chiru, A. Marcu, C. Luculescu, I. Tiseanu)
5. **Upgrade of Gamma-Ray Cameras: Neutron Attenuators** (M. Curuia, M. Anghel, T. Craciunescu, M. Gherendi, S. Soare, V. Zoita)
6. **Upgrade of the JET Tangential Gamma-Ray Spectometer KM6T** (S. Soare, M. Curuia, T. Craciunescu, M. Gherendi, V. Zoita)
7. **AMS and FCM Measurements of Tritium in Laser Cleaned Tiles and Tritium Depth Profiles in JET Divertor Tiles** (C. Stan-Sion, M. Enachescu, M. Dogaru, A. Petre, G. Kizane, L. Baumane, J. Gabruesnoks, M. Halitovs, L. Avotina, A. Zarins, J. Likonen, S. Koivuranta, M. Kiisk)
8. **Motion Estimation within the MPEG Video Compressed Domain for the Determination of Pellets Extrusion Velocity** (T. Craciunescu, A. Murari, I. Tiseanu, P. Lang)

Physics of the Tokamak Plasma

LARGE SCALE FLOWS AND SELECTION MECHANISMS FOR VORTICITY DISTRIBUTION IN THE PRESENCE OF EXTERNAL TORQUE – Understanding of the connection between the plasma rotation and the inflow/outflow of impurities

Florin Spineanu, Madalina Vlad, Daniela Nendrean

[1]*EURATOM-MEdC Association, National Institute for Laser ,Plasma and Radiation Physics, Bucharest, Romania*

Abstract

The behavior of the impurities in the tokamak plasma, in various regimes, is indicative of the confinement state and has a considerable effect on the loss of energy. We review briefly in the text a series of experiments that show the connection between the rotation of plasma (toroidal and poloidal) and the radial inflow/outflow of the impurities. Since the plasma rotation is due to spontaneous organization of plasma and, to a large extent, to the torque injected in plasma by various external heating mechanism, we provide the general neoclassical argument relating the torque to the transversal Neutral Beam Injection. The basis of our argument is the self-organization of vorticity field in two-dimensional plasma (the strong confining magnetic field allows such an approximation). The pinch of density (radial inflow) would suggest that the asymptotic limit is a singular vortex on the magnetic axis, as is the case in fluids. We show however that this limit is not a solution of the self-organized vorticity (self-dual), therefore the pinch of density should also be connected with injected torque. However we underline the simultaneous presence of two mechanisms of distribution of rotation profile in the poloidal cross section: the self-organization, consisting of concentration of vorticity and the external torque combined with the neoclassical rotation. These two mechanisms can compete or can be combined sinergetically. From the resulting behavior of the vorticity (the projection along the toroidal direction) we can understand the behavior of the density (via the Ertel's law). Then we can assume that the impurities will follow the bulk ion distribution.

Papers

[1] F. Spineanu and M. Vlad, "*Self-duality of the relaxation states in fluids and plasmas*", Physical Review E 67 (2003), 046309, 1-4.

[2] F. Spineanu, M. Vlad, K. Itoh, S. –I. Itoh, '*Stationary vortical structures in stationary turbulence*', Journal of Plasma and Fusion Research Series 6 (2004) 89-93.

[3] F. Spineanu, M. Vlad, *"Stationary vortical flows in 2-dimensional plasma and planetary atmosphere"*, Physical Review Letters 94 (2005) 235003.

Conferences

[1] F. Spineanu, M. Vlad, S. Benkadda, *„The basic evolution of the angular momentum density in a field-theoretical model of vorticity transport"*, 49th Annual Division of Plasma Physics Meeting, Orlando, Florida, USA, November 2007

[2] F. Spineanu, M. Vlad, *„A field theoretical model of self-organization of the vorticity field in two-dimensional plasma and in planetary atmosphere",* 49th Annual Division of Plasma Physics Meeting, Orlando, Florida, USA, November 2007

[3] F. Spineanu, *"The scale length problem from Euler fluid to magnetized plasmas",* International Workshop on Multiscale Methods in Fluid and Plasma Turbulence: Application to magnetically confined plasmas in fusion devices, Centre International de Recherches Mathematiques, Luminy, 21-25 April 2008, invited.

[4] F. Spineanu, M. Vlad, "*A model for the toroidal rotation reversal based on inverse Ranque-Hilsch effect"*, 13th International workshop on H-mode physics and transport barriers, Oxford, UK, 10 – 12 October 2011.

Reports

[1] F. Spineanu, M. Vlad, „*A field theoretical approach to the description of coherent structures in two-dimensional fluids and plasmas*", electronic preprint arXiv.org/Physics0909.2583 (2009)

Introduction

There are several experimental observations on the radial transport of background plasma ions and of the impurities, which are not yet explained. This refers to:

- Density pinch, which means the tendency of the basic ions density to shrink to the magnetic axis.

- The strange manifestation of the density of impurity ions in a plasma acted upon by the Neutral Beam Injection (NBI), sometimes even by the Ion Cyclotron Radiation Heating (ICRH). This means that the ions either accumulate on the axis (for counter-rotation) or are expelled toward the edge (for co-rotating plasma). Here counter- and co-rotation represent the direction of the toroidal plasma rotation compared with the direction of the electric current flowing through the plasma.

The fact that the density of background ions can rise to high levels due to density-pinch is potentially dangerous since it can reach the threshold for the unstable MHD modes, due to the rise of the beta factor in the central region.

The fact that the impurities can accumulate in the center of the discharge is detrimental for fusion regimes since the impurities can be heavy (tungsten, for example) and their radiation will cool the core.

On the other hand one knows that the NBI is able to produce plasma rotation and that ICRH is also injecting some torque into the plasma.

This explains the necessity of studying the processes by which torque introduced in plasma via additional heating interacts with the already-present rotation and eventually compete. Understanding of this competition and/or synergetic interaction should lead to clarifications regarding the evolution of ion density and of impurities.

We look to the quantitative effects of the additional heating on the plasma rotation. This means to calculate the amount of torque which is injected in the plasma by NBI and to compare with the rotation which is known to exist in tokamak, as shown by experiments. This is intended to see the effectiveness of the injection of torque on the formation of a new vorticity profile. The instrument is the kinetic equation for fast ions resulting from NBI.

The main objective is to derive an explicit connection between the heating and its characteristics (for example direction, in the case of tangential injection) and the evolution of the background ions and of impurities. This should help to choose the correct scenarios for the discharges in JET or ITER.

Experiments revealing the connection between impurity radial fluxes and plasma rotation

In the following we review experimental results on the effect on rotation of the change of the confinement regime.

The paper "Rotation and Transport in Alcator C-Mod ITB plasmas" by **Fiore Rice NF50 2010** on Alcator C-mod describes the formation of the Ion Transport Barrier (ITB) in the ICRF heating off axis. A significant slowing of the intrinsic toroidal central rotation during the formation of the ITB. ITB lasts at least $10 \times \tau_e$. The density is stronlgy peaked. The impurities begin to accumulate in the core, often triggering a disruption of the H -mode. We can *comment* on these observations. We begin by citing the work "Observation of spontaneous Toroidal Rotation Inversion in Ohmically Heated Tokamak Plasmas" by **Bortolon Duval Pochelon Scarabosio (Lausanne)**. They observe in L -mode a toroidal rotation which is *counter-current* direction. When the density exceeds a well-defined threshold, there is *reverse* of rotation to *co-current* direction.

The toroidal rotation in the plasma core, in the equilibrium of the L -mode is counter-current. When there is transition to the H -mode the rotation reverses and becomes co-current.

Then we can detect a possible connection: normally the Alcator C-mode plasma is in L -mode and the plasma in the core rotates toroidally in the *counter-current*. Then it is applied off-axis a heating by ICRH. It is known that ICRH also injects torque in the plasma and this provokes poloidal rotation. This poloidal rotation is found as an Internal Transport Barrier and this leads to increase of the density in the plasma core. We possibly find the same situation as on **TCV Lausanne**: The increase of density in the center beyond a threshold due to the formation of the ITB triggers the reversal of the toroidal rotation: the plasma is now rotating *co-current* (similar to an H -mode).

The paper on **Observation of central toroidal rotation in ICRF**, Rice, Nuclear Fusion 38 (1998) 75 : In the L-mode the impurities rotate toroidally in direction *opposite* to the current. (*Counter-current*). In the paper **Varenna ICRH Torque** it is mentioned that there is a pinch of particles during the RF heating, because a toroidal acceleration displaces the trapping ion turning points accross the magnetic surfaces. The turning points are displaced inwardly for *heated* ions. This effect is due to the neoclassical polarization and represents a connection between the toroidal and poloidal rotations.

Usually the impurities have *inward* flux in a tokamak. This is due to their radial gradient being created by high density at the edge and low density in the plasma core.

The paper **NBI influence on impurity Isler** ISX-B tokamak. It is mentioned that theoretical works in neoclassics have revealed that:

1) NBI and electric current in the same direction (*co-injection*). This is a characteristic of the H -mode. It can reduce the inward diffusive flow of impurities.
2) NBI and electric current in opposite direction (*counter-injection*) This is a characteristic of the L -mode. It has the effect of accumulation of impurities in the centre.

In general, in Ohmically heated discharges: classical and neoclassical processes lead to flux of impurities toward the centre. However in reality the accumulation of impurities is slow or even inexistent. One has to use empirical anomalous diffusion coefficients to explain this. In the paper of **Isler** it is shown that the Argon is concentrated in the centre but only in Deuterium and *not* in Hydrogen.

Conclusion for Argon:

1) the Ar accumulation in the centre is *inhibited* by **co-injection**, (exactly like in H -mode) and
2) the Ar accumulation in the centre is *enhanced* by **counter-injection** (as it is the case in the L -

mode)

The same conclusions for the *iron*.**The influx of Fe toward the centre is very fast in** *counter-injection (which suggests L-mode)*. Plasma begins to cool in the centre rapidly. By contrast, the *co-injection* of NBI does not lead to accumulation of Fe in the plasma centre. In the paper **Neoclassical Poloidal Rotation Stacey** it is mentioned that experiments on ISX-B with NBI have shown that there is a low concentration of impurities in the center of the tokamak when the *magnetic field* the *current*, and the *neutral beam* are all in the same direction. (H-mode, co-injection).

Conclusion on the *toroidal rotation*: Characteristics: (1) strong connection between the rotation velocity and the plasma pressure (or stored energy) $v_{tor} \sim p_i$ or W_s; (2) inverse proportionality with the plasma current I_p , $v_{tor} \sim 1/I_p$; (3) no dependence on collisionality

NBI-fast ion drift-kinetic equation

The mechanism of momentum transfer to the plasma, in the case of injection into trapped ion orbits, is (A) **a** $\mathbf{j}\times\mathbf{B}$ **torque which results from** *fast ion radial current*. The birth of fast ions and their subsequent orbital motion cause a **radial current**. This current must be cancelled by a **radial current flowing in the rest of the plasma**. This *radial current* causes a torque on the plasma.

In addition, (B) there is a torque from due to **collisional friction with the fast ions**.

$$T = -\left\langle \mathbf{j}_{fast} \cdot \nabla \psi \right\rangle - I \left\langle \frac{1}{B} \left(F_{\parallel fast-e} + F_{\parallel fast-i} \right) \right\rangle$$

One writes the **drift-kinetic equation** for the *fast ions*.

$$\frac{\partial f}{\partial t} + \left(v_{\parallel} \hat{b} + \mathbf{v}_D \right) \cdot \nabla f = C_{fast} f + S_{fast}$$

where the drift velocity of the guiding centre is $\mathbf{v}_D = v_{\parallel} \hat{b} \times \nabla \left(\frac{v_{\parallel}}{\Omega} \right)$ and the notations are introduced $\xi = \frac{v_{\parallel}}{v} = \left(1 - \lambda B\right)^{1/2}$; $E = \frac{v^2}{2}$; $\mu = \lambda E$. The **spatial variables** are ψ, θ, ϕ and the **velocity space** variables are $v, \lambda, \sigma \,(= \text{sign of } v_{\parallel})$. The **fast ion collision term** is $C_{fast} f = C_{fast-e} f + C_{fast-i} f$

The perturbative expansion of f **for the solution of the drift-kinetic equation for the fast ions**.

$$f = f_{-1} + f_0 + f_1 + \ldots$$

The **zeroth order equation** is

$$v_\parallel \hat{b}\cdot\nabla f_0 = -\mathbf{v}_D\cdot\nabla\psi\frac{\partial f_{-1}}{\partial\psi} - \frac{\partial f_{-1}}{\partial t} + C_{fast} f_{-1} + S_{fast}$$

We write the **radial part of the guiding centre drift velocity** $\mathbf{v}_D\cdot\nabla\psi = I v_\parallel \hat{b}\cdot\nabla\theta\frac{\partial}{\partial\theta}\left(\frac{v_\parallel}{\Omega}\right)$. By performing the bounce averaging the radial displacements averages to zero **(because there is no electric field and no ripple)** $\overline{(\mathbf{v}_d\cdot\nabla\psi)} = 0$. The **bounce averaged zeroth-order** equation

$$\frac{\partial f_{-1}}{\partial t} = \overline{C}_{fast} f_{-1} + \overline{S}_{fast}$$

Note. It results that the lowest order function f_{-1} which is constant on the magnetic surfaces has a variation in the velocity space given by the *source* of fast ions and *the collisions*. It will result that the **source** is essential for a stationary **radial current** of fast ions, even if the collisions and the limitator do not remove ions from plasma. Before solving the equation, we calculate the **radial current of fast ions**.

The *magnetic surface-averaged radial fast ion current density* is

$$\left\langle \mathbf{j}_{fast}\cdot\boldsymbol{\nabla}\psi\right\rangle = e_{fast}\left\langle \int d^3 v\, \mathbf{v}_d\cdot\boldsymbol{\nabla}\psi\, f\right\rangle$$

where we have to replace f by the solution of the *drift-kinetic equation for the fast ions*. Then f here should be seen as $f_{-1} + f_0 + \ldots$.

The following **surface average operator** is used $\langle A\rangle = \frac{\oint \frac{d\theta}{\mathbf{B}\cdot\nabla\theta} A}{\oint \frac{d\theta}{\mathbf{B}\cdot\nabla\theta}}$. The equation gives

$$\left\langle \mathbf{j}_{fast}\cdot\nabla\psi\right\rangle = e_{fast}\left\langle \int d^3 v \mathbf{v}_D\cdot\nabla\psi f\right\rangle = e_{fast}\left\langle \int d^3 v I v_\parallel \hat{b}\cdot\nabla\theta\frac{\partial}{\partial\theta}\left(\frac{v_\parallel}{\Omega}\right)\right\rangle$$

and we perform an integration by parts in θ :

$$e_{fast}\left\langle \int d^3 v \mathbf{v}_D\cdot\nabla\psi f\right\rangle = -e_{fast} I\left\langle d^3 v\left(\frac{v_\parallel}{\Omega}\right) v_\parallel \hat{b}\cdot\nabla f\right\rangle$$

Now we must replace f by its expansion. The lowest order f_{-1} does not depend on the parallel coordinate (in the surface) so it will not contribute. The first contribution is from the term f_0 . This is obtained in equation where we have to insert the equation:

$$v_\parallel \hat{b}\cdot\nabla f_0 = -\mathbf{v}_D\cdot\nabla\psi\frac{\partial f_{-1}}{\partial\psi} + C_{fast} f_{-1} - \overline{C}_{fast} f_{-1} + S_{fast} - \overline{S}_{fast}$$

The first term on the right will not contribute after **surface-averageing**

$$e_{fast} I \left\langle \int d^3 v \left(\frac{v_\parallel}{\Omega} \right) \mathbf{v}_d \cdot \nabla \psi \frac{\partial f_{-1}}{\partial \psi} \right\rangle = \frac{1}{2} e_{fast} I^2 \left\langle \int d^3 v \, v_\parallel \hat{b} \cdot \nabla \theta \frac{\partial}{\partial \theta} \left[\left(\frac{v_\parallel}{\Omega} \right)^2 \right] \frac{\partial f_{-1}}{\partial \psi} \right\rangle$$

The integrand is the product of a *odd function* of $v_\parallel$ ($v_\parallel$) with an *even function* of $v_\parallel$ (f_{-1}). The integral on the velocity space is **zero**. This result is great importance: it shows that the surface averaged radial current of the ions is zero. If we expected to have an effective current simply due to the difference in radial drift motions between the ions and the electrons, this result shows clearly that it cannot exist.

The radial current due to the difference between iond and electron drifts exists, but only locally. When it is integrated over the magnetic surface, it gives zero.

The **surface-averaged** radial current of fast ions is

$$\left\langle \mathbf{j}_{fast} \cdot \nabla \psi \right\rangle = -e_{fast} \left\langle \int d^3 v \left(\frac{v_\parallel}{\Omega} \right) \left[C_{fast} f_{-1} - \overline{C}_{fast} f_{-1} + S_{fast} - \overline{S}_{fast} \right] \right\rangle$$

If the injection is made in **trapped particle region** the function f_{-1} will not depend on the **direction** of the parallel velocity so its integral is zero. The result is then

$$T = m_{fast} \left\langle \frac{I}{B} \int d^3 v \, v_\parallel S_{fast} \right\rangle = \left\langle \dot{M}_\phi \right\rangle$$

The conclusion is that the torque exists only if there is a source of fast ions. Also at stationarity, the time-derivative of the distribution function is zero and, for **trapped and untrapped** particles, the torque is given by equation (torsource) which reflects **the angular momentum conservation in the neutral injection**.

We dispose of a picture of "natural" plasma rotation profiles. This is derived from fundamental principles governing distribution of vorticity in a fluid in two-dimensions. We note from the equation

$$\frac{dn}{dt} - \frac{n_0}{B_0 \Omega_{ci}} \frac{d}{dt} \nabla_\perp^2 \phi = 0$$

that the evolution of the vorticity $\nabla_\perp^2 \phi$ imposes a similar evolution of the density. This means that the tendency of the vorticity to collapse on the center and form a singular filament of vorticity will impose a similar behavior for the density

$$\frac{d}{dt} \omega \equiv \frac{d}{dt} \nabla_\perp^2 \phi$$

has an evolution that reflects the pinch of ω toward the center. It results that n will also have a pinch toward the center.

$$\frac{\partial n}{\partial t} = \frac{n_0}{B_0 \Omega_{ci}} \frac{\partial}{\partial t} \nabla_\perp^2 \phi \quad or \quad \frac{\partial}{\partial t} \frac{1}{c_s \rho_s} v_{dia} \sim \frac{1}{B_0 \Omega_{ci}} \frac{\partial}{\partial r} \frac{\partial}{\partial t} \nabla_\perp^2 \phi$$

taking u very slowly changing (since the profile of vorticity is driving the density, and the density must move faster for an initialization of profile of u),

$$-\frac{\partial}{\partial t}\left(1-\frac{v_{dia}}{u}\right) \approx \frac{c_s \rho_s}{B_0 \Omega_{ci}} \frac{1}{u} \frac{\partial}{\partial t} \frac{\partial \omega}{\partial r}$$

The accumulation to the center of the vorticity means that

$$\frac{1}{u} \frac{\partial}{\partial t} \frac{\partial \omega}{\partial r} \rightarrow 0$$

over almost all plane, with the exception of a small region around the center. Then $\frac{\partial}{\partial t}\left(1-\frac{v_{dia}}{u}\right) \rightarrow 0$ which means that the factor $1-v_{dia}/u$ tends to become a constant in time.

$$v_{dia} \rightarrow u$$

Again we have invoked the fact that the vorticity evolves such as to vanish over almost all plane. This can be realized only if the density will evolve such that its diamagnetic velocity tends to become equal to the rotation velocity.

Possible concentration of vorticity on the axis of the tokamak

The stationary states of the Euler equation are given by the *sinh*-Poisson equation

$$\Delta \psi + \lambda \sinh \psi = 0$$

or, since ψ is streamfunction and $\omega = -\Delta \psi$, $\omega = \sinh \psi$. **Is the singular vortex a solution of the stationary Euler equation (or: *sinh*-Poisson eq.)?** We have

$$\psi(r) = \overline{\omega} L^2 \ln(r/L) \qquad \qquad \omega(r) = \overline{\omega} L^2 \delta(r)$$

and normalized $\psi \rightarrow \ln(r)$ $\qquad \omega \rightarrow L^2 \delta(r)$ then

$$-L^2 \delta(r) + \lambda \frac{1}{2}[\exp(\ln r) - \exp(-\ln r)] = -L^2 \delta(r) + \lambda \frac{1}{2}\left(r - \frac{1}{r}\right)$$

We conclude that the singular vortex is NOT a solution of the sinh-Poisson equation.

The *physical* energy of the singular vortex. It is calculated with the formula of the Lamb-Oseen vortex and then taking the limit $L_v \rightarrow 0$.

$$E^{phys} = \lim_{\varepsilon \rightarrow 0+} \frac{n_0 m_0}{2} \int d^2 r \, v_\theta^2 = \frac{n_0 m_0}{2} \lim_{\varepsilon \rightarrow 0+} \int d^2 r \left\{ \frac{\gamma_v}{r} \left[1 - \exp\left(-\frac{r^2}{L_v^2} \right) \right] \right\}^2$$

where

$$\gamma_v = \frac{a^2}{2} \frac{\overline{\omega}}{1 - \exp\left(-a^2 / L_v^2\right)}$$

The integral on the first region, close to origin

$$\int_0^{\varepsilon} 2\pi r dr \frac{\gamma_v^2}{r^2} \left[1 - \exp\left(-\frac{r^2}{L_v^2}\right)\right]^2 = 2\pi\gamma_v^2 \int_0^{\varepsilon} dr \left(1 - 1 + \frac{r^2}{L_v^2}\right)^2 = 2\pi\gamma_v^2 \left[\frac{1}{L_v^4} \frac{r^5}{5}\right]_0^{\varepsilon} = 2\pi\gamma_v^2 \frac{\varepsilon^5}{L_v^4}$$

The second region gives a non-singular, finite quantity in the limit $\varepsilon \to 0$. However the limit $L_v \to 0$ produces a singularity of the type

$$\begin{aligned} E^{phys}\Big|_{\text{singular vortex}} &\sim \ln a - \ln \varepsilon \\ &\to +\infty \end{aligned}$$

The physical energy of the singular vortex is infinite. Where from this energy could come if the system evolves toward the singular vortex? The *physical* energy for the singular vortex but using the field-theoretical conclusion: the *sinh*-Poisson eq.

$$E^{phys} = \lim_{\varepsilon \to 0+} \frac{1}{2} \int d^2 r \, \omega\psi = \lim_{\varepsilon \to 0+} \frac{1}{2} \int 2\pi r dr \, \omega\psi = \lim_{\varepsilon \to 0+} \frac{1}{2} \int 2\pi r dr \psi \sinh \psi$$

and use

$$\psi(r) = \overline{\omega} L^2 \ln(r / L)$$

and normalized

$$\psi \to \ln(r)$$

$$\begin{aligned} E^{phys} &= \lim_{\varepsilon \to 0+} \frac{1}{2} \int 2\pi r dr (\psi \sinh \psi) = \lim_{\varepsilon \to 0+} \frac{1}{2} \int 2\pi r dr \left\{ \ln r \frac{1}{2} \left[\exp(\ln r) - \exp(-\ln r)\right] \right\} \\ &= \lim_{\varepsilon \to 0+} \frac{1}{2} \frac{1}{2} 2\pi \int_{\varepsilon}^{1} r dr \left[\ln r \left(r - \frac{1}{r}\right)\right] = \lim_{\varepsilon \to 0+} \frac{1}{2} \frac{1}{2} 2\pi \int_{\varepsilon}^{L} dr \left(r^2 \ln r - \ln r\right) \end{aligned}$$

It results

$$\begin{aligned} \text{for sinh - Poisson: } E^{phys}\Big|_{\text{singular vortex}} &= \lim_{\varepsilon \to 0+} \frac{1}{2} \frac{1}{2} 2\pi \int_{\varepsilon}^{L} dr \left(r^2 \ln r - \ln r\right) \\ &= \lim_{\varepsilon \to 0+} \frac{\pi}{2} \left(-\frac{1}{9} - \frac{1}{3} \left(\frac{\varepsilon}{L}\right)^3 \ln \frac{\varepsilon}{L} + \frac{\varepsilon^3}{9L^3} + 1 + \frac{\varepsilon}{L} \ln \frac{\varepsilon}{L} - \frac{\varepsilon}{L} \right) \\ &= \frac{\pi}{2} \frac{8}{9} \end{aligned}$$

which is not divergent and is not zero. The fact that the energy of the *singular vortex* (as limit of the Lamb-Oseen vortex) is NOT zero is compatible with the fact that it is not a solution of the *sinh*-Poisson equation. If it were a solution of *sinh*-Poisson equation then its energy would have to be zero, as all self-dual states.

Conclusion

We support the following phenomenological model for the behavior of the impurities in tokamak.

The fluxes of bulk ions and of impurities are strongly connected with the plasma rotation. This rotation may be spntaneous or may be imposed via NBI and ICRH. The rotation can be both toroidal and poloidal.

The poloidal rotation is subject to an intrinsic process of self-organization, leading to concentration of the vorticity in a small region around the magnetic axis.

The density is driven to follow the vorticity.

Conflicting effects on rotations (NBI versus rotation sustained by coherent convective cells developing in the meridional cross section) lead to redistribution of the vorticity. Then the density follows.

INVESTIGATION OF HELICAL PERTURBATIONS IN TOKAMAKS

C.V.Atanasiu[1], A.Moraru[2], D.Dumitru[1]

[1]National Institute for Lasers, Plasma and radiation Physics, Bucharest, Romania

[2]University Politehnica of Bucharest, Romania

Abstract

During the period January-December 2011, the theoretical and modelling research activity of the "Mathematical Modelling for Fusion Plasmas Group" of the National Institute for Lasers, Plasma and Radiation Physics (NILPRP), Magurele - Bucharest, Romania has been focalized on two directions:

***1. Resistive wall modes stabilization**, by modelling RWM in a 3D geometry by considering real wall geometry with holes, in the thin wall approximation. We started with the implementation of our numerical code to calculate the wall response to the external kink mode perturbations on the ITM Gateway Platform.*

***2. Evaluation of flow stabilization effects on ITER equilibrium states** with the objective to extend the generic linear static equilibrium solutions applied to realistic ASDEX Upgrade equilibria, to ITER equilibria (ITER shaping, poloidal beta, poloidal current, safety factor on axis, internal inductance) with sheared flow parallel to the magnetic field with Alfvén Mach numbers on the order of 0.01 and to investigate the potential stabilizing effect of the flow by applying a sufficient condition for linear stability of equilibria with parallel flow.*

Detailed results

1. Resistive wall modes stabilization

We have considered a sharp-boundary toroidal plasma separated by a vacuum gap from the wall and other current-currying current elements. The perturbed magnetic field can be expressed as

$$\tilde{\mathbf{B}} = \tilde{\mathbf{B}}^{pl} + \tilde{\mathbf{B}}^{w} + \tilde{\mathbf{B}}^{ext}, \tag{1.1}$$

where $\tilde{\mathbf{B}}^{pl}$ corresponds to the plasma contribution, $\tilde{\mathbf{B}}^{w}$ corresponds to the wall contributions (as response to the plasma perturbation) and $\tilde{\mathbf{B}}^{ext}$ is due to the electrical currents flowing outside the wall. We have considered a coordinate system (a,ϑ,ζ) attached to the wall, while the plasma surface will be described by the coordinate system (a',ϑ',ζ') with straight field lines. ϑ and ζ represent the poloidal and toroidal angles, respectively, while $a=a_0$ and $a'=a'_0$ represent the wall surface and the plasma surface, respectively. We made the assumption that from the Fourier series of the flux function perturbation ψ of the external kink mode a single harmonic with the wave numbers m and N will be considered only.

The eddy current distribution in the thin wall is described by the known diffusion equation [1, 2]

$$\nabla^2 U(t,\theta,\zeta) = d\sigma \frac{\partial B_n(t,\theta,\zeta)}{\partial t}, \tag{1.2}$$

where $U=U(t,\vartheta,\zeta)$ is the stream function of the eddy currents introduced by the relation

$$\mathbf{J} = \nabla U \times \mathbf{n}, \tag{1.3}$$

with $\mathbf{J}$ the linear eddy current density, $\mathbf{n}$ the external normal to the wall, B_n the normal to the wall component of the magnetic field, d the wall thickness and σ the electrical conductivity of the wall. Let us ignore for the moment the external component of the magnetic field. Thus, if on the plasma surface ($a'=a'_0$) the perturbed magnetic field produced by the plasma (a real value) was excited by many modes, it can be written as (with γ the growth rate of the mode)

$$\begin{gathered} B_n^{pl}(a'_0,\theta',\zeta') = \sum_{m,N} \underline{B}_{m,N}^{pl}(a'_0)\exp[\gamma t + \mathrm{i}(m\theta' - N\zeta')], \\ \underline{B}_{m,N}^{pl}(a'_0)\exp[\gamma t + \mathrm{i}(m\theta' - N\zeta')] = \underline{B}_{-m,-N}^{pl}(a'_0)\exp[\gamma t - \mathrm{i}(m\theta' - N\zeta')], \quad \text{with } \infty > m, N > -\infty, \end{gathered} \tag{1.4}$$

In fact, the plasma, i.e. the mode, rotates along the ϑ' and ζ' directions with constant angular speeds

$$\Omega_\theta = \frac{d\theta'}{dt} = \text{const}, \; \Omega_\zeta = \frac{d\zeta'}{dt} = \text{const}. \tag{1.5}$$

We have considered all the values in the coordinate system frame of the wall and with the following space-time dependencies

$$B_n^{pl}(t,\theta,\zeta)=\sum_{mN}\underline{B}_{mN}^{pl}(a)\exp[\gamma^r t+\mathrm{i}\alpha+\mathrm{i}\omega t],$$

$$B_n^{w}(t,\theta,\zeta)=\sum_{mN}\underline{B}_{mN}^{w}(a)\exp[\gamma^r t+\mathrm{i}\alpha+\mathrm{i}\omega t+\mathrm{i}\beta_b]=\sum_{mN}\underline{\hat{B}}_{mN}^{w}(a)\exp[\gamma^r t+\mathrm{i}\alpha+\mathrm{i}\omega t],$$

$$U(t,\theta,\zeta)=\sum_{mN}\underline{U}_{mN}(a)\exp[\gamma^r t+\mathrm{i}\alpha+\mathrm{i}\omega t+\mathrm{i}\beta_U]=\sum_{mN}\underline{\hat{U}}_{mN}(a)\exp[\gamma^r t+\mathrm{i}\alpha+\mathrm{i}\omega t], \tag{1.6}$$

$$\underline{\hat{B}}_{mN}^{w}(a)=\underline{B}_{mN}^{w}(a)\exp[\mathrm{i}\beta_b],\ \underline{\hat{U}}_{mN}(a)=\underline{U}_{mN}(a)\exp[\mathrm{i}\beta_U]$$

with $\omega=m\Omega_\vartheta-N\Omega_\zeta$ the angular frequency, and $\beta=\beta(\vartheta,\zeta)$ the phase due to the *RL* circuit character of the wall. In general, $\beta_b\neq\beta_U$. $\alpha=m\vartheta-N\zeta$ and γ^r is the growth rate of the perturbed magnetic field in the plasma reference system.

The diffusion equation (1.2) becomes

$$\nabla^2\left[\underline{\hat{U}}_{mN}(\theta,\zeta)\exp[\mathrm{i}\alpha]\right]=(\gamma^r+\mathrm{i}\omega)d\sigma\times\left[\underline{\hat{B}}_{mN}^{pl}(\theta,\zeta)+\underline{\hat{B}}_{mN}^{w}(\theta,\zeta)\right]\exp[\mathrm{i}\alpha]. \tag{1.7}$$

For a general wall structure, we have considered a curvilinear coordinate system (*u,v,w*) where two of the covariant basis vectors

$$\mathbf{r}_u\equiv\frac{\partial\mathbf{r}}{\partial u},\mathbf{r}_v\equiv\frac{\partial\mathbf{r}}{\partial v},\ \ \mathbf{r}_u\cdot\mathbf{n}=0,\ \mathbf{r}_v\cdot\mathbf{n}=0, \tag{1.8}$$

are tangent to the wall surface. Where **r** is the vector from an arbitrary origin to a variable point, and **n** is the external normal to the wall. The third basis vector is chosen as

$$\mathbf{r}_w\equiv\frac{\partial r}{\partial w}\equiv d\,\frac{\mathbf{r}_u\times\mathbf{r}_v}{|\,\mathbf{r}_u\times\mathbf{r}_v\,|}, \tag{1.9}$$

where *d* is the wall thickness. The current density **j** [A/m^2] is coplanar with the wall surface $\mathbf{j}\cdot\mathbf{r}^w=0$ and can be expressed with the help of a stream function *I*, in a similar manner with the definition (1.2)

$$\mathbf{j}=\nabla I\times\mathbf{r}^W=\frac{1}{dD}\frac{\partial I}{\partial u}\mathbf{r}_u-\frac{1}{dD}\frac{\partial I}{\partial v}\mathbf{r}_v,\ D^2\equiv g_{uu}g_{vv}-g_{uv}^2 \tag{1.10}$$

The correspondent surface current density **J** [A/m] is given by

$$\mathbf{J}\equiv d\int_0^1\mathbf{j}dw=\frac{1}{D}\frac{\partial I}{\partial v}\mathbf{r}_u-\frac{1}{D}\frac{\partial I}{\partial u}\mathbf{r}_v. \tag{1.11}$$

Starting from the known connection between the electrical field, electrical potential and the magnetic vector potential

$$\mathbf{E} = -\nabla \varphi_E - \frac{\partial \mathbf{A}}{\partial t} = \frac{\mathbf{j}}{\sigma}, \ \mathbf{B} = \nabla \times \mathbf{A}, \tag{1.12}$$

multiplying by Ohm's law by $(r^w \cdot \nabla \times)$ and being interested in the normal component of the magnetic field (**n**=**r**^{w}/|**r**^{w}|), we obtain

$$d\,\frac{\partial(\mathbf{r}^W \cdot \mathbf{B})}{\partial t} = -\frac{1}{D}\left\{\frac{\partial}{\partial u}\left[\frac{1}{\sigma d}\left(\frac{g_{uv}}{D}\frac{\partial I}{\partial v} - \frac{g_{vv}}{D}\frac{\partial I}{\partial u}\right)\right] - \frac{\partial}{\partial v}\left[\frac{1}{\sigma d}\left(\frac{g_{uu}}{D}\frac{\partial I}{\partial v} - \frac{g_{uv}}{D}\frac{\partial I}{\partial u}\right)\right]\right\}. \tag{1.13}$$

In Fig. 1, constant U lines are given for B^{pl} of the form

$$B^{pl}(u,v) = B_0 \exp(\gamma t)\cos\left[m\frac{2\pi(u-u_{in)}}{u_{fin}-u_{in}} - N\frac{2\pi(v-v_{in)}}{v_{fin}-v_{in}}\right] \tag{1.14}$$

For the determination of the stream function U, appropriate boundary conditions have been fixed on all contours (for both, holes and wall). B^{pl} has been considered only as l.h.s of (19), while B^w was taken as an iterative correction, i.e., we have a linear problem. Thus, the well-known method of solving differential equation (the general solution of our non-homogeneous differential equation is the sum of the fundamental solutions to the homogeneous equation and any particular solution to the non-homogeneous equation) has been used. By using this method, we have developed an efficient and fast solving algorithm.

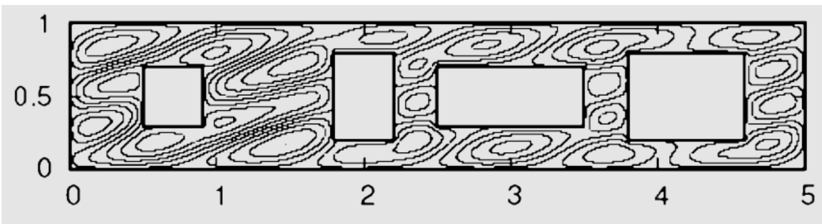

Figure 1 - Constant U lines for an equivalent wall geometry with holes. m=3, N=2.

2. Evaluation of flow stabilization effects on ITER equilibrium

Generalized Grad-Shafranov equation with flow

We have continued our previous work by extending the generic linear static (no flow) equilibrium solutions, developed by us in Ref. [3] and applied to a realistic ASDEX Upgrade equilibria, to an ITER equilibria with sheared flow parallel to the magnetic field. As ITER parameters we have considered: shaping, poloidal beta, poloidal current, and safety factor on axis, internal inductance and accessible flows with Alfvén Mach numbers on the order of 0.01 [4-6].

To investigate the potential stabilizing effect of the flow, we have applied a sufficient condition for linear stability of equilibria with parallel flow. If for static ideal MHD equilibria, there is a powerful tool - "the energy principle" providing necessary and sufficient conditions for linear stability, in the presence of flow, the stability problem is much complicated because the force operator becomes non-Hermitian and only sufficient conditions can be obtained (Lyapunov).

Next step: Derivation of novel equilibrium solutions with flow by application of the Bogoyavlenskij transformation

Bogoyavlenskij introduced new symmetry transforms of the ideal MHD equilibrium equations [7]. In

certain classes of plasma configurations, Bogoyavlenskij symmetries break geometrical symmetry, thus giving rise to important classes of non-symmetric MHD equilibrium solutions. The Bogoyavlenskij symmetries form an infinite-dimensional group of transformations with eight connected components in the case of incompressible plasmas, and four connected components in the case of compressible plasmas.

The MHD equilibrium equations, which under the assumptions of infinite conductivity and negligible viscosity has the form:

$$\rho\times\mathbf{V}\times\nabla\times\mathbf{V}-\frac{1}{\mu}\mathbf{B}\times\nabla\times\mathbf{B}-\nabla P-\rho\nabla\frac{\mathbf{V}^2}{2}=0, \tag{2.1}$$

$$\nabla\cdot\rho\mathbf{V}=0, \nabla\times(\mathbf{V}\times\mathbf{B})=0, \nabla\cdot\mathbf{B}=0 \tag{2.2}$$

$$\nabla\cdot\mathbf{V}=0 \tag{2.3}$$

Bogoyavlenskij found that the ideal MHD equilibrium equations (2.1)-(2.3) possess the following symmetries: if {**V**(**r**);**B**(**r**); *P*(**r**); *ρ*(**r**)}*g* is a solution of (1)-(3), where the density *ρ*(**r**) is constant on both magnetic field lines and streamlines, then {$\mathbf{V}_1$(**r**);$\mathbf{B}_1$(**r**); P_1(**r**); ρ_1(**r**)} is also a solution, where:

$$\begin{aligned}
&\mathbf{B}_1=b(\mathbf{r})\mathbf{B}+c(\mathbf{r})\sqrt{\mu\rho}\mathbf{V},\\
&V_1=\frac{c(\mathbf{r})}{a(\mathbf{r})\sqrt{\mu\rho}}\mathbf{B}+\frac{b(\mathbf{r})}{a(\mathbf{r})}V,\\
&\rho_1=a^2(\mathbf{r})\rho, P_1=CP+(C\mathbf{B}^2-\mathbf{B}_1^2)/(2\mu)
\end{aligned} \tag{2.4}$$

where $b^2(\mathbf{r})-c^2(\mathbf{r})=C=const., a(\mathbf{r}), b(\mathbf{r}), c(\mathbf{r})=$ functions constant on magnetic surfaces $\Psi=const.$

Conclusions

If tearing modes can be stabilized both theoretically and experimentally, the EKMs have not been stabilized experimentally with plasma rotation or feedback control, although theoretical results indicate it is possible; experimentally, the stabilization effect of the RWMs has been demonstrated but it has not been found to be robust. In a next step, we intend to add in our model some feedback coils and sensors and to take dissipation processes in plasma into account, like anomalous plasma viscosity, charge-exchange with cold neutrals, neoclassical flow-damping, sound-wave damping, etc., as in our analytical model for a cylindrical, large aspect ratio tokamak approximations. Little can be done more analytically for RWM - main part has to be numerical.

For the present stage of our research, we did not find a stabilising effect of the flow and have to continue our investigation; to consider a plasma flow with arbitrary direction with respect to **B;** a conjecture that equilibrium nonlinearity may activate flow stabilization will be also checked; to derive novel equilibrium solutions with flow by applying the Bogoyavlenskij transformations in an axisymmetric tokamak geometry.

Acknowledgement

Part of this work has been carried out (and represents our present activity) in close collaboration with our colleagues from the Tokamak Physics Department of the Max-Planck-Institut für Plasmaphysik, Garching, Germany, and the Association EURATOM-Hellenic Republic, University of Ioannina, during the mobilities 06.06.11-03.09.11 and 07.11.11-06.12.11.

References

[1] C.V. Atanasiu, A. Moraru, L.E. Zakharov, Rev. Roum. Sci. Techn. – Électrotechn. et Énerg., **54**, 2, (2011).
[2] C.V. Atanasiu, A. Moraru, L.E. Zakharov, The 7th Int. Symp. on ATEE, May 12-14, 2011, Bucharest, Romania.
[3] C. V. Atanasiu, S. Günter, K. Lackner, I.G. Miron, Phys. Plasmas **11**, 3510 (2004).
[4] H. Tasso, G. N. Throumoulopoulos, Phys. Plasmas **5**, 2378 (1998).
[5] G. N. Throumoulopoulos, H. Tasso, G. Poulipoulis, J. Plasma Phys. **74**, 327 (2008).
[6] G. N. Throumoulopoulos, H. Tasso, Phys. Plasmas **14**, 122104 (2007).
[7] O. I. Bogoyavlenskij, Phys. Review E **66**, 056410 (2002).

EFECTS OF THE STOCHASTICITY AND RF HEATING ON THE TRANSPORT IN FUSION PLASMA

Nicolae Pometescu, Gyorgy Steinbrecher

University of Craiova, Faculty of Exact Sciences, Physics Department

Abstract

The main objective was study of the effects on the transport of the 3d stochastic field by studying the linear stochastic stability of the Hamaguchi-Horton equations. The methods developed previously for the linear stochastic instability analysis of the stochastic differential equations where applied to the study of stability of the linearized Hamaguchi-Horton equation that describes the evolution of the electric potential fluctuations. The stochastic aspects are modelled by the random perturbation in the term that is related to the temperature and density gradients. The global modelling of the fluctuations of the ion and electron temperatures, the gradient length of density and ion temperature was performed by adding to the diamagnetic velocity a random term modelled by temporal white noise field with very general spatial correlations. Deterministic linear evolution equation was derived for the equal time two point correlation functions related to the electrostatic potential fluctuations. The large time behaviour of the correlation function of the electrostatic fluctuations was studied. The main result is the occurrence of new kind of instabilities induced by fluctuations of the background temperature and density fields. Exact analytic results were obtained for the eigenvalues in terms of the correlation function of the driving noise, the parameters of the diamagnetic drift velocity, gradient length of the temperature and density fields. The contribution to the local diffusion coefficients was estimated. In order to study effects of radio-frequency (RF) heating on the transport of Ni impurities was analysed experimental data from two shots (74354 without ICRH and 74355 with ICRH) in JET. Data was implemented in a kinetic model to analyse poloidal asymmetry and in a fluid model to obtaine the difusivity, convective velocity and peaking factor. The frequency of the eigenmodes was evaluated from the approximate form of the dispersion equation by using Mathematica.

<u>Papers</u>

[1] G. Steinbrecher, X. Garbet, Y. Sarazin, *Linear stability of the stationary solutions of self-organized criticality model of the edge plasma turbulence*, Physics AUC 21 (2011) 55-60.

[2] N. Pometescu and JET EFDA Contributors, *ITG modes in JET plasma*, Phys. AUC 2011, pg.48-55

<u>Conferences</u>

[1] G. Steinbrecher, *3-dimensional linear stochastic stability analysis of the Hamaguchi-Horton equations*, MEdC Association Day, Bucharest-Magurele, Romania, 16 December 2011.

<u>Reports</u>

[1] G. Steinbrecher, *Stochastic Methods, part III: Stochastic linear stability analysis*, Seminar, IRFM-Cadarache, France, 9 Dec. 2011

[2] N. Pometescu and G. Steinbrecher, *Effects of the stochasticity and RF heating on the transport in fusion plasma*, MEdC Association Day, , Bucharest-Magurele, Romania, 16 December 2011

Detailed results

- *Statistical properties of the edge turbulent transport. 3D field effects in edge turbulent transport.*

Methods were developed previously for the linear stochastic instability analysis of the stochastic differential equations [1-4]. These methods where applied to the study of the stability of the linearized Hamaguchi-Horton equation that describes the evolution of the electric potential fluctuations [5]: $\partial_t \nabla_\perp^2 \delta\tilde{\Phi} = -V_{ds}\kappa_i \partial_y \nabla_\perp^2 \delta\tilde{\Phi}$. Here $\delta\tilde{\Phi}$ is the normalized electrostatic potential fluctuation; the symbol V_{ds} denotes the ion-acoustic diamagnetic velocity. We used also the notation $\kappa_i = T_{e,0} / T_{ion,0}(1 + L_n / L_{T,ion})$ for the non-dimensional quantity related to electron and ion temperatures [5]. $L_n, L_{T,ion}$ are the characteristic lengths of the density and ion temperature fluctuations. The stochastic aspects are modelled by the random perturbation in the term that is related to the temperature and density gradients. The global modelling of the fluctuations of the ion and electron temperatures, the gradient length of density, ion temperature, is performed by the replacement $V_{ds}\kappa_i \to V_{ds}\kappa_i + \xi(\mathbf{r},t)$. Here the random field $\xi(\mathbf{r},t)$ is a temporal white noise with arbitrary special correlations, defined as follows: $\langle \xi(\mathbf{r},t)\xi(\mathbf{r}',t') \rangle_\xi = \delta(t-t')K(\mathbf{r},\mathbf{r}')$, with prescribed spatial correlation function K, obtained from experiments or first principle modelling. The components of the vector **r**=(x,y,z) are the usual local notations in the shearless slab model [5]: radial, poloidal and toroidal coordinates. We emphasize that no further restriction on the correlation function K(.,.) are imposed.

The following results were obtained [4, 6-7]: The first one is a deterministic linear homogenous differential equation in 6 spatial and time variables, of the two-point equal time correlation function $\langle \delta\Psi(\mathbf{r},t)\delta\Psi(\mathbf{r}',t) \rangle$ where $\delta\Psi = \nabla_\perp^2 \delta\tilde{\Phi}$. Its large time behaviour was studied by the usual Liapunov method, by seeking solutions of the form [1-4] $\langle \delta\Psi(\mathbf{r},t)\delta\Psi(\mathbf{r}',t) \rangle = \exp(\lambda t) Z(r,r')$, with the main result: the closed analytic form for the exponents ($i = \sqrt{-1}, n \in \mathbf{Z}_+$):

$$\lambda_n = inV_{ds}\kappa_i + \frac{1}{2\pi}\int_0^{2\pi} K(x,u+v,z,x',u-v,z')du$$

In particular, the Liapunov exponent of the most dangerous instability is given by

$$\{\mathrm{Re}(\lambda)\}_{Maximal} = \frac{1}{2\pi}\int_0^{2\pi} K(x,u,z,x,u,z)du$$

that is always positive. From this result, we can estimate the contribution of the instability induced by external noise to the local diffusion coefficient $\delta D_{diff} \approx L(x)^2 \mathrm{Re}(\lambda)_{Maximal}$ where $L(x)$ is the length of the flux surface at the radial distance 'x'.

- *Influence of the radio-frequency heating on the impurities transport*

Experimental observations on several tokamaks have shown that the auxiliary heating by ICRH can avoid the impurity accumulation in the plasma core and, also, can be one of the sources of asymmetry and influence impurity accumulation and transport. In the previous study [8] the transport of Ni impurities in JET was studied using a multifluid model and applied specially for the center region by using experimental data from the shots 69808 (the reference discharge without RF power) and 68383 (with the maximum ICRF power of 8.3 MW applied to electrons in Hydrogen Minority Heating scheme). In the present stage, the transport of Ni impurities was analysed using experimental data from the shots 74354 (without ICRH) and 74355 (with ICRH) in JET implemented in a kinetic model [9] to analyse poloidal asymmetry and in a fluid model to obtaine the difusivity, convective velocity and peaking factor. The frequency of the ITG eigenmodes was evaluated from the approximate form of the dispersion equation [10] and the difusivity, convective velocity and peaking factor was evaluated for the evaluated eigenmode frequencies [11]. The asymmetry revealed in the kinetic model is mainly given by the asymmetry of the magnetic drift frequency. The fluid model do not reveals the asymmetry properties of the diffusivity and convective velocity.

Conclusion

The fluctuations of the density and temperature gradients give rise to a new kind of instability. The corresponding Liapunov exponents were computed by analytic methods, under very general conditions that include also those from the work programme. These results are useful for the elaboration of optimal strategy for the first principle simulation of large tokamaks. Whenever information about the spatial correlation function of the noise is available, the previous results can be used for concrete study of the instabilities in the edge plasma of existing tokamaks, in the framework of Hamaguchi-Horton model.

The transport of Ni impurity was analysed using experimental data from the shots 74354 and 74355 in JET implemented both in a kinetic and a fluid model. The asymmetry revealed in the kinetic model is mainly given by the asymmetry of the magnetic drift frequency. The fluid model do not reveals the asymmetry properties of the diffusivity and convective velocity but reproduce the suppression of the ITG turbulence in the region of heat power deposition and increasing of the convective velocity in the neighboring region

Acknowledgement

The reported work includes contributions from the following people outside the EUATOM-MEdC Association: X. Garbet, Y. Sarazin, (IRFM, EURATOM- CEA, IRFM, Cadarache, France), B. Weyssow, (Association EURATOM-Etat Belge, Department of Statistical Physics and Plasma, ULB, Bruxelles, Belgium) and JET EFDA contributors.

References

[1] Steinbrecher G., Weyssow B., Phys. Rev. Lett. 92 (2004) 125003-1 - 125003-4.

[2] G. Steinbrecher, X. Garbet, *Stochastic Linear Instability Analysis*, International Workshop on Hamiltonian Approaches to ITER Physics, 2-6 Nov. 2009, CIRM, Marseille, France.

[3] G. Steinbrecher, X. Garbet. B. Weyssow. ArXiv: (2010) 1007.0952v1 [math. PR].

[4] G. Steinbrecher, *Stochastic Methods, part III: Stochastic linear stability analysis*, Seminar, IRFM-Cadarache, France, 9 Dec. 2011.

[5] R. Balescu, Aspects *of Anomalous Transport in Plasmas*, (2005) Taylor & Francis.

[6] G. Steinbrecher, *3-dimensional linear stochastic stability analysis of the Hamaguchi-Horton equations*, MEdC Association Day, Bucharest -Magurele, Romania, 16 December 2011.

[7] G. Steinbrecher, X. Garbet, Y. Sarazin, Physics AUC, 21 (2011) 55-60.

[8] N. Pometescu, *J. Phys.: Conf. Ser.* 260 (2010) 012016

[9] T Fülöp and S Moradi, Phys. Plasmas 18 (2011) 030703

[10] N. Pometescu, Phys. AUC (2011) 48-55

[11] N. Pometescu and G. Steinbrecher, *Effects of the stochasticity and RF heating on the transport in fusion plasma*, MEdC Association Day, , Bucharest -Magurele, Romania, 16 December 2011.

ANOMALOUS TRANSPORT IN PLASMA. STOCHASTIC PROCESSES AND TRANSPORT IN TURBULENT PLASMA

I.Petrisor[1], M. Negrea[1], Dana Constantinescu[2]

[1]*Department of Physics, Faculty of Exact Sciences, University of Craiova, Romania*

[2]*Department of Applied Mathematics, Faculty of Exact Sciences, University of Craiova, Romania*

Abstract

We have analyzed the guiding centre trajectories, which are integrated in the presence of a stochastic electrostatic potential, and an explicitly given magnetic field. The purpose is to find how the transport is influenced by the different Kubo numbers. A basic result of this investigation is given.

The interaction of charged particles (electrons and different species of ions) with frozen electromagnetic fields derived from nonlinear magneto- hydrodynamic simulation was investigated. Various regimes of frozen (prescribed) turbulence were able to be generated with TURBO code like an input for the movement of charged particles in such prescribed turbulence.

In order to study the quasi-periodic oscillations of plasma parameters, a low dimensional model was proposed [P1].

It was proved that, for specific values of the parameters, the model exhibits several types of oscillations (ELM/sawtooth, chaotic, simple/double periodic orbits), in qualitative agreement with the experiments made in ASDEX-Upgrade tokamak.

For the tokamak setting, such as ITER is, the low shear of the monotonous safety factor may open new perspectives to improve the magnetic confinement. Using a mathematical model it was proved that the electron cyclotron current drive could be used to locally modify the safety factor and to create a transport barrier in a prescribed position [P2].

Papers

[1] D. Constantinescu, O. Dumbrajs, V. Igochine, K. Lackner, R. Meyer-Spasche, H. Zohm, and ASDEX Upgrade Team, A low-dimensional model system for quasi-periodic plasma perturbations, Physics of Plasmas 18, 062307 (2011), doi:10.1063/1.3600209.

[2] M.-C. Firpo, D. Constantinescu, Study of the interplay between magnetic shear and resonances using Hamiltonian models for the magnetic field lines, Physics of Plasmas 18, 032506, 2011, doi:10.1063/1.3562493.

[3] D. Constantinescu M-C Firpo, M. Negrea, I. Petrisor, C.C. Lalescu, Study of the magnetic reconnection during the sawtooth instability, Romanian Journal of Physics, 2011, Vol. 56, pp. 163–167

[4] D. Constantinescu and M-C Firpo, Mapping models for magnetic configurations in Tokamaks, Physics AUC, vol 21, 2011, 101-113.

[5] M. Negrea, I. Petrisor, H. Isliker, A. Vogiannou, L. Vlahos, D. Constantinescu, and C. C. Lalescu. On the diffusion of impurities in tokamak plasma, Romanian Journal of Physics, 56 Supplement, P. 74–78, 2011.

[6] M. Negrea, I. Petrisor, H. Isliker, A. Vogiannou, L. Vlahos and B. Weyssow, Ion and impurity transport in turbulent, anisotropic magnetic fields, Plasma Phys. Control. Fusion 53 (2011) 085022 (25pp), doi:10.1088/0741-3335/53/8/085022.

Conferences

[1] M-C Firpo D. Constantinescu, Internal transport barriers in non-twist magnetic configurations with monotonous safety factor, communication presented in "5th International Workshop on Stochasticity in Fusion Plasmas", Julich, April 11-14, 2011.

[2] D. Constantinescu, M.-C. Firpo, Modifying locally the safety profile to improve the confinement of magnetic field lines in tokamak plasmas, communication presented in "5th International Workshop on Stochasticity in Fusion Plasmas", Julich, April 11-14, 2011, published in Nucl. Fusion 52 (2012) 054006 doi:10.1088/0029-5515/52/5/054006.

[3] M.-C. Firpo and D. Constantinescu, Interplay of Magnetic Shear and Resonances in Magnetic Fusion Devices, invited talk, mini-conference on Nontwist Hamiltonian Systems: Theory and Applications, 2011 SIAM Conference on Dynamical Systems, May 22-26, 2011, Snowbird, Utah, USA.

[4] C.C. Lalescu, D. Carati, M. Negrea, and I. Petrisor, Virtual particle transport in turbulent MHD kolmogorov flow. Presentation made at the Particles in turbulence 2011 Conference in Potsdam, March 2011.

Reports

[1] C.C. Lalescu, Test Particle Transport in Turbulent Magnetohydrodynamic Structures, Ph.D. thesis, 2011.

Detailed results

1. Test particles simulations for investigate transport mechanisms of particles and/or impurities in edge turbulence simulations

We have analyzed the guiding center trajectories, which are integrated in the presence of a stochastic electrostatic potential, and an explicitly given magnetic field. The guiding center equation for our model is rewritten here for convenience:

$$d\mathbf{r}/dt = v_{||}\mathbf{b}/|\mathbf{b}| + (\mathbf{e} \times \mathbf{b})/b^2$$

The fields **e** and **b** are obtained from TURBO code and $v_{||}$ is the parallel velocity of the particle [C4]. The autocorrelation function for the "electrostatic" potential is given here:

$$<\phi(0, 0, 0, 0)\phi(x, y, z, t)> = \exp[-(x^2+z^2)/2\lambda^2_{perp}] \exp[-(|y|/\lambda_{parallel}] \exp[-t/\tau_c]$$

where λ_{perp} and $\lambda_{parallel}$ are the correlation lengths and τ_c is the correlation time. In our model we assume that the toroidal coordinate can be rescaled so that the time-dependency will no longer be needed and the autocorrelation potential function is

$$<\phi(0, 0, 0, 0)\phi(x, y, z, t)> = \exp[-(x^2+z^2)/2\lambda^2_{perp}] \exp[-(|y|/\lambda'_{parallel}]$$

where

$$\lambda'_{parallel} = \lambda_{parallel} + v_{||}\,\tau_c$$

The requirement of many modes turns into a requirement of a lot of computation time for the simulations. From a theoretical point of view, once a field is described by a spectrum that has this shape (i.e. for large k it is proportional to k^{-1}), it cannot really be described by a finite Fourier series. When it comes to numerical simulations, this theoretical limitation can be somewhat questioned. For instance, it is perfectly natural that the numerical trajectories have errors due to the use of a non infinitesimal time step. Investigations were performed for four values for each Kubo number: K = {0.2, 0.5, 1, 5} and K_s = {0.1, 0.5, 1, 2}. A seventh order spline on six points was used, with a fourth order GRK scheme. The purpose is to find how the transport is affected by the different Kubo numbers. A basic result of this investigation is given here. In Figure 1.a) the mean squared displacement (MSD) in the radial direction is shown. The transport is subdiffusive, reaching at most a regime of ~ $t^{1/2}$. This plot shows very nicely how, for a fixed electrostatic Kubo number, radial transport is reduced by increasing the shear Kubo number [P5, P6].

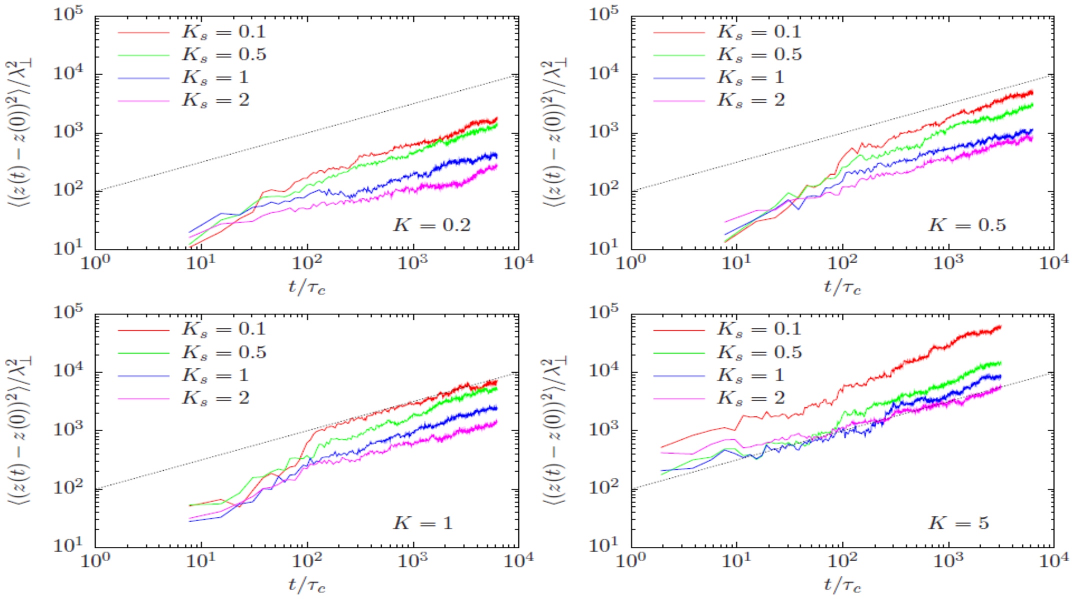

Figure 1.a - Radial MSD *for various K and K_s. A curve ~ $t^{1/2}$ is shown with a dotted line for reference*

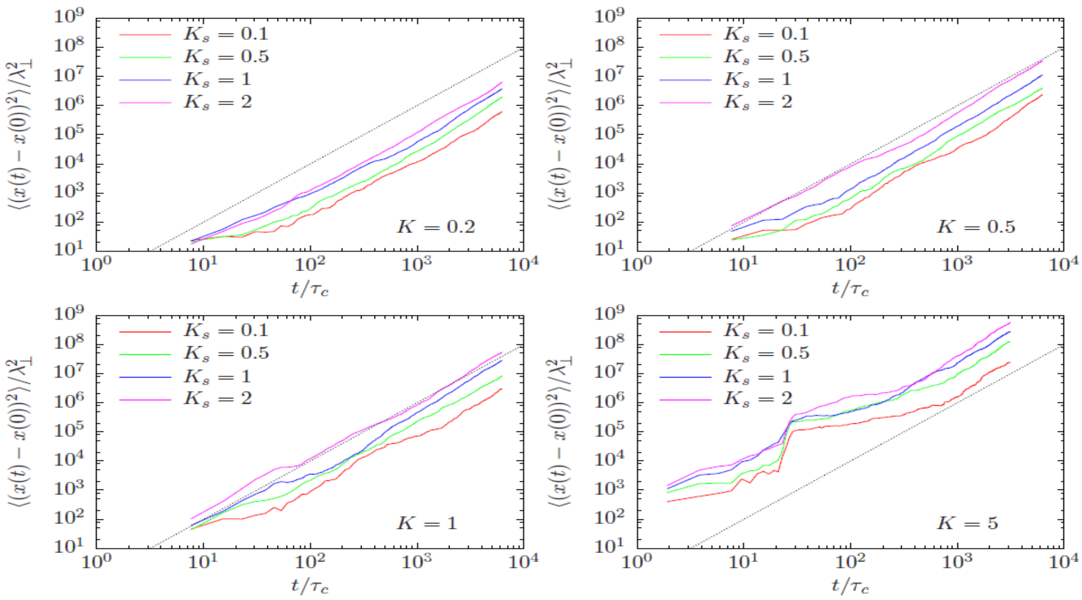

Figure 1.b - Poloidal MSD *for various K and K_s. A parabolic behavior (~t^2) is shown for reference*

The reverse happens for the poloidal transport, which is increased with the shear Kubo number [see Figures 1.b)]. The result is that in order to better contain the ions characterized by these parameters in the tokamak, shear should be increased [P5-6, C4, R1]. The studies on this project are in progress.

2. Stochastic magnetic field line diffusion and the influence of MHD modes on electron transport

We considered in slab sheared geometry an electrostatic turbulence represented by an electrostatic stochastic potential $\Phi(\mathbf{X}, Z, t)$, where $\mathbf{X} = (X, Y)$ are the Cartesian coordinates in the plane perpendicular to the main magnetic field. The z component of the magnetic field B_z depends on the radial coordinates X and has the form $B_z = B_0(1 + X/R)^{-1}\mathbf{e}_z$. The global magnetic field is unperturbed and it depends on the distance from the main symmetry axis Oz having the form

$$\mathbf{B} = B_0[b(X)\mathbf{e}_z + s(X)\mathbf{e}_y]$$

where $s(X) \equiv XL_s^{-1}$ with L_s the shear length and $b(X) \equiv (1 + X/R)^{-1}$ with R the major radius of the tokamak. The guiding center trajectories are determined from

$$\frac{d\mathbf{X}}{dt} = U\mathbf{b} + \frac{\mathbf{E} \times \mathbf{B}}{B^2}$$

where U is the parallel velocity, which we will approximate with the thermal one, i.e. V_{th}. Dimensionless quantities x, y, z, τ and φ are defined in terms of the dimensional variables by the following expressions

$$\mathbf{x} = \frac{\mathbf{X}}{\lambda_\perp}; \quad z = \frac{Z}{\lambda_\parallel}; \quad \tau = \frac{t}{\tau_c}; \quad \Phi(\mathbf{X}, t) = \varepsilon\varphi\left(\frac{\mathbf{X}}{\lambda_\perp}, \frac{Z}{\lambda_\parallel}, \frac{t}{\tau_c}\right)$$

Here, $\lambda_\perp$ is the perpendicular correlation length, $\lambda_\parallel$ is the parallel correlation length along the main magnetic field, τ_c is the correlation time of the fluctuating electrostatic field and ε is a dimensional quantity measuring the amplitude of the electrostatic field fluctuation. With the parameters defined above, the guiding center equations become:

$$\frac{dx}{d\tau} = -K(1 + \alpha_R x)\frac{\partial\varphi}{\partial y}$$

$$\frac{dy}{d\tau} = K(1 + \alpha_R x)\frac{\partial\varphi}{\partial x} + K_s x$$

$$\frac{dz}{d\tau} = K_{zs} x \frac{\partial\varphi}{\partial x} + K_z b^{-1}(\alpha_R x)$$

The study is in progress and the reversed shear will be analyzed.

3. Studies of particle transport using stochastic modeling with application to the edge turbulent transport including the study of turbulent zonal flow

The wider purpose of this work is the understanding of particle transport in turbulent (fully ionized) plasma. Plasmas are generally composed of several species of charged particles, but in this approach the plasma is modelled with the incompressible MHD equations. This means only a main species is considered; the particles themselves are treated as passive. This is a common approximation for impurities in fusion plasmas. The interaction of charged particles (electrons and different species of ions) with frozen electromagnetic fields derived from nonlinear magneto- hydrodynamic simulation was investigated. Various regimes of frozen (prescribed) turbulence were able to be generated with TURBO code like an input for the movement of charged particles in such prescribed turbulence. We investigated the effect of a given turbulence in the transport of different charged particles. Few cases of superdiffusion and subdiffusion, next to normal diffusion, depending on the different turbulence regimes have been investigated in order to evaluate the full transport coefficients and anomalous diffusion exponents as functions of the Reynolds number and particle species. The approximation of a large charged impurity, for which collisions can be approximated by a drag term, is:

$$\dot{\mathbf{r}} = \mathbf{v}$$

$$\dot{\mathbf{v}} = \alpha(\mathbf{e}(\mathbf{r}) + \mathbf{v} \times \mathbf{b}(\mathbf{r}))$$

where: α corresponds to the charge to mass ratio in the Lorentz force, and η is the inverse of a friction timescale. This model is a natural extension of the usual model for particles with mass moving in turbulent Navier-Stokes fluids. For this particular study, a turbulent regime of $\mathrm{Re} = \mathrm{Re}_m = 100$ was chosen, in order to be built upon in future work. For the particles, two values of β (1 and 10) are investigated, and four pairs (γ, St): $(1/2,1),(1/2,1/10)$, $(1/4,1)$ and $(1/4,1/10)$.

The fluid equations are solved with a pseudo-spectral solver, in a periodic box of dimensions $6\pi L \times 2\pi L \times 2\pi L$, using a uniform, rectangular grid with $784 \times 128 \times 128$ nodes [C4].

For the needed numerical simulations we used the computer facilities of ULB, Belgium, in collaboration with the research group from ULB, Belgium. The study is in progress.

4. Development of non-linear MHD models of ELM cycle, including the effect of magnetic or pellet perturbations

In [P1] we proposed a low dimensional model describes the quasi-periodic dynamics of plasma using the displacement “y” of the magnetic field end the pressure gradient “z” as main unknowns. This “minimal model” describes a system with interplay of the drive and relaxation dynamics. It is based on two equations: the first one responsible for the relaxation dynamics and the second for the drive:

$$\frac{d^2}{dt^2} y = (z-1)y - \delta \frac{d}{dt} y \qquad \frac{d}{dt} z = \eta\left(h - z - y^2 z\right) \tag{1}$$

The rich dynamics of the system and some bifurcation phenomena were analyzed for various values of the parameters (the normalized power input into the system *h*, the dissipation/relaxation of perturbations δ, and the ratio η between the normal heat diffusion and the heat diffusion due to perturbations). The most important feature of our system is the fact that the instability can develop only above the critical input power $h > 1$. This reminds a typical behavior of the plasma in such regimes. In spite of its simplicity, the system (1) exhibits a complicate behavior for various combinations of parameter values. The main dynamical zones in the plane of parameters (δ, η), for $h = 1.5$ are presented in Figure 2a.

In zone I, we have damped oscillations. In zone II, simple periodic oscillations occur, while in zone III, we observe double periodic oscillations. In zone IV, chaotic oscillations are observed and in zone V, all orbits are periodic. When (δ, η) are near the upper boundary of zone V, the period of the oscillations is short and the rise time is comparable with the crash time. When η decreases the oscillations are mainly of ELM/saw tooth type, with a long rise time and a short crash time.

From the estimates obtained in experiments (red box in Figure 2a), $8\cdot 10^{-3} \le \delta \le 8\cdot 10^{-1}$ and $6\cdot 10^{-4} \le \eta \le 4\cdot 10^{-2}$, we can conclude that very different plasma behavior can be obtained for one and the same heating power: ELM/sawtooth oscillations, chaotic oscillations, and double-periodic oscillations.

In order to include the pellet injection's effects in the model we introduced the pellet perturbation $P(t)$ in the equation describing the relaxation dynamics. The system can be written in the form

$$x' = [z + P(t) - 1]y - \delta x, \quad y' = x, \quad z' = \eta\left(h - z - y^2 z\right) \tag{2}$$

We considered a periodic perturbation of Gaussian-type

$$P(t) = a \cdot \exp\left(-\left(t - t_{period} \cdot \mathrm{int}\left(t / t_{period}\right) - \delta_p\right)^2 / b\right)$$

where a is the perturbation amplitude, t_{period} is the perturbation, period, δ_p is the perturbation shift, and b is the perturbation width. The symbol "int" means integer.

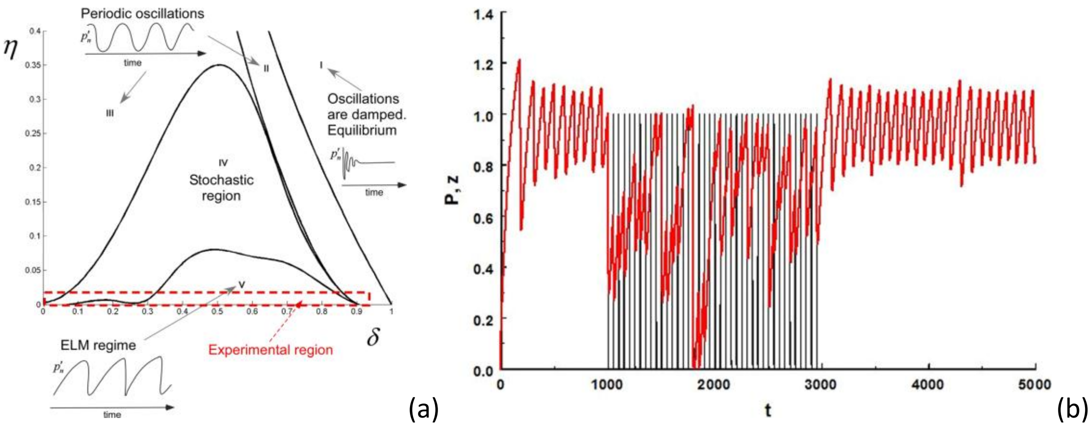

Figure 2 - (a) Dynamical zones of oscillations in (δ, η) plane for $h = 1.5$; (b) ELMs (z, red) with pellet injection. Pellet injection was switched on at $t = 1000$ and switched off at $t = 3000$. Perturbations $P(t)$ are shown by black lines; their amplitude is normalized to unity

This perturbation changes the plasma stability but does not affect the power balance equation, which is the case of a real pellet. To illustrate how this model works, we choose the following values of the system parameters: $\eta = 0.009$, $\delta = 0.2$, $h = 1.5$, which lead us into the space where ELMs exist (zone V, in Fig. 2). In Fig. 2b is presented the evolution of ELMs before, in the presence and after the activation of pellet perturbation.

5. **The investigation of the effects of a non-axisymmetric magnetic field on the transport properties (formation of the transport barriers) and the characterization of edge turbulence**

Using some Hamiltonian models for the magnetic field lines, the dual impact of low magnetic shear is shown in a unified way. The approach can be applied to assess the robustness versus magnetic perturbations of general (almost) integrable magnetic steady states, including non-axisymmetric ones such as the important single-helicity steady states. This analysis puts a constraint on the tolerable mode amplitudes compatible with ITBs and may be proposed as a possible explanation of diverse experimental and numerical signatures of their collapses. The Hamiltonian of the model (i.e. the poloidal magnetic flux): $H(\theta,\psi,\zeta)=\int d\psi / q(\psi)+K\frac{2\psi}{1+\psi}\sum_{n=-M}^{M}\cos(4\theta-n\zeta)$, depends on the safety factor $q=q(\psi)$ and on the perturbation amplitude *K*.

It was proved that, away from resonances, the low magnetic shear induces a drastic enhancement of magnetic confinement that favors robust internal transport barriers (ITBs) and stochastic transport reduction. When low shear occurs for values of the winding function of the magnetic field lines close to low-order rationals, the amplitude thresholds of the resonant modes that break internal transport barriers by allowing a radial stochastic transport of the magnetic field lines may be quite low.

In order to quantify the impact of the specific value of the minimum of the *q*- profile of its inverse, we defined by K_c the minimal value of the stochasticity parameter *K* above which there exists some initial condition with $\psi<0.1$ whose evolution escapes the physically accessible phase space by crossing the border $\psi=1$ in less than 5000 toroidal turns [P2-P4]. In Figure 3 one can observe that the largest values of K_c correspond to local maxima of the winding function (inverse of the safety) factor which are far from the main rationales 1/4, 2/4, 3/4 etc.

Other aspects related to the existence of internal transport barriers in Hamiltonian models for the description of magnetic field lines in tokamaks were pointed in [P2-P4, C1-C3].

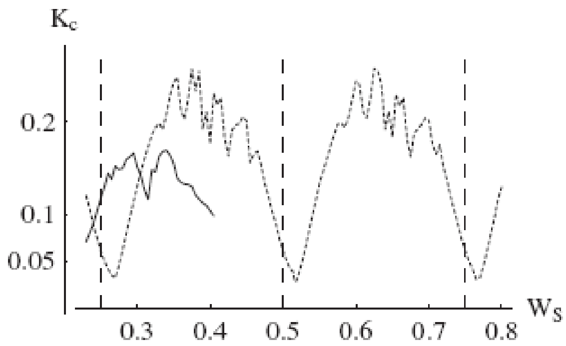

Figure 3 - The critical value of K_c *as a function of the inverse of the minimum of the q-profile,* W_s*, for the parabolic family* $W_p(\psi)=W_s-c(\psi-0.5)^2$ *(dashed line) and in the linear case* $W_l(\psi)=W_s-c(\psi-0.5)$ *(plain line). The vertical dashed lines mark the locations of the resonances* $W_s=1/4,\ 2/4,\ 3/4$

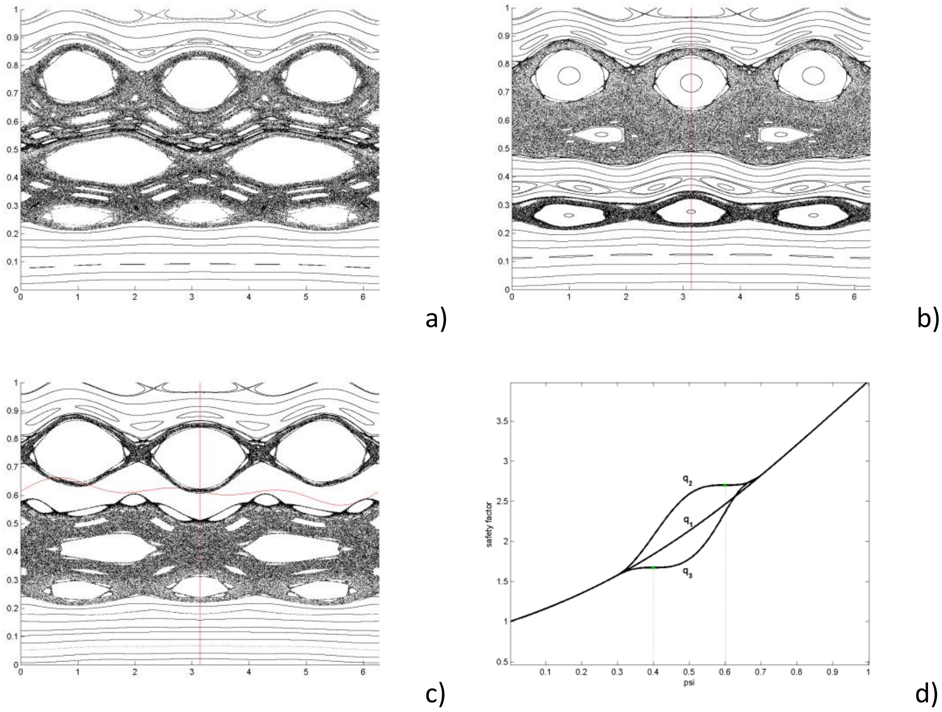

Figure 4 - a) Phase portrait of the uncontrolled system; b) Phase portrait of the controlled symmetric tokamap ($\psi_1 = 0.3$, $\psi_0 = 0.4$ and $\psi_2 = 0.7$); c) The phase portrait of the controlled symmetric tokamap ($\psi_1 = 0.3$, $\psi_0 = 0.6$, $\psi_2 = 0.7$); d) q_1 is the safety factor of the initial tokamap; q_2 is the safety factor of the controlled tokamap from Fig. 4.b); q_3 is the safety factor of the controlled tokamap from Fig. 3.c)

In [C2] a methodology to improve the confinement of the magnetic field lines though the creation of transport barriers is proposed. A local modification of the safety profile creating a low shear zone is shown to be sufficient to locally enhance drastically the regularity of the magnetic field lines without requesting a reversed shear. A possible mathematical procedure to flatten locally the winding profile $W(\psi)$ in order to produce a transport barrier preventing the outer diffusion of magnetic field lines is the following. Figure 4 exemplifies the theoretical results. In Figure 4.a) is shown a chaotic phase portrait, without transport barriers separating significant chaotic zones. The main modes (3,2), (2,1), (3,1), having the rotation numbers 2/3, respectively 1/2 and 1/3 can be observed around $\psi = 0.25$, respectively $\psi = 0.45$ and $\psi = 0.75$. Some phase portraits of the controlled system (Figures 4

3.b), 3.c)) point out the existence of internal transport barriers in the low shear zone, visible in Figure 4.d). The optimal benefits of low shear are obtained when the value q_0 of the safety profile in the low shear zone is sufficiently far from the main resonance values m/n with low m and n, in the case of large enough values of those (m, n) mode amplitudes. A practical implementation in tokamak plasmas should involve electron cyclotron current drive to locally modify the magnetic shear.

Conclusion

A more detailed analysis of this problem is extremely necessary. The methods are relatively general and can be used for a large class of problems where “turbulent” fields are prescribed rather than taken from direct numerical simulations of fluid equations. Furthermore, even if the methods were constructed and presented in the context of particles in fluid turbulence, they can be successfully applied to problems of physics that are quite distinct. The interaction of charged particles (electrons and different species of ions) with frozen electromagnetic fields derived from nonlinear magneto-hydrodynamic simulation was investigated. Various regimes of frozen (prescribed) turbulence were able to be generated with TURBO code like an input for the movement of charged particles in such prescribed turbulence. For the needed numerical simulations we used the computer facilities of ULB, Belgium, in collaboration with the research group from ULB, Belgium. The study is in progress. We intend to continue the project PTRANSP (HPC-FF) in collaboration with the research group from ULB, Belgium. The credit (mono-processor hours) is given monthly. We intend to investigate mainly the relative influence of large scale field structures versus small scale fluctuations on particle transport. The conclusion can be drawn that pellet injection increases the ELM frequency almost by a factor two. After pellet injection stops, the number of ELMs is almost the same as before of injection. It is interesting to note that not all pellets trigger an ELM. For example, the pellets at t = 1400, 1700, 1950, 2350, and 2800 do not trigger an additional ELM (z continues to rise in spite of pellet injection).This prediction coincides with experimental observations.

The model can be generalized to include external perturbations, for example, the pellet injection to influence ELMs or the electron cyclotron current drive to influence saw teeth. The proposed model does not qualify for a complete description of the plasma phenomena such as ELM/saw tooth, which require full scale nonlinear simulations. However, we believe that our model provides useful tools for understanding the basic physics.

Acknowledgement

The reported work includes contributions from the following people outside the EURATOM-MEdC Association: Heinz Isliker, Anastasios Vogiannou, Loukas Vlahos (EURATOM - Hellenic Republic Association, Section of Astrophysics, Astronomy and Mechanics, Department of Physics, University of Thessaloniki, Thessaloniki, Greece), Daniele Carati and Cristian Lalescu (EURATOM – Belgium State Association, Statistical and Plasma Physics, Universite Libre de Bruxelles, Belgium), Marie-Christine Firpo (Laboratoire de Physique et Technologie des Plasmas (CNRS UMR 7648), Ecole Polytechnique, 91128 Palaiseau Cedex, France), O. Dumbrajs (Association Euratom-UL, Institute of Solid State Physics, University of Latvia, Latvia), V. Igochine, K. Lackner, R. Meyer-Spasche, H, Zohm (Max-Planck Institut für Plasmaphysik, Association Euratom-IPP, Germany).

NONLINEAR EFFECTS OF THE ExB DRIFT ON TRANSPORT AND STRUCTURE GENERATION IN TURBULENT PLASMAS

M. Vlad, F. Spineanu

National Institute of Laser Plasma and Radiation Physics

Abstract

Ion trajectory trapping (or eddying) in the structure of the turbulent potential has complex effects on transport, which we have studied during the last decade by developing a new semi-analytical approach. This work was continued in 2011 with (milestone 1) and it was extended to electron heat transport (milestone 2) and to the self-consistent study of turbulence evolution (milestone 3).

1) Transport and convection of impurities and particles in edge plasma turbulence

A nonlinear effect that appears in toroidal geometry due to the poloidal motion of the ions induced by the motion along magnetic lines and by the flows generated by the moving potential contributes to impurity pinch. This theoretical results obtained in 2009 were developed by evaluating the strength of this process in conditions relevant for JET and ITER edge plasmas. We have shown that this nonlinear transport mechanism can determine a significant contribution to ion transport.

2) Regimes of electron transport in small scale turbulence

Electron trapping can appear in small scale turbulence of the ETG type. A theoretical study of electron heat transport based on test particle approach was developed for determining the regimes of electron transport. The effects of large scale potential fluctuations on electron transport were analyzed in this frame. Anomalous regimes with increased diffusion were shown to appear in the presence of electron trapping.

3) Nonlinear evolution of drift type turbulence and particle trapping in the turbulent potential

We have shown that the evolution of the drift type turbulence beyond the quasilinear stage is strongly influenced by ion stochastic trapping combined with the turbulent potential motion with the diamagnetic velocity. This conclusion is drawn from an analytical study of test modes on turbulent plasmas.

Papers

[1] M. Vlad, F. Spineanu, *Nonlinear evolution of drift turbulence: inverse cascade, zonal flows, intermittency*, Romanian Journal of Physics 56 Supplement (2011) 23-29.

Conferences

[1] M. Vlad, F. Spineanu, *Nonlinear evolution of drift turbulence: inverse cascade, zonal flows, intermittency*, 38th EPS Conference on Plasma Physics, June 27 – July 1 2011, Strasbourg, France, oral paper O4.416.

[2] M. Vlad, F. Spineanu, *Nonlinear stochastic advection and structure generation in two-dimensional ideal fluids*, 64th Annual Meeting of the APS Division of Fluid Dynamics, November 20–22, 2011, Baltimore, Maryland, USA, oral presentation M6.00008.

Reports

[1] M. Vlad, F. Spineanu, Nonlinear evolutionof drift type turbulence and particle trapping in the structure of the turnulent potential, Association Day Meeting, Bucharest, December 2011.

Detailed results

1. Transport and convection of impurities and particles in edge plasma turbulence

The fluxes of impurities show in some experiments a strongly anomalous diffusion. In general it accompanies plasma rotation which is known to affect the instabilities, in particular the Ion temperature gradient - driven turbulence. Since the motion of particles takes place in a turbulent plasma dominated by eddies with large radial extension, the changes induced by rotation will also modify the fluxes. There are at least two ways by which the transport fluxes are modified when the background turbulence changes due to rotation:

1) the radial correlation length of the turbulence is reduced by the sheared flows, thus leading to a decrease of the typical random step of the particles in a diffusive regime
2) the coexisting dynamical behaviors of trapping versus long jumps is affected by the change in the turn-over time of the eddies and of the geometry of moving separatrices

The first process must be investigated on the basis of decorrelations induced by regular patterns of flow and can be done within the paradigm of diffusion. It regards the bulk of particle density and leads to redefinition of the diffusion coefficients on the basis of growth rates and eigenfunction adapted to the presence of rotation.

The second process affects a smaller number of particles but it is highly efficient in modifying the extreme behavior consisting of either trapping or the fast propagation. These processes have the usual nature of statistical events but they are *atypical* and can be quantitatively important. One example is the processes that are *non-self-averaging*.

Generically a particle can be trapped in an eddy and remain there until a collision or a scattering on a transient wave-like event allow it to escape. This can be represented as a barrier-type problem with the particularity that the height of the barrier is now itself fluctuating. There are studies of non-self-averaging statistical processes issued from a fluctuation of the height of the energy barrier, with the result that non-self-averaging is due to the variation from sample to sample, equivalently, from a state of the random environment to another state. The time to pass over the barrier is in any case random. But, if the free-energy height of the barrier is not changing, the random process of overcoming the barrier will self-average and will not vary from sample to sample. A diffusive behavior is expected. If the turbulent environment is affected itself by a random factor then the process is non-self-averaging. A small amount of particles will have different, extreme, statistics. This is relevant for impurities since in experiments with Argon seeding it has been observed that a fraction of the Argon atoms travel to the center in a faster than a diffusive flux.

Ion dynamics can be modeled as a random-random process, described by the Langevin equation

$$\dot{x} = \frac{1}{\gamma} F(x) + \eta(t).$$

Particle motion is determined by a random environment represented by a quenched random force F with the statistical properties

$$\langle F(x) \rangle = F_0$$
$$\langle F(x)F(x') \rangle - \langle F(x) \rangle^2 = \sigma\delta(x-x')$$

and by a noise η(t) representing collisions, which is a zero average Gaussian white noise. Depending on the noise amplitude, several types of behavior appear: anomalous dispersion for small amplitude, anomalous average displacement at intermediate values and normal diffusion for large amplitude noise.

The above discussion and analytical results show the importance of collisions for impurity and ion transport and the necessity to introduce them in the 2-dimensional test particle model.

A new mechanism of impurity accumulation/loss was found in 2009 [8]. It is a nonlinear effect connected to the ratchet pinch [4-6] generated by the gradient of the magnetic field in turbulent plasmas. It appears in toroidal geometry due to the poloidal motion of the impurity ions induced by the motion along magnetic lines and by the flows produced by the moving potential. This poloidal motion determines a time oscillation of the peaking factor (defined as the ratio of the ratchet pinch velocity and the diffusion coefficient). The time oscillation is determined by the variation of the confining magnetic field on the magnetic surface. Particle collisions are included and their dependence space dependence is taken into account. A computer code based on Monte Carlo simulation was developed.

The collisional diffusion coefficient depends on the mass number A and charge Z through the Coulombian logarithm. It also depends on space through the Larmor radius due to the magnetic field inhomogeneity as $\chi=\chi_0(1+x_1/R_0)^2$, where χ_0 corresponds to the reference magnetic field B_0. We have shown in [6] that collisions can determine the decrease and also increase of the ratchet velocity, depending on parameters of the turbulence. These are nonlinear effects that appear in the presence of trapping or eddying motion, i.e. when the turbulence has a slow time variation and the collisional perturbations are weak. For stronger perturbations, trapping is eliminated and the ratchet pinch is reduced and destroyed.

An important effect is produced by the inhomogeneity of the collisional diffusivity due to the gradient of the magnetic field. It determines a direct contribution to the pinch: an average collisional velocity appears due to the space dependence of the diffusivity χ induced by the magnetic field. In the range of the collisional diffusivity χ_0 around 0.1, the ratchet velocity has a strong dependence of this parameter, in the sense that large variations of the pinch velocity appear for relatively small variations of χ_0. The diffusivity of impurity ions for ITER plasmas is expected to be in this range. Consequently, the mass-charge dependence given by collisions determines important variation of the ratchet pinch. The latter decreases with the increase of A.

A different periodic poloidal motion of the particles appears in the nonlinear stage of the drift turbulence (see Section 3). The trapped particles are advected by the moving potential with the effective diamagnetic velocity while the free ones move in the opposite direction. These particle flows compensate such that the total flux is zero.

The "macroscopic" effect of the pinch velocity appears in the peaking factor $p=aV_R/D$, which is the measure of direct to diffusive transport. Here a is plasma radius, V_R is the local ratchet pinch velocity and D is the local diffusion coefficient. For quasilinear turbulence, this ratio does not depend on the poloidal motion of the ions. In the nonlinear stage of turbulence, the variation of the peaking factor on the magnetic surface appears, with larger values in the high field side.

The direction of the pinch velocity is toward the symmetry axis of the torus. A periodic poloidal motion determines a pinch velocity that change periodically from inside to outside of the plasma. For uniform poloidal rotation, the larger values of p inside torus determine a loss mechanism. If the poloidal rotation is not uniform, the loss mechanism can be amplified (for smaller rotation velocity inside the torus) or it can be attenuated or even transformed in an accumulation mechanism (if the rotation velocity is smaller outside the torus). The shape of the plasma also contributes to this mechanism.

The series of calculations performed with the Monte Carlo code in toroidal geometry have shown that in the conditions of JET plasmas impurity accumulation is much enhanced by the above mechanism (macroscopic motion), especially for small mass particles. Collisions do not always hinder the process and, in some conditions, contribute to a weak increase of the effect. Preliminary results for ITER plasmas show that impurity accumulation is weaker in this case. We note that the model contains many parameters which can strongly influence the results and that further analysis is necessary in connection with experimental and simulation results.

2. Regimes of electron transport in small scale turbulence

A theoretical study of electron heat transport based on test particle approach is developed. Test particle approach means essentially to consider a given turbulence (described by a known spectrum or Eulerian correlation). The heat transport coefficient is evaluated using the “test particle expression”, which is obtained writing the formal solution for the fluctuation of the temperature as the integral along electron trajectories and by using the scale separation of fluctuations and averages. The transport coefficients for various models for the spectrum, including the existence of large scale potential fluctuations is obtained. This semi-analytical approach is in some sense independent and complementary to the self-consistent simulations. It cannot include self-consistence condition but it can determine the regimes of transport as functions of turbulence and plasma parameters.

A computer code was developed based on the decorrelation trajectory method [1]. It determines the transport coefficients for electrons and ions for two scale stochastic potential. The model includes the parallel motion, the diamagnetic velocity (potential rotation) and plasma rotation, collisions and the parallel motion. The diffusion coefficients are determined using the decorrelation trajectory method [1, 2]. The later is based on a set of smooth trajectories determined by the Eulerian correlation of the turbulence and by all the other components of particle motion.

We have considered a multi-scale spectrum of the stochastic potential, modelled by the superposition of two Gaussian components one with small wave numbers and the other displaced at large wave numbers. We have previously shown that the transport does not strongly depend on the shape of the spectrum and thus this simplified model is adequate for determining the transport regimes.

We have shown that electron trapping can appear and that this process determines a reach class of anomalous diffusion regimes. Trajectory trapping is effective when the combined action of the decorrelation mechanisms is weak enough. Trapping influences not only the values of the diffusion coefficients but also their scaling laws.

Well defined transport regimes can be identified only when there is no trapping (quasilinear conditions) or when one of the decorrelation mechanisms dominates. This corresponds to the case when one of the characteristic decorrelation times is much smaller than the others. When they have comparable values, the diffusion coefficient is a complicated function of all these characteristic times. The model is rather complex and contains 10 independent parameters: seven parameters that describe the turbulence, the collisional diffusion coefficient χ, the poloidal rotation velocity V_p and the parallel velocity v_z.

We have shown that it is possible to obtain transport coefficients that are completely different of the sum of the transport coefficients produced separately by the large scale turbulence and respectively small scale turbulence even when the spectrum is composed by two well separated parts. Since the calculation time for exploring the space of the 10 independent parameters of the model is too long, we have investigated until now two physically relevant domains. First domain corresponds to electron heat transport in small scale turbulence, taking into account collisions, poloidal rotation and parallel motion. The second study evaluates the influence of the large scale stochastic potential on electron heat transport.

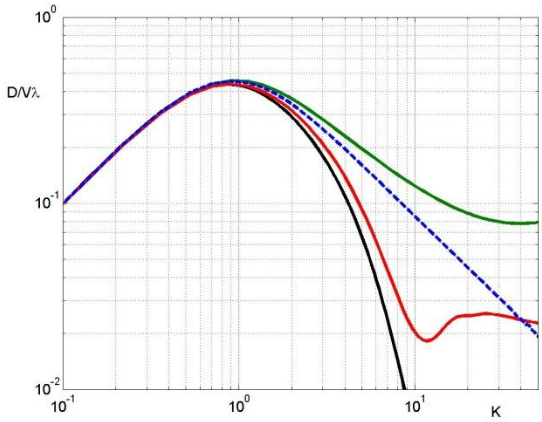

Figure 1. The diffusion coefficient as function of K for several values of V_p/V, $\chi/V\lambda$: 0, 0 (blue); 0.4, 0 (black); 0, 0.02 (green); 0.4, 0.02 (red).

2.1. Electron heat transport in ETG type turbulence

We have shown that electron trapping or eddying can appear and that in these conditions the transport is strongly modified. The collisions and the poloidal rotation can have very strong influence in these conditions if they are weak enough. An example of the strong influence produced by the decorrelation mechanisms is presented in Fig. 1. The diffusion coefficient D_0 due to the ExB drift for a time dependent potential is represented as function of the Kubo number by the blue line. The diffusion coefficient is sensibly increased if particle collisions with a small collisional diffusivity $\chi \ll V\lambda$ are considered (green line). We note that the direct contribution of collisions χ is negligible in Fig. 1.

A weak poloidal rotation with a velocity V_p that is smaller than the amplitude V of the ExB drift determines a strong decrease of the radial diffusion (black line). When poloidal rotation and collisions act together, the diffusion coefficient (red line) can be smaller or larger than D_0, depending on the values of K, χ and V_p. Fig. 1 also shows that at small Kubo numbers (in the absence of trapping) the diffusion coefficients are not changed.

2.2. Effects of the large scale turbulence on the electron transport

Essentially, the large scale determines local average velocities $\mathbf{V}_L$. They are randomly oriented and combine with the poloidal rotation of the electrons. Strong influence on electron heat transport appears when V_L are smaller than the amplitude of the small scale ExB drift.

For V_p=0, the large scale average velocity is tangent to the contour line of the large scale potential. In the presence of trapping in the structure of small scale potential, $\mathbf{V}_L$ determines a strong modification of the diffusion, which becomes non-isotropic with the diffusion coefficient along $\mathbf{V}_L$ much larger than in the perpendicular direction. Also, an average flow of the non-trapped electrons appears in the direction of the average velocity. These effects are similar to those induced by the poloidal motion in single scale turbulence but with a very important difference. The much increased parallel diffusion and the parallel velocity induced by the poloidal velocity do not contribute to the effective transport because they are in the magnetic surface of the confining configuration. The parallel effects induced by the large scale have the random orientation of the contour lines of the large scale potential. Thus, the parallel increased diffusion has a radial component, which can strongly increase the effective electron heat transport. Moreover, the average parallel velocity, which has random orientation, determines a supplementary term in the mean square displacement that corresponds to a new contribution to the electron diffusion coefficient. The latter depends on the fraction of trapped electrons and can bring a significant contribution.

In the presence of poloidal rotation velocity V_p, the transport becomes much more complicated due to the contribution of V_p to the decorrelation from both small and large scale potential. Large variations of the diffusion coefficient appears for small changes of the parameters, which are not easy to understand. When the local average velocity produced by the large scale potential is larger than the amplitude of the small scale potential fluctuations, the electron heat transport is strongly reduced.

3. Nonlinear evolution of drift type turbulence and particle trapping in the turbulent potential

We have shown that trajectory trapping or eddying in the structure of the turbulence potential is the main physical reasons for the strong nonlinear effects that were observed in numerical simulations: inverse cascade, zonal flows, nonlinear damping and intermittent evolution. The conclusion is drawn from a study of test modes on turbulent plasmas, which is based on a new analytical method. This is a Lagrangian approach that describes the effects of trapping on trajectory statistics. We consider the drift instability in slab geometry with constant magnetic field (along z axis). We start from the basic gyrokinetic equations for the distribution of electrons and ions.

Test modes on turbulent plasma with given statistical characteristics of the stochastic potential were studied. Their growth rates γ and frequencies ω are determined as functions of the statistical characteristics of the background turbulence with potential $\phi(x,t)$. A small wave perturbation $\delta\phi$ is introduced and the solutions for the perturbations of electron and ion densities are obtained using the method of the characteristics as integrals along particle trajectories in the background potential of the source terms determined by the density gradient (paper [1], conference [C1]). The background turbulence produces the stochastic E×B drift that influences the distribution of the ion displacements P(x,t). The average propagator is determined using P(x,t) in the background potential. We have shown that P(x,t) is strongly modified when trapping appears [1,2]. Trapped trajectories form quasi-coherent structures, which determine non-Gaussian P(x,t) with a narrow peak. Trapping combined with the motion of the potential with the diamagnetic velocity V_{*e} determines ion flows when the amplitude of the E×B velocity is larger than V_{*e}. The trapped ions move with the potential while the other ions drift in the opposite direction. Although these opposite (zonal) flows compensate such that the average displacement is zero, they determine the splitting of P(x,t). The averages in the ion perturbation are estimated using these results and the solution of the dispersion relation is obtained (see paper [1]).

The growth rate and the frequency of the drift modes give an image of the turbulence evolution. We show that, starting from a weak initial perturbation with very broad wave number spectrum, a sequence of processes appear at different stages as transitory effects and that the drift turbulence has an oscillatory (intermittent) evolution.

3.1. Trajectory diffusion and damping of small k modes

At small amplitude of the turbulence a stabilizing contribution due ion diffusion appears, which leads to the damping of the large k modes and to maximum growth rate at $k\sim 1/\rho$. The well known result of Dupree [8] is reproduced.

3.2 Trajectory structures and large scale correlations

The increase of the turbulence amplitude V above the effective diamagnetic velocity V_{*e} determines ion trapping or eddying. As we have shown, this strongly influences the statistics of trajectories. The distribution of the trajectories is not more Gaussian due to trapped trajectories that form quasi-coherent structures. At this stage the trapping is weak in the sense that the fraction of trapped trajectories n_{tr} is much smaller than the fraction n_f of free trajectories ($n= n_{tr}/n_f <<1$). The peaked distribution modifies the average propagator by the factor which is determined by the average size S_i of the trapped trajectory structures. This factor modifies only the effective diamagnetic velocity in a way that is similar with the finite Larmor radius effect. The displacement of the position of the maximum of γ toward small k appears. The maximum of γ moves to smaller k values of the order of $1/S_i$ and the size of the unstable k range decreases. The maximum growth rate decreases. Thus, ion trapping determines the increase of the correlation length of the potential and the decrease of the average frequency (proportional with k_2). In this nonlinear stage, turbulence evolution becomes slower and leads to ordered states (narrower spectra with maximum at smaller k).

3.3. Ion flows and turbulence damping

The evolution of the potential determines the increase of the fraction of trapped ions. This determines a non-negligible average flux of the particles trapped in the moving potential. As the E×B drift has zero divergence, the probability of the Lagrangian velocity is time invariant, i. e. it is the same with the probability of the Eulerian velocity. The average Eulerian velocity is zero and thus the flux of the trapped ions that move with the potential has to be compensated by a flux of the free particles. These particles have an average motion in the opposite direction with a velocity V_f such that $n_{tr}\ V_{*eff} + n_f\ V_f = 0$. The velocity on structures method that we have recently developed shows that the probability of the displacements splits in two components that move in opposite direction. Thus, opposite ion flows are generated by the moving potential in the presence of trapping. They modify both the effective diamagnetic velocity and the growth rate. It determines the increase of the effective diamagnetic velocity and consequently the decrease of the growth rate first for small k and as n increases for all values of k.

3.4. Generation of zonal flow modes

The density fluctuations in the background turbulence determine a new term in the growth rate. This term is not zero for $k_2=0$ as the drift modes growing rate and it can generate modes with $k_2=0$ and $\omega=0$ (zonal flow modes). We have estimated this term for different amplitudes of the turbulence. For quasilinear turbulence this term is zero and at weak trapping it is negligible. Only for strong turbulence when trapping is strong this contribution becomes important due to the ion flows produced by the moving potential. This effect is essentially determined by the anisotropy that is generated by the difference in the average velocity of the trapped ions and the average velocity of the free ions. When n=1, the ion flows are symmetrical and R_{11} vanishes. A clear connection of the zonal flow modes with the ion flows induced by the moving potential appears.

3.5. Effects of a DC electric field

We have also studied the effects of a (constant) electric field E on the evolution of the drift turbulence. Several regimes were identified, which depend on the average poloidal rotation velocity $v_E = E/B$, including its orientation. Interesting effects appear in the conditions where ion trajectory trapping is present. When v_E is along the diamagnetic velocity, it determines the decrease of the effective velocity of the potential. This leads to the decrease of the amplitude of the ExB drift for which the nonlinear damping appears. Consequently, the maximum of the amplitude of the intermittent potential decreases. An electric field that produces rotation in the opposite direction determines intermittent evolution of the turbulence with increased maxima.

References

[1] M. Vlad, F. Spineanu, J. H. Misguich, R. Balescu, Phys. Rev. E 58 (1998) 7359.

[2] M. Vlad, F. Spineanu, Phys. Rev. E 70 (2004) 056304.
[3] M. Vlad, et al., Plasma Physics and Controlled Fusion **46,** 1051 (2004).
[4] M. Vlad, F. Spineanu, S. Benkadda, Physical Reviews Letters 96 (2006) 085001.
[5] M. Vlad, F. Spineanu, S. Benkadda, Physics of Plasmas **15** (2008) 032306.
[6] M. Vlad, F. Spineanu, S. Benkadda, Plasma Physics Controlled Fusion **50** (2008) 065007.
[7] M. Vlad, F. Spineanu, Annual Report 2009 of the MEdC Association.
[8] T. H. Dupree, Phys. Fluids 15 (1972) 334.

NON-RESONANT ERROR FIELDS AND NTV EFFECTS ON GLOBAL TOKAMAK PLASMA STABILITY

Iulian Gabriel Miron

National Institute of Laser, Plasma and Radiation Physics, EURATOM-MEdC, Romania

Abstract

Within the frame of a kinetic (particle) description, the neoclassical toroidal viscosity (NTV) term is dependent on the nonlinear influence of the perturbed magnetic fluxes and their radial (flux coordinate) derivatives at the level of the plasma internal non-ideal, inertial layers (IL). The mode coupling and, consequently, the non-resonant error field influence become intrinsically linked with the NTV torque action. The IL toroidal angular equation of motion assumes the new NTV term nonlinearity, becoming more difficult to be analytically solved.

The NTV torque expressions are derived for different collisionality regimes: the plateau and collisional transport regimes versus the collisionless transport regime. For the collisional case, the NTV drag force can be viewed as the toroidal force due to the particle drift fluxes across the magnetic surface, associated with the lack of the axisymmetry of the perturbed magnetic fields. The ions diffuse faster and give rise to a net radial current. The resulted radial nonambipolar flux of particles causes the toroidal drag force. The same effect is due to the bounce averaged trapped particle drifts for the case of the collisionless transport regime.

The theoretical kinetic model assumes a 3-dimensional perturbative description within an axisymmetric, 2-dimensional equilibrium geometry. The thin inhomogeneous resistive wall approximation is considered. An active system consisting of a number of rectangular, radially thin coils and detectors centred at the same local coordinates system is considered, the magnetic flux measured by the detector being amplified and fed back into the coils. The inhomogeneous resistive wall and the radial feedback coils and detectors are supposed to lie on magnetic surfaces.

Detailed Results

Introduction

The following milestones have been achieved under the frame of the above objective:

i) 2-dimensional model representation of the toroidal moment equation using the kinetic description of NTV and ii) Solving the toroidal equation of motion for different collisionality regimes to prove global plasma deceleration.

The calculus is performed within the large aspect ratio approximation. The natural (flux) coordinates are used with the corresponding metric coefficients that are functions of the toroidicity, Shafranov shift, ellipticity and triangularity parameters.

This work has also been accomplished under the EFDA Task Agreement WP11-MHD-02-02-01/MEdC.

Achievements

We have to solve the following toroidal moment equation, characteristic for every IL inside the plasma

$$\frac{d\Omega_\varphi}{dt} = T_{\varphi EM} + T_{NTV} + T_\eta \tag{1}$$

Ω_φ is the toroidal angular velocity of the IL, T_{NTV} is the NTV torque and $T_{\varphi EM}$ is the perturbed electromagnetic torque developed by the interaction of the IL characteristic mode of instability with the corresponding error field mode. $T_\eta = -\eta_2(\Omega_\varphi - \Omega_{\varphi 0})/(\rho_m r_s^3 \delta_s^2)$. η_2 is the perpendicular viscous coefficient (the gyroviscous components of the perturbed stress tensor have been neglected) [1]. ρ_m is the mass density of the IL, r_s is the "radial" flux coordinate and δ_s is the "radial" half-width of the IL. We have previously obtained the following electromagnetic torque that acts on the IL that develops at the magnetic surface level, in axisymmetric 2-dimensional geometry

$$\begin{aligned} T_{\varphi EM} = &-\frac{4\pi^2}{\mu_0 R_0 r_s q_s^2} \sum_m \alpha_s^m (m - nq_s) \sum_{\substack{j=-3 \\ j\neq 0}}^{3} \frac{1}{j}(m+j)(m+j-nq_s)\,\mathrm{Re}\left(\phi_{s-}^{mn}\phi_{s-}^{m+jn}\,*\right) \\ &\times\left\{\left[\frac{r_s}{R_0} + a\varepsilon r \Lambda_{js}^{/\,/}\right]\delta_{|j|1} - \frac{2a\varepsilon}{r_s}\left[(j^2-1)\Lambda_{js} - r_s(1 - r_s q_s{}'/q_s)\Lambda_{js}{}'\right](1-\delta_{|j|1}) + \vartheta(\varepsilon^2)\right\} \end{aligned} \tag{2}$$

a, R_0 and $\varepsilon = a/R_0$ are the plasma boundary "radial" flux coordinate (minor radius), the major radius and the inverse aspect ratio, respectively. α_s^m measures the radial jump of the perturbed magnetic flux across the IL. q_s is the safety factor of the r_s corresponding magnetic surface. m and n are the poloidal and toroidal numbers characteristic to the Fourier description of the instabilities. * means complex conjugate. $\Lambda_{js} \equiv \Delta_s \delta_{|j|1} + E_s \delta_{|j|2} + T_s \delta_{|j|3}$ (*j=1,2,3* and δ Kronecker delta). Δ_s, E_s and T_s are the Shafranov shift, ellipticity and triangularity at $r = r_s$. The parameterization of the perturbed plasma velocity, $\mathbf{v} = (1/B)\nabla(d\phi/dt)\times\mathbf{B}$, defines the (m,n) Fourier components, ϕ_{s-}^{mn}, of the perturbed scalar electric potential at $r = r_{s-}$ ($r_{s+} - r_{s-}$ defines the radial width of the IL) . $\mathbf{B}$ is the equilibrium magnetic field. ' means the radial derivative.

To solve the toroidal moment equation (1), the following mathematical steps have been acquired: (a) the dynamic perturbed MHD equations have been obtained, (b) the dynamic feedback perturbed equations have been derived (the error field terms provide the equations inhomogeneity), (c) the dynamic perturbed jump equations across the IL have been obtained, (d) the complete system of equations have been Laplace transformed, (e) the perturbed magnetic flux functions as solutions of the algebraic inhomogeneous complete system of the dynamic perturbed equations have been obtained and solved, (f) the solutions $\{\phi_{s-}^{mn}, \phi_{s-}^{'mn}\}_{m,n}$ have been derived by applying the inverse Laplace transform, (g) finally the above exact solutions have been used to obtain the exact expressions of the NTV and electromagnetic torques.

An explicit expression for the neoclassical toroidal viscosity is needed.

$$T_{NTV} = -\int_{r_{s-}}^{r_{s+}} dr \left\langle \mathbf{e}_{\varphi} \cdot \nabla \cdot \mathbf{\Pi} \right\rangle \tag{3}$$

is the NTV torque, where $\langle .. \rangle = (1/4\pi^2) \oiint J d\theta d\varphi$ is the flux surface average in the natural flux coordinates (r, θ, φ), J the jacobian and $\mathbf{\Pi}$ is the perturbed stress tensor. $\mathbf{e}_{\varphi} = \nabla \varphi$ is the covariant toroidal basis vector.

Starting from previous results [2]-[5], we have adapted the flux surface averaged forces due to NTV to the general natural (flux) coordinates, rather than Hamada coordinates. Our calculations lead to the following expressions of the collisional (ν) and collisionless $(1/\nu)$ NTV torques

$$\begin{aligned} T_{NTV,\nu} = \Omega_{\varphi} \sum_{m,n} \lambda_{s\nu}^{mn} \Big\{ & T_{1s}^{mn} \left|\phi_{s-}^{mn}\right|^2 + T_{2s}^{mn} \operatorname{Re}\left(\phi_{s-}^{mn} \phi_{s-}^{/mn*}\right) + T_{3s}^{mn} \operatorname{Im}\left(\phi_{s-}^{mn} \phi_{s-}^{/mn*}\right) + T_{4s}^{mn} \left|\phi_{s-}^{/mn}\right|^2 \\ & + \sum_{\substack{j=-3 \\ j\neq 0}}^{3} \Big[T_{1s}^{mnj} \operatorname{Re}\left(\phi_{s-}^{mn} \phi_{s-}^{m+j,n*}\right) + T_{2s}^{mnj} \operatorname{Im}\left(\phi_{s-}^{mn} \phi_{s-}^{m+j,n*}\right) + T_{3s}^{mnj} \operatorname{Re}\left(\phi_{s-}^{mn} \phi_{s-}^{/m+j,n*}\right) \\ & + T_{4s}^{mnj} \operatorname{Im}\left(\phi_{s-}^{mn} \phi_{s-}^{/m+j,n*}\right) + T_{5s}^{mnj} \operatorname{Re}\left(\phi_{s-}^{/mn} \phi_{s-}^{/m+j,n*}\right) \Big] \Big\} \end{aligned} \tag{4}$$

and

$$\begin{aligned} T_{NTV,1/\nu} = \Omega_{\varphi} \sum_{m,m',n} \lambda_{s1/\nu}^{mn} \Big\{ & T_{1s}^{mm'n} \operatorname{Re}\left(\phi_{s-}^{mn} \phi_{s-}^{m'n*}\right) + T_{2s}^{mm'n} \operatorname{Im}\left(\phi_{s-}^{mn} \phi_{s-}^{m'n*}\right) + T_{3s}^{mm'n} \operatorname{Re}\left(\phi_{s-}^{mn} \phi_{s-}^{/m'n*}\right) \\ & + T_{4s}^{mm'n} \operatorname{Im}\left(\phi_{s-}^{mn} \phi_{s-}^{/m'n*}\right) + T_{5s}^{mm'n} \operatorname{Re}\left(\phi_{s-}^{/mn} \phi_{s-}^{/m'n*}\right) + T_{6s}^{mm'n} \operatorname{Im}\left(\phi_{s-}^{/mn} \phi_{s-}^{/m'n*}\right) \Big\} \end{aligned} \tag{5}$$

with the derived Fourier component of the perturbed scalar electric potential at $r = r_s$ flux coordinate), $\{\phi_{s-}^{mn}, \phi_{s-}^{'mn}\}_{m,n}$ that we have derived in a previous objective

$$\phi_{s-}^{mn}(t) = \Lambda^{mn} + \sum_{j=1}^{6L} \Lambda_j^{mn} \exp\left(\tau_j t\right) \equiv \left[\frac{\Delta^l}{\Delta}\right]_{\tau=0} + \sum_{j=1}^{6L} \left[\frac{\left(\tau - \tau_j\right)\Delta^l}{\tau\Delta}\right]_{\tau=\tau_j} \exp\left(\tau_j t\right), \quad l = 1,..,L \tag{6}$$

$$\phi_{s-}^{/mn}(t) = \overline{\Lambda}^{mn} + \sum_{j=1}^{6L} \overline{\Lambda}_j^{mn} \exp\left(\tau_j t\right) \equiv \left[\frac{\Delta^l}{\Delta}\right]_{\tau=0} + \sum_{j=1}^{6L} \left[\frac{\left(\tau - \tau_j\right)\Delta^l}{\tau\Delta}\right]_{\tau=\tau_j} \exp\left(\tau_j t\right), l = L+1,..,2L \tag{7}$$

$L=(m_2-m_1+1)(n_2-n_1+1)$ where the (m,n) mode spans $m=m_1,..,m_2$ and $n=n_1,..,n_2$. Δ is the Laplace transformed $2L\,x\,2L$ determinant of the perturbations linearized system and Δ^l is the same determinant with the l column replaced by the error field inhomogeneous terms column. $\{\tau_j\}_{j=1,..,6L}$ are the roots $\Delta_s=0$. A more compact expression for the NTV torque is

$$T_{NTV,\nu,1/\nu}(t)=\Omega_\varphi\left\{T_{s\nu,1/\nu}+2\sum_{j=1}^{6L}\mathrm{Re}\left[T^j_{s\nu,1/\nu}\exp(\tau_j t)\right]+\sum_{j,k=1}^{6L}T^{jk}_{s\nu,1/\nu}\exp\left[\left(\tau_j+\tau_k^*\right)t\right]\right\} \tag{8}$$

$\lambda^{mn}_{s\nu,1/\nu}$, $T^{mn}_{1s},..,T^{mn}_{4s}$, $T^{mnj}_{1s},..,T^{mnj}_{5s}$, $T^{mm'n}_{1s},..,T^{mm'n}_{6s}$ are functions of plasma bulk, IL and feedback system parameters [6]: ρ (plasma mass density), η_2 (perpendicular viscous coefficient), δ_s (IL width), r_s (IL radial flux position), q_s (IL safety factor), p_s (pressure), $\Omega_{\varphi 0}$ (unperturbed plasma rotation), r_w, r_f, r_d (resistive wall, active feedback and detector coil radial flux coordinates), δ_f (active feedback coil radial thickness), $\delta\theta_f$, $\delta\varphi_f$ (poloidal and toroidal active feedback coil leg angular extents), $\Delta\theta_f$, $\Delta\varphi_f$ (poloidal and toroidal active feedback coil angular extents), G_d, G_p (derivative and proportional gains), $\Delta\theta_d$ (detector poloidal angular extent), $\Delta\varphi_d$ (detector toroidal angular extent), δ_{w1} (aluminium wall thickness), δ_{w2} (stainless steel wall thickness), $\Delta\varphi_{w2}$ (stainless steel wall toroidal angular extent), N (the common number of aluminium and stainless steel wall segments), $\{\theta_p\}_{p=1,..,M}$ (the randomly disposed poloidal angles where the feedback coils and detectors are centered), $\Delta_{s,w,f,d}$, $\Delta'_{s,w,f,d}$, $E_{s,w,f,d}$, $E'_{s,w,f,d}$, $T_{s,w,f,d}$, $T'_{s,w,f,d}$ (Shafranov shift, ellipticity triangularity and its radial derivatives at r_s, r_w, r_f, r_d), p_i (ion plasma pressure), $\nu_i=\pi\sqrt{2}n_iZ_i^4e^4\ln\Lambda/\sqrt{m_iT_i^3}$ (ion collision frequency), $v_{Ti}=\sqrt{2KT_i/m_i}$ (ion thermal speed). $T_{s\nu,1/\nu}$, $T^j_{s\nu,1/\nu}$ and $T^{jk}_{s\nu,1/\nu}$ include the m, n summation over the poloidal and toroidal modes taken into account. The electromagnetic torque at the IL at r_s is

$$T_{\varphi EM}(t)=T_s+2\sum_{j=1}^{6L}\mathrm{Re}\left[T_s^j\exp(\tau_j t)\right]+\sum_{j,k=1}^{6L}T_s^{jk}\exp\left[\left(\tau_j+\tau_k^*\right)t\right] \tag{9}$$

with T_s, T_s^j, T_s^{jk} explicit coefficients with the above parametric dependency.

Our explicit derived torques expressions allow us to determine the solution of the general equation (1), $\Omega_\varphi(t)=\Omega_{\varphi h}(t)+\Omega_{\varphi nhp}(t)$, where

$$\Omega_{\varphi h}(t)=\Omega_{\varphi 0}\exp\left\{\left(T_{s\nu,1/\nu}+\frac{T_\eta}{\Omega_\varphi-\Omega_{\varphi 0}}\right)t+2\sum_{j=1}^{6L}\mathrm{Re}\left[\frac{T^j_{s\nu,1/\nu}}{\tau_j}\left(\exp(\tau_j t)-1\right)\right]+\sum_{j,k=1}^{6L}T^{jk}_{s\nu,1/\nu}\left[\exp\left((\tau_j+\tau_k^*)t\right)-1\right]\right\} \tag{10}$$

is the general solution of the homogeneous equation and

$$\Omega_{\varphi nh}(t)=\Omega_{\varphi h}(t)\int_0^t\frac{1}{\Omega_{\varphi h}(t')}\left[T_{\varphi EM}(t')-\frac{T_\eta}{\Omega_\varphi-\Omega_{\varphi 0}}\Omega_{\varphi 0}\right]dt' \tag{11}$$

is a particular solution of the inhomogeneous equation.

According to the experimental observations [4], during the times of interest, $T_{NTV,\nu,1/\nu} >> T_{\varphi EM}, T_{\eta}$. Thus, the general solution of the homogeneous equation closely approximates the general solution of the toroidal moment equation. The damping of the toroidal rotation due to NTV is rapid compared with the rotation damping due to the electromagnetic and viscous torques.

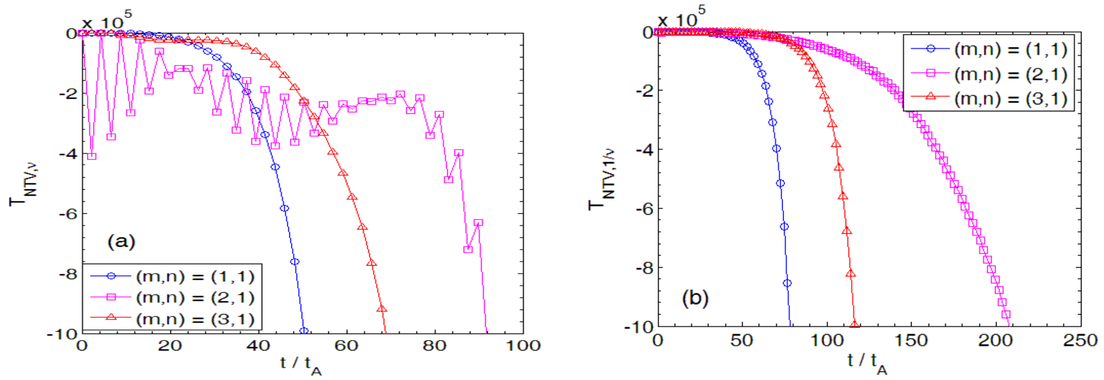

Figure 1 - Normalized collisional (a) and collisionless (b) NTV torques corresponding to (1,1), (2,1) and (3,1) inertial layers. $\Omega_{z0}/(2\pi) \cong 5\,kHz$.

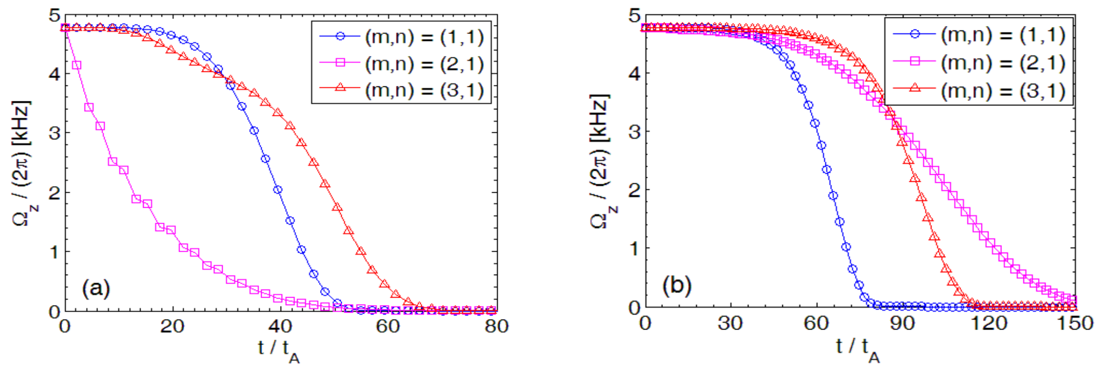

Figure 2 - Toroidal angular velocity of the (1,1), (2,1) and (3,1) plasma inertial layers in the collisional (a) and collisionless (b) case, respectively. $\Omega_{z0}/(2\pi) \cong 5\,kHz$.

Figures 1(a) and 1(b) clearly show the dynamic increase of the absolute value of T_{NTV} in the collisional and collisionless case respectively (t_A is the Alfven time). The increase of the NTV torque is abrupt, during the times of interest, and corresponds to the rapid damping of the toroidal rotation, as it is shown in Figure 2. As is expected, the faster damping of the toroidal rotation in the collisional case is obvious for both the internal (1,1), (2,1) modes and the edge plasma mode, (3,1).

More results have been found. The higher the initial toroidal angular rotation is, the faster the damping and braking of the toroidal rotation occurs. Also, in the collisional case, the damping of the higher values of the toroidal rotations is very abrupt, suggesting that a low collisional regime and a medium value for the initial plasma toroidal rotation could be the best compromise in order to minimize the NTV braking effect and to preserve a reasonable order of rotation as to stabilize the plasma perturbations. According to other obtained dependencies, a higher β_N corresponds to a weaker NTV braking effect. The damping effect is postponed and less abrupt. As the radial flux coordinate position of a magnetic surface is lower, a higher plasma boundary ellipticity is required in order to minimize the NTV damping effect on the rotation of the IL developed at the corresponding magnetic surface. On the other hand, for the optimally chosen boundary ellipticities, the toroidal rotation of the innermost IL drops to zero faster than the rest of the inertial layers corresponding toroidal rotations. Thus, for global stability requirements, the innermost IL optimal ellipticity is to be chosen. For all the involved magnetic surfaces, a slight negative radial derivative of the plasma boundary ellipticity provides the lowest NTV damping effect. We have also found that a positive boundary triangularity is optimal in order to provide a weaker NTV braking effect, especially for the most inner inertial layers. No behavioral pattern has been found for the radial derivative of the triangularity.

Conclusions

We have derived clear and explicit expressions for the neoclassical toroidal viscosity torques for different collisionality regimes. An analytic expression for the plasma toroidal angular rotation velocity has been obtained. The theoretical description has been performed within a 3-dimensional perturbations approach for an axisymmetric 2-dimensional equilibrium geometry. Both the collisional and the collisionless cases have been studied. The global NTV damping effect has been clearly showed. The conditions for a lower damping effect have been obtained by choosing suitable plasma parameters.

General perspectives

The derivation of a theoretical model that describes the effect of the resonance between the RWM frequency and the magnetic precession drift or bounce frequency of the thermal trapped particles on the RWM stabilization is proposed. The proposed model does not follow the kinetic MHD energy principle, but starts from the perturbed MHD equations with the kinetically derived pressure tensor term. The bounce and precession motions of the thermal trapped particles are considered. The proposed model includes a 3-dimensional description of the magnetic perturbations for a 2-dimensional, axisymmetric equilibrium magnetic field geometry (toroidicity, Shafranov shift, ellipticity and triangularity parameters are considered).

References

[1] S.I. Braginskii, Rev. Plasma Phys. 1 (1965) 205-311.

[2] K.C. Shaing, S.P. Hirshman and J.S. Tolliver, Phys. Fluids 29 (1986) 2548-2555.

[3] K.C. Shaing, Phys. Plasmas 10 (2003) 1443-1448.

[4] W. Zhu et al., Phys. Rev. Letters 96 (2006) 225002.

[5] K.C. Shaing, S.A. Sabbagh and M.S. Chu, Nucl. Fusion 50 (2010) 025022

[6] I.G. Miron, Plasma Phys. Control. Fusion 50 (2008) 095003.

FUNDAMENTAL AND APPLIED DATA TO THE ATOMIC, MOLECULAR, NUCLEAR SURFACE (AMNS) ACTIVITY AND TO FURTHER DEVELOPMENT OF DOCUMENTATION ON AMNS CODES

V. Stancalie, A. Mihailescu, V.F. Pais, A.O. Stancalie, O. Budriga

National Institute for Laser, Plasma & Radiation Physics, Bucharest, Roamnia

Abstract

The activity is closely related to participation in the international Atomic Data Analysis System (ADAS) project and the IAEA's Co-ordinated Research Project in "Light Element Atom, Molecule and Radical Behaviour in the Divertor and Edge Plasma Regions" which aims to deliver the best atomic data for fusion plasma diagnostics at JET and ITER. The main issue addressed here is the accuracy of atomic data used in the spectral identification for plasma modeling. The present work refers to the calculation of fundamental and applied atomic data for Ar III ion. Two independent atomic structure calculations have been performed. Results from the Breit-Pauli – and Dirac-Atomic –R-matrix relativistic calculations are analyzed comparatively. Cross sections for the electron impact excitation are provided for selected weak and intercombination transitions, allowing explicitly for resonance effects. Convergence of the partial wave expansion is ensured by examining the partial collision strengths at collision energies up to 20Ry. Radiative rates, weighted length oscillator strength, line strengths, as well as the ratios of velocity to length oscillator strengths are also provided. The calculated values are compared with existing experimental data in Atomic Structure Database of the National Institute for Standards and Technology wherever available. Agreement between theory and experiments is reasonably good, the energy difference average percentage of the low-lying levels usually agreeing to within 1% of each other. These results represent the first such detailed calculation for this atomic system and are of interest for plasma modeling.

Papers

[1] V. Stancalie, V.F. Pais, A. Mihailescu, Contributors to the EFDA-TF-ITM, *Fine-Structure Splitting Calculation in the Ar III ion: Comparison of Perturbative (Breit-Pauli) and Non-Perturbative (MCDF-EAL) Predictions* Eur. Phys. J. D. 66 -3(2012)84 (15pp).

[2] V. Stancalie, *Forbidden transition in excitation by electron impact in Co 3+: an R-matrix approach* Phys. Scr. 83(2011)025301 (8pp).

Conferences

[1] V. Stancalie, *Contribution of near threshold states to dielectronic recombination in recombining plasma with Li-like Al ions,* 5th Conference on Elementary Processes in Atomic Systems, 21-25 June 2011, Belgrade, Serbia.

[2] A. Mihailescu, VF Pais, O. Budriga, V. Stancalie, *Breit-Pauli R-matrix fine structure splitting calculation in Ar III ion*, International Student Workshop on Laser and applications, May 31-June 4, Bran, Romania

Reports

[1] V. Stancalie, Atomic data for plasma modelling, 2nd Technical Meeting on Light Element Atom, Molecule and Radical Behaviour in the Divertor and Edge Plasma Regions, 23-25May 2011, Vienna.

Detailed results

1. *Introduction*

Accurate atomic data for Ar and its ions are important in fusion related diagnostics. Considerable demand exists for electron excitation data for the ions of Ar. The cross sections and rates must be determined at typically tens of thousands of energy values. The interest in forbidden transitions between the lowest nine terms arising from the $3s^23p^4$ and $3s3p^5$ configurations in Ar^{2+}, $1s^22s^22p^63s^23p^4(^3P)$ ground configuration, comes from the experimental observations of their presence in the divertor plasma in Tokamak fusion devices. Johnson and Kingston [1] and Galavis *et al.* [2] have explicitly investigated the electron excitation amongst the nine lowest- lying states of Ar^{2+}. Following the five-state *R*-matrix calculation reported by Johnson and Kingston [1], the interaction with the $3s3p^5$ levels constitutes a major portion of the coupling of the $3s^23p^4$ levels with higher states. Furthermore, the interactions with other states, particularly those within the n =3 complex also have some influence. The first relativistic BPRM results from the electron impact excitation of Ar^{2+} are dated 2009 [3]. In order to improve upon the previously reported R-matrix calculations for the first nine levels of this ion, these authors have included more resonance channels, i.e. the radial orbitals with $n \leq 5$, and more configurations, which have not been calculated before, using the R-matrix method.

The aim of this work is to investigate the fine structure splitting in the Ar III ion, with the emphases being on the lowest nine levels. Therefore, we consider two independent atomic structure calculations within the R-matrix method. Results from the *B*reit –*P*auli and the *D*irac-*A*tomic *R*-*M*atrix relativistic calculations are analysed comparatively. Comparing results from these two independently developed computational schemes reduces the chance of systematic error, and provides an excellent method for direct verification of the numerical implementation when choosing an appropriate test case.

2. Structure calculation

Present *Breit-Pauli R-matrix* (BPRM) calculation is carried out in an *ab initio* manner in the close-coupling R-matrix method. Firstly, we consider two carefully constructed 'model' calculations, which has been designed specifically to stabilize the order of the levels (odd or even). In the first 'model' calculation, two groups of five configurations were included corresponding to each parity. For the even parity group, configurations included are: $3s^23p^4$, $3p^6$, $3s3p^43d$, $3s^23p^23d^2$, $3p^43d^2$ and giving rise to 126 fine structure levels. For the odd parity, configurations are: $3s3p^5$, $3s^23p^33d$, $3p^53d$, $3p^33d^2$ and $3s^23p3d^3$ which give rise to 184 fine structure levels. In the second model calculation, we have included 24 terms arising from the configurations: $3s^23p^4$, $3s3p^5$, $3s^23p^33d$ and $3p^6$. Configuration interaction was limited to single and double excitations within the n = 3 complex. The one- and two-electron radial integrals are computed by STG1 of the BPRM codes using one-electron target orbitals generated as shown before. The calculations consider all possible bound levels for $0 \leq J \leq 7$ with n < 4, $l \leq n$-1, $0 \leq L \leq 9$, and (2S+1) =1,3,5 even and odd parities. The intermediate coupling calculations are carried out on recoupling the *LS* symmetries in a pair-coupling representation in stage RECUPD. The (e + core) Hamiltonian matrix is diagonalized for each resulting $J\pi$ in STGH. Comparing our BPRM results with the only reported BPRM calculation on this atomic system[3] a better accuracy is obtained for the lowest nine levels, as output from our calculation. Agreement between theory and experiments is reasonably good, the energy difference average percentage of the low-lying levels usually agreeing to within 1.9 % of each other. An exception to this is the theoretical energy for ${}^{1}D_2$ level which differs from the experimental value by 10.9% [4].

Separately, we have initiated a full relativistic calculation using the *Dirac-R matrix* method. It is essentially the relativistic or Dirac version of the *R*-matrix. The Dirac Hamiltonian for the (N+1)-electron system, in atomic units, is written as:

$$H^{N+1} = \sum_{i=1}^{N+1} - ic\boldsymbol{\alpha} \cdot \nabla_i + (\beta - 1)c^2 - \frac{Z}{r_i} + \sum_{j=i+1}^{N+1} \frac{1}{|\mathbf{r}_j - \mathbf{r}_i|} \tag{1}$$

where *i* and *j* index the individual electrons, Z is the charge of an infinitely heavy point nucleus, the electron mass has been substracted, and $\boldsymbol{\alpha}$ and β are the usual Dirac matrices constructed from Pauli spin and unit matrices. The first three one-electron terms in the Hamiltonian are a momentum term, mass term and the electron-nucleus Coulomb attraction. The final two-electron term is the Coulomb electron-electron repulsion. We used MCDF-EAL option with and without QED in the general-purpose relativistic atomic structure package GRASP, while for determining the collision strengths the Dirac Atomic R-matrix Code (DARC) is used. An initial calculation has been done to stabilize the order of the levels (odd or even). For the even groups, the reference set contains {$3s^23p^4$, $3p^6$, $3s3p^43d$, $3s^23p^23d^2$, $3p^43d^2$, $3s^23p^34f$, $3p^54f$}, and for the odd groups {$3s3p^5$, $3s^23p^33d$, $3p^53d$, $3s3p^33d^2$, $3s^23p3d^3$, $3s^23p^34s$}. Our calculations are fully relativistic and configuration interaction (CI) has been included. All possible configurations, such that $\Delta n = 0$, namely $3s^23p^4$, $3s3p^5$, $3s^23p^33d$, $3p^6$, were included in average level (EAL) calculation, while $1s^2$, $2s^2$ and $2p^2$ shells were kept full. These *jj*-coupled CSF's result in a set of 48 levels that are limited to the following symmetry –parity combinations $J^{\pi} = 0^{\pm}, 1^{\pm}, 2^{\pm}, 3^{-}, 4^{-}, 5^{-}$. We have calculated levels energy, the dominant CSF's that contribute to these levels, radiative rates, weighted length oscillator strength, line strengths, as well as the ratios of velocity to length oscillator strengths. The calculated values are compared with existing experimental data in Atomic Structure Database of the National Institute for Standards and Technology wherever available. Agreement between theory and experiments is reasonably good, the energy difference average percentage of the low-lying levels usually agreeing to within 1% of each other.

3. Scattering Calculation

The process that we seek to study can be described by:

$$\begin{array}{c} e^- + Ar^{2+}(3s^23p^2\ {}^3P) \rightarrow Ar^{2+*}\ (3s^23p^5,\ 3s^23p^43d,\ 3s3p^6,\ 3s3p^53d,\ 3s^23p^33d^2,\ \text{or}\ 3s3p^43d^2) \\ \downarrow \\ Ar^{2+}\ (3s^23p^4,\ 3s3p^5, 3s^23p^33d,\ \text{or}\ 3s3p^43d) \end{array} \tag{2}$$

In constructing the target state wavefunction in *BPRM calculation* we included all levels in the target approximation with the electronic configuration $3s^2 3p^4$, $3s3p^5$, $3s^2 3p^3 3d$ and $3s3p^4 3d$. At this level of accuracy, we used FARM (Burke and Noble, Comput.Phys.Comm.1998) with energies shifted to NIST energies.

Separately, *the DARC code* was used for the scattering process within full relativistic approach. All possible transitions among the all 48 fine-structure target levels are considered in this part of the calculation. The MCDF results have been used as input for the threshold energies. The *R*-matrix boundary was fixed at r = 9.84 Bohr radii, and the constant b that arises in the boundary condition set to b = 0. The radial Dirac equations have been solved for 18 continuum angular momentum K values, 20 continuum orbitals per angular momentum. The Dirac Hamiltonian matrix for the (N +1)-electron system in the inner radial region is constructed for the following J^π combinations: $1/2^\pm$, $3/2^\pm$, $5/2^\pm$, $7/2^+$, $9/2^+$, $11/2^+$ and all corresponding possible channels. The total number of channels thus generated was 1257, with a dimension of 4420 for the largest Hamiltonian matrix. The collision strengths, Ω_{if}, between initial and final levels i and f, respectively, were evaluated at over 5000 distinct incident electron energies in this 'fine mesh' region, for a number of selected transitions. For energies above the highest-lying target level we adopted a coarsed mesh of 0.05 Ry (0.0125 scaled Ry), and the collision strengths were evaluated at 200 incident energies in this 'coarse mesh' region. Because of the diagnostic importance, we have investigated the total collision strengths for the ^3P_J - $^3P_{J'}$ fine structure transitions. Figure 1 presents the total collision strengths for the $3s^2 3p^4$ ($^3P_2 - {}^3P_1$) transition (1-2), i.e., from level 1 to level 2. The total collision strength for $3s^2 3p^4$ ($^3P_2 - {}^3P_0$) and $3s^2 3p^4$ ($^3P_1 - {}^3P_0$), i.e. from level 1 to level 3, is plotted in Fig.2.

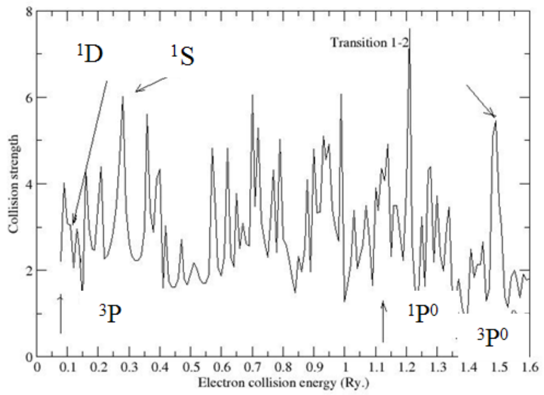

Figure 1 - Total collision strength for the $3s^2 3p^4$ $^3P_2 - {}^3P_1$ transition in Ar III.

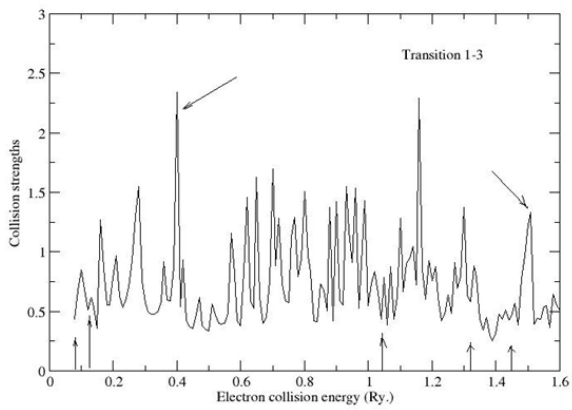

Figure 2 - Total collision strength for the $3s^2 3p^4$ $^3P_2 - {}^3P_0$ transition in Ar III.

For the allowed $^1P^0 - {}^1D$ (i.e. from level 4 to level 14) and $^1P^0$ -^1S (i.e. from level 5 to level 14) transitions, the corresponding collision strengths are shown in Fig.3 and Fig.4, respectively.

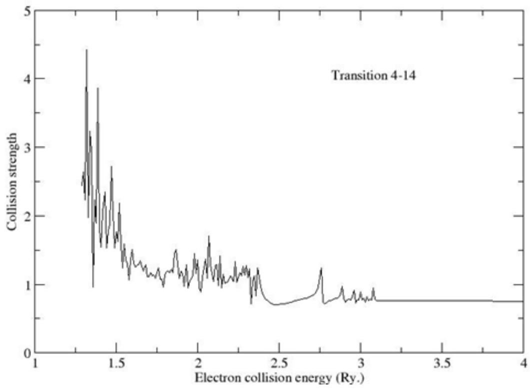

Figure 3 - Total collision strength for the 3s23p4 1D2 – 3s3p5 1P0 transition in Ar III.

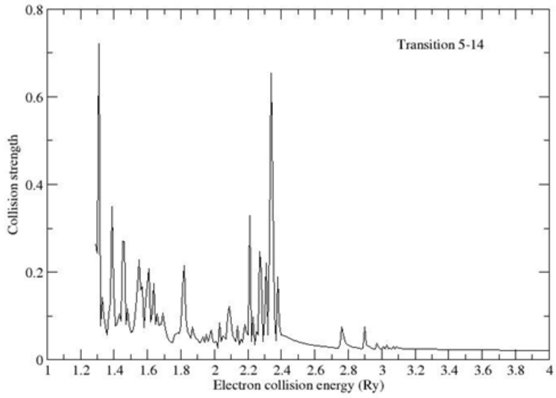

Figure 4 - Total collision strength for the 3s23p4 1S0 – 3s3p5 1P0 transition in Ar III.

Conclusion

This work presents the first application of DARC code on the ArIII ion. The full relativistic calculation includes the *n* = 4 orbitals, and nine non-relativistic configuration state functions. The MCHF results for energies, together with the results obtained when the transverse Breit interaction and QED contributions are included in the calculations agree with the experimental data to better than 1.5%. The length velocity oscillator strength data as obtained from the Dirac-Atomic *R*-matrix calculation are in good agreement with the experimental values. In this calculation the inclusion of resonance-energy region has been practically feasible at all energies assuring a consistent framework where the resonance effects are taken into account.

The present paper adds complementary results to previously reported BPRM atomic data for Ar^{2+}. Our calculated energies are less accurate comparing with the experimental data reported by the NIST table, and better results have been obtained for the lowest nine levels comparing with other relativistic calculations reported in Ref. 16. The FARM code has been used for scattering calculations and the experimental energies have been used this time.

Our final dataset is archived in the Atomic, Molecular, Nuclear and Surface (AMNS) database (http://www.efda-itm.eu).

Acknowledgement

The reported work supported by the European Communities under the contract of Association between EURATOM and MEdC, was carried out within the framework of the European Fusion Development Agreement.

References

[1] C. T. Johnson and A. E. Kingston, J. Phys. B: At. Mol. Opt. Phys. **23**, 3393(1990).

[2] J.M. Munoz Burgos, S. D. Loch, C. P. Ballance, and R. F. Boivin, A&A **500**,1253(2009).

[3] V. Stancalie, VF Pais, A. Mihailescu, Eur. Phys. J.D 66(2012)84.

EXTENDING THE ITM WEB PORTAL

V.F. Pais, V. Stancalie, A. Mihailescu, A.O. Stancalie, O. Budriga

National Institute for Laser, Plasma & Radiation Physics, Bucharest, Romania

Abstract

The longer term goal of the ITM-TF is to provide the European fusion community with a validated suite of simulation tools for ITER exploitation and to provide the basis for a complete simulation environment for fusion plasmas generally available for use also for modelling on current devices and in support of theory and modelling in general. IMPs have dual responsibilities in that they should continue to develop and manifest the physics foundations for Integrated Modelling in standalone packages targeting the code platform environment while they are also supporting the integration efforts towards scenario modelling tools.

The increased number of users and software projects using the portal tools has made the portal less responding then when it was first designed. This led to the necessity of analyzing existing tools in order to identify where the bottlenecks were. Furthermore, the years of working with the portal have produced a certain amount of feedback from the users.

After analyzing the various components of the portal, it was identified Shibboleth, the central authentication component, as not being the most suitable for its task. This was due to the difficulty in configuring for multiple authentication sources combined with the session expiration that was identified by some users. Having this in mind, it was decided to implement a new single sign on mechanism that would replace Shibboleth and offer better response to the actual needs of the task force.

Papers

[4] F. Iannone, B. Guillerminet, F. Imbeaux, G. Manduchi, A. Maslennikov, V. Pais and P. Strand , "*Gateway: new High Performance Computing facility for EFDA Task Force on Integrated Tokamak Modelling*", Fusion Engineering and Design 85 (2010), pp. 410-414.

[5] V.F. Pais, S. Balme, H.S.Akpangny, F. Iannone, P. Strand, "*Enabling remote access to projects in a large collaborative environment*", Fusion Engineering and Design 85 (2010), pp. 633-636

Detailed results

The longer term goal of the ITM-TF is to provide the European fusion community with a validated suite of simulation tools for ITER exploitation and to provide the basis for a complete simulation environment for fusion plasmas generally available for use also for modelling on current devices and in support of theory and modelling in general. IMPs have dual responsibilities in that they should continue to develop and manifest the physics foundations for Integrated Modelling in standalone packages targeting the code platform environment while they are also supporting the integration efforts towards scenario modelling tools.

The ITM Portal acts as an interface between users and the various tools available on the ITM Gateway. This means that the portal has to be very responding to user requests. This translates into a very small time for processing the request and generating a response.

The increased number of users and software projects using the portal tools has made the portal less responding then when it was first designed. This led to the necessity of analyzing existing tools in order to identify where the bottlenecks were. Furthermore, the years of working with the portal have produced a certain amount of feedback from the users.

After analyzing the various components of the portal, it was identified Shibboleth, the central authentication component, as not being the most suitable for its task. This was due to the difficulty in configuring for multiple authentication sources combined with the session expiration that was identified by some users.

Even more, the Jboss based central content serving system was identified as providing less then optimal response times. This seems to be due to the interaction between the four components of this sub-system: apache, tomcat, jboss and shibboleth.

Nevertheless, the overall architecture of the portal is in accordance with the user requirements and thus it must be kept:

At the beginning of this year, the components of the portal were:

- Shibboleth [1]: single sign-on mechanism, with Java-based identity provider (IdP) and native service provider (SP).
- Apache Tomcat [2]: servlet container for the Shibboleth IdP.
- JBoss Application Server [3,4]: portal server and servlet container.
- Apache HTTPD [5]: front-end server, exposing the various services offered by Shibboleth and JBoss to the external world.
- OpenLDAP [6]: directory solution for managing user accounts and user groups, with information exported from the Gateway network information system.
- GForge with Subversion: version handling tool and collaborative environment.
- JBoss Wiki: wiki based collaborative environment, based on Java servlets deployed in the JBoss AS servlet container.

After careful consideration of the detected slow-downs, it was decided to change the Shibboleth authentication component with a custom made one. This however must be a drop-in replacement for almost all the other components, including GForge. Furthermore, the Jboss portal will be replaced by a simpler mechanism of accessing content. Nevertheless, the possibility of keeping the Jboss portal is investigated. In this case, it will remain a sub-component of the overall ITM portal, but it will no longer serve as the central point for user access. This decision being justified by the fact that most users do not need advanced features offered by JBoss. Instead, most users simply access the documentation pages or other modules outside of Jboss, which places an unnecessary load on this sub-system, simply for serving regular content.

The new single sign on component is based on PHP and therefore it does not require modifications to the existing software processes on the server. This means that the update procedure used for other Gateway nodes can be applied to portal servers, potentially leading to increased security of the overall system. Furthermore, using advanced "rewriting" techniques inside the Apache web server, it is possible to protect any kind of web application. This includes folders, php based applications and java based applications.

A test deployment was performed on a separate portal machine. This allowed testing of the new system in parallel with the Shibboleth component without impacting regular users. After a period of about a month it was decided to replace the Shibboleth component completely in order to integrate the new component in the main portal.

A new feature that was requested from the SSO component is the ability to have "external users". This means users with very limited access to specific tools, mostly subversion, without having a full account on the Gateway cluster. The new SSO component was developed having in mind multiple authentication sources. This includes both LDAP, providing integration with the Gateway user base, and custom files allowing the possibility to add new users.

Since at some point it may happen to have the same user account in both authentication sources, it was decided to give priority to Gateway accounts. Thus, if a user is created in both authentication repositories, by mistake, it will be detected inside the Gateway user base and these access rights will be given to it. In this case, if a user account exists in both places it will have only the access rights available as a task force member.

By replacing the Shibboleth component, the new portal structure available at the end of the year can be summarized as follows:

- Single Sign-on: custom designed mechanism, based on PHP.
- Apache HTTPD [5]: front-end server, exposing the various services offered by all the components to the external world.
- OpenLDAP [6]: directory solution for managing user accounts and user groups, with information exported from the Gateway network information system.
- GForge with Subversion: version handling tool and collaborative environment.
- Documentation: pages provided by the documentation project.

- Portal solution: custom portal mechanism providing access to various tools from a single interface.
- Tools: various tools developed by the ITM (like the Catalog Query Tool) or administrative tools (like LDAP Admin).

Currently, the new portal infrastructure is under testing by both „power users" (developers, task force leadership) and „regular users". Several problems were identified as bugs during the early stages of release, but these were immediately corrected. Since the new SSO system is developed in PHP an attack that would threaten the servers is not possible. The only problems that may appear are related to functionality and in some cases these are just feature requests.

The SSO tool has two components: the Identity Provider (IDP) and the Service Provider (SP). They were both developed as REST web services, potentially allowing for easy integration in desktop applications that can not use the easy integration provided by the Apache web server to server based applications.

The steps involved in performing authentication and authorization are as follows:

a. SP checks to see if the user is authenticated
b. If the user is not authenticated, it is redirected to a page provided by the IDP
c. The user authenticates at the IDP. The username and password are received only by the IDP on a secure channel. No authentication data is sent to the SP
d. If the user successfully authenticates at the IDP, it is redirected to the SP.
e. Once the SP receives a request that seems authenticated, it will query the IDP for authorization data. This is a special call that happens only between SP and IDP without any user interaction and therefore it is secured. Furthermore, only authorization data (user rights) is sent to the SP. The authentication data (user credentials) are received only by the IDP during the „authenticate" call and this information is not stored on disk. Instead a special „token" is created that allows access to authorization data.

Currently, authorization is performed based on ITM user groups. This information corresponds to ITM projects and task force leadership. Therefore it is very easy to grant users access to restricted areas based on the projects they are involved with. If a user gets involved with a new project, the account is moved or added to a new group. In this case the changes are automatically reflected in the SSO component, because it is using the same user base as the ITM Gateway cluster.

In case of external users, it is envisaged to implement a generic „external" group allowing easy implementation of access rules (ACLs) for all the external users. In some cases, it is possible to have additional user groups in order to further restrict (or expand) the user rights.

Acknowledgement

The reported work supported by the European Communities under the contract of Association between EURATOM and MEdC, was carried out within the framework of the European Fusion Development Agreement.

Plasma Wall Interaction

PERMEATION MEASUREMENTS

C. P. Lungu, C. Porosnicu, I. Jepu, A. M. Lungu, P. Chiru, C. Ticos, C. Luculescu

National Institute for Laser, Plasma and Radiation Physics, Association EURATOM MEdC

Abstract

Eurofer membranes of 40 mm in diameter 0.5 mm thickness were coated with 5-6 micrometer thick Be-W films the coatings, prepared by the TVA method were characterized as point of view of morphology by scanning electron microscopy (SEM) and as composition by energy dispersive spectrometry (EDS). Permeation measurements of the coated Eurofer membranes were performed at 1 bar upstream hydrogen pressure and 400 °C. The registered permeation flux was between q = 4·109 H2/(s cm2) and q = 4.5·108 H2/(s cm2). In comparison to uncoated membranes, the corresponding permeation reduction factor was of 100-420, an order of magnitude higher than that of pure beryllium films tested before. When comparing our data with the published data, our data range is rather narrow. It manifests both high reactivity of the Be film with all active gases and the Be-W film ability for hydrogen trapping.

Papers

1. V. Nemanic, B. Zajec, M. Zumera, C. Porosnicu, C.P. Lungu, *Hydrogen permeability of beryllium films prepared by the thermionic vacuum arc method*, Fusion Engineering and Design 86 (2011) 2421–2424

Conferences

2. C. P. Lungu, C. Porosnicu, I. Jepu, V. Nemanic, B. Zajec, M. Zumer *Deposition, characterization and hydrogen permeation through Be and Be/W films*, SEWG meeting on Fuel retention and Fuel removal & Dust, 27 nov-1dec 2011, Bratislava, Slovakia

Detailed results

Introduction

The planned application of both metals beryllium and tungsten together as first wall materials of the next step fusion device ITER is based on the foreseen advantageous properties of these metals for the respective locations in the plasma vessel [1]. Erosion, transport, and redeposition of both materials during operation will lead to transport of elements onto surfaces of different materials. Due to kinetic energy of impinging particles and elevated wall temperatures, alloys and compounds consisting of the present elements will be formed. These 'mixed materials' exhibit strongly altered physical and chemical properties compared to the intended properties of the pure elements which were originally installed. Of all binary systems considered in previous studies, beryllium–tungsten received least attention although Be–W alloys bear the potential of drastically reduced melting temperatures compared to pure W.

Recent investigations of blanket concepts from the European Power Plant Conceptual Study (PPCS) indicate that in the case of reduced activation steel as a structural material a fraction of the particle flux impinging onto the first wall of a blanket module from the plasma can diffuse through the structural material into the coolant. This will lead to tritium contamination of the coolant. For this reason we suggest to integrate a tritium permeation barrier into the plasma-facing side of a blanket module. Since a tungsten coating is proposed as a plasma-facing material, while alumina is considered to be one of the most efficient permeation barriers, we investigated the permeation barrier performance of such combinations of thin coatings: coatings of tungsten and alumina with thicknesses in the µm range deposited on a fusion relevant material, EUROFER 97 steel. The following combinations were examined: bare EUROFER, EUROFER with a tungsten coating, EUROFER with an alumina coating, and the combination EUROFER-alumina-tungsten. The coatings were produced by vacuum arc deposition for alumina and by magnetron sputtering for tungsten. While a 1 µm tungsten coating reduces the permeated flux by roughly 1 order of magnitude, a 1 µm alumina coating leads to a reduction of about three orders of magnitude. The deposition of tungsten on top of an alumina coating, in turn, reduces its barrier performance by about a factor of two. Recently, we also focused our attention on another crystalline coating, namely erbium oxide. It can easily form the required crystalline structure, is stable with respect to liquid tritium breeder materials like lithium, maintains its electrical properties under neutron irradiation etc. Investigations included both thermal load test and permeation measurements to find out how erbia is compatible with other materials at elevated temperatures as well as how well it suppresses hydrogen transport. It is found that a 1 µm thick crystalline erbia coating on EUROFER reduces the tritium permeability by a factor up to 103, while revealing good temperatures, thermo-mechanical stability being deposited on different substrates. Since the coating is comparable with crystalline alumina in terms of its efficiency but possesses some advantages over alumina and is easier to be produced, erbia is proposed as an alternative material for permeation barrier coating.

Considering the cost and required minimum thickness of Be that will be involved in the plasma-wall interaction, the first large area of Be testing in JET will be realized by Inconel and erosion-marker tiles coated with a thick Be film. Such coatings with excellent adhesion and other mechanical properties that fulfill high demands have been prepared by the TVA [4, 5] and thermal evaporation in vacuum deposition methods [6]. So far, no data exist on the hydrogen transport through these Be films which may influence the tritium retention when such tiles are used in fusion experiments.

In this report, we present the characterizations of the Be-W films prepared by TVA method and the results of the hydrogen permeation measurements performed in cooperation with specialist for JSI, Ljubljana, Slovenia [7].

Preparation of Be-W films.

The Be-W films were deposited on the EUROFER membranes as well as on the witness samples of 12 mm x 15 mm x 0,5 mm silicon (111).

The deposition system was equipped with two TVA evaporators having circular symmetry. Beryllium and tungsten rods cooled in the lower part were used as anodes. The deposition parameters and technological records are presented:

SEM measurements

In order to study the morphology of the prepared samples was used a FEI scanning electron microscope.

The SEM images, taken on the surface of coating deposited on Si witness samples and crossection revealed rough surfaces (Fig 1-4) and compact films, shown in Fig. 5-6:

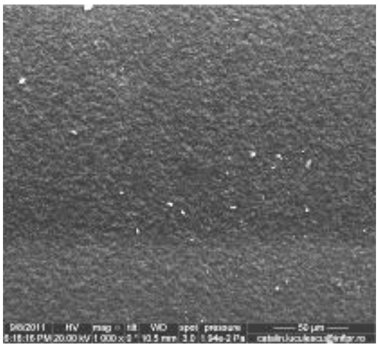

Figure 1 - SEM image of the sample 20110907_Be3_W1_1000x

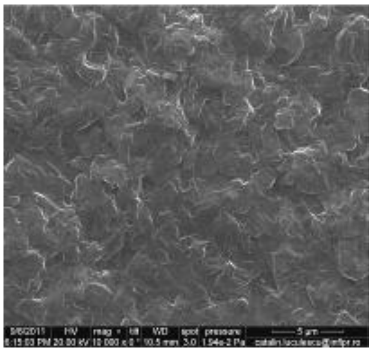

Figure 2 - SEM image of the sample 20110907_Be3_W1_10000x

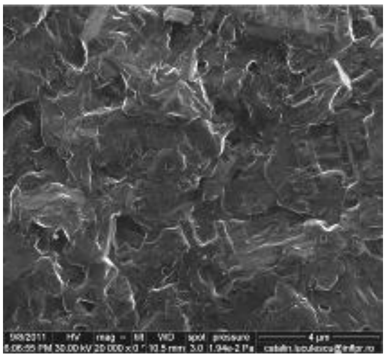

Figure 3 - SEM image of the sample 20110907_Be3_W1_20000x

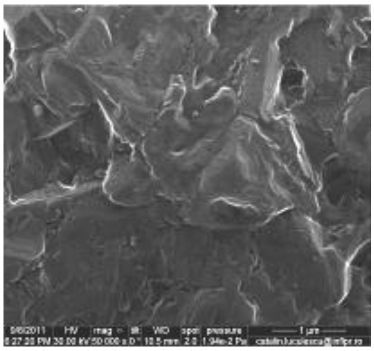

Figure 4 - SEM image of the sample 20110907_Be3_W1_50000x

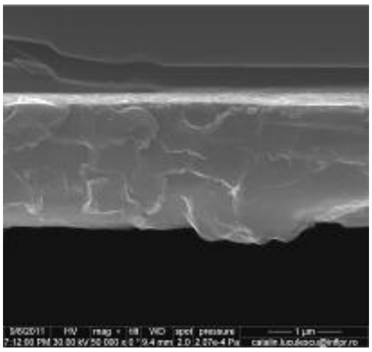

Figure 5 - SEM image of the sample 20110907_Be3_W1_50000x cross-section

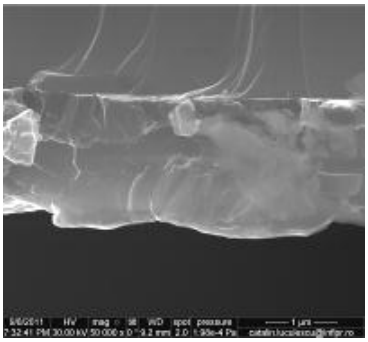

Figure 6 - SEM image of the sample 20110907_Be3_W1_50000x cross-section_002

After the permeation tests, the samples were investigated by SEM technique and the surface morphology of one of the samples is presented in Fig. 7. On can observe a linear crack due to the pressure on the membrane at the end of the permeation test (The sample was stick on the permeation test holder due to the Au gasket used for sealing)

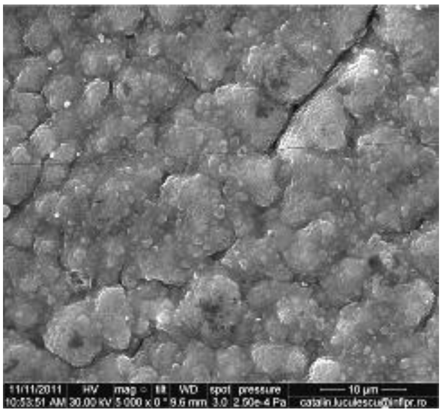

Figure 7 - SEM image of the Eurofer membrane coated with Be-W film after the permeation test

AFM measurements correlate well to SEM results, roughness changes with deposition conditions (Fig.8)

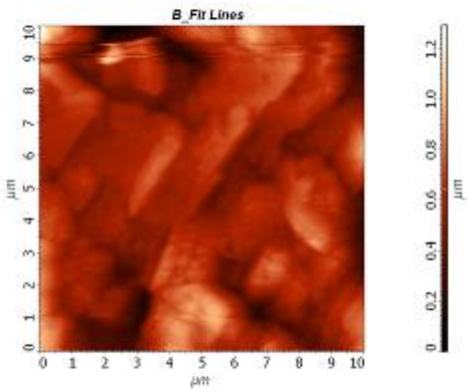

Figure 8 - AFM image of the Be-W film

1. EDS measurements

The Be and W relative concentration was measured using the energy dispersive spectroscopy (EDS) module of the SEM apparatus.

Every sample was measured in three different locations on the surface, the results being presented in Tables 1-3.

Table 1 - EDS measurement performed on sample: 20110907_Be3_W1_5kV_1000x_a.spc

Element	Wt %	At %
Be	70.60	94.65
C	1.45	1.46
O	1.25	0.94
Ni	4.35	0.90
Si	1.61	0.69
W	20.74	1.36
Total	100.00	100.00

Table 2 - EDS measurement performed on sample 20110907_Be3_W1_5kV_1000x_b.spc

Element	Wt %	At %
Be	67.84	94.14
C	1.4	1.46
O	1.28	1.00
Ni	5.48	1.17
Si	1.59	0.71
W	22.42	1.53
Total	100.00	100.00

Table 3 - EDS measurement performed on sample 20110907_Be3_W1_5kV_1000x_c.spc

Element	Wt %	At %
Be	67.76	94.13
C	1.51	1.58
O	1.26	0.99
Ni	4.34	0.93
Si	1.78	0.79
W	23.35	1.59
Total	100.00	100.00

2. Permeation measurements

Using the system realized at the Josef Stefan Institute (JSI) Ljubljana, Slovenia, the prepared samples were tested at 400^{o}C to verify film integrity and its capability for hydrogen isotopes migration [7].

The value of permeation reduction factor (PRF) was initially rather high on the analyzed samples:

Sample a: Final value between PRF 300 and 400 was always achieved after initial maximum (at ~60 s) which declined each time to stated values.

Sample b: Flux stable within 30 minutes PRF ~260 to ~420

Behavior of the PRF of different samples was different due to morphology.

Initial behavior of H flux on the Be-W side to 1 bar at 675 K. PRF after 2000 s: ~260 in the 1st exposure, ~420 after the 2nd exposure ~340 after the 4th exposure.

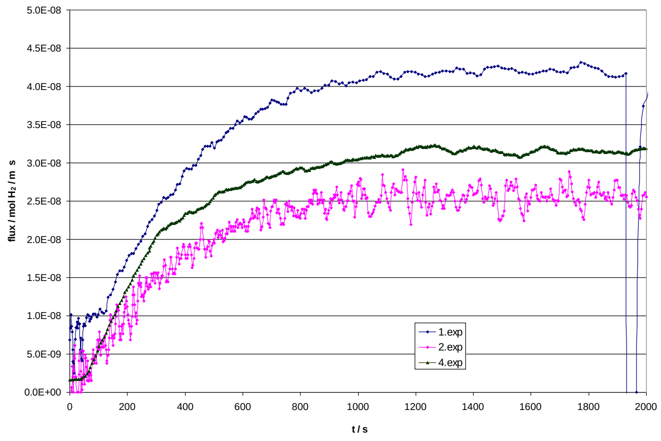

Figure 9 - Initial behavior of hydrogen flux after exposure of the Be/W side to 1 bar at 400 °C. The achieved PRF after 2000 s is PRF ~260 in the first exposure, PRF ~ 420 after the second exposure and PRF ~340 after the fourth exposure.

Another sample exhibited a different initial behavior of hydrogen flux after the exposure of the Be/W side to 1 bar at 400 °C. The achieved PRF after 2000 s in the first exposure was the only very stable one, PRF ~100.

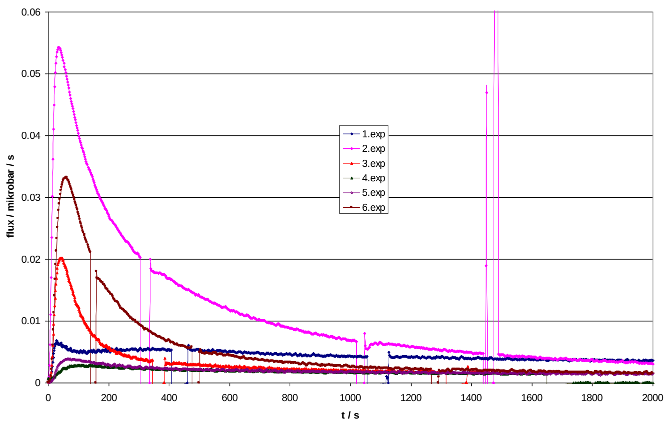

Figure 10 - Initial behavior of hydrogen flux after exposure the Be/W side to 1 bar at 400 °C. he achieved PRF after 2000 s in the first exposure was the only very stable one, PRF ~100.

The results of hydrogen permeation through TVA deposited Be-W films on Eurofer do not express just the film property, but could be influenced by two additional facts: film porosity and surface reactions before and during the measurements. The term “film porosity” must be understood as an overall effect of all imperfections causing the He leak between the Au gasket and the Be-W layer. It is far from being proved what is the influence of this microporosity confirmed by He leak on the hydrogen permeation flux and what could be the value for a perfect Be-W film.

Surface reactions could not be eliminated by the present experimental setup. Before the admission, hydrogen was purified to the ppb level of all active gases, but on the long-term scale, desorption of water or other gases from hot parts of the permeation cell could cause oxidation of the Be film. We may first show that permeability of two bare Eurofer samples matches very well with the published value for solubility and diffusivity of Eurofer, which confirms that the setup gives reliable and repeatable results. The average time-lag of 6.5 s was determined from several repeated cycles giving a diffusivity constant of D (400 ◦C) = 6.4×10−5 cm2/s. The permeability coefficient was determined to be P (400 ◦C) = 1.0×1013 H2/(msPa0.5) and the hydrogen solubility Ks (400 ◦C) = 1.56×1017 H/(cm3 Pa0.5). Obtained parameters are in very good agreement with published transport parameters for hydrogen and deuterium in Eurofer [9]. The permeation fluxes through the investigated samples evidently show that the Be-W films have a substantially lower permeability compared to the substrate.

The values for the Be permeability lie between P_{Be} (400 ◦C) = 1.95×109 H_2/(msPa0.5) and PBe (400 ◦C) = 1.15×1010 H2/(msPa0.5). Surprisingly, the estimated values for P_{Be} (400 ◦C) obtained from published data on bulk Be permeability cover the same range of values as we obtained. From Ref. [8], the permeability according to the data cited from Ref. Jones and Gibson is P_{Be} (400 ◦C) = 1.29×109 H_2/(msPa0.5), while according to cited Ref. Al'tovskiy [10] PBe (400 ◦C) = 3.03×1010 H_2/(msPa0.5). In several older experiments, the solubility and diffusivity were measured and reported separately and each of both quantities differs greatly. The published and extrapolated diffusivity of Be at 700K spans over 9 orders of magnitude and consequently the calculated permeability, regardless which data for solubility is used. The data for diffusivity in the high-grade Be of Abramov et al. [11] are almost equal to the data from Macaulay-Newcombe and Thompson [12] meaning that both data may be used as credible. The most credible estimated value for permeability may be the one when solubility of Macaulay-Newcombe and Thompson [13] is taken. The value is substantially higher P_{Be} (400 ◦C) = 3.74×1013 H_2/(msPa0.5). On the other hand, Wampler found in his experiment that the deuterium permeability in Be at 600 ◦C is seven orders of magnitude lower than expected from "published data" [14]. If data in Ref [14] are correct, then the registered flux in our experiments means that our Be films were porous on the microscopic level. Several SEM pictures of rough and polished surfaces were examined, but all films are dense with a very low number of detected pinholes. It is thus beyond the scope of this experimental work to determine the true internal mechanism of the hydrogen transport through investigated Be and Be-W films.

Conclusions

Eurofer membranes of 40 mm in diameter 0.5 mm thickness were coated with 5-6 micrometer thick Be-W films by the TVA method. Permeation measurements of the coated Eurofer membranes were performed at 1 bar upstream hydrogen pressure and 400 °C. The registered permeation flux was between $q = 4\cdot10^9$ H_2/(s cm^2) and $q = 4.5\cdot10^8$ H_2/(s cm^2). In comparison to uncoated membranes, the corresponding permeation reduction factor was of 100-420, an order of magnitude higher than that of pure beryllium films tested before. When comparing our data with the published data, our data range is rather narrow. It manifests both high reactivity of the Be film with all active gases and the Be-W film ability for hydrogen trapping.

Acknowledgement

The reported work includes contributions from the following people outside the EUATOM-MEdC Association: Vincenc Nemanič, Bojan Zajec, Marko Žumer, "Jožef Stefan" Institute (JSI), Jamova 39, 1000 Ljubljana, Slovenia

References:

[1] R.R. Parker, Nucl. Fusion 40 (2000) 473.

[2] T. Hirai, H. Maier,M. Rubel, Ph. Mertens, R. Neu, E. Gauthier, J. Likonen, C. Lungu, G. Maddaluno, G.F.Matthews, R.Mitteau, O. Neubauer, G. Piazza, V. Philipps, B. Riccardi, C. Ruset, I. Uytdenhouwen, Fusion Eng. Des. 82 (2007) 1839–1845.

[3] H. Maier, T. Hirai, M. Rubel, R. Neu, Ph. Mertens, H. Greuner, Ch. Hopf, G.F. Matthews, O. Neubauer, G. Piazza, E. Gauthier, J. Likonen, R. Mitteau, G. Maddaluno, B. Riccardi, V. Philipps, C. Ruset, C.P. Lungu, I. Uytdenhouwen, Nucl. Fusion 47 (2007) 222–227.

[4] C. P. Lungu, I. Mustata, V. Zaroschi, A. M. Lungu, A. Anghel, P. Chiru, M. Rubel, P. Coad G. F. Matthews and JET-EFDA contributors, Phys. Scr. T128 (March 2007) 157–161

[5] T. Hirai, J. Linke, M. Rubel, J.P. Coad, J. Likonen, C.P. Lungu, G.F. Matthews, V. Philipps, E. Wessel and JET-EFDA contributors, Fusion Engineering and Design, 83, 2008, 1072-1076.

[6] T Hirai, J Linke, P Sundelin, M Rubel,W Kühnlein, EWessel,J P Coad, C P Lungu, G F Matthews, Phys. Scr. T128 (March 2007) 166–170

[7] V.Nemanic, B.Zajec, M. Zumer, JVST A, 28(4) (2010) 578

[8] R.A.Causey, JNM, 300, (2002) 91-117

[9] G.A. Esteban , A. Peña, F. Legarda, R. Lindau, Fusion Engineering and Design 82 (15-24) (2007) 2634-2640

[10] R.M. Al'tovskiy et al., Russ. Metall. 3 (1981) 51

a. Nikroo, H.W. Xu, K.A. Moreno, K.P. Youngblood, J. Cooley, C.S. Alford S.A. Letts, and R.C. Cook, Fusion Science and Technology, 51, 4 (2007) 553-555

[11] E.Abramov, M.P. Reim, D.A.Thompson, W.W. Smeltzer, JNM, 175 (1990) 90-95

[12] R.G.Macaulay-Newcombe, D.A. Thompson, JNM, 212-215 (1994) 942-947

[13] W.R. Wampler, JNM, 196-198 (1992) 981-985

PREPARATION OF THE BE CONTAINING LAYERS FOR D RETENTION AND CHARACTERIZATION

C.P Lungu[1], C. Porosnicu[1], I. Jepu[1], A. Anghel[1], A. M. Lungu[1], P. Chiru[1], C. Ticos[1], C. Luculescu[1], *V. Kuncser[2], C. Teodorescu[2], M. Văleanu[2], N. Gheorghe[3], G. Schinteie[4], C. Valsangiacom[5], A. Leca[2], S. Sandu[2], G. Gheorghe[2], A. Stoica[2]*

[1]National Institute for Laser, Plasma and Radiation Physics, Magurele, Romania, Association EURATOM MEdC

[2]National Institute of Material Physics, Magurele, Romania, Association EURATOM MEdC

Abstract

Using the thermionic vacuum arc method ternary Be-C-W samples were prepared on graphite and silicon substrates at room temperature. The samples were thermally treated after the deposition under high vacuum conditions (10^{-8} mbar) in order to avoid supplementary oxidation of the ternary system. All structures have been characterized following different processing stages, with respect to morphological/structural and diffusional aspects, via XPS.

RBS measurements were performed to investigate the films compositions, the position of the oxygen and to see if there is a mixture of the three elements. Deuterium implantation experiment was performed in the High Current Ion Source. The amount of D retention was determined by nuclear reaction analysis using 3He (d, p) α reaction. The fitting of the experimental data form RBS and NRA measurements was done using SIMNRA code, developed at IPP Garching.

Structural aspects and atomic intermixing processes in Be/W bilayers deposited on Si(001) substrates with Fe buffer layers enriched in the ^{57}Fe Mössbauer isotope have been studied via atomic force microscopy, grazing incidence X ray diffractometry, X ray reflectometry, X ray fotoemission spectroscopy and conversion electron Mössbauer spectroscopy.

From RBS measurements it was observed that the relative concentration slightly changes with thermal treatment, reason why it is assumed that the states of chemical bonding also changes. NRA measurements showed that as the thermal treatment temperature increases, the deuterium is implanted deeper inside the sample, the total amount of D being the same. Thermal desorption spectroscopy (TDS) profiles for the Be-C-W samples showed clear dependence of D-retention on the thermal treatment temperature.

The total amount of deuterium retained and released as a function of thermal treatment temperature was estimated. No significant differences were observed regarding the retention behaviour. The release of deuterium slightly decreases with the increase of the thermal treatment temperature. However, more than 90% of the nuclear fuel was released during the TDS experiment.

Papers

[1] C. Porosnicu, A. Anghel, K. Sugiyama, K. Krieger, J. Roth, C.P. Lungu, *Influence of beryllium carbide formation on deuterium retention and release, Journal of Nuclear Materials*, *Volume 415, Issue 1, Supplement*, *1 August 2011*, *Pages S713-S716*

[2] V. Kuncser, P. Palade, G. Schinteie, S. Sandu, L. Trupina, C. P. Lungu, N. Gheorghe, C.V. Teodorescu, C. Porosnicu, I. Jepu, C.P. Lungu and G. Filoti, *Structural aspects and atomic intermixing processes in Be/W bilayers deposited on Si(001) substrates with Fe buffer layers*, Journal of Alloys and Compounds 512-1,(2012), 199-206.

Conferences

[1] C. Porosnicu, I. Jepu, A. Anghel, C.P.Lungu, K. Sugiyama, K. Krieger, J. Roth, C. Sion, *Characterization of Be - H co-deposited films prepared by thermionic vacuum arc method*, Nuclear materials of the E-MRS 2011 Spring & Bilateral Meeting, May 9 to 13, 2011, Nice, France.

Reports

[2] C. P. Lungu, C. Porosnicu, I. Jepu, A. M. Lungu, P. Chiru, V. Zaroschi, C. Stan-Sion, Mihaela Enachescu, Preparation of Be containing layers for D retention and characterization, Joint annual meeting of SEWGs "ITER Material Mix" and "Material Migration" on May 19-20, 2011 at the Aalto University, Helsinki, Finland

Detailed results

Introduction

The application of several materials at the first wall of ITER leads under operation to the formation of compounds. The retention mechanisms for deuterium and the influence of surface composition, structure, and temperature are essential fundamental properties which enable predictions of the behavior of multi-component first walls in e.g. JET and ITER. The MEdC Association by the research group of the National Institute for Laser, Plasma and Radiation Physics, has a broad experience in preparing and characterization of mixed films using the original thermionic vacuum arc (TVA) method.

It is necessary to investigate the D retention in multilayer and mixed materials and of surface versus bulk retention in systems with mixed layers on pure substrate materials as function of temperature. Studies on the composition and structure of mixed materials and of incident flux composition are necessary. The influence of the impact of D in such systems was studied using dual beam facility at IPP Garching, Germany. A set of samples were coated on special ^{57}Fe layers pre-deposited silicon substrates in order to be characterized at the National Institute of Material Physics, Magurele, Romania.

Complex characterization of Be/W multilayer containing films

Fe buffer layers enriched in the 57Fe Mössbauer isotope have been grown directly on Si(001) substrates or on thin W underlayers by rf sputtering. A partial reduction of the films have been obtained via their subsequent hydrogenation. Be(30nm)/W(30nm) bilayers have been grown on the hydrogenated Fe tracer layers, via a thermo ionic vacuum arc method [1] and a thermal treatment, performed in vacuum, at 600C for 10 min was subsequently applied. All structures have been characterized following different processing stages, with respect to morphological/structural and diffusional aspects, via AFM, GIXRD, XRR, XPS and CEMS

According to our previous experience related to rf spurring of very thin Fe films on Si substrates, the quality of the films can be much enhanced with respect to their crystalline structure, surface roughness and especially reducing oxidation, via a subsequent hydrogenation [2].

The presence of the C 1s peaks in the XPS spectra of the WFH sample, of decreasing intensity at higher etching time, proves the expected contamination with carbon species down to a depth of a few nm into the material. The specific XPS peaks of W (both 4f and 4d) have been observed just after an etching of 5 nm, within a shift of 3-4 eV toward larger binding energies, as compared to the data reported in [3], for a W clean film. According to a further discussion, this shift seems to be related to an oxidation process taking place in the W film just before the Fe deposition (open to air is required by the sputtering machine, in order to change the target).

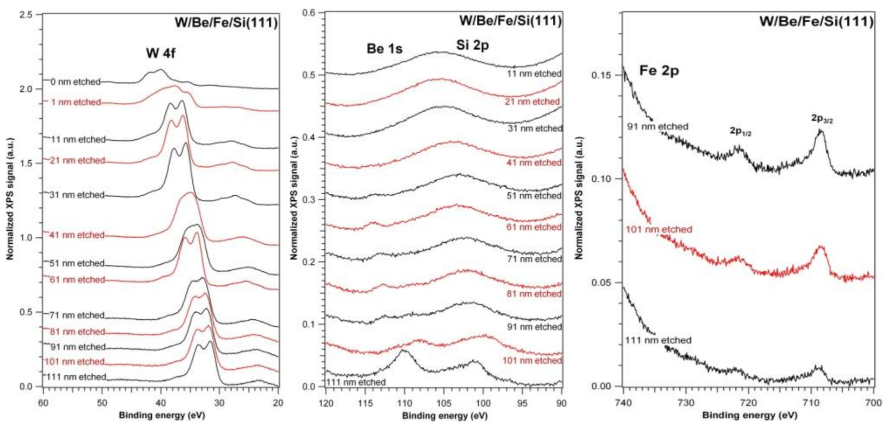

Figure 1 - XPS spectra of the FH1BW sample recorded in the W 4f region (4f5 with a higher binding energy than 4f7) recorded after subsequent etching depths (a) and in the Be 1s/Si 2p region (b) and in the Fe 2p binding energy range (c).

The XPS spectra collected on the as deposited sample FH1BW at different etching depths, in the energy ranges belonging to W 4f, Be 1s and Fe 2p are shown in figure 1. It might be directly observed that Be signals start to be present only at depths higher than 40 nm and disappears at depths higher than 90 nm (the Si 2p3 signal at about 100 eV becomes evident at an etching depth of 110 nm). The binding energy of Be 1s, shift slightly from higher values approaching 115 eV, specific to oxidized Be in the upper part of the Be film, down to lower values of about 112 eV, specific to neutral Be phase, toward the interface with the Fe layer.

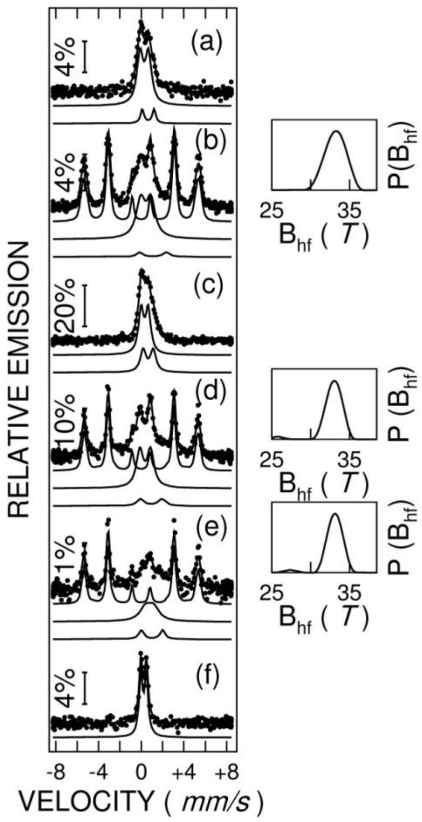

Figure 2 - CEM spectra at RT of the following samples: WF (a), WFH (b), F1 (c), FH1 (d), FH1BW (e) amd FH1BWT (f)

A same shifting trend of the binding energy versus the etching depth is observed also in the case of the W 4f peaks, indicating an enhanced oxidation of the W films, especially at the most surface layers of nm thickness, where the unusual large shift might suggest an unusual high oxidation state of W. In addition, at variance to the Be case, the XPS data show the presence of the W atoms down to the deeper etching depth of 100 nm. Most probably, this unexpected finding has to be correlated with an enhanced top-down diffusion of the W atoms during the growing process, aspect which has to be carefully investigated in further studies.

The significant presence of Fe is evidenced only at etching depth of about 100 nm and moreover, the observed binding energies (e.g. about 708 eV for the 2p3/2 XPS peak) indicates that the Fe film is mainly in its metallic state. Hence, the XPS data are in agreement with the overall geometrical structure of the film, observed by XRR, of type Si/Fe(≈5nm)/Be(≈45nm)/W(≈45nm), but also evidence an unexpected diffusion of the W atoms into the Be films and also an increasing oxidation of the structure, at its upper part.

The CEM spectrum of sample F1 can be decomposed in two components with similar hyperfine parameters as for the no hydrogenated sample WF. The two components were accordingly assigned to Fe^{3+} positions in superparamagnetic Fe_2O_3 and to the atypical Fe^{2+} of defect FeO (see table 1). It is worth mentioning at this point, that Fe-Si phases giving rise to paramagnetic like central components of similar hyperfine parameters as for Doublet1 in table 1 can not be disregarded in case of the F1 sample. Before giving a definite support against the assignment of the Doublet1 in the Mössbauer spectrum of sample F1 to an Fe-Si phase, we will analyze briefly the CEM spectrum of sample FH1. Similar to the case of the hydrogenated sample WFH, it was fitted by a sextet with distributed magnetic hyperfine field, assigned to metallic Fe and by two doublets (see table 1). The first one, Doublet1, was assigned to Fe^{3+} in strongly distorted positions belonging to a mixture of Fe_2O_3 and Fe_3O_4 oxides whereas the second, Doublet2, to Fe^{2+} ions in Fe_3O_4. The relative content of metallic Fe in this sample is of 59% and the rest of Fe oxide phases is of 41% (Fe_2O_3 and Fe_3O_4 seems to be in almost equal proportion in this sample). It is to mention that in the case of the alternative assignment of the Doublet1 to an Fe-Si phase in both F1 and FH1 samples, the Fe content of the Fe-Si phase in FH1 sample has to be less than half from its value in sample F1 (the rest of Fe precipitating into metallic Fe). Amoung the Fe-Si phases giving rise to paramagnetic patterns in the Mössbauer spectrum are metastable c-FeSi phases [4], amorphous and crystalline Fe_xSi_{1-x} phases with x<0 and α-, β- and γ-$FeSi_2$ [5] (Fe_3Si thin films and Fe_xSi_{1-x} with x >0.5 shows finite hyperfine fields in the Mössbauer spectra [6]). Average quadrupole splittings of about 0.5-0.7 mm/s are compatible with most of these compounds, but their isomer shifts show peculiar behavior. In Fe_xSi_{1-x} phases with x.>0.5, the IS values decrease continuously with x, from about 0.27 mm/s at x=0.5 down to 0.00 mm/s at x=1 (pure Fe) [4]. In addition, the isomer shift decreases by decreasing the conductive character of the films [5], e.g. from about 0.27 mm/s in conducting FeSi or α-$FeSi_2$ to 0.20 mm/s in γ-$FeSi_2$ and further to about 0.07 mm/s in the more semiconducting β- $FeSi_2$. It is to mention that according to [7] a similar decreasing trend has been observed also in amorphous Fe_xSi_{1-x} from larger values in the more conductive $Fe_{0.5}Si_{0.5}$ to slightly lower values in the more semiconducting $Fe_{0.2}Si_{0.8}$. Hence, isomer shift values lower than 0.28 mm/s are expected in all Fe-Si compounds at room temperature, with slightly decreased positive values for those paramagnetic compounds with a more pronounced semiconducting behavior expectedly induced at a higher Si relative content. Looking to the data in table 1 (for the F1 and FH1 samples), IS values higher than 0.32 mm/s are clearly observed and in addition, the IS value for Doublet1 in sample FH1 is slightly higher than in sample F1, in spite of an presumably assumed Fe-Si paramagnetic phase of higher Si content in the FH1 sample. The above mentioned disagreements disregard the assignation of the doublet1 component in the Mössbauer spectra of samples F1 and FH1 to Fe-Si phases and justify the assumption of a relatively low atomic interdifussion at the Fe/Si interface, which will be further considered for the next two samples.

The CEM spectrum of sample FH1BW has also evidenced the presence of the sextet assigned to metallic Fe, of a higher relative spectral contribution than in the previous sample FH1 (68% instead of 59%) as well as of the two doublets responding for Fe^{3+} and Fe^{2+} species (the relative amount of magnetite seems to prevail in this sample over the Fe_2O_3). Finally, the CEM spectrum of sample FH1BWT shows just a doublet with IS = 0.20 mm/s and QS = 0.52 mm/s, standing for a strong intermixing of the Fe/Be/W layered structure. While the XPS data collected on the FH1BW sample have shown a strong penetration of the W atoms close to the Fe buffer layer as well as an almost complete metallic character at the Fe/Be interface (W, Be and Fe showing typical binding energies for more reduced species), it rises up the question of the strongest diffusion at the Fe/Be interface (a sharp Si/Fe interface is assumed, based on the previously mentioned aspects). According to [8] slightly negative IS values (between -0.15 and -0.13 mm/s) corresponds to tungsten rich Fe-W alloys, in disagreement with the positive IS value of the doublet, mentioned in table 1. On the other hand, low positive IS values are mentioned for Fe-Be systems (a paramagnetic phase appears for Be concentrations exceeding 75%). Hence, the data in Table 1 are consistent with a strong diffusion of the Fe atoms inside the Be layer, as induced by the thermal treatments of the Si/Fe/Be/W multilayer annealed for 10 min at 600 C.

Influence of Thermal Treatment on Deuterium Retention and Release Behaviour for Ternary Be-C-W Thin Films

An unwanted side effect related to the plasma wall interaction of the boundary plasma with the surrounding walls is that the sputtered atoms from the plasma facing-components (PFC) materials, namely beryllium (Be), carbon (C) and tungsten (W) as well as plasma fuel, can be redeposited on other plasma-facing or remote surface areas. As a result of these processes, layers of so-called mixed materials of binary (Be_xC_y, Be_xW_y, W_xC_y) and ternary systems ($Be_xC_yW_z$) will form on the PFC's surfaces. These mixed materials will change the tritium retention/desorption behavior of the original PFC as well as their thermo-mechanical properties.

Be-C-W ternary mixed layers were prepared by the Thermionic Vacuum Arc (TVA) deposition method. The TVA device is equipped with two independent deposition sources which allow the preparation of mixed films by plasma co-deposition in high vacuum conditions. For ternary Be-C-W layers, one of the sources was tungsten, and beryllium carbide (Be_2C) was used as the other. In order to study the influence of thermal treatment on chemical state of deposited elements and its deuterium (D) retention and release, the samples were thermally treated after deposition under high vacuum conditions (10^{-8} mbar) at different temperatures (475 , 675 , 875 , and 1075K).

Surface analysis performed by **X-Ray Photoelectron Spectroscopy (XPS)** was carried out on a Quantera SXM equipment, with a base pressure in the analysis chamber of 10^{-9} Torr. The X-ray source was Al K_α radiation (1486.6eV, monochromatized) and the overall energy resolution is estimated at 0.75 eV by the full width at half maximum (FWHM) of the $Au4f_{7/2}$ line.

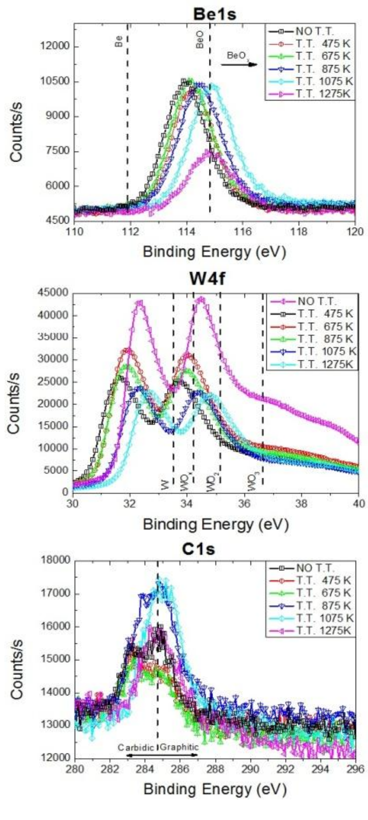

Figure 3 - High resolution photoelectron spectra of the most

From the XPS spectra, after Ar cleaning (1keV, 0.5 min) the incorporated C was found as carbides (Be_2C and/or WC) and C-C bondings as graphitic C. The mentioned carbides are present on the surface up to 875K (or lower in the range 675-875K). There is a threshold at 875K above which we notice no contribution of the carbides on the surface. The only remaining C species are the graphitic one.

The stoiciometric BeO is formed up to 875K while above this temperature the Be1s binding energies increases suggesting the occurrence of some non-stoichiometric oxide BeOx. The kinetics of oxidation display that W is slowly oxidized and reaches the WO state only at 1275K. Another threshold can be noticed at 1275K exhibiting a large difference between the relative concentrations of the Be and W as compared with the previous temperatures.

Thus, the W rel. conc. suddenly increases at the expense of the decreasing Be relative concentration, the amount of oxygen remaining rather constant. This experimental finding can be explained by a strong tendency of W to segregate from the subsurface region to the top of the surface.

Retention and desorption studies on Be-C-W films

Deuterium implantation experiment was performed in the High Current Ion Source. The energy of D ion beam was 600 eV D3+ (200 eV/D), and the incident direction was normal to the target surface. The implantation was carried out at a room temperature with the flux of ~ 3 x 10^{19} D/m^{2}s. The implantation fluency was 10^{22}D/m^2. RBS measurements were performed to investigate the films compositions, the position of the oxygen and to see if there is a mixture of the three elements. The amount of D retention was determined by nuclear reaction analysis with using ^{3}He (d, p) α reaction.

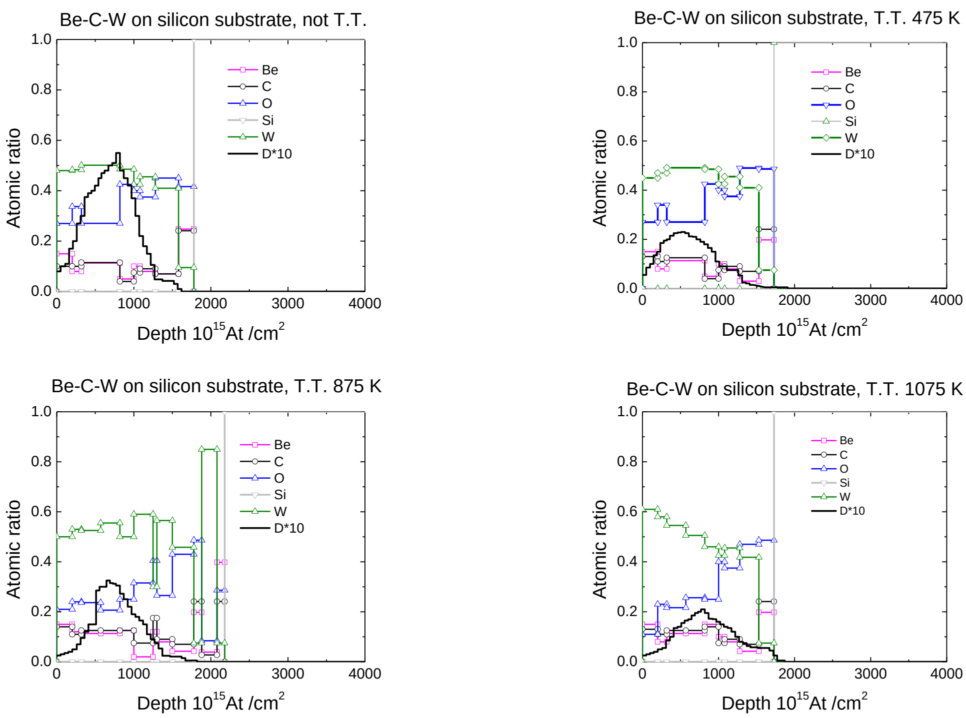

Figure 4 - The composition of the layers computed from RBS measurements, as well the deuterium depth profiles, from NRA measurements. The measurements were performed for samples treated at certain temperatures, as shown on the graphs.

The main aspect underlined by RBS measurements is that relative concentration slightly changes with thermal treatment. Tungsten concentration increases towards the surface, while oxygen concentration increases. It is assumed, as shown by XPS results that the states of chemical bonding also changes, oxides (BeO, WO_X), as well as carbides (Be_2C, W_2C) and beryllides (Be_2W, $Be_{12}W$) forming or dissociating at a certain temperatures included in this study.

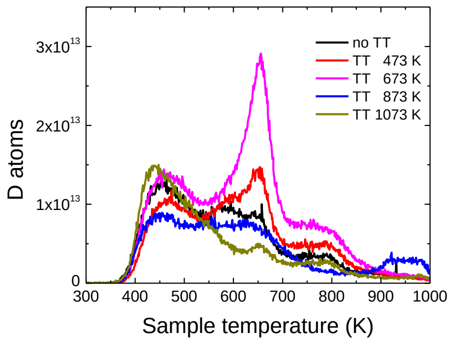

Figure 5 - TDS spectra for the total deuterium desorbtion behaviour

Also, NRA measurements showed a different behaviour of the D retention. As the thermal treatment temperature increases, the deuterium is implanted deeper inside the sample, the total amount of D being the same, but the local concentration at a certain depth, being lower.
In TESS facility at IPP Garching, thermal desorption spectroscopy (TDS) experiment was performed for the implanted samples.

TDS profiles for the Be-C-W samples showed clear dependence of D-retention on the thermal treatment temperature. Samples treated at 473 and 673 K present a high peak around 660K and as the thermal treatment temperature increases, this peak disappears. This behaviour is attributed to the chemical state change.

After the TDS experiment was performed the total amount of deuterium that remained inside the samples was measured using NRA. The total amount of deuterium retained and released as a function of thermal treatment temperature was estimated. No significant differences were observed regarding the retention behaviour. The release of deuterium slightly decreases with the increase of the thermal treatment temperature. However, more than 90% of the nuclear fuel was released during the TDS experiment.

Conclusions

Be(30nm)/W(30nm) bilayers have been grown on the hydrogenated Fe tracer layers, viatThermo ionic vacuum arc method and a thermal treatment, performed in vacuum, at 600C for 10 min was subsequently applied. All structures have been characterized following different processing stages, with respect to morphological/structural and diffusional aspects, via AFM, GIXRD, XRR, XPS and CEMS.

Using the thermionic vacuum arc method multilayer (500nm Be/100nmCand 500nm Be/100nm W) as well as ternary Be-C-W samples were prepared on graphite and silicon substrates at room temperature. The samples were thermally treated after the deposition under high vacuum conditions (10^{-8} mbar) in order to avoid supplementary oxidation of the ternary system.

All structures have been characterized following different processing stages, with respect to morphological/structural and diffusional aspects, via SEM, EDS and XPS.

Deuterium implantation experiment was performed in the High Current Ion Source. The energy of D ion beam was 600 eV D3+ (200 eV/D), and the incident direction was normal to the target surface. The implantation was carried out at a room temperature with the flux of ~ 3 x 10^{19} D/m^2s. The implantation fluency was 10^{22}D/m^2. This value was chosen due to the expected particle fluence to the ITER first wall.

RBS measurements were performed to investigate the films compositions, the position of the oxygen and to see if there is a mixture of the three elements. The amount of D retention was determined by nuclear reaction analysis with using 3He (d, p) α reaction. The fitting of the experimental data form RBS and NRA measurements was done using SIMNRA code, developed at IPP Garching.

From RBS measurements the relative concentration slightly changes with thermal treatment, it is assumed that the states of chemical bonding also changes. XPS measurements confirmed the formation of these chemical states as well as their change with the thermal treatment temperature. NRA measurements showed that as the thermal treatment temperature increases, the deuterium is implanted deeper inside the sample, the total amount of D being the same.

In TESS facility at IPP Garching, thermal desorbtion spectroscopy (TDS) experiment was performed for the implanted samples. TDS profiles for the Be-C-W samples showed clear dependence of D-retention on the thermal treatment temperature.

The total amount of deuterium retained and released as a function of thermal treatment temperature was estimated. No significant differences were observed regarding the retention behaviour. The release of deuterium slightly decreases with the increase of the thermal treatment temperature. However, more than 90% of the nuclear fuel was released during the TDS experiment.

Acknowledgement

The reported work includes contributions from the following people outside the EUATOM-MEdC Association: W. Jacob, K. Sugiyama, K. Krieger, J. Roth, IPP Garching, Germany

References

[1] C.P.Lungu, I.Mustata, G.Musa, V.Zaroschi, A.M.Lungu and K.Iwasaki: Vacuum 76 (2004) 127

[2] V. Kuncser, F. Tolea, G.Schinteie, I.Jepu, P.P alade, Digest Journal of Nanomaterials and Biostructures 6(1) 2011 199-206

[3] http://www.lasurface.com/database/spectrexps.php

[4] M.Walterfang, W.Keune, K.Trunov, R.Peters, U.Rucker, K.Westerholt, Phys.Rev B. 73 (2006) 214423

[5] J.Desimoni, F.H.Sanchez, M.B.Fernandez van Raap, H.Bernas, C.Clerc and X.W.Lin, Phys.Rev.B 51(1) 1995 86-90

[6] K.Trunov, M.Walterfang, W.Keune. N.K.Utochkina and A.Trunova, Thin Solid Films 516 (2008) 6205-6209

[7] F.H.Sanchez, M.B.Fernandez van Raap and J.Desimoni, Phys.Rev.B 44 (1991) 4290

[8] G. Le Caer, P. Delcroix, T.D.Shen and B. Malaman, Phys.Rev B 54(18) (1996) 12775-12786

X-RAY MICRO-TOMOGRAPHY STUDIES ON GRAPHITE AND CFC SAMPLES FOR POROSITY NETWORK CHARACTERIZATION

Ion TISEANU, Teddy CRACIUNESCU, Cosmin DOBREA, Adrian SIMA

EURATOM-MEdC Association, National Institute for Lasers ,Plasma and Radiation Physics, Bucharest, Romania

Abstract

The carbon-carbon fibre reinforced composites (CFC) offer attractive properties for plasma-facing components (PFC) in the ITER divertor.

The spatial distribution of porosity and density of these materials has to be determined for assessing their performance at high temperatures and/or intense radiation fields. The CFC porosity plays a major role in both fabrication and operating of PFCs: i) the quality of actively cooled components depends on the metal impregnation inside the macro-pores of the CFC, ii) a significant part of the fuel retention is due to the codeposition mechanism inside CFC porosity.

In the current reporting period we apply cone beam X-ray microtomography for the comparative characterization of three types of CFC materials relevant for fusion technology: NB31 and NB41 (Snecma) and DMS870 (Dunlop). X-ray microtomography is a powerful tool for the simultaneous determination of porosity factor and for the 3D visualization of the pore network. Carbon fiber composite armors have been successfully used for actively cooled plasma facing components (PFCs) of the Tore Supra (TS) tokamak. They were also selected for the divertor of the stellarator W7-X under construction and for the vertical target of the ITER divertor. The NB11 material was used for TS whereas NB31 material is used for W7-X and the NB41 is retained for ITER.

The investigation was carried out at the INFLPR newly upgraded X-ray tomograph (http://tomography.inflpr.ro). The system is equipped with a state-of-the-art nano-focus X-Ray tube capable to provide x-ray images with feature recognition down to one micron.

The overall main challenge was to achieve the required micron range of the spatial resolution for the rather macroscopic samples. Indeed, CFC has a multiscale architecture: from single fibres with diameter of a couple of microns one fabricates fibre bundles of fractions of mm cross-sections which are arranged in textile structures with space period of several mm. A dedicated porosity factor calculation procedure was consistently applied to CFC samples of similar dimensions which are scanned in the same optimized tomography configuration.

Architecture difference between NB31 and DMS870 CFC samples is clearly revealed in the tomography cross sections and density plots represented in the figures attached.

Our current 3D micro-tomography reconstructions with 2.5 microns voxel resolution for relatively large samples of CFC (N11, NB31 and DMS780) are considered a good basis for the characterization of the initial porosity of the new CFC ITER reference material NB41.

Papers

[1] Tiseanu, I., Tsitrone, E., Kreter, A., Craciunescu, T., Loarer, T., Pegourie, B., Dittmar, T., X-ray micro-tomography studies on carbon based composite materials for porosity network characterization, (2011) Fusion Engineering and Design, Volume 86, Issue 9-11, October 2011, Pages 1646-1651

[2] Tiseanu, I., Craciunescu, T., Pegourier, B., Maier, H., Ruset, C., Mayer, M., Dobrea, C., Sima, A., Advanced x-ray imaging of metal-coated/impregnated plasma-facing composite materials, Phys. Scr. T144 (2011), in print

[3] Tiseanu I. T. Craciunescu, M. Rubel, G. De Temmerman, C. Dobrea, A. Sima, Microstructural Characterization of CFC Materials by X-ray Microtomography, presented at the EUROMAT2011, 12-15 September 2011, Montpellier, France

[4] Tiseanu, E. Tsitrone, A. Kreter, T. Craciunescu, T. Loarer, B. Pégourié, T. Dittmar, X-Ray Micro-Tomography Studies on Carbon Based Composite Materials for Porosity Network Characterization, Fus. Eng. Des. (in print), DOI: 10.1016/j.fusengdes.2011.04.079.

Detailed results

Micro-tomographic experiments have been carried out on a high resolution X-ray micro-tomography facility of INFLPR, EURATOM-MEdC (http://tomography.inflpr.ro). The main component is an open type nanofocus X-ray source (W target on Be or Al window, Mo target on Be and W target on diamond, maximum high voltage of 225 kVp at up to 30 W maximum power). X-rays are detected by means of a high-resolution image intensifier or amorphous silicon flat panel sensors. Offset CT geometry was used in order to allow enhanced spatial resolution (up to 2.5 µm/voxel). The tomography analysis is able to provide useful quantitative information about the porosity network of the CFC samples and can be used to identify the relevant mechanism for fuel retention into the material bulk like: fuel localization in the bulk of CFC or in the trapping sites (porosity) along fibers, or codeposition into CFC open pores.

Qualitative evaluation of the CFC morphology

Morphology differences between different sorts of CFC materials used in fusion facilities are shown in Fig. 1. The tomographic cross-sections reveals the orderly packed ex-pitch fibres in the X–Y planes (left panel) and the relatively lower density, less ordered ex-PAN fibres as displayed in the same figure (right panel). Microscopic pores with sizes from the unit voxel to couple of tens of microns are located inside the fibre bundle. The macroscopic pores, which are more relevant for the fuel retention mechanism, are mainly elongated gaps (fraction of mm wide and up to few mm long) located at the boundary of the fibre bundles. The tomography reconstructions were performed on rather macroscopic samples 5x5x5 mm^3 with space resolution of ≈ 6 μm/voxel.

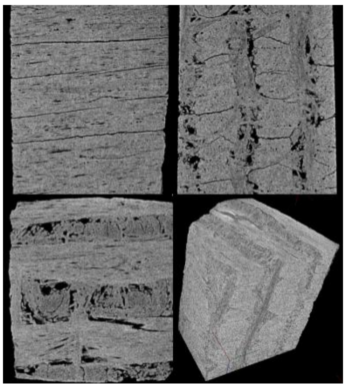

NB31

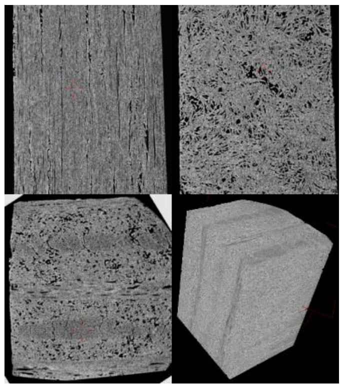

DMS780

Figure 1 – Morphology differences between two types of CFCs: NB31 (3D structured) and DMS780 (2D structured)

One can continue with a semi-quantitative analysis of the density histograms of the reconstructed images. Figure 2 shows a comparison of the NB31 and the newest CFC material NB41 – the reference CFC for ITER. As seen from Fig 2 the density histograms of the two materials are quasi-identical but the morphologies somehow differ.

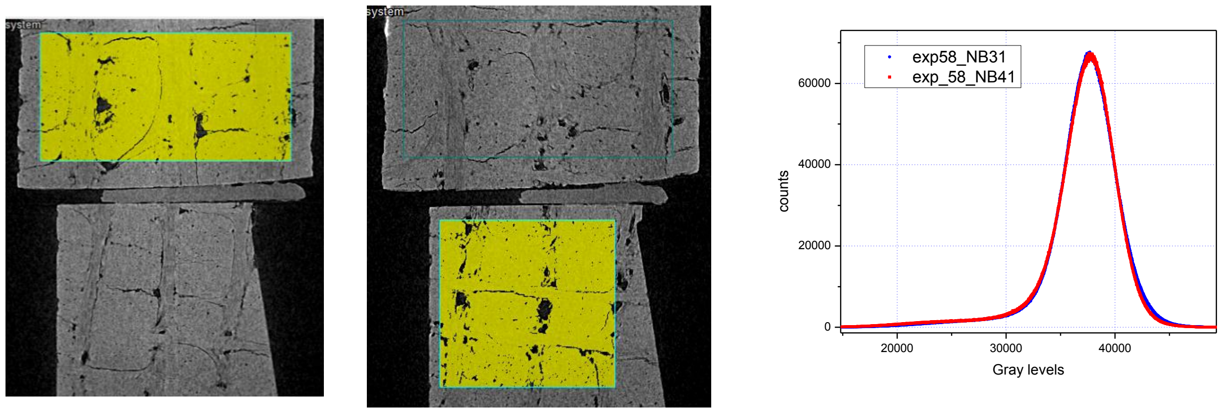

Figure 2 - Comparison of the morphology vs. density histograms of the NB31 (above in the montage) and the new ITER reference CFC NB41 (bellow in the montage).

Quantitative evaluation of the CFC porosity factor

A procedure for a quantitative evaluation of the sample porosity factor has been recently introduced and tested in [Tiseanu, I.et al, *X-ray micro-tomography studies on carbon based composite materials for porosity network characterization*, (2011) Fusion Engineering and Design, Volume 86, Issue 9-11, October 2011, Pages 1646-1651]

For the quantitative analysis of the porosity structure in terms of total void fraction, network connectivity, wall thicknesses we used the powerful 3-D visualization and measurement software: VGStudioMax, Volume Graphics GmbH, Heidelberg, Germany, www.volumegraphics.com. The data post-processing comprises several steps: (1) finding the optimal choice for the threshold level, in order to create a correct border between CFC and porous regions. A detailed inspection of this demarcation is performed while navigating through the reconstructed volume along transversal, longitudinal and sagital cross-sections; (2) following validation, the reconstructed volume is segmented and the porous structure is extracted as an independent object which can be represented also as a 3D structure; (3) determination of the absolute value of the porosity factor by using the VGStudioMax volume analysis module. The defect analysis tool can be used to determine other parameters as: voids volume, size and projected area distribution.

With this method we obtained porosity factors for all fusion technology relevant CFC materials, in good agreement with the manufacturer specifications (Table 1).

Table 1: Porosity factors evaluated from tomography reconstructions

Material **Fusion Facility**	**NB31** **AUG**	**DMS780** **JET**	**N11** **TS**	**NB41** **ITER**
Porosity factor (%)	8.1	9.4	10.5÷12	6.4

Here we evaluate a new method to determine the porosity factor based on a non-porous reference material. As reference material we used Fine Grain Graphite (FGG) which is free of macroscopic pores (pores equal or larger than the spatial resolution of the microtomography method).

Figure 3 shows tomography cross-sections through two samples measured together: NB41 and FGG. In the associated density histograms on can see the typical asymmetric pattern of a porous material (NB41) compared with the symmetric histogram displayed by the FGG. The method for porosity evaluation would make use of this difference in the density profiles. However due to differences in the average densities of the two materials (average density of NB41 around 5% higher than the density of FGG) we could not yet implement a reliable method for porosity evaluation.

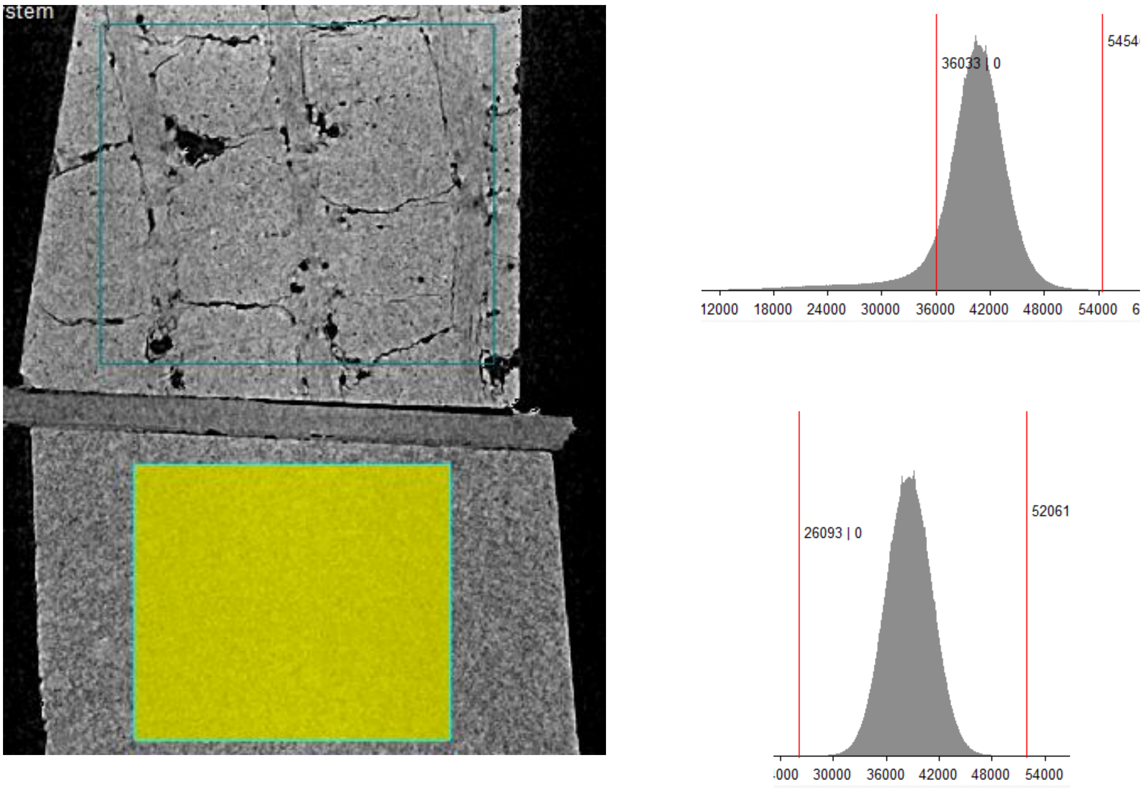

Figure 3 - Comparisons of the density histograms of NB41 CFC (top) and FGG (bottom). The low density tail of the NB41 histogram contains the porosity information

A similar method but without using a non-porous reference material is illustrated in Figure 4. The density histogram of a reconstructed volume fragment is compared with a symmetrised histogram. The symmetrisation operation consists of fitting the high density side of the histogram with a Gaussian curve. The porosity factor is calculated as the ration between the area under the density histogram and the area of the fitted Gaussian curve. The values shown in Fig 4 are in good agreement with manufacturer specifications. One can note that the method accounts very well to the excessive porosity of the 2D DMS780 CFC material.

Upgrade of the X-ray detection system

The nanoCT tomograph of INFLPR has been upgraded in what concerns the X-ray detection system with a newly developed CMOS flat panel detector capable of higher space resolution (75 μm/pixel) and improved digital output (14 bits) at superior SNR. The new detector has been mechanically implemented in our CT system and first images were obtained. Figure 5 shows a digital radiography of a NB41/NB31 stack of samples.

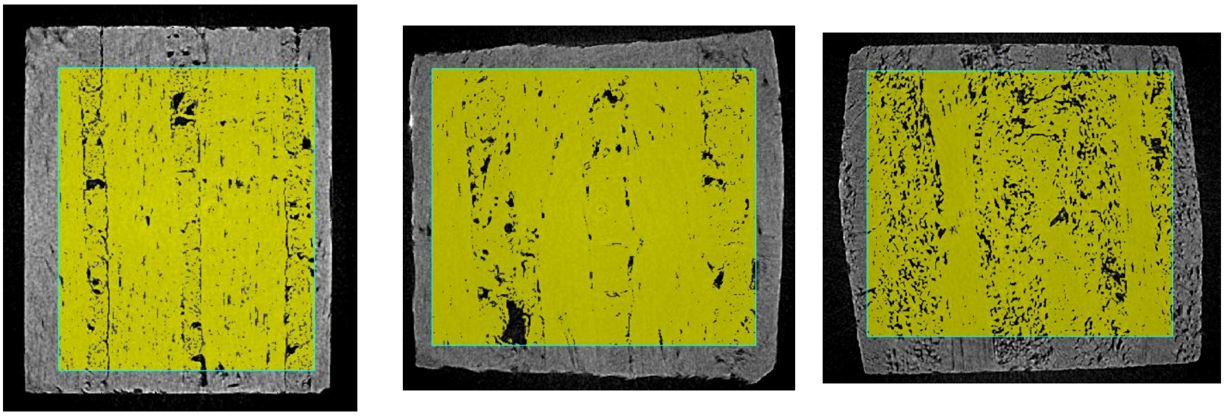

NB41 NB31 DMS780

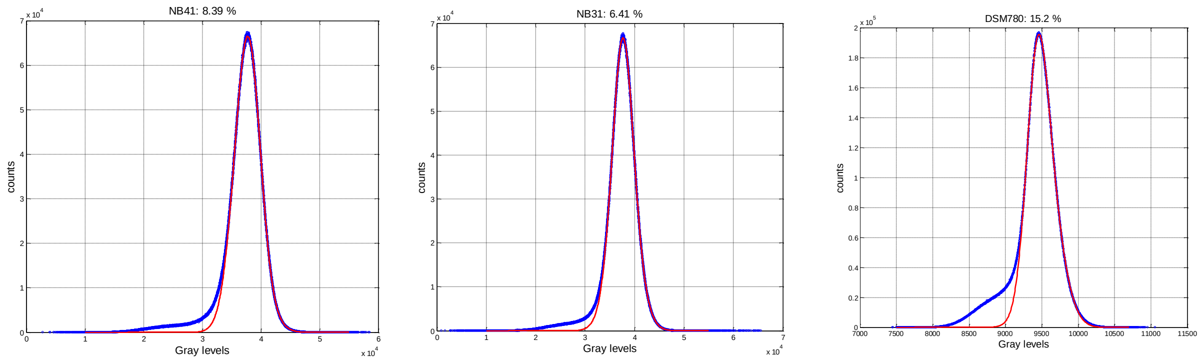

8.4 % 6.4% 15.2%

Figure 4 - Porosity factor evaluation based on the asymmetry of the density histograms.

The quality of the digital radiography is superior as resolution and SNR to the previous detection system. This put us in the position to deliver high quality tomography images and consequently better results concerning composite materials porosity description and characterization of bonding technology.

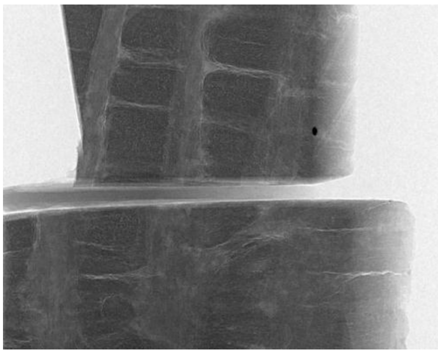

Figure 5 - X-ray detection upgraded setup. Preliminary examination of the NB31/NB41 CFC.

Due to their excellent resistance to excessive high heat and thermal shock loads, CFC is the favored candidate armour materials for ITER's plasma facing components [1]. The intense heat flux received by these components requires active water cooling. This is achieved through a welding - active metal casting (AMC) [2] - between the metallic water loop made of Cu alloys and the CFC material. To improve the relatively weak mechanical bond between CFC and Cu often the composite surface is coated by Ti/TiC. This procedure leads to an increased wettability of CFC by molten copper [3].

Tomographic reconstructions used here provide additional useful information concerning the the quality of the brazing of CFC to Cu and also about the morphology of the interface of CFC with Cu heat sink. All the experiments were performed on our X-ray transmission tomography facility [4]. A high power diamond target was used in order to improve photon statistics. It allows a ten-fold increase in the thermal conductivity as compared to the conventional transmission targets. Therefore high energy electron beams can be kept in focus to maintain the small focal spot size required for high image resolution.

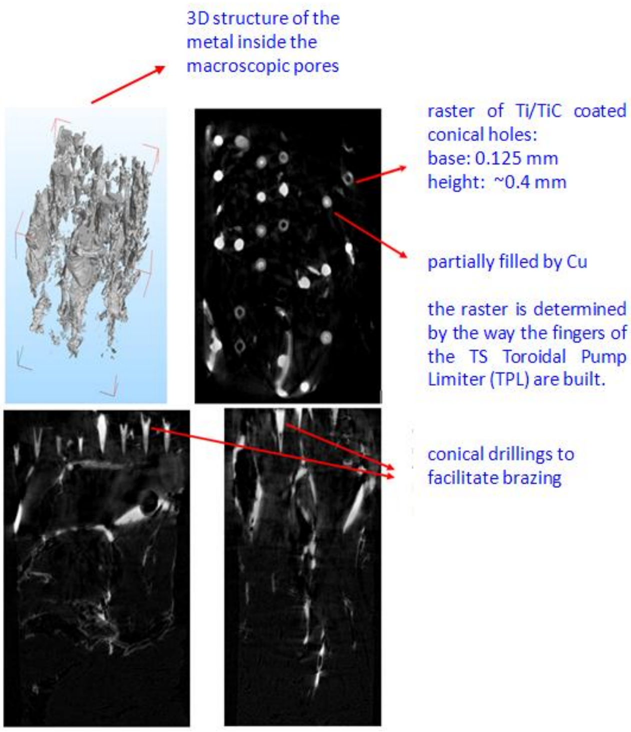

Figure 7 - Cu heat sink region of a DITS sample: 3D reconstructed volume (top-left), axial (top-right), sagital (bottom-left) and transversal (bottom-right) cross-section.

Despite the wide range of the X-ray attenuation coefficients displayed by this region which induces strong artefacts the tomographic analysis reveals a strong connectivity of the pores along the main fibre direction. Fig. 7 reveals also that the CFC macroscopic pores are nicely coated by metal (Ti) and the slimmest ones are totally filled by Cu. In this case Ti plays the beneficial role of a CT contrast media which emphasize the pore contours. The presence of the raster of conical drillings (base diameter of 0.125 mm and maximum height of 0.4 mm) totally coated by Ti and partially filled by Cu is due to the way the fingers of the TS Toroidal Pump Limiter (TPL) are built. One can image the use of the 3D reconstructed model of the infiltrated metal as input data for the evaluation of the thermal properties of the CFC – heat sink assembly.

Conclusion

Microtomography analysis was used for the 3D modelling of the fusion technology relevant CFC materials. High resolution morphology of rather macroscopic CFC samples was obtained. A procedure for the quantitative evaluation of the sample porosity factor has been introduced that produces realistic results for three types of CFC analysed. The results obtained by 3D micro-tomography analysis of statistically relevant volumes of CFC can be considered as a good basis for the characterization of the initial porosity of the new CFC ITER reference material NB41. This analysis will be systematically applied to several post mortem TS samples which involve Cu/Ti/NB11 CFC and to the new bonding technology that it is developed for W7-X and ITER. The X-ray detection system of the nanoCT tomograph of INFLPR has been upgraded with a newly developed CMOS flat panel detector capable of higher space resolution (75 μm/pixel) and improved digital resolution (14 bits) at superior SNR.

Acknowledgement

The reported work includes contributions from the following people outside the EURATOM-MEdC Association: Tsitrone, B. Pégourié, T. Loarer, T. Dittmar (*Association EURATOM-CEA, CEA Cadarache, France),* H. Maier, M. Mayer (*Max-Planck-Institut für Plasmaphysik, EURATOM Association, Garching, Germany),* A. Kreter (*Institute for Energy Research - Plasma Physics, Forschungszentrum Juelich, Association EURATOM-FZJ, Germany),* A. Hakola, S. Koivuranta, J. Likonen (VTT, Association EURATOM-Tekes, Espoo, Finland).

References

[1] G. Federici et al., *J. Nucl. Mater.* 684(2005)337–339.

[2] A. Grosman et al., *J. Nucl. Mater.* 821(2005)337-339.

[3] M. Salvo et al. 2008 *J. Nucl. Mater.* 374(2008)69–74.

[4] I.Tiseanu et al., *Surface & Coatings Technology* 10.1016/j.surfcoat.2011.03.049.

[5] M. Misawa, I. Tiseanu - Oblique View cone beam X-ray Tomography System*, Patent 2003/03/06, 10/379702 (USA), 0903887.9 (Germany), 0305013.5(United Kindom)*

[6] G.F. Matthews et al., *Phys. Scr.*, T128(2007)137-143.

X-RAY MICROBEAM ABSORPTION/FLUORESCENCE METHOD AS A NON-INVASIVE SOLUTION FOR INVESTIGATION OF THE EROSION OF W COATINGS ON GRAPHITE/CFC

Ion TISEANU, Teddy CRACIUNESCU, Cosmin DOBREA, Adrian SIMA

EURATOM-MEdC Association, National Institute for Lasers ,Plasma and Radiation Physics, Bucharest, Romania

Abstract

The thickness of tungsten layers deposited on carbon substrates is measured by a combination of non-destructive X-ray based techniques: i) high resolution X-ray absorption and ii) X-ray fluorescence mapping iii) X-ray backscattering. The thickness and the composition maps are obtained using a 2D X-ray fluorescence/backscattering scanning technique. The X-ray fluorescence mapping can be also used also for the determination of the spatial distribution of high Z materials deposited on low density matrixes.
The sensitivity and the calibration of the X-ray methods for the W coating thickness analysis were carried out on a non-exposed, tungsten coated FGG sample with three thickness steps determined by metallographic cut on SEM.
In 2011 we have analysed the measurements done in the last part of 2010 on the tungsten coated tiles from the ASDEX Upgrade outer divertor strike point. Due to short time available in the 2010 for measurements, rather coarse 2-dimensional distribution of W thickness at the tile surface was obtained.

In October 2011 the marker tiles returned to MEdC for measurements of the erosion patterns after the 2010-2011 AUG campaign. Rather highly spatially resolved erosion mappings were collected and preliminary correlations with the RBS measurements were carried out. Further data analysis is in progress.

Additionally we measured some marker tiles of the ITER-like wall program which are available in our laboratory since they are coated here by Combined Magnetron Sputtering and Ion Implantation.

Papers

[1] I. Tiseanu, M. Mayer, T. Craciunescu, A. Hakola, S. Koivuranta, J. Likonen, C., C. Dobrea, X-ray microbeam transmission/fluorescence method for non-destructive characterization of tungsten coated carbon material, *Surface & Coatings Technology 205 (2011) S192–S197,* doi:10.1016/j.surfcoat.2011.03.049

[2] I. Tiseanu, T. Craciunescu, B. Pegourier, H. Maier, C. Ruset, M. Mayer, C. Dobrea, A. Sima, *Advanced X-ray imaging of metal coated/impregnated plasma-facing composite materials,* Physica Scripta T-145(2011) 014073.

Detailed Results

1 Introduction

The Work Programme involves experiments on material erosion and transport in several European fusion devices (ASDEX Upgrade, Tore Supra, TEXTOR, MAST, JET for comparison) and linear plasma generators (PSI-2, PILOT/Magnum). It is coordinated by the SEWG Material Migration

The 2011 activities focused on cross machine comparisons of main wall erosion and local re- and co-deposition, characterisation of outer and inner divertor erosion as well as the migration of impurities from main chamber to divertor and inside the divertor.

Tungsten erosion, subsequent tungsten transport, and redeposition are of great interest, because a full tungsten divertor is foreseen to be used during the deuterium-tritium operational phase of ITER. The erosion of tungsten and carbon marker layers was extensively studied in the outer divertor of ASDEX.

During 2010, in INFLPR we have implemented and qualified the X-ray micro-beam absorption/fluorescence method as a non-invasive solution for investigation of the erosion of W coatings on graphite/CFC. In 2010-2011 we measured the W thicknesses of tungsten coated tiles from the ASDEX Upgrade outer divertor strike point. The 2-dimensional distribution of W thickness at the tile surface was obtained. In the following program (WP2011), there is a need to measure a whole poloidal section of 14 tiles.

Additionally we will measure some tiles of the ITER-like wall program. These W coated CFC tiles are available in our laboratory since they are coated in INFLPR by Combined Magnetron Sputtering and Ion Implantation. Since the thickness of the tungsten on the ITER like wall tiles is significantly larger (>10 µm) as compared with 0.5-2 µm of the ASDEX Upgrade tiles we will employ a different source of X-ray with a higher energy.

Our approach is based on a combination of non-destructive techniques. Thus the coating uniformity analysis is performed using i) high resolution X-ray absorption and ii) X-ray fluorescence mapping iii) X-ray backscattering. The thickness and the composition maps are obtained using a 2D X-ray fluorescence/backscattering scanning technique. The X-ray fluorescence mapping can be used also for the determination of the spatial distribution of high Z materials embedded in low density matrixes (i.e. marker layers, W inclusions, high density dust).
Global erosion, redeposition and transport of first-wall materials have been extensively studied in ASDEX Upgrade during the last seven years, using post-mortem surface analysis of tiles [1]. Specially prepared divertor or limiter tiles are used, which contain thin marker stripes for erosion/deposition measurements and are analyzed before and after exposure. Also regular tiles were analysed after exposure. Long-term samples are installed at the vessel walls or in remote areas without direct plasma contact. All samples are typically exposed during one discharge campaign.
The need for a fast and nondestructive method, which allows the quantitative determination of the thickness of a tungsten coating on a carbon material on large areas, led us to evaluate a combined transmission/fluorescence X-ray (µXRTF) technique. It is proved that this technique allows a good

spatial resolution (several 10 µm), and it is fast enough to allow measurements for thousands of data points. Consequently 2-D erosion pattern on a whole divertor tile may be retrieved.

This project is included in the EFDA Workprogramme 2011 Plasma Wall Interaction, SEWG Material Migration WP11-PWI-03-02

2. Methods and materials

The method for tungsten coating analysis was implemented using the Tomo-Analytic system, which was developed especially for the fusion materials analysis [2-3]. Tomo-Analytic is a combined X-ray fluorescence (µXRF) and cone-beam µXCT system for the noninvasive 3-D morphology and composition mapping. The key element of the µXRF component is a policapillary lens which provides a focal spot size in a range from few tens to a few hundreds of micrometers. A significant increase of the X-ray intensity (up to three orders of magnitudes) is obtained [4] which allows improved detection sensitivity.

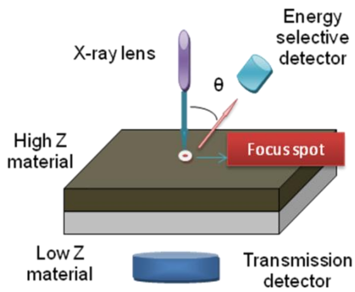

Figure 1 – Setup of the X-ray transmission/fluorescence module.

Tomo-Analytic is a configurable and versatile tool in which different measuring methods can be accommodated for the characterization of the thickness uniformity of FGG/CFC with metallic coatings (Fig. 1):

- µXRF) the coating X-ray fluorescence peak intensities are converted to elemental concentrations and/or film thicknesses.
- µXRFS) the X-ray fluorescence radiation emitted by the substrate is attenuated by the coating material; a correlation can be derived between the secondary emissions and the coating thickness.
- µXRFB) the coating thickness is determined from the correlation with the attenuation of the X-ray back-scattered radiation by a substrate with low effective atomic number. This procedure has the advantage to be more suitable to carry out reference free thickness measurements.
- µXRT) the geometry for the µXRT method is presented in Fig. 2. The X-rays are detected by an energy selective detector after passing through the investigated sample where they are attenuated accordingly with the composition and thickness of the materials.

The optimal measurement configurations and the irradiation parameters were obtained by MCNP-5 Monte Carlo simulations [5].

The sensitivity and the calibration of the X-ray methods (µXRFB and µXRT) for the W coating thickness analysis were carried out on a non-exposed, tungsten coated FGG sample with three thickness steps determined by metallographic cut on SEM (Fig. 2).

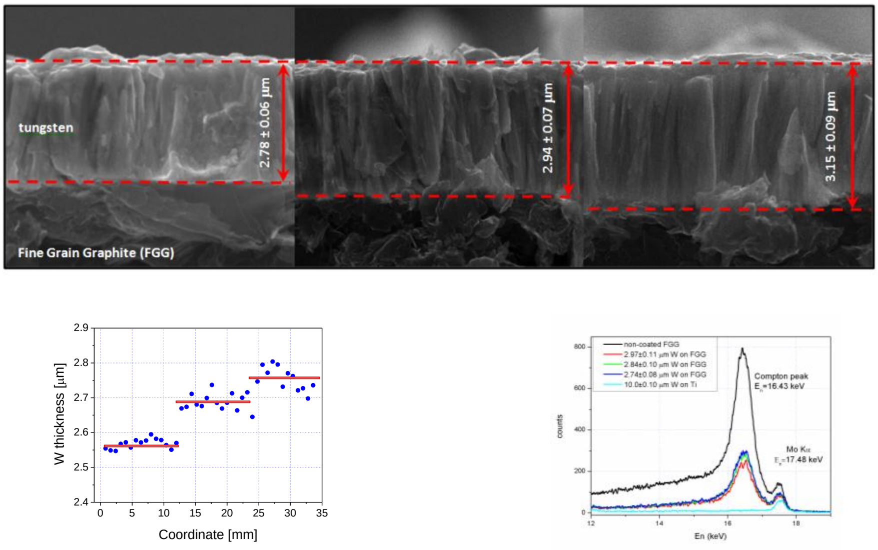

Figure 2 – Methods calibration: non-exposed FGG calibration sample with three thickness steps determined by metallographic cut on SEM (top); corresponding µXRT line profile (bottom-left); µXRFB method - Compton elastic scattering intensities as a function of tungsten coating thickness and substrate material (bottom-right).

Discussion of the SEM and the µXRFB thickness values was detailed in Ref. 3. Accordingly, the reliability of the µXRT method is limited if a polychromatic incident X-ray spectrum is used. Therefore a new experimental geometry was implemented (Fig. 3). It comprises a quasi-monoenergetic X-ray source (MoKα line of 17.48 keV) and an energy selective detection system (150 eV energy resolution).

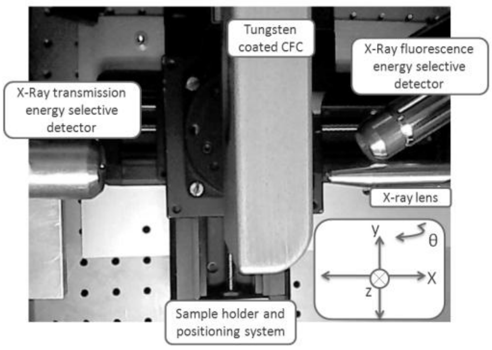

Figure 3 – Tomo-Analytic geometry for combined fluorescence/transmission experiments.

Table 1 summarises the W thickness values and their associated standard deviations. The relatively large scattering of the SEM values is attributable to the roughness of the W layer. For the µXRT method one uses the SEM samples with a FGG substrate of only 0.5 mm. This FGG substrate has an

X-ray transmission coefficient of 95% as calculated with the program of Ref. 6-7. The errors associated to the thicknesses values are standard deviations calculated over series of several tens of measurements points and do not include the systematic error due to the X-ray attenuation cross-sections.

The reliability of the µXRT method is limited if a polychromatic incident X-ray spectrum is used. Therefore a new experimental geometry was implemented (Fig. 2). It comprises a quasi-monoenergetic X-ray source (MoKα line of 17.48 keV) and an energy selective detection system (150 eV energy resolution). Table 1 summarises the W thickness values and their associated standard deviations. The relatively large scattering of the SEM values is attributable to the roughness of the W layer. For the µXRT method one uses the SEM samples with a FGG substrate of only 0.5 mm. This FGG substrate has an X-ray transmission coefficient of 95% as calculated with the program of Ref. 7. The errors associated to the thicknesses values are standard deviations calculated over series of several tens of measurements points and do not include the systematic error due to the X-ray attenuation cross-sections.

The calibration procedure proves that the µXRT method ensures fast and high resolution analysis and could resolve well below 5% in W thickness difference. Another advantage of the µXRT method is that it can be used for thicker W layers as it does not reach a saturation thickness required by the methods based on X-ray fluorescence. Thus, with the Mo anticathode X-ray tube used in our configuration one can measure up to 20 µm W. This value represents the W thickness range of the W coated JET ITER-like wall tiles and of the FGG coated tiles of AUG.

Table 1 – Calibration of the X-ray methods for W coating thickness analysis.

Layer no	Layer thickness / standard deviation		
	SEM	µXRFB	µXRT
1	2.78 ± 0.06	2.74 ± 0.08	2.69 ±0.05
2	2.94 ± 0.07	2.84 ± 0.10	2.87 ±0.05
3	3.15 ± 0.09	2.97 ± 0.11	3.10 ±0.06

3. Experiments and Results

The tungsten coatings have been deposited on FGG and CFC samples by Combined Magnetron Sputtering and Ion Implantation (CMSII) technology. This was recently used for W coating of about 2,000 CFC tiles for the ITER like Wall project at JET and approx. 1,000 FGG tiles for ASDEX Upgrade tokamak at IPP Garching. The CMSII technique involves simultaneous magnetron sputtering deposition and high energy ion bombardment. A high voltage pulse discharge ($U = 30 – 50$ kV, $\tau = 20$ µs, $f = 25$ Hz) is applied on the substrate alternatively with the DC bias. The periodical ion bombardment increases the surface mobility of the deposited atoms which leads to a high densification of the coating. Glow Discharge Optical Spectrometry (GDOS) is currently used for measurement of the coating thickness and impurities as a quality control technique for industrial production. More details about the fusion relevant W coatings including equipment and technology can be found in [8].

The µXRT technique with quasi-monochromatic spectrum was applied on a 5 mm thick FFG sample coated with ~10 µm W on top of a Mo interlayer of ~2.5 µm. The average result expressed in W equivalent thickness is 10.6 ± 0.2 µm. The GDOS analysis on a witness sample coated simultaneously with the FGG sample gives 9.2 µm for W and ~ 2.5 µm of Mo. As 2.5 µm of Mo is equivalent with ~0.3 µm of W in terms of X-ray attenuation at 17.5 keV one can notice an overestimation of ~10% of the W layer thickness. One possible reason of this overestimation is the inaccurate compensation of the non-linear pulse pileup effect for the measurements with and without W coating layer.

Also we have mapped with high space resolution (150 µm step) the W thickness of similar coating layers on a 5 mm thick DMS780 CFC sample (Fig. 4).

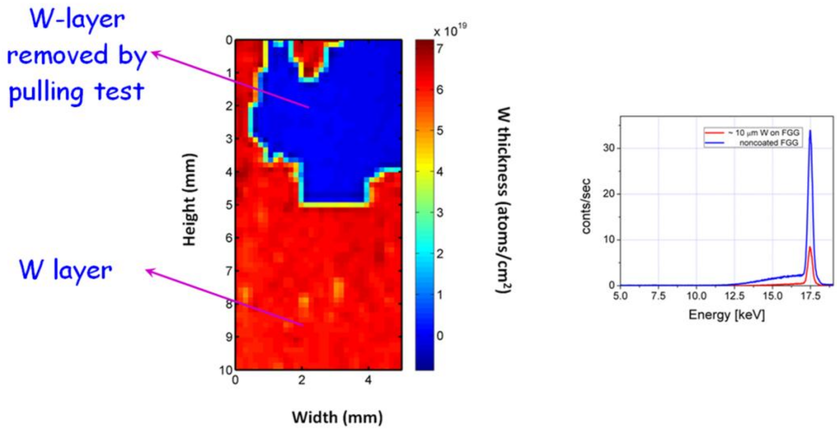

Figure 4 - W coating uniformity mapping by µXRT. An area of 10x5 mm2 was scanned with 0.15 mm step (left panel). The quasi-monoenergetic energy spectra of the X-ray beam transmitted through the coated and uncoated DMS780 CFC sample (right panel).

One can see the quasi-monoenergetic energy spectra of the X-ray beam transmitted through the coated and uncoated DMS780 CFC sample (right panel). A transmission coefficient (T=0.185) is obtained by normalizing the intensity of the X-ray beam transmitted through the coating to that transmitted through the coating free area resulted during a pulling test. With the program in [14] one can estimate an average W equivalent thickness of 9.9 ± 0.2 µm. No GDOS data is available for comparison.

ASDEX Upgrade fine grain graphite tiles were coated with tungsten of typical thicknesses (0÷1.5 µm). The coating uniformity analysis is performed using the X-ray transmission µXRT and the X-ray fluorescence mapping by procedures µXRF and µXRFB.

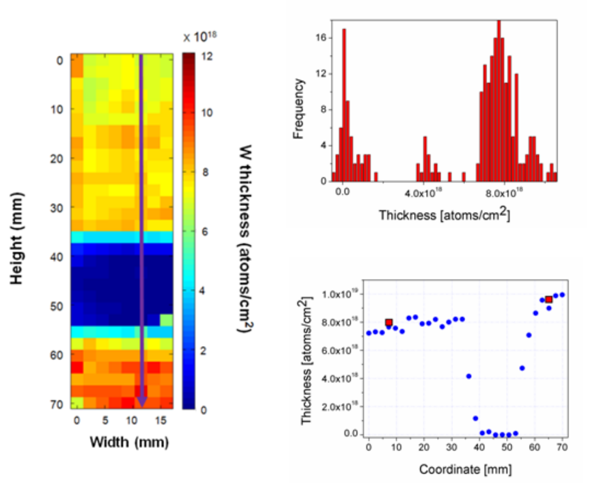

Figure 5 - Post-mortem analysis of a W coated FGG divertor tile: W thickness map determined by µXRFB for the region of interest (70x16 mm2) shown in Fig. 3 (left), histogram of the thickness values (top-right), thickness profile along the vertical line shown on the thickness map and comparison with RBS measurements(red squares) of reference [1].

A 2-D tungsten thickness map obtained with the reference free XRF3 technique is shown in Fig. 5 (left). In the thickness histogram (top-right) one can see traces of redeposited tungsten, especially in the vicinity of the borders of the non-coated FGG stripe.

One can estimate the detectability limit of the method as equal to one standard deviation of the derived W thickness value. The main source of statistical errors is associated with the determination of the net (background subtracted) peak intensities which occurs in the term ln(I/I0). This is carried out by a non-linear multi-peak fitting procedure. For practical integration times per measuring point under one minute the standard deviation of the ln(I/I0) term is ≈3% which, leads to a detectability limit of the order of several tens of nm. Another quantitative analysis is allowed by the line profile which indicates a thickness gradient, previously observed in [1]. Also one remark the good agreement with the RBS values (marked as red squares) in two regions of the sample.

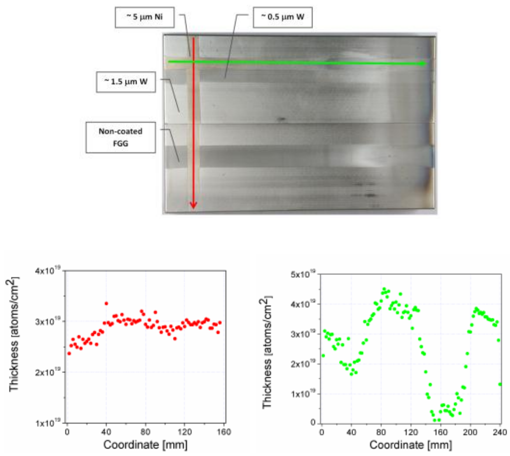

Figure 6 – Marker tiles of 160x240 mm2 (top.) The erosion profiles along poloidal and toroidal directions as measured by the XRF3 technique applied to the corresponding Ni stripes (bottom).

Line profiles of the W/Ni coatings were measured with the purpose to assess the erosion/redeposition in the all-tungsten divertor of ASDEX Upgrade (Fig. 6). The Ni/W thickness absolute values could be derived and they are in good agreement with the measurements carried out in [1]. Fig. 6 shows the erosion profiles along the poloidal and toroidal directions as measured by the µXRF3 technique applied to the corresponding Ni stripes. In all measurements it is possible to detect redeposition of Ni/W on non-coated graphite stripes.

Divertor marker tiles 01b/3 & 01b/4 at the outer strike point of AUG for the 2010/2011 discharge campaign have been measured by digital microradiography and microfluorescence.

Figure 7 presents a microradiography image of tile 01b/4 before the irradiation in AUG. The tile will be inspected immediately after the irradiation campaign in order to reveal the plasma erosion pattern.

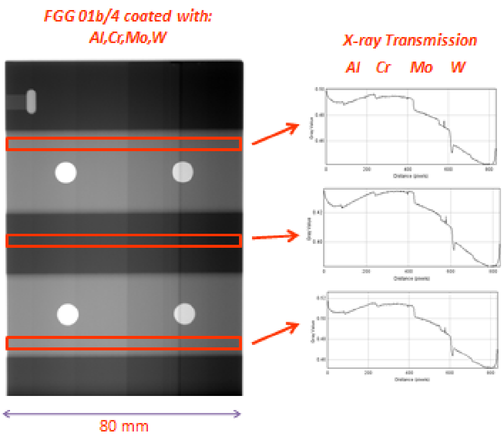

Figure 7 – Marker tile FGG 01b/4 coated with stripes of Al, Cr, Mo and W (left.) Line profiles transversal on the coated stripes (right).

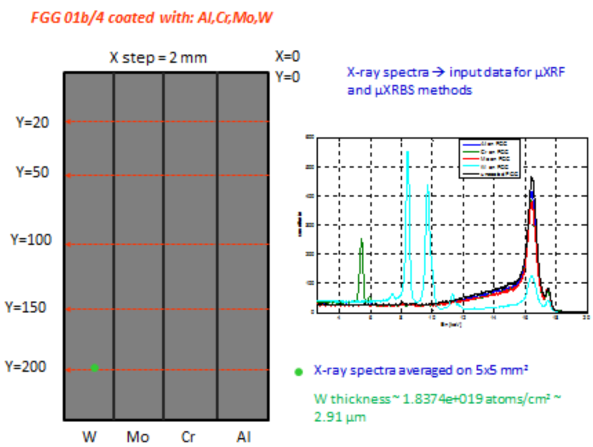

Figure 8 – Marker tile FGG 01b/4 coated with stripes of Al, Cr, Mo and W (left). Fluorescence X-ray spectra corresponding to the coated stripes (right).

Same tiles were inspected by microfluorescence (µXRFB) on a grid as shown in Fig. 8.

4. Outlook

An instrument as well as associated measuring methods have been developed and qualified as a non-invasive solution for investigation of the thickness of W coatings on carbon materials substrates. The Tomo-Analytic instrument is a combined X-ray fluorescence (µXRF) and cone-beam µXCT system for the non-invasive 3-D morphology and composition mapping. These techniques would be applied on W coated FGG tiles from the all-tungsten divertor of AUG and in the postmortem analysis of ITER-like wall W coated tiles.

Divertor marker tiles at the outer strike point of AUG were already characterized before the 2010/2011 discharge campaign using both X-ray techniques and ion beam analysis. The tiles will be analyzed again after the discharge campaign in autumn 2011 using both X-ray techniques in order to determine the 2-dimensional pattern of net erosion of W and some other elements at the outer AUG strike point. The results will be compared to ion beam analysis. The determined net erosion data will be compared to gross erosion data obtained by spectroscopy.

References

[1] M. Mayer, et al. *J. Nucl. Mater. 390-391 (2009) 538*.

[2] I. Tiseanu, et al., *Proc.of Fachtagung Prozessnahe Röntgenanalytik*, PRORA 2009, Berlin, Germany, 2009.

[3] I. Tiseanu, et al. *Surface & Coatings Technology* ***205*** *(2011) S192–S197,* doi:10.1016/j.surfcoat.2011.03.049

[4] A. Bjeoumikhov et al. 2005 *Rev. 292 Sci. Instrum.* ***76*** *063115-1.*

[5] MCNP-5 - Los Alamos National Laboratory, MCNP – A General Monte Carlo N-Particle Transport Code, Version 5, vols. I–II, 20058, LA-UR-03-1987 and LA-CP-03- 0245.

[6] M.J. Berger, et al., XCOM: Photon Cross Section Database. Web Version 1.2. Available from: http://physics.nist.gov/xcom, National Institute of Standards and Technology, Gaithersburg: MD 20899, USA; August 1999.

[7] B.L. Henke, E.M. Gullikson, and J.C. Davis. *X-ray interactions: photoabsorption, scattering, transmission, and reflection at E=50-30000 eV, Z=1-92*, Atomic Data and Nuclear Data Tables Vol. 54 (no.2), 181-342 (July 1993).

[8] C. Ruset, et al., *Physica Scripta, T128, 171-174 (2007)*

SHEATH PROPERTIES AND RELATED PHENOMENA OF THE PLASMA WALL INTERACTION IN MAGNETISED PLASMAS. APPLICATION TO ITER

C. Agheorghiesei, V. Anita, S. Costea, C. Costin, G. Popa, L. Sirghi, M. L. Solomon

Faculty of Physics, Alexandru Ioan Cuza University of Iaşi, Romania

Abstract

All four objectives of this phase have been accomplished as follows:

(i) The new electric circuit for measuring 2D distributions of the ion saturation current in Pilot-PSI was created. Each of the 61 probes is negatively biased with respect to the local floating potential using a capacitor. The capacitors are charged by a dc power supply between discharge shots and discharged by the ions collected from the plasma during the discharge shots. The current flowing through each capacitor is the ion saturation current collected by the corresponding probe. Preliminary test measurements were performed in an argon discharge.

(ii) A new electrostatic analyser was designed and manufactured, improving the previous version. It was used to measure the ion distribution function and the ion saturation current that reaches the centre of Pilot-PSI target.

(iii) Numerical simulations of the charged particle fluxes that are collected by a plane or cylindrical probe placed in a magnetized plasma column were performed using a Particle-In-Cell (PIC) and a Monte Carlo (MC) code. PIC Code addresses the issue in a self-consistent manner while the MC code follows the motion of the charged particles without collisions and without electric field (plasma and probe are the same potential). It was calculated the fraction of charged particles coming from the plasma column that are collected by the plane or cylindrical probe, depending on the radial position of the particles in the plasma source, the magnetic field strength and the probe's length. Particle flux collected by the plane probe increases with the magnetic field and becomes saturated when the Larmor radius of the charged particles becomes smaller than the probe's radius. For the cylindrical probe of several mm long the flux of particles decreases when increasing the magnetic field strength.

(iv) A probe array has been manufactured for correlation measurements in the divertor region of COMPASS tokamak. The 15 cylindrical probes (tungsten wires of 5 mm length and 2 mm diameter) are distributed along the poloidal direction with a linear resolution of 2.5 mm and they are aligned to the divertor tiles surface.

Conferences

[1] L. Sirghi, C. Costin, V. Anita, M. L. Solomon, G. Popa, M. van de Pol, R. S. Al, J. Rapp, *Turbulence of magnetized plasma column at a floating and current-driving target surface in Pilot-PSI*, 30th ICPIG, August 28 – September 2, 2011, Belfast, Northern Ireland, UK (poster)

[2] C. Costin, V. Anita, M. L. Solomon, L. Sirghi, G. Popa, M. van de Pol, R. S. Al, J. Rapp, *Cross-correlation signal analysis of a multi-probe system acting as target in Pilot-PSI, 9th International Workshop on Electrical Probes in Magnetized Plasmas (IWEP 2011)*, September 21-23, 2011, Iasi, Romania (oral presentation)

[3] M. L. Solomon, I. Mihaila, C. Costin, G. Popa, *On the particular behavior of current-voltage characteristic of electrical probes in magnetized plasma, 9th International Workshop on Electrical Probes in Magnetized Plasmas (IWEP 2011)*, September 21-23, 2011, Iasi, Romania (oral presentation).

Detailed results

Measurements of the ion flux at the target in Pilot-PSI

New circuit for ion saturation measurements

The multi-probe system consisting of 61 probes was used for preliminary measurements of the radial distribution of the ion saturation current reaching the floating target of Pilot-PSI, at different operating conditions: discharge current of 80, 100 and 120 A; magnetic field strength of 0.4 T; 3.6 slm argon gas flow. Real time ion currents measurements were done with a multi-channel data acquisition system. The idea of these measurements is based on the fact that the ion current collected by a plasma probe is approximately constant if the applied voltage is sufficiently negative with respect to the floating potential.

A new circuit was designed (Fig.1) and manufactured (Fig.2-3) in order to measure the ion saturation current distribution on the target of Pilot-PSI. All collectors are connected to 61 capacitors (470 µF) by using relay contacts. The capacitors are alternatively charged with electrons from a power supply and discharged by ions from the plasma beam during a discharge shot. The entire device was made of 6 modules, 5 modules with 12 channels each while the last module contains 6 channels and the delay, commutation and manual trigger circuits. A photo of a single module is shown in Fig.3. The floating potential registered on different probes revealed values of approximately 0 V at the edge of the plasma beam; in the center of the plasma beam values of -80 V were registered at a magnetic field of 0.4 T and -162 V at magnetic field of 0.8 T. Thus, a value of -250 V was considered acceptable for the charging voltage, this voltage being more negative than the lowest floating potential measured in the system. Before every shot the capacitors are simultaneously charged by using one DC power supply. The relay's contact K-1 assures that every condenser connected to a probe is independently discharged by localized ion current and there is not interaction between measuring channels.

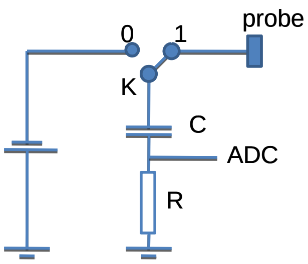

Figure 1 -. Schematic of one channel measuring circuit

Figure 2 - Assembled measuring modules

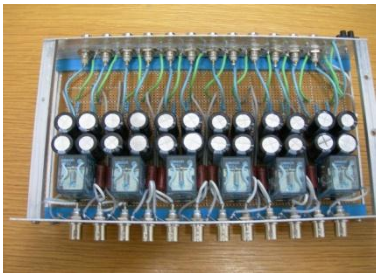

Figure 3 - One module with 12 measuring channels

The voltages developed on every resistor R (56 Ω) in the discharging period (by ion saturation currents) are simultaneously measured by a multi channel data acquisition system. The ion saturation currents are deduced from the voltage drop on the resistors. All collectors are connected and disconnected by using 61 relay contacts in the time of charging and discharging period. A delay circuit triggered by the trigger signal from Pilot-PSI and realized with a 555 timer integrated circuit generates a trigger signal for the data acquisition system in order to assure that the measurements are made at a constant applied magnetic field. A second timer generates a 12 V ON–OFF control voltage for the relays coils in order to assure the variable discharging time of condensers by ion saturation currents. This is necessary to be adjusted in order to assure a small variation of condensers voltage during the measurements. After every measurement the circuits automatically charge the condensers and optically signalize when the measuring system is ready for a new acquisition.

<u>Design and construction of a new ion energy retarding electrostatic analyzer (IERA)</u>

The last IERA experiments encountered a few problems: (i) Lack of the temperature control leading to melting of IERA components; (ii) Contamination of IERA grids and plate due to the use of carbon diaphragm in hydrogen plasma; (iii) Lack of a good separation of electron components due to high density plasma at the level of the electron-separation grid; (iv) Lack of a good resolution of the I-V characteristic in the retarding region of the thermal ions. A new IERA has been designed and constructed. A sketch of the new IERA and a photo of the device are given in Fig.4. The design has the following improvements:

1. To avoid the overheating of IERA grids and plate, a thick (0.7 mm) stainless steel diaphragm with a hole of 0.8-1.2 mm is used to separate the dense plasma of Pilot-PSI from the inner parts of the IERA. The thermal inertial of the diaphragm was increased by covering most of its surface with the thick front lid of the IERA. The distance from the diaphragm to the grids was increased to 7 mm. The plasma inside the analyzer is separated from the biased charge separation grid by a floating grid.
2. Contamination of the inner parts of the IERA was reduced or prevented by using of stainless steel diaphragm (instead of carbon one) and by the increase of the distance between diaphragm and the important inner parts of the IERA. A floating grid was used to provide a better separation of plasma.
3. The geometry of the analyzer was modified by decreasing the aperture of the plasma separation diaphragm (0.8-1.2 mm) and increase of the distance between diaphragm and grids (7 mm).
4. The software controlling the data acquisition was improved by taking variable voltage steps.

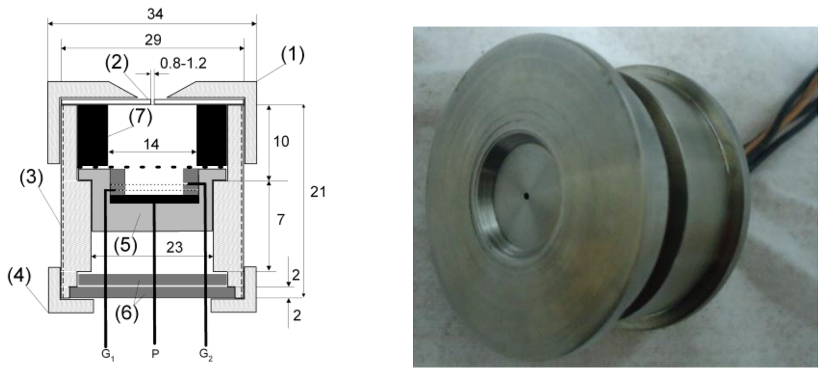

Figure 4 - Sketch and photo of the ion energy retarding analyzer used in Pilot-PSI plasma machine. Main components: (1)-front lid (stainless steel); (2) –diaphragm (stainless steel); (3) –main body (stainless steel); (4) back lid (stainless steel); (5) -insulating support of plate and grids (ceramic), (6) insulated back lid pieces (ceramic); (7) stainless steel ring to tight a gap of 7 mm between the diaphragm and plasma separation grid. G_2 is the electron separation grid, G1, the secondary emission suppression grid, and P, the collector.

Experimental results obtained with IERA in Pilot-PSI device

Figure 5 presents a typical I-V characteristic obtained for the grid G_2 during a hydrogen plasma pulse of 1.5 s at discharge current of 120 A and magnetic strength of 0.4 T. This characteristic shows the common features of a single Langmuir probe I-V characteristic, with an ion saturation current of about 8 mA, the floating potential at -18 V and the exponential increase of electron current at potential > -18 V. This reveals the fact that plasma enters into the device through the small admission pin hole and reaches the grid G_2. A part of the plasma particles are collected by the separation grid (transparency factor is about 0.5). Therefore, the saturation ion current collected by the device is estimated to 16 mA. This computes a density of hydrogen ion current of about 2 A/cm^2 (1.25×10^{23} ions$\cdot$m$^{-2}\cdot$s^{-1}) in the center of the Pilot-PSI machine at a distance of 40 cm from the cathode, for B = 0.4 T. This value can be used to estimate the ion thermal energy from $j_{i0} = e \cdot n \cdot \sqrt{kT_i / 2\pi m_i}$, where T_i is the ion temperature, m_i the ion mass, and n the plasma density. Considering the results of electron density measurements, $n = 0.3\times10^{20}$ m^{-3}, a value of about 1 eV was computed for T_i. This value is close to the electron temperature measured by either Thomson scattering or Langmuir probe methods. The goal of the IERA measurements was to measure also the ion energy. Figure 6(a) presents a typical IERA I-V characteristic obtained in Pilot-PSI plasma machine for hydrogen plasma at pressure of 3 Pa, discharge current of 120 A and B = 0.4 T. The IERA device was mounted at a distance of 40 cm from the cathode and kept floating during the measurements. Some of measurements were performed with the target and IERA biased at a negative potential (-50 to -70 V) to reject the plasma electrons and capture the positive ions. In this configuration the target and the IERA body worked as a second cathode to make an arch discharge with the plasma column, fact that overheated and destroyed the IERA device. The IERA I-V characteristics showed an ion saturation current of about 1.5 mA, about 10% of the total ion current. The rest of 90% has been collected by the three grids of the analyzer. This is happening because the device fails to work properly in the very dense plasma of the Pilot-PSI, the electron contribution to the collector being significant. Thus, the plate of the IERA collected a small electron current even at large negative potentials (-100 V) on the separation grid.

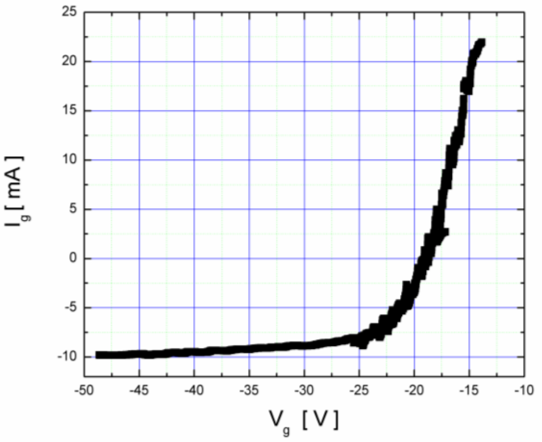

Figure 5 - A typical I-V characteristic of the grid G_2 of the IERA in Pilot-PSI plasma at distance of 40 cm from the cathode, I = 120 A and B= 0.4 T

This is explained by the effect of plasma screening of the grid electric filed. The Debye length computed for T_e = 1 eV and n_e = 0.3×10^{20} m^{-3} is about 1.5 μm, which is much shorter than the distance between grids and plate (100-200 μm) or grid hole diameter (20 μm). An important feature of the I-V characteristic is that the device failed to completely separate the electrons. However, the first derivative of plate current is spread over a large interval of biasing voltage. In conclusion, the first derivative of IERA I-V characteristic cannot be used to find information on the ion energy (see Fig. 6(b)).

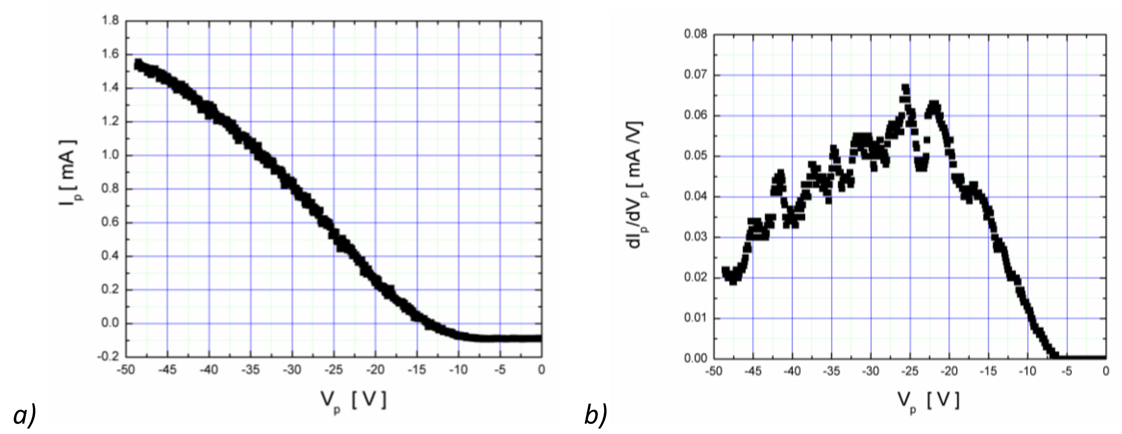

Fiure 6 - (a) Typical I-V characteristic of the plate of the IERA in Pilot-PSI plasma at distance of 40 cm from the cathode, I = 120 A and B = 0.4 T. The ion separation grid was based at -100 V and the target and IEA body was kept floating. (b) First derivative of the ion current

Ion flux simulations by MC code

A Particle-In-Cell Monte Carlo Collision (PIC-MCC) code was developed to simulate the charged particle fluxes collected by a plane probe placed in a strongly magnetized plasma column, perpendicularly on the magnetic field lines. Due to the cylindrical symmetry, the 3D problem was simplified and the simulation box was reduced to a rectangular plane whose dimensions are the cylinder length (2 cm) and the cylinder radius (0.75 cm), in a two-dimensional domain (r,z). By rotating this rectangular plane, the whole cylinder can be recreated. The Monte Carlo (MC) procedure was used to determine the collision probability, the angle of deflection of collided particles and the type of the collisional elementary processes. The PIC code follows the particles trajectory in the combined electric and magnetic fields present in the discharge.

A plasma source is considered at Z_{max} through which electrons and ions are introduced in the simulation box. A plane probe (2mm disc diameter) is placed at z = 0, centered on the symmetry axis, collecting the ion flux (Fig. 7). The charged particles are introduced with a Maxwell distribution, by taking the electron temperature and the ion temperature of 2 eV.

The magnetic field lines are parallel to the plasma column axis and the magnetic flux density is constant. The buffer gas is Argon, at a pressure of 5 mtorr and 400 K temperature. The collisional processes taken into account in the code are electron-neutral elastic, excitation and ionization processes and for the ions, the elastic and the resonant charge exchange processes. The probability of these processes is handled by the MC code, using of the collision cross sections taken from literature. The number of points on the grid was carefully picked so that the Debye length is larger than the grid step. This led to a grid of 200x512 points. Time step was carefully picked so that the fastest inserted particle cannot move more than a grid step during a time step. Plasma potential is obtained by solving Poisson equation in two dimensions using Fast Fourier Transform (FFT) on the longitudinal axis and tri-diagonal matrix method on the radial axis. The electric field was computed via 6 points.

An example of spatial voltage distribution when the probe is biased at -10 V is plotted in Fig.8. The simulation was made for argon at 5 mtorr and a magnetic field strength of 0.1 T, with a space grid of 200×512 nodes. The potential has a smooth evolution in the entire volume but electron and ion space distributions exhibit large noise. Electron velocity distribution function remains Maxwellian but at a lower temperature with respect to the plasma source due to energy loss via collisions.

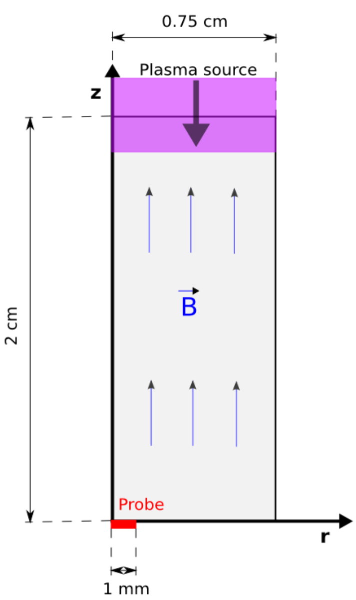

Figure 7 - Simulation domain

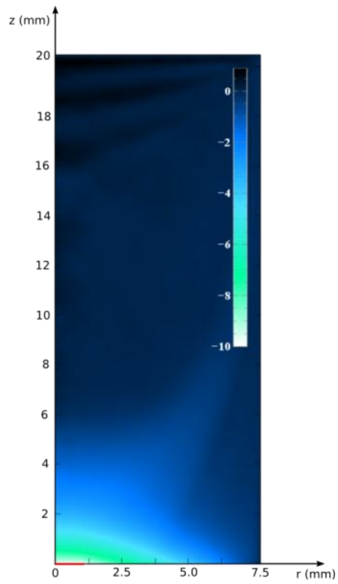

Figure 8 - Voltage map for a probe bias of -10 V

In parallel with PIC simulations, a Monte Carlo code was used for the same spatial arrangement (Fig.7). The MC code calculates the fraction of particles introduced in the simulation domain that is collected by the probe. Both electrons and ions are introduced in the simulation domain with Maxwellian distribution. Particles trajectory is not affected by collisions. The probe and the plasma have the same potential and, therefore, no electric field is present in the volume and no charged sheath near the probe. Plasma is confined by an uniform axial magnetic field of 0.4, 0.8 or 1.2 T (the usual operating values for Pilot-PSI). The probe is either plane (a disc with the diameter of 0.89 mm) or cylindrical (the same diameter and various lengths), disposed parallel to the magnetic field lines. The dimensions of the simulated probe correspond to the multi-probe system used in Pilot-PSI.

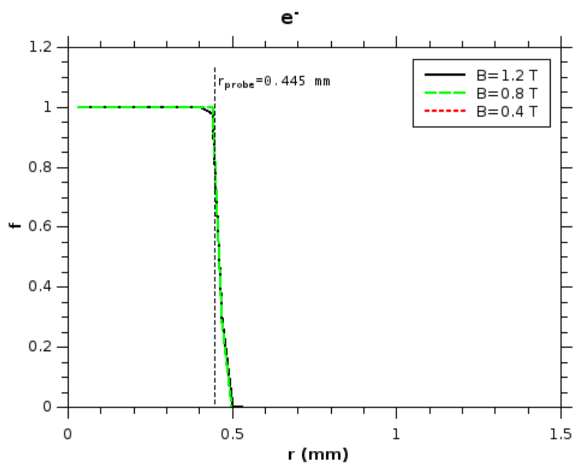

Figure 9 - The fraction of electrons collected by the probe vs. electron's position in the plasma source

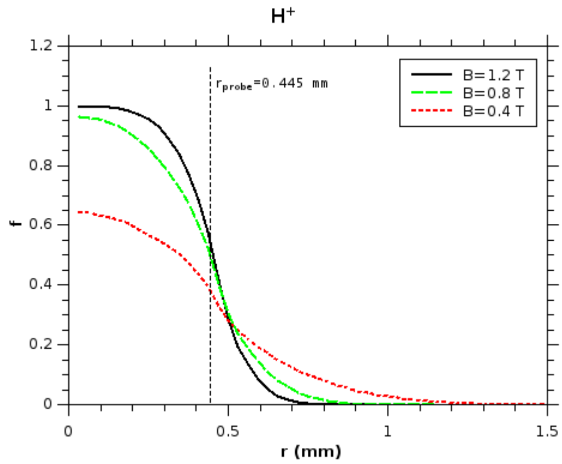

Figure 10 - The fraction of H^+ ions collected by the probe vs. ion's position in the plasma source

In Figs.9, 10 and 11 it is plotted the fraction of the charged particles (electrons, H^+ and Ar^+ ions) that reach the plane probe with respect to the radial position of the particles in the plasma source. For the mentioned magnetic field strengths and for a temperature of 2 eV, the mean Larmor radius for the 3 types of charged particles is: 4-12 μm for electrons, 0.17-0.5 mm for H^+ and 1-3 mm for Ar^+. It can be observed that the electrons are collected by the probe from the same area of the plasma column as the probe's area due to their smaller Larmor radius with respect to probe's radius (0.445 mm). For the heavy ions, with the increase of their Larmor radius increases also the collecting area from the plasma. The total number of collected particles increases with the magnetic field strength and it saturates when the Larmor radius of the charged particles becomes smaller than the probe's radius. For a cylindrical probe, the fraction of H^+ ions collected by the probe is plotted versus the probe's length in Fig.12. The fraction *F* is calculated from the total number of particles introduces in the simulation volume through the plasma source. When the probe's length is 0 mm the cylindrical probe is equivalent with a plane probe. If the total number of collected particles increases with the magnetic field strength for a plane probe (Figs.9-11), the situation is reversed for cylindrical probes.

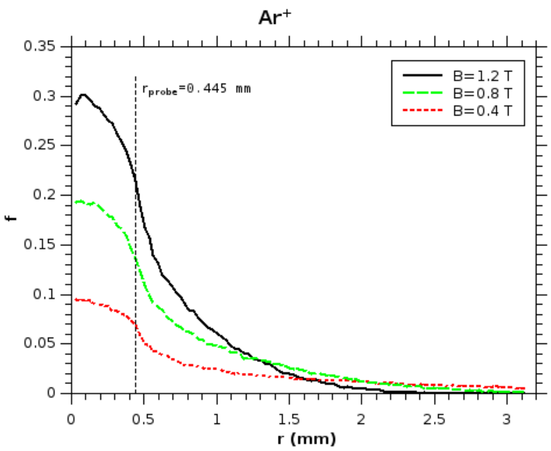

Figure 11 - The fraction of Ar^+ ions collected by the probe vs. ion's position in the plasma source

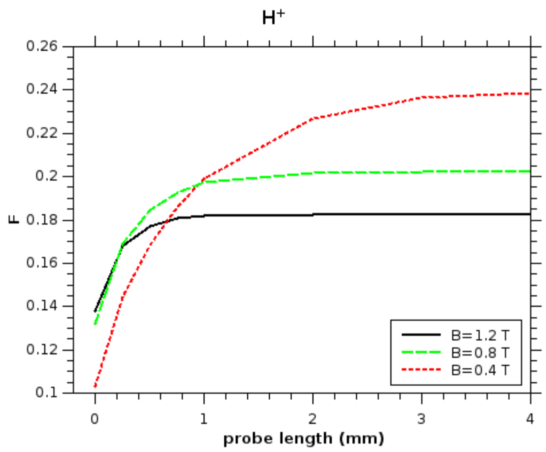

Figure 12 - The fraction of H^+ ions collected by the probe vs. cylindrical probe's length

Correlation measurements in the divertor region of COMPASS tokamak by electrical probes

<u>Manufacturing the probe array</u>

The new probe array designed for the divertor region of COMPASS tokamak was manufactured. It consists of 15 cylindrical Langmuir probes of 5 mm length and 2 mm in diameter made of tungsten. The probes are embedded in a ceramic support which is protected by a graphite shield-head (Fig.13). The linear resolution of the array is 2.5 mm in horizontal direction. The frontal face of the probe array is inclined at the same angle as the divertor tiles surface. Thus, the probes will cover the same poloidal region in the tokamak vessel as the first 8 Langmuir probes from the old 39-probe array embedded in the divertor tiles.

The probe array will be inserted in COMPASS tokamak through a bottom port, in the high field side region of the divertor. Only one free bottom port of the tokamak was available in 2011 for the installation of the new probe array in the divertor region, but this port was obstructed by the cooling system of the tokamak coils. The cooling system was redesigned and the replacement of the tubes will be made in 2012. The new probe array will allow investigations of plasma parameters correlation both in poloidal and toroidal direction.

Figure 13 - Divertor probe array

Conclusion

Plasma diagnostic experiments realized in 2011 were focuses on two major objectives: (i) characterisation of Pilot-PSI plasma beam by electrical methods (multi-probe system and electrostatic analyser) and (ii) plasma diagnostic and correlation measurements in the divertor region of COMPASS tokamak by arrays of electrical probes. Two numerical codes, 2D PIC-MCC and 2D MC, were used in order two calculate the charged particle fluxes collected by a plane or cylindrical probe placed in a strongly magnetized plasma column.

Acknowledgement

The experimental part for WP11-PWI-03-03 was realized on Pilot-PSI machine at FOM Institute for Plasma Physics “Rijnhuizen”, Association EURATOM/FOM, Nieuwegein, The Netherlands and the work for WP11-DIA-01-01 was made in collaboration with Institute of Plasma Physics, Academy of Sciences of the Czech Republic, Association EURATOM/IPP.CR, Prague, Czech Republic.

Fusion Materials Development

CONSOLIDATION AND DENSIFICATION OF W AND SIC COMPOSITES

A. Galatanu[1], J. Riesch[2], B. Popescu[1], P. Palade[1], M. Enculescu[1]

[1] *National Institute of Materials Physics, Bucharest-Magurele, Romania*

[2] *Max Plank Institute fur Plasmaphysik,Garching, Germany*

Abstract

Fibers insertion into materials has multiple advantages, increasing their toughness and allowing for tuning some of the composite properties (e.g. thermal conductivity). In particular, W fibers insertion might be used to enhance damage toleration of a W matrix, thus making the resulting W composite a potential structural material, compatible with W plasma facing components in the fusion reactor. In this view we were able to consolidate by hot pressing the W fibers / W metal composites realized by IPP Garching. Also SiC-W based composites have been identified to offer promising solutions for the structural parts in fusion reactor in-vessel components, but unfortunately they suffer from unacceptable final porosity and gas permeability as well as insufficient thermal conductivity at high temperatures. To correct some of these problems we have realized SiC-W composites by FAST technique using beta SiC nanopowders and 20% weight W micro or nano grains dispersions. Insertion of W nano particles in the SiC matrix resulted in 300% increase of thermal conductivity at 1000 C.

Papers

[1] J. Riesch,, T. Höschen, A. Galatanu, J.-H. You, ICCM18 proceedings, to be published in 2012

Conferences

[1] J. Riesch, J.-Y. Buffière, J. Du, A. Galatanu, P. Hahn, T. Höschen, S. Kimmig, M. Köppen, M. di Michiel, M. Scheel, A. Zivelonghi, Ch. Linsmeier, and J.-H. You P. Niculescu, *Synthesis of tungsten-fibre reinforced tungsten composites and in situ observation of cracking by high energy synchrotron tomography*, 13th International Workshop on Plasma-Facing Materials and Components for Fusion Applications / 1st International Conference on Fusion Energy Materials Science, May 09th - 13th, 2011 in Rosenheim, Germany

[2] J. Riesch, J.-Y. Buffière, J. Du, A. Galatanu, P. Hahn, T. Höschen, S. Kimmig, M. Köppen, M. di Michiel, M. Scheel, A. Zivelonghi, Ch. Linsmeier, and J.-H. You, *Tungsten-fibre reinforced Tungsten composites: a novel concept for improving the thoughness of Tungsten*, Eighteenth International Conference on Composite Materials, Jeju Island, Korea August 21-26, 2011

Detailed Results

1. Introduction

Fabrication process development for fusion reactors remains an important point for many components of the DEMO design. W composites offer a promissing route for structural materials, but W-W composites need a complicated fabrication procedure and remain with a high porosity. SiC-based composites also have been identified to offer promising solutions for the structural parts in fusion reactor in-vessel components, but unfortunately they have unacceptable final porosity and gas permeability as well as insufficient thermal conductivity at high temperatures.

Fibers insertion into materials has multiple advantages, increasing their toughness and allowing for tuning some of the composite properties (e.g. thermal conductivity). In particular, W fibers insertion might be used to enhance damage toleration of a W matrix and hot pressing of the composite can further consolidate the material. For SiC-W based composites it is important in a first step to increase the material density and to obtain a higher thermal conductivity.

2. W-W composites

Tungsten is a key material for fusion reactors due to its refractory nature, excellent surface erosion resistance and a good thermal conductivity. However, its inherent brittleness below the ductile to brittle transition temperature (DBTT) restricts its use as structural material. Recently, IPP Garching group proposed a novel toughening method for tungsten reinforcing W by W fibres coated with engineered interfaces (Wfibre/Wmatrixcomposites). In those composites the toughening is primarily based on local cracking at the fibre/matrix interfaces. As a main matrix crack is deflected along the interfaces, stored strain energy is dissipated by interfacial debonding and frictional sliding leading to controlled overall fracture and eventually increase of toughness. Simultaneously, local stress concentration is reduced so that the ultimate load carrying capacity is enhanced. A key factor to exploit this mechanism is to optimise the interface properties. One of the fundamental prerequisites in this regard is that the fracture energy of the interface has to be essentially lower than that of the fibre reinforcements to enable preferred debonding.

To realize the W fibers, chemical vapour deposition (CVD) can be used on individual fibers consisting of a tungsten filament (diameter: 150 µm) coated with a thin film (thickness: 1 µm) to form a well-defined interface layer using magnetron sputtering (PVD) and then embedded into a thick mantle of dense tungsten (1-1.5 mm) produced by CVD. For multi-filament composite chemical vapour infiltration (CVI) technique can be used. Here the conventional CVD process is combined with an additional infiltration step to fill porous or fibrous preforms. The CVI technique is alreadyused for the fabrication of fibre-reinforced ceramic composites.

In this work the CVI process on tungsten was applied by the Garching group to fabricate multi-filament bulk composites of Wf/Wm system. The composites consisted in W fibers, with a W oxide layer and an outer W layer. Dedicated equipment was used to achieve a reasonably high matrix filling quality by means of a controlled temperature gradient. The sample densification obtained by this method was around 80% (see Fig. 1a).

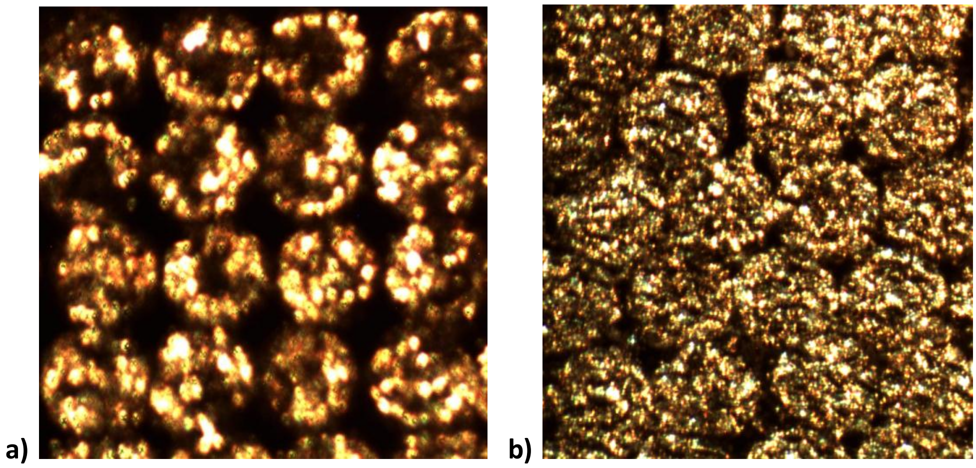

Figure 1 - a) Wf/Wm composite realized by CVI and
b) W fibers (IPP Garching) consolidated by hot pressing at 1700 C.

In the frame of EFDA cooperation we have also used our hot pressing equipments to consolidate W fibers composites realized by the IPP Garching. To achieve this a special mold was designed and created to accomodate the composite shape. Several tests have been performed to obtain the best densification. Figure 1b presents the result obtained on composites after hot-pressing.

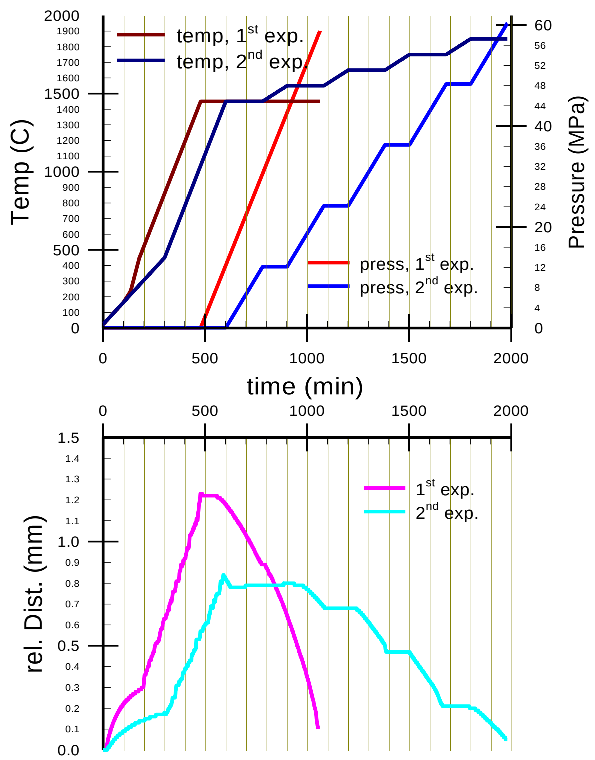

Figure 2 - Start and refined final hot presing procedure for W- composites (top) and the resulting densification of the samples (bottom)

In Fig. 2 the hot-pressing procedure for the W composites is plotted for the start and final refined algorithms. In the bottom figure the variation of pistons relative distance must be refered to the initial dimensions to obtain the absolute densification in the HP work. The best results show a densification of about 15% which brings the final density of the composites at about 93% of the theoretical value.

The results show that the HP procedure can be succesfuly applied to consolidate the W composites. However, the final quality of the samples depends on the initial quality of the fiber matrix (i.e. fibers positions and stress). The consolidated composites prooved an important increase of the mechanical properties.

3. SiC-W composites

SiC-W composites have been realized by sintering in SPS equipement. We have started with beta SiC nanopowders and inserted 20% weight W micro or nano grains. The thermal conductivity of materials is usually decreased by using nano-structured materials, due to additional scattering on an increased number of interfaces. On the other side, sintering of nano-powders at high pressure and temperature produces more dense materials with reduced porosities and eventually with superior mechanical properties. To get a balance between these two effects we have started our experiments with nanopowders of beta SiC. A reference sample was realized by SiC without any insertions by sintering at 1850 C with 120 MPa pressure. The procedure is depicted in Figure 3, in the top panel.

The same process parameters were used to produce composites with micro and nano W powders dispersed in the SiC matrix. To avoid oxidation of W nanopowders, the work was performed in glove box under Ar. For all the samples, the sintering procedure applied resulted in a strong contraction of the sample, even during cooling. One should note that using an SPS allowed for short times and high pressures on one hand, and reduced the grain increase on the other hand.

The thermal properties of the resulting materials have been investigated up to 1000 C using a LFA thermal analyzer. In Figure 4 (upper picture), the thermal diffusivity of the samples is plotted against temperature. A strong enhancement of diffusivity can be observed at room temperature and this enhancement is preserved in the whole temperature range. Surprisingly, the composite material with W nano-particles exhibits a larger value of diffusivity, in spite of the presence of additional interfaces. One possible explanation might reside in a better particle dispersion.

In the middle picture of Figure 4, the specific heat of the same materials is plotted. Due to the larger value of specific heat of W, the composites show an enhanced value as compared to the pure SiC material. Larger W grains in a low conducting matrix are able to store more heat, especially at high temperatures, thus the composites containing micro sized W exhibit the largest specific heat value.

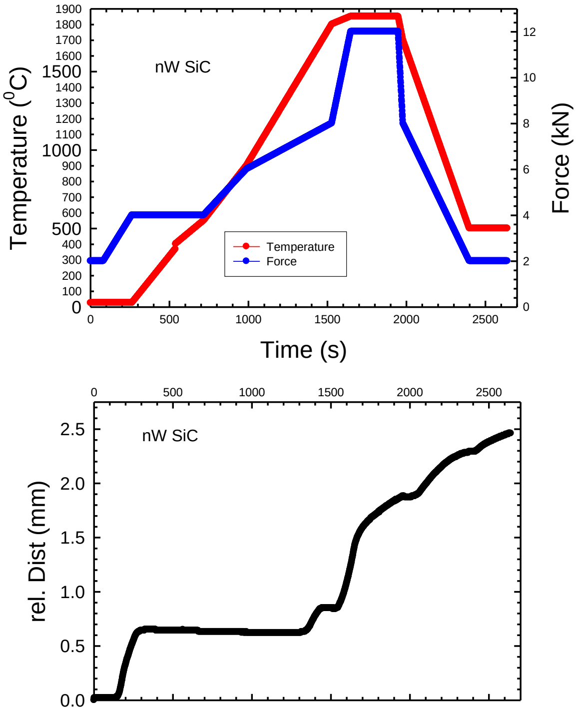

Figure 3 - Sintering of beta SiC-W composites (top: process parameters, bottom: contraction evolution during the sintering process for nW-SiC composites)

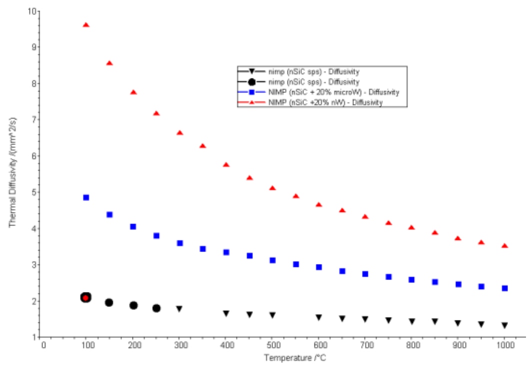

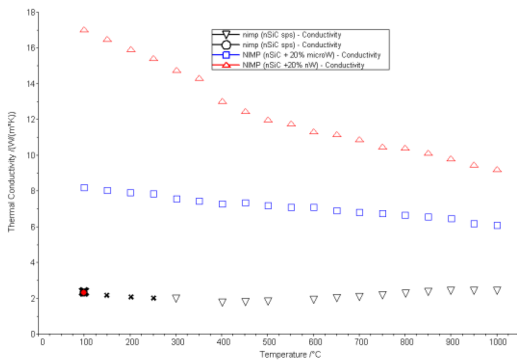

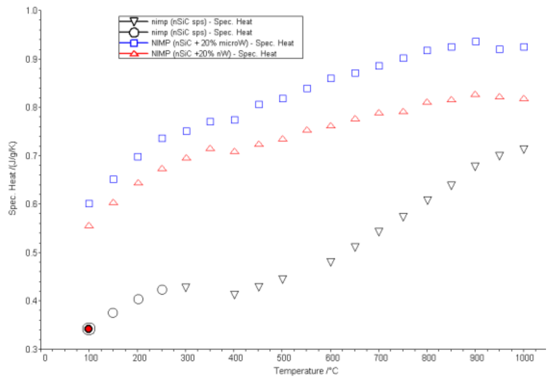

Figure 4 - Thermal properties of different SiC-W composites.

- *Top-left plot: thermal diffusivity*
- *Bottom-left plot: specific heat*
- *Top-right plot: thermal conductivity.*

In the bottom picture of Figure 4, the resulting thermal conductivity of the samples is displayed. A consistent increase in the conductivity values for W containing materials is obvious in the whole temperature range. It is important to note that even for the materials containing nano W, the 1000 C thermal conductivity value is lower than the required 20 W/m/K. Nevertheless, taking into account the relative unsophisticated preparation, an increase of 300% is significant. Moreover, the nanostructure of SiC is a reason for lower conductivity, as shown also at room temperature by the pure SiC material. Values of 6 to 10 W/m/K are usual for SiC at RT. On the other hand, one should keep in mind that a lower porosity and better behavior unde irradiation are expected for nanostructured materials.

Conclusions and future steps

The HP procedure can be successfully applied to consolidate the Wf-Wm composites. However, the final quality of the samples depends on the initial quality of the fiber matrix (i.e. fibers positions and stress). The consolidated composites proved an important increase of the mechanical properties.

Direct sintering of nanometric powder of beta SiC with dispersed W nano particles produces materials with a 300% increased thermal conductivity at 1000 C. The procedure can be tuned to enhance the effect and refined to improve the other required properties. A next important step will be to provide a complete structural characterization for such composites and to establish a correlation between morphology and physical properties of the samples.

Acknowledgement

The reported work includes contributions from the following people outside the EUATOM-MEdC Association: Johann Riesch&co-workers (Euratom IPP Association, Max Plank Institute fur Plasmaphysik, Garching, Germany

JOINING W WITH STEEL USING FGM AND DIRECT PULSE SINTERING ROUTES

A. Galatanu, B. Popescu, M. Valeanu, M. Enculescu

National Institute of Materials Physics, Bucharest-Magurele, Romania

Abstract

Different routes for joining W with steel are investigated. A new route is proposed for a joint between W and steel using W-steel FGM and the results are compared with that ones obtained by plasma sintering/hot press direct joining and plasma sintering/hot press brazing using V based alloys. In the first stage the basic process steps have been tested in order to define the best route for FGM joining process. W-(Plansee) and Eurofer 97 (KIT) have been joined using W-steel FGM realizing compact samples with well defined shapes and dimensions for mechanical tests and also cylindrical shaped samples for thermal properties investigations using our laser flash equipment. Thermal properties investigations have been proved as an efficient tool to asses the joints quality between W and steel. The present results have been obtained in the frame of MAT-WWAlloys-01-01 and PPPT-IV.3.1.5.a1 topics.

Detailed Results

1. Introduction

The development of the DEMO fusion reactor is a priority of the EU. In this frame the construction of the reactor structure is a complex and fast evolving domain. This includes joining, machining, fabrication process development, and mock-up testing on the basis of the current He cooled divertor design. Thus identification of fabrication related material issues and implications for tungsten materials development are important. In general, W is going to be used as armour material while Eurofer is going to be used as structural material, with the expectation that ODS steels will replace Eurofer in various parts of the structure in the future. Until now, the joining process by classical brazing has not been successful so far with respect to low activation brazing materials. Therefore, unconventional solutions as pulse sintering/joining/powder brazing are promising alternatives which have to be developed and investigated in detail.

2. W-steel Functional Gradient Material joining route

2.1. Process description

As preliminary test have already shown, it is possible to join directly steel with steel using a spark plasma device. Thus we worked to demonstrate the possibility of direct joining of W plates with a W-steel FGM and further to another steel plate. There are several possible routes for this process and in this view we performed both multi-step or single step procedures using different FGM compositions and morphologies. Table 1 presents the performed work breakdown according to these lines.

Table I. Routes for joining W to steel using W-steel Functional Gradient Materials

Type of process	Step	Step description	Materials used
single step joining	1	W + W-steel FGM + steel	W plate/foil, steel plate/foil W/steel powder mixtures
two steps joining	1	W-steel FGM	W/steel powder mixtures
	2	W + FGM + steel	W plate, steel plate W-steel FGM
three steps joining	1	W-steel FGM	W/steel powder mixtures
	2	W + FGM + steel = composite	W thin foil, steel thin foil, W-steel FGM
	3	W + composite + steel	W plate, steel plate step 2 composite
four steps joining	1	W-steel FGM	W/steel powder mixtures
	2	W + FGM + steel =	W thin foil,

		composite	steel thin foil, W-steel FGM
	3	W + composite = first joint material	W plate step 2 composite
	4	first joint material + steel	steel plate step 3 material

2.2. Results and assesment of the methods.

Single step joining allows for a direct joining in short time and reduces surface related pre-steps. The SPS parameters depend strongly on the plate dimensions. The grains morphology affects the surface contact. A thicker FGM layer affects the W-FGM interface quality. A thinner FGM layer make the procedure closer to brazing and needs a larger temperature gradient to avoid melting.

Two steps joining implies more time and requires surface preparations which is more difficult for the FGM surface (with a higher porosity). As a correction, mixing some nm sized W powder improoves the procedure. Such an improovement can be used also in the other procedures. Applied pressure in the second step is less efficient as in the direct step.

Three steps joining allows for a joining material to be used in different shapes and dimensions. Surface preparations and lower applied pressure efficiency are here also present as problems. It is also difficult to choose the correct SPS parameters in the third step due to a strong dependence on the composite parameters.

Four steps joining allows again for a joining material to be used in different shapes and dimensions. Surface preparations and lower applied pressure efficiency are here also present as problems. It is possible to adjust the step 3 and 4 parameters according to the W and steel joining parameters, respectively.

2.3. FGM composition and morphology

As pointed above the end surfaces of the FGM present a higher degree of porosity as the middle part. This results from the SPS working procedure, i.e. the use of graphite foils as an electrical contact between die pistons and material. An improovement can be reached either using a very thin foil of W or steel respectively at the contact region, or by mixing into the FGM powder of nm W particles, especialy at the W reach side and of nm steell particles at the steel reach side. Since both materials are at the nm size flambable, the entiere work for mold preparation should be carried out in a glove box in Ar. This was also beneficialy to the reduction of oxide content in the sample. Commercialy available 60 nm W and steel powders have been used.

Figure 1 - SEM image of a contact region between 2 different concentration layers of a W-steel FGM.

Regarding the composition, the FGM layers were realized according to the results obtained in the previous year. The layers have been realized by powders of W and steel in W:steell weight proportions of 3:1, 2.5:1, 2:1, 1.5:1, 1:1, 1:2 and 1:3. The mixtures are prepared in glovebox in Ar atmosphere with less than 5 ppm water and less than 20 ppm oxygen. Layers of 0.2-0.5 g/cm^2 of these mixture have been set in the molds together with W and Eurofer 97 plates at the corresponding margins. Such compositions are able to provide a good morphological gradient, as shown in Figure 1. The additional mixing of nm sized powders was made respecting the above proportions.

2.4. SPS parameters and molds.

The final samples have been prepared in a single step joining procedure. To prepare samples for mechanical tests it was necessary to design and realize new molds. The resulting sample shapes should be rectangular prisms with at least 27 mm x 4 mm x 4 mm. These molds have been created from a special high density graphite by mechanical work. One important point was to choose the best temperature and pressure for sintering the FGMs. Since Eurofer is a Cr based steel we had to take into account the Cr-Fe phase diagram. Accordingly the sintering temperature was limited to 1200 C and therefore the sintering duration was slightly increased up to 20 min. The applied pressure was increased during sintering with a low rate up to 50 MPa. The samples have been sinterd by SPS in low pressure Ar atmosphere.

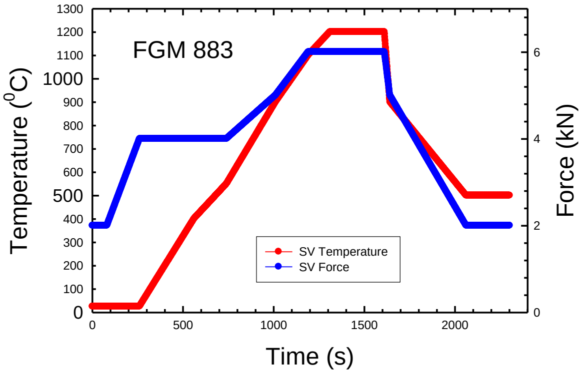

Figure 2 - SPS procedure used to realiza W-Eurofer 97 FGMs

The SPS procedure used is depicted in Figure 2. The samples were compacted at room temperature with about 15 MPa, then slowly pressed up to 30 MPa. The temperature was thereafter increased to about 800 C. Above this value pressure was again applied up to 1100 C and about 50 MPa. Finaly the temperature was increased to 1200 C and preserved for 5 min. Then both pressure and temperature have been gradually decreased. The resulted materials shown densities of 12 g/cm^3, indicating a dense material.

3. W-steel direct SPS joining and powder brazing routes

Rapid joining a first wall material as W to the structural materials, like Eurofer or ODSFS remains an open problem in the DEMO concept. We have shown that it is possible to make such a joint using FAST (field assisted) sintering equipments (e.g. SPS or PPS). Two routes are explored and assessed. The first one is to use the high current of FAST to directly join a W plate to an Eurofer plate. The second one is a derived brazing route, using a W-V (V is a low activation material) powder mixture.

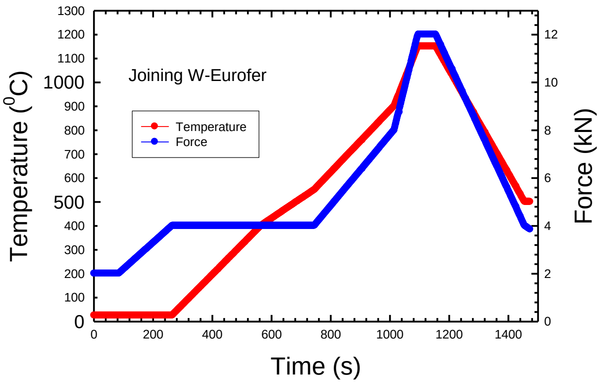

Figure 3 - Joining process parameters for W and Eurofer 97 plates.

For both direct and brazing procedures, the same pulse heating / applied pressure cycle was used, as depicted in Figure 3. The main point is to keep a high temperature as short as possible to avoid interdiffusion or large scale melting of the steel. Such a process provided a good contact between the materials with mechanical properties to be evaluated in future stages.

4. Thermal properties of W-steel joints

Investigation of the thermal properties of W-steel FGMs requires a reference term. While W is a relatively well known material, the particular alloy Eurofer 97 is less known since it was produced in a limited batch for DEMO. Our samples have been investigated for theirs thermal properties between room temperature and 800 C together with reference materials as pure W and standard Eurofer 97 steel. Thus in a first step we have analysed Eurofer 97 thermal properties and observed a thermal diffusivity higher than in the usual ferritic steels (values between 6.5-7 mm^2/s at RT). Meanwhile, the specific heat at RT is almost typical for ferritic steels, with a low value of 0.45 J/g/K.

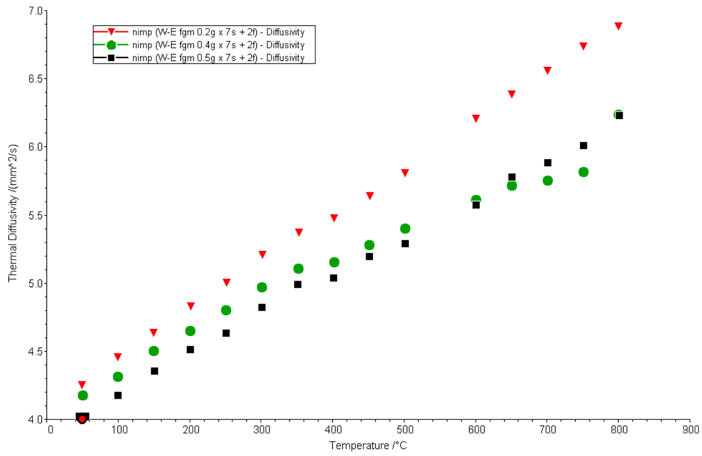

Figure 4 - Thermal diffusivity of different W-Eurofer FGMs.

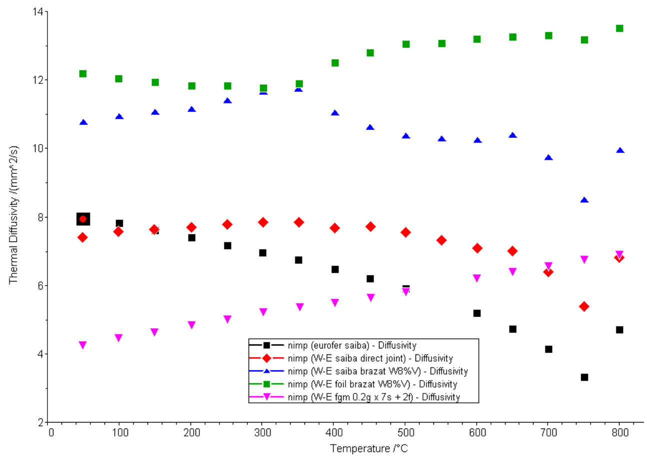

Figure 5 -. Thermal diffusivity for different W-Eurofer joints.

In Fig. 4, the thermal diffusivity of some typical W-Eurofer FGMs is plotted for temperatures up to 800 C. Comparing with both Eurofer and W references, one should note the increase of diffusivity with increasing temperature. A second important feature is related to the decreasing values of diffusivity with increasing layer thickness. Finaly, the reduction of the diffusivity value becames smaller as the layer thickness increases. This behavior can be explained taking into account the evolution of specific heat: the specific heat value increases with the layer thickness and the increment decreases with increasing thickness. This suggests that the gradient effect is decreased for increasing layer thickness. Although only a qualitative assessment can be provided for the studied materials at that incipient stage, thermal properties of the joined samples might offer important information about the quality of the joint. A development of the theoretical approach is needed for a quantitative evaluation of interface contributions or oxide dispersion in materials.

The effect of different compositions in the FGMs used for joining W to Eurofer was also investigated. W-steel and W-Fe FGMs were realized by similar layers with similar proportions of constituents. The resulting samples have similar geometries, implying that the differences are related to FGM material nature. W-Fe FGMs have higher diffusivities as W-steel FGMs, consistent with the Fe higher diffusivity as compared to that one of Cr based steels.

Fig. 5 shows the thermal diffusivity for different types of joints between W and Eurofer 97. For comparison, the Eurofer bare material is also shown. A direct joint (without any addition) of a thin W plate (0.1 mm thick) to a thicker Eurofer plate (0.7 mm) shows most of the characteristics of the bare Eurofer plate, but with increased values at temperatures above 400 C. The same observations applies to the joint realized between similar W and Eurofer plates respectively, when using a W-8%V brazing layer. However here the diffusivity increases, due to the addition of more W. The V contribution can be observed in a shape change of the diffusivity temperature dependence around 400 C. Decreasing the Eurofer foil thickness results in an increased thermal diffusivity at higher temperatures, while the overall curve shape changes toward an increasing diffusivity with increasing temperatures. Finally, for comparison, a (W plate)-(W-Eurofer FGM)-(Eurofer plate) joint shows lower values at low T and an ascending shape with increasing temperatures.

5. Conclusions

A new route was tested for a direct joint between W and steel using W-steel FGM in spark plasma furnace. We have investigated and optimized the process parameters for both multi-step or single step procedures and the most appropriate structure for the W-steel FGM to be used. Samples with different composition have been realized and theire mechanical properties will be investigateded by our EFDA WWAlloys partners.

The thermal properties of the single step FGM joints have been investigated at high temperatures. Increasing of the layer thickness produces an enhancement of the specific heat and a decrease in the thermal diffusivity value, indicating a decrease of the gradient effect in the joint. This suggest that an ideal joint need a relatively small transition distance, at best less than 1 mm, while maintaining at least 7-8 layers.

W and steel plates have been joined also using a direct SPS route and a powder brazing route and the thermal diffusivity was measured and compared to that one of bulk materials and FGMs. The differences were evaluated in terms of interface contributions to thermal transport. In further stages the joining procedure will be refined using various materials and composites. The evaluation of the joint quality and properties will be developed adding different investigation techniques as XPS, Moessbauer spectroscopy and mechanical tests. The method might be developed toward an useful quantitative joint quality evaluation tool.

GROWTH OF SIC BASED COMPOSITES BY LASER AND RADIO-FREQUENCY DISCHARGE METHODS

M. Filipescu, F. Stokker-Cheregi, D. Colceag, V. Ion, R. Birjega, A. Nedelcea, M. Dinescu

EURATOM-MEdC Association, National Institute for Lasers ,Plasma and Radiation Physics, Bucharest, Romania

Abstract

Recently, beside its applications in electronics, silicon carbide is studied for applications in the nuclear filed. A simple and versatile method to grow SiC-based structures is considered to be Pulsed Laser Deposition (PLD). The addition of a Radio-Frequency discharge beam to the PLD system, (RF-PLD), leads to a substantial improvement of the films properties in terms of morphology, structure and composition. The identification of a fabrication route to produce either SiC thin films with closed porosity or structured compounds based on SiC (as fibres, tubes, nanoparticles, naostructured thin films) is the main goal of this project. These depositions were carried out in high vacuum or in non-reactive atmosphere (Argon or Argon-Helium mixture) starting from different ceramic targets (SiC, W+SiC or graphite+SiC). The influence of deposition parameters (as wavelength, substrate temperature, gas pressure, radio-frequency power) on the structure, surface's morphology, composition and optical properties of SiC structures was studied by Atomic Force Microscopy, Transmission Electron Microscopy, Scanning Electron Microscopy, Secondary Ion Mass Spectroscopy and spectroellipsometry.

SiC thin films with closed porosity were obtained by RF-PLD method in low pressure (0.005 mbar of Ar) and heating the silicon substrate to 600°C.

SiC nanostructures as clusters, toroidal features, rolling 3D-sheets, fibres, were obtained by RF-PLD technique at high pressures (1 and 2 mbar), keeping the substrate at 600°C.

The WSiC composites as micrometric long structures with tubes shape and scattered "grains" that are tending to accumulate in chains and structures with different shapes as nanoparticles, fibres, "smashed corn flakes" and bubbles were obtained by PLD and RF-PLD at 2 mbar of Ar when the substrate is heated at 600°C.

Carbon nanostructures embedded into a SiC matrix were obtained as grains that formed 3D structures like walls or as grains with smaller sizes that are gather in chains with lengths of hundreds of nanometers by PLD and RF-PLD in 0.05 mbar of Ar, at Ts=600°C.

Conferences

[1] M. Filipescu, F. Stokker-Cheregi, D. Colceag, A. Nedelcea, L. C. Nistor, M. Dinescu, *Characterization of SiC based compounds obtained as nanostructures by laser and Radio-frequency discharge methods*, E-MRS Conference, Spring Meeting, May 14-18, 2012, Strasbourg, France.

Detailed Results

Introduction

Until few years ago, silicon carbide as thin film has been studied due to its applications in electronics [1]; recently, SiC was also included in the category of nuclear ceramics. SiC has high-temperature stability [1] and resistance to oxidation [2]. Its high thermal conductivity, coupled with its low thermal expansion coefficient and high strength, gives this material exceptional thermal shock resistant quality [3]. Recently, intensive work has been focused on production of SiC based composites one-dimensional nanostructured, such as nanotubes, nanofibres, nanowires, nanorods, and nanowhiskers, because of their high potential uses in the nuclear field. SiC based nanostructures have been obtained by different techniques: plasma enhanced chemical vapour deposition [4], chemical vapour deposition [5], electron beam evaporation [6], RF magnetron sputtering [7], Laser-Assisted CVD [8], technique of concentric electro-spinning [9], polymer blend technique [10], etc. These methods present many disadvantages. As an alternative, laser based methods have become widely used for obtaining thin films on different supports. Among these, Pulsed Laser Deposition (PLD) emerged as an attractive solution [11]. PLD (or laser ablation) involves the interaction of a laser beam with a target material (solid or liquid) producing a plume that transports the particles onto a substrate, where a thin film is formed [12]. PLD is a clean, versatile and flexible method. The addition of a Radio-Frequency (RF) discharge beam to the PLD system leads to a substantial improvement of the films morphology and crystalline structure. This RF beam leads to an increased reactivity, acting on the thin layer between the laser pulses, when the atoms are settled down to form a thin film [13].

The identification of a fabrication route to produce either SiC thin films with closed porosity or structured compounds based on SiC (as fibres, tubes, nanoparticles, nanostructured thin films) is the main goal of this project.

The influence of deposition parameters (as wavelength, substrate temperature, gas pressure, radio-frequency power) on the structure, surface morphology, composition and optical properties of SiC based composite structures was studied by X-ray diffraction (XRD), Atomic Force Microscopy (AFM), Scanning Electron Microscopy (SEM), Secondary Ion Mass Spectroscopy (SIMS) and ellipsometry.

Experimental set-up; results and discussions

The basic experimental PLD set-up consists in a laser, a reaction chamber equipped with a vacuum system that can go down to 10^{-6} mbar, a target rotation-translation system and a heater (substrate holder) that can go up to 800°C. Adding a radio-frequency discharge to the basic PLD system, a newly hybrid method was developed.

In the ***first stage,*** the main goal has been the identification of a fabrication route to produce either SiC thin films with closed porosity or SiC nanostructures.

Two techniques were applied: PLD and RF-PLD. Starting from a SiC ceramic target, these depositions were carried out in high vacuum or in non-reactive atmosphere (Argon or Argon-Helium mixture). The deposition temperature varied from room temperature (RT=21°C) up to 600°C. Radio-frequency power was set at 100 W.

For the *first set of experiments* consisting in obtaining of SiC thin films with closed porosity (very compact) two types of lasers were used: the YAG:Nd laser (266 nm) and an ArF laser (193 nm). Different types of substrates (Si(100), MgO, quartz, sapphire) were used as collectors. The depositions were made in high vacuum or non-reactive gas at pressures between 0.005 – 0.5 mbar.

From studies performed on different SiC thin films it was found that:

i) irradiating the target at a laser wavelength of 266 nm, the roughness of SiC thin films decreases and droplets sizes became smaller than in the case of using a 193 nm wavelength. Both surfaces are compact, without pores or cracks. Taking into account the fact that the absorption coefficient is higher at 266 nm [14], we have chosen to use this wavelength;
ii) by adding a Radio-frequency discharge to the PLD system, for SiC samples deposited on Si(100) at RT, 0.1 mbar Ar, 3 J/cm^2, the surface is changing: a nanostructuring of the surface and a tendency to form nanoparticles were observed
iii) decreasing the gas (Ar+He) pressure of from 0.5 mbar to 0.005 mbar the roughness of SiC surfaces strongly decreases (from 9 nm to 0.1 nm).

i) the film composition depends on substrate temperature and RF presence: thin films grown at room temperature by PLD, have a bigger content of oxygen and a sharper interface than those deposited at 600°C. Sample obtained at high temperature by PLD presents a lower content of oxygen, a nearly uniform distribution of elements in film (silicon, carbon and oxygen). Adding RF discharge to the PLD system, an improvement was observed. The layer deposited by RF-PLD has a sharper interface and very uniform distribution of elements inside the layer; even the oxygen content seems to be smaller.

The best SiC layers from the closed porosity point of view were obtained by heating the substrate at 600°C in 0.005 mbar (Ar+ He) gas pressure, in the presence of RF discharge; these are dense, pores and droplets free, having a roughness in the angstroms range (fig. 1).

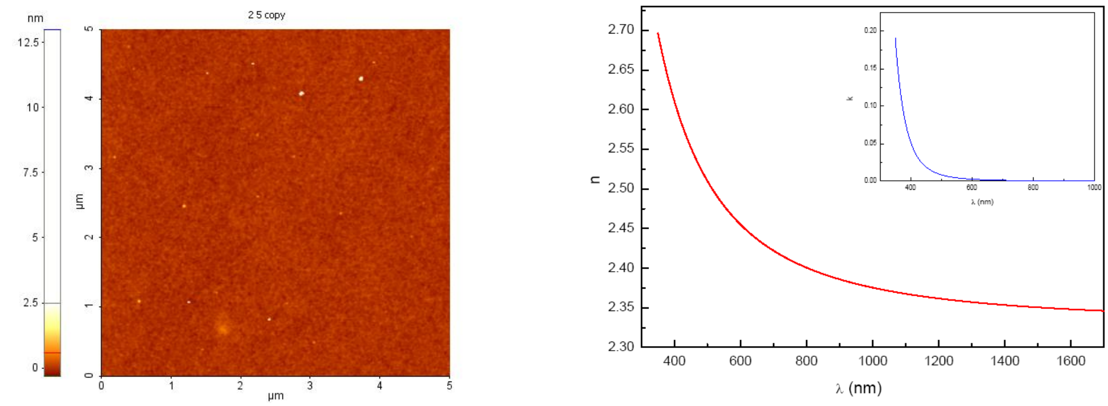

a) RMS: 0.1 nm b)

Figure 1 - SiC thin film obtained by RF-PLD at 600°C on Si(100), in a mixture of Ar+He at 0.005 mbar a) AFM image and b) dependence of refractive indices and extinction coefficients (inset) results from Cauchy-Urbach fit

For the *second set of experiments* consisting in growth of SiC nanostructures, a YAG:Nd laser working at 266 nm was used. The depositions were made in gaseous atmosphere at high pressure (from 1 to

30 mbar Ar or mixture of Ar and He). For growing of SiC as fibers/nanotubes, $Ni/SiO_2/Si$ substrates were used.

Studies performed on SiC nanostructures showed that:

ii) the addition of radio-frequency discharge to the PLD system allows clusters formation on Si substrate at room temperature, in 2 mbar of Argon for a distance target-substrate of 4 cm;

iii) when approaching the substrate to the target (3 cm) the AFM investigations revealed surfaces with features like "cotton" and islands containing nanoparticles with sizes around 70 nm (fig. 2a); the presence of some toroidal formations, like curls, was revealed by TEM; this could be the early stage of nanotubes formation (fig. 2b);

iv) by heating the substrate ($Ni/SiO_2/Si$) to 600°C, in the presence of the RF discharge in a mixture of Ar and He, the pressure influence on the morphology is revealed: for a pressure of 2 mbar (fig. 3a), nanostructures like fibres (length around 350 nm and width of 100 nm) that form isolated islands surrounded by nanoparticles (sizes around 40 nm) have been observed. Increasing the gas pressure to 4 mbar, islands with nanoparticles (diameters of 150 – 200 nm) and some fibres (width of 50 nm) appeared (fig. 3b).

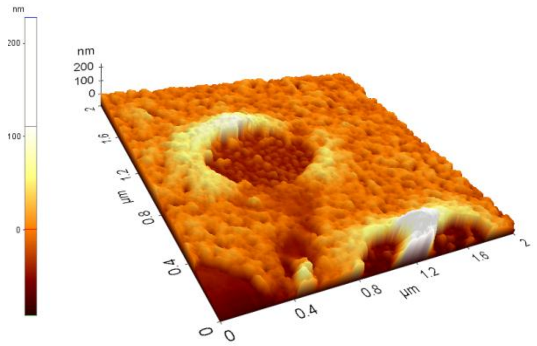

a)

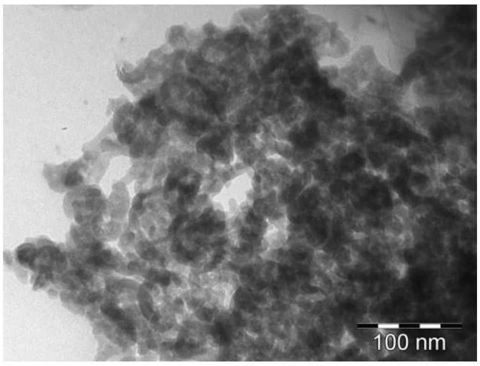

b)

Figure 2 - SiC sample grown on Si(100) at RT by RF-PLD in 2 mbar of Ar, investigated by a) AFM and b) TEM

a)

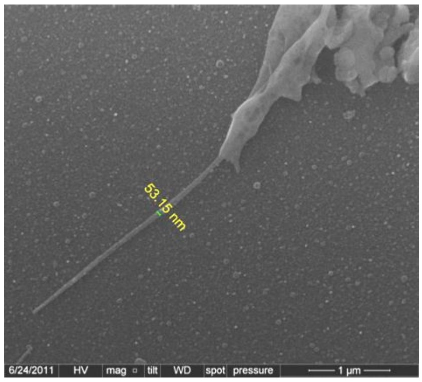

b)

Figure 3 - SEM and AFM images for SiC samples obtained by RF-PLD on $Ni/SiO_2/Si$ substrate in a mixture of $Ar+O_2$ at pressure of a) 2 mbar and b) 4 mbar

In the ***second stage,*** in order to obtain structured compounds based on SiC (SiC, SiCW, CNS-SiC) as fibres, tubes, nanoparticles, nanostructured thin films, three sets of experiments were performed. The PLD and RF-PLD experimental set-ups were used as deposition techniques.

The *first set of experiments* was carried out to produce structured SiC as fibers, tubes, nanoparticles or nanostructured thin films by PLD or RF-PLD methods. A beam with wavelength of 266 nm produced by a YAG:Nd laser irradiated a SiC (Nicalon) target. Si(100) plates heated (600°C) or kept at room temperature, during the depositions were used as substrates. Distance between target and substrate was set at 3 cm. The depositions were performed in high vacuum or in Argon gas.

The XRD pattern target of SiC (Nicalon) have put in evidence the presence of the predominant 3C-SiC (β-SiC) and 6H-SiC phases, while 4H-SiC phase is in a low amount.

Surfaces' morphologies of SiC thin films were investigated by AFM using a Park XE100 system. In order to establish the influence of substrate temperature (T_s) on the film surface morphology, depositions by PLD in vacuum, at RT and 600°C were performed. Smooth thin films with thickness around 200 nm were obtained, in both cases. "Grains" with sizes between 120-200 nm were observed. When the substrate is heated during the deposition, these grains are tending to aggregate in the form of short chains.

With the addition of an Ar-RF discharge (100 W power) to the PLD process we noticed morphology changes with increasing pressure, while the substrates were kept at 600°C. Different kinds of structures (chains, 3D-sheets, fibers) are revealed by SEM investigations (fig. 4). It can be observed that using a pressure of 0.05 mbar of Ar, grains with diameters around 100 – 150 nm gather in longer chains with length between 400 nm and 5 microns (fig. 4a). Micrometric long 3D-sheets that are tending to roll as tubes and thin fibers with length of microns were found when samples were deposited in 1 mbar of Ar (fig. 4b). Increasing gas pressure up to 2 mbar, structures mentioned before disappeared and, this time, grains with sizes of 50 – 100 nm form shorter chains with lengths of 120 – 200 nm.

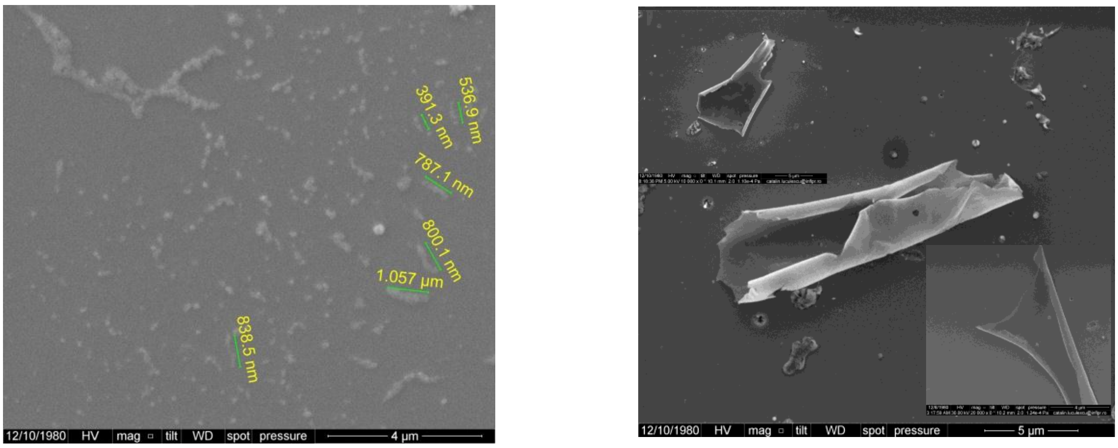

a) b)

Figure 4 - SEM images of SiC samples grown by RF-PLD at T_s=600°C and Ar pressure of a) 0.05 mbar and b) 1 mbar

The *second set of experiments* was focused on growth of 3D-SiC fibres with Tungsten.

A sectorial target consisting of ¾ SiC and ¼ Tungsten was irradiated with a wavelength of 266 nm. Silicon (100) plates heated at 600°C during the depositions were used as substrates. RF discharge in 2 mbar of Argon gas was added to the PLD process for some experiments.

SEM investigations revealed the role of radio-frequency in the development of structures based on SiCW compound. Using the PLD technique, micrometric long structures as tubes shape and scattered "grains" that are tending to accumulate in chains and clusters on Si substrate were obtained. Different stages of development of these tubes, starting from sections of tubes that are tending to roll up to completely closed tubes, can be observed on the surface (fig. 5).

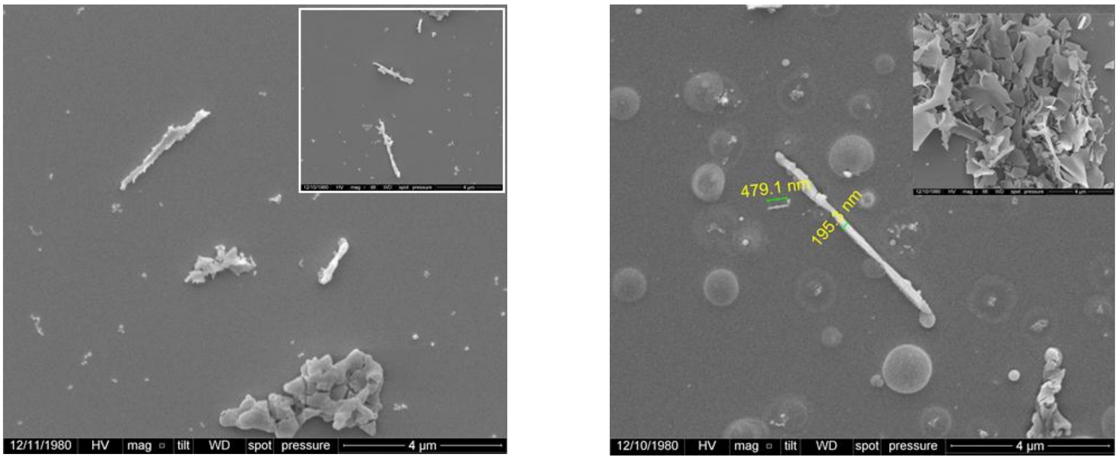

a) b)

Figure 5 - SEM images for SiCW obtained in 2 mbar of Ar at 8 J/cm^2 and T_s=600°C by a) PLD and b) RF-PLD

The *third set of experiments* is related to producing carbon nanostructures embedded into a SiC matrix by laser ablation.

These depositions consisted in the irradiation of a sectorial target made of ¾ SiC and ¼ Graphite with a laser working at wavelength of 266 nm. As collector Si (100) kept at 600°C during the depositions was used. The distance between target and substrate was of 3 cm. A pressure of 0.05 mbar of Argon gas was used and the Radio-frequency discharge was maintained at 100 W.

Taking into account that the graphite target is two times thicker then SiC target, the laser spot area on graphite is two times bigger then area on SiC target. Therefore, the laser fluence has different values on this sectorial target: 8 or 6 J/cm^2 on SiC and 4 or 3 J/cm^2 on graphite.

AFM and SEM investigations have put in evidence the presence of grains that are assembled in chains on the surfaces of samples obtained by PLD and RF-PLD in 0.05 mbar of Ar, at Ts=600°C. Randomly, in the case of samples obtained by PLD, grains with sizes of 150-200 nm form 3D structures like walls with heights around 100 nm and length of 2-3 microns (fig. 6a). When adding RF to the PLD system, it can be noticed that grains with smaller sizes (between 80-150 nm) are formed on the surface of the Si substrate. The same tendency to gather in chains with lengths of hundreds of nanometers has been observed (fig. 6b).

SIMS analyses have shown that films prepared from sectorial target (¾ SiC and ¼ of graphite) present a specific increase in the carbon level along with a diminished silicon signal. Since this type of deposition was carried out in argon atmosphere, at 0.05 mbar, the level of oxygen in the thin film is extremely low.

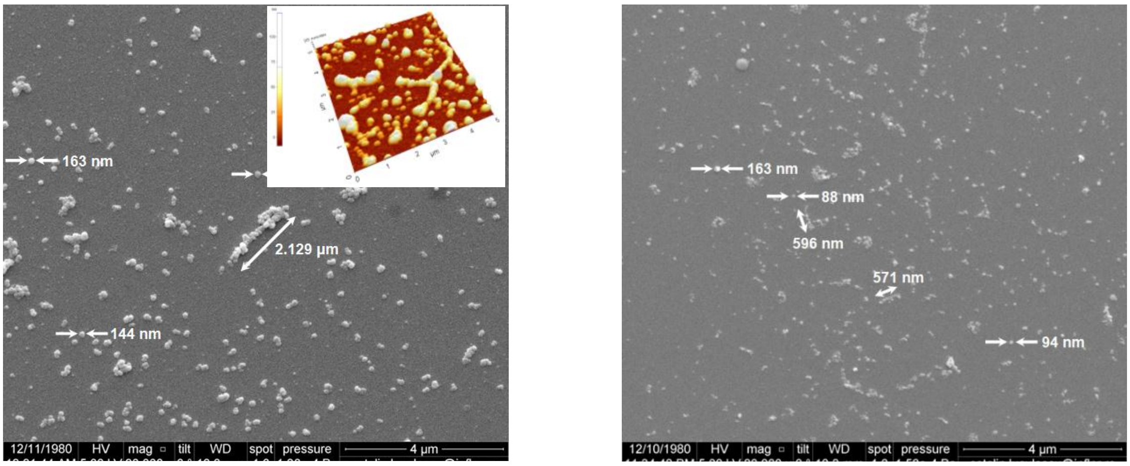

a) b)

Figure 6 - Images of CNS-SiC samples obtained in 0.05 mbar of Ar, Ts=600 ℃, 8/4 J/cm^2 by a) PLD (SEM and AFM in set) and b) RF-PLD (SEM)

Conclusion

Experiments and investigations performed during this project result in different composites based on SiC: nanostructured thin films, nanoparticles, nano-tubes, sheets, fibers.

In the first stage of the project, the suitable fabrication route to obtain ***SiC thin films with closed porosity*** has been identified as ***RF-PLD method*** in low pressure (0.005 mbar) and heating the silicon substrate to 600°C.

Nanostructures as clusters, toroidal features, fibres have been obtained by ***RF-PLD technique*** at high pressures (2 and 4 mbar), keeping the substrate at 600°C and the distance between target and substrate of 3 cm.

In the second stage of the project, ***SiC, WSiC and CNS-SiC nanostructures*** have been obtained by ***PLD and RF-PLD technique*** in the ***presence of argon gas*** (0.05 and 2 mbar), keeping the substrate at ***600°C*** and the distance between target and substrate of 3 cm.

References

[1] M.A. Capano, J. Appl. Phys. 78, (1995) 4790-4792;

[2]Tang Chunhe, Guan Jie, J. Nucl. Mat. 224, Issue 1, (1995) 103-108;

[3] Tomori Tosin, Melkote Shreyes N. and Kotnis Mahesh, Materials and Manufacturing Processes, 18:6, (2003) 943-963

[4] T. Rajagopalan, X. Wang, B. Lahlouh, and C. Ramkumar, Partha Dutta, S. Gangopadhyay, J. Appl. Phys., 94 (2003) 8;

[5] D. Dietrich, H. Podlesak, G. Marx, B. Wielage, Fresenius J. Anal. Chem. 361, (1998) 568-569;

[6] G. V. Bunton, J. Phys. D: Appl. Phys. 3 (1970) 232-235;

[7] N. Ledermann, J. Baborowski, P. Muralt, N. Xantopoulos, J. -M. Tellenbach, Surface and Coatings Technology, 125, 1-3, (2000) 246-250 ;

[8] Y. Kamlag, A. Goossens, I. Colbeck, J. Schoonman, Chemical Vapor Deposition 9, Issue 3, (2003) 125–129;

[9] Harvey A. Liu and Kenneth J. Balkus Jr, Materials Letters 63, Issue: 27 (2009) 2361-2364;
[10] N. Patel, R. Kawai and A. Oya, Journal of Materials Science 39 (2004) 691-693;
[11] D.B. Chrisey, G.K. Hubler, Pulsed laser Deposition of Thin Films, John Wiley & Sons, New York, 115 (1944);
[12] D. Brodoceanu, N. D. Scarisoreanu, M. (Morar) Filipescu, G. N. Epurescu, D. G. Matei, P. Verardi, F. Craciun, M. Dinescu, Plasma Production by Laser Ablation, PPLA 2003, World Scientific (2004) 41-46;
[13] G. Dinescu et al., Proceedings SPIE 5448 (2004) 136-143;
[14] S.L. Shi, S.J. Xu, X.J. Wang, G.H. Chen, Thin Solid Films 495 (2006) 404 – 406.

GROWTH OF SiC THIN FILMS WITH CLOSED POROSITY BY LASER AND PLASMA METHODS

M. Filipescu, D. Colceag, V. Ion, R. Birjega, A. Nedelcea, M. Dinescu

EURATOM-MEdC Association, National Institute for Lasers ,Plasma and Radiation Physics, Bucharest, Romania

Abstract

Until few years ago, silicon carbide has been studied due to its applications in electronics; recently, SiC was also included in the category of nuclear ceramics. Thin films of SiC have been obtained by different techniques (chemical, physical) some of them having several major disadvantages. As an alternative, laser based methods have become widely used for obtaining thin films on different supports. Among these, Pulsed Laser Deposition (PLD) emerged as an attractive solution. The addition of a Radio-Frequency (RF-PLD) discharge beam to the PLD system can lead to a substantial improvement of the films morphology and crystalline structure. The aim of this work is to obtain β-SiC thin films using pulsed laser deposition.

In order to obtain SiC thin films with closed porosity (very compact), PLD and RF-PLD methods were used. The deposition parameters might have a major influence on growing compact, crystalline thin films with low roughness and without pores. Therefore, studies regarding their influence on SiC thin films properties were performed by Atomic Force Microscopy (AFM), X-Ray Diffraction (XRD), Secondary Ion Mass Spectroscopy (SIMS) and spectroelipsometry.

Studding by AFM the surfaces' morphologies of samples deposited by PLD and RF-PLD, in the same conditions of pressure, laser fluence and substrate temperature, it can be observed that the RF addition to the PLD set-up results in layers with higher roughness. Also, a high pressure and high temperature corroboration leads to obtaining SiC thin films with rough surface and big droplets. From SIMS investigation it was observed that samples prepared at Ts=600°C, have a considerable bigger density than those prepared at room temperature. Spectroellipsometry revealed that only for SiC thin film grown by PLD in vacuum at a high temperature and high laser fluence, a tendency to become crystalline can be observed. Therefore, it was found that crystalline, closed porosity layers of silicon carbide were obtained by PLD in vacuum, when the substrate is heated to 600°C.

Detailed Results

1 Introduction

In the last years beside its applications in electronics [1], silicon carbide was studied as nuclear ceramics. SiC has high-temperature stability [1] and resistance to oxidation [2]. Its high thermal conductivity, coupled with its low thermal expansion coefficient and high strength, gives this material exceptional thermal shock resistant quality [3].

Thin films of SiC have been obtained by different techniques [4 – 9], etc. These methods present some major disadvantages as large consumption of material required for the processing, or because they don't offer accurate and precise thickness control of the resulting structures.

As an alternative, laser based methods have become widely used for obtaining thin films on different supports. Among these, Pulsed Laser Deposition (PLD) emerged as an attractive solution. PLD (or laser ablation) involves the interaction of a laser beam with a target material (solid or liquid) producing a plume that transports the particles onto a substrate, where a thin film is formed. PLD is a clean, versatile and flexible method. The addition of a Radio-Frequency (RF-PLD) discharge beam to the PLD system could leads to a substantial improvement of the films morphology and crystalline structure.

The aim of this work is to obtain crystalline SiC thin films with closed porosity by simple PLD or by RF-PLD.

Equipments as: X-ray Diffractometer (XRD), Atomic Force Microscope (AFM), Secondary Ion Mass Spectrometer (SIMS), ellipsometry spectrometer were used to characterize the SiC thin films.

2 Experimental set-up, results and discussions

The experimental PLD set-up consists in a YAG:Nd laser, a reaction chamber equipped with a vacuum system that can goes down to 10^{-6} mbar, a target rotation-translation system and a heater (substrate holder) that can go up to 800°C. A second complex deposition system was built by adding to the described PLD system a second small chamber, connected to the PLD one. In this second chamber a radio-frequency discharge is ignited in a gas (using a RF generator) and expands as a beam of excited and ionised species in the PLD chamber. By directing this beam towards the substrate an increased reactivity is induced: taking into account that the generator's frequency is 13,56 MHZ, the beam acts on the thin layer in the interval between the laser pulses, when the atoms are settled down to form a thin film [10].

In order to obtain SiC thin films with closed porosity (very compact), PLD and RF-PLD methods were used. A YAG:Nd laser working at 266 nm irradiates a SiC ceramic target with a number of pulses between 20000 and 80000. All depositions were carried out in high vacuum or in argon gas. In order to obtain compact, crystalline thin films with low roughness and without pores, the substrates were heated up to 600°C. Silicon (100), Si coated with photoresist and titanium were used as substrates. The distance between the target and collector was set at 4 cm. The substrate's temperature varied from room temperature (RT=21°C) up to 600°C; the substrate was heated with 20°C/min and cooled with 10°C/min. Laser fluence was varied in the range of 3 - 7 J/cm^2. Radio-frequency power was set at 100 W.

The deposition parameters (laser fluence, substrate temperature, gas pressure and RF power) might have a major influence on growing compact, crystalline thin films with low roughness and without pores. Therefore, studies regarding their influence on SiC thin films properties were performed.

The XRD patterns were collected on a PANalytical X'Pert MRD system in a continuous scan mode. The crystalline phases were identified using the data provided by the JCPDS-International Centre for Diffraction Data (ICDD). In the SiC target the 3C-SiC and the 6H-SiC phases are present. The XRD patterns of the films recorded in a Bragg-Brentano geometry, besides the peaks of the Si(001) substrate ((004) and (002)), consist of a diffuse-scattering indicating an X-ray amorphous structure or a fine grain structure.

Surfaces' morphologies of SiC thin films were investigated by AFM using a Park XE100 system, working in non-contact mode. To determine thickness of the SiC deposited layers, silicon substrates partially cover with photoresist were used as collectors. After depositing the SiC thin film, the substrates were washed in acetone for 10 minutes in an ultrasonic bath to dissolve the photoresist pattern. The difference in height (Δz) between the top of deposited layer and the silicon substrate was measured by AFM.

Thickness for a sample grown by PLD in vacuum, at room temperature, as results of target's irradiation with 20000 laser pulses is around 150 nm, while for a sample grown by RF-PLD, in 0.05 mbar of argon at RT, the thickness decreases 3 times (55 nm).

Areas starting from 2×2 μm^2 up to 20×20 μm^2 were scanned, in order to reveal lack of pores and the compact features of SiC thin films.

Studding the surfaces' morphologies of two samples deposited by PLD and RF-PLD, in the same conditions of pressure (0.05 mbar argon), laser fluence (3 J/cm^2) and temperature (600°C), it can be observed that the RF addition to the PLD set-up results in layers with higher roughness (fig.1).

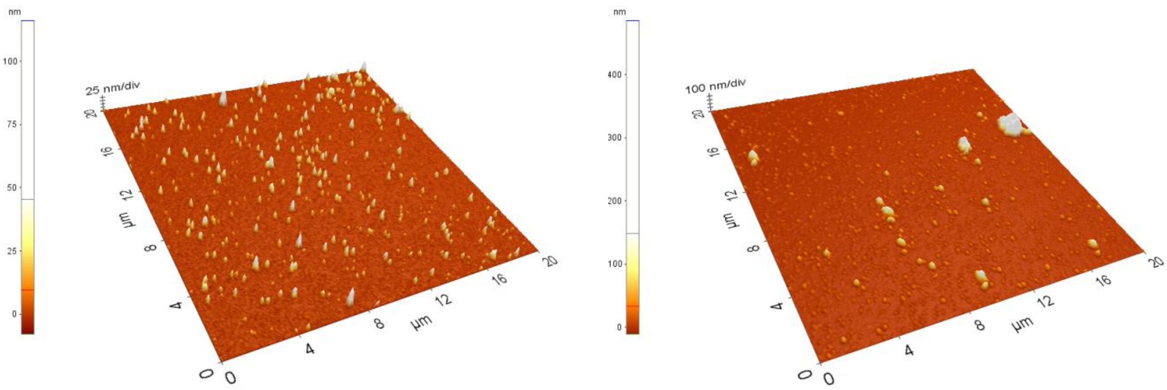

a) RMS=12 nm b) RMS=23 nm

Figure 1 - AFM images for SiC thin films deposited by a) PLD and b) RF-PLD

The substrate temperature and gas deposition pressure seem to lead to very different behaviours of growing process (fig.2):

i) for samples deposited in vacuum by PLD, when the Si substrate is heated at 600°C, thin film surface is more compact, pores free, uniform, with roughness below 2 nm compared to the layers deposited at RT (thin film with droplets and higher roughness, of around of 6 nm);
ii) for samples grown by RF-PLD in 0.05 mbar of argon, the high substrate temperature of 600°C leads to appearance of big droplets and therefore to a higher roughness (over 20 nm); the surface of SiC thin film obtained at RT presents a nanostructured feature, and a roughness below 2 nm.

Thus, a high pressure and high temperature corroboration carry on obtaining SiC thin films with rough surface and big droplets.

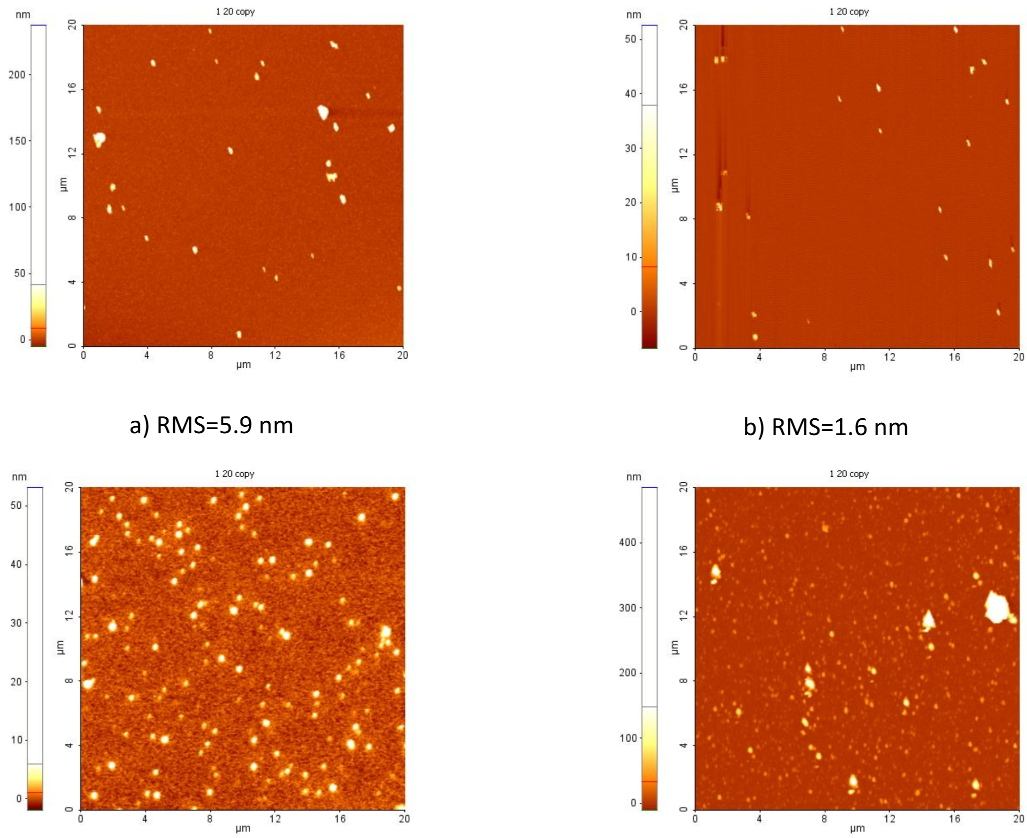

a) RMS=5.9 nm

b) RMS=1.6 nm

c) RMS=1.4 nm

d) RMS=23 nm

Figure 2 - AFM images of SiC thin films deposited in a) vacuum, RT, 7 J/cm^2, 0 W, b) vacuum, 600°C, 7 J/cm^2, 0 W, c) 0.05 mbar Ar, RT, 3 J/cm^2, 100 W and d) 0.05 mbar Ar, 600°C, 3 J/cm^2, 100 W

Laser fluence is another deposition parameter that influences the morphology of SiC thin films. For samples grown by PLD in vacuum at room temperature, the increasing of laser fluence from 3 J/cm^2 to 7 J/cm^2 leads to the appearance of droplets on the surfaces of thin films (fig.3).

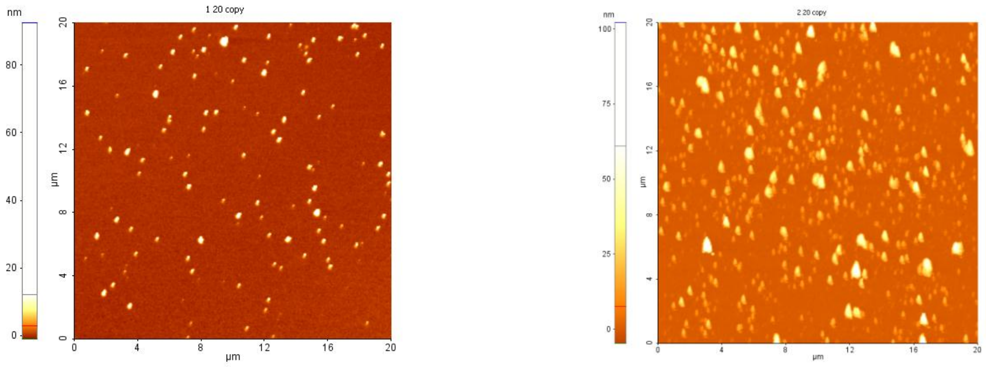

a) RMS=1.9 nm b) RMS=7.5 nm

Figure 3 - AFM images of SiC surfaces deposited by PLD in vacuum, RT, a) 3 J/cm^2 and b) 7 J/cm^2

SIMS analysis on the deposited thin films has been carried out in order to determine the chemical composition and in-depth behavior of elements; the measurements have been done using an apparatus from Hidden Analytical. Depth profiles registered for the samples obtained in vacuum at a laser fluence of 3 J/cm^2 show that the film is homogenous for its entire thickness. Since one of the main concerns has been avoiding the contamination with oxygen, the level of this element within the film has been monitored. Oxygen signal is weak, close to the background level of the SIMS installation chamber as it can be seen in the figure 4a) (the oxygen level does not decrease when the ion beam penetrates the substrate). The SIMS analysis have shown that SiC thin films present a remarkable sharp interface with no diffusion whatsoever between the deposited layer and the substrate.

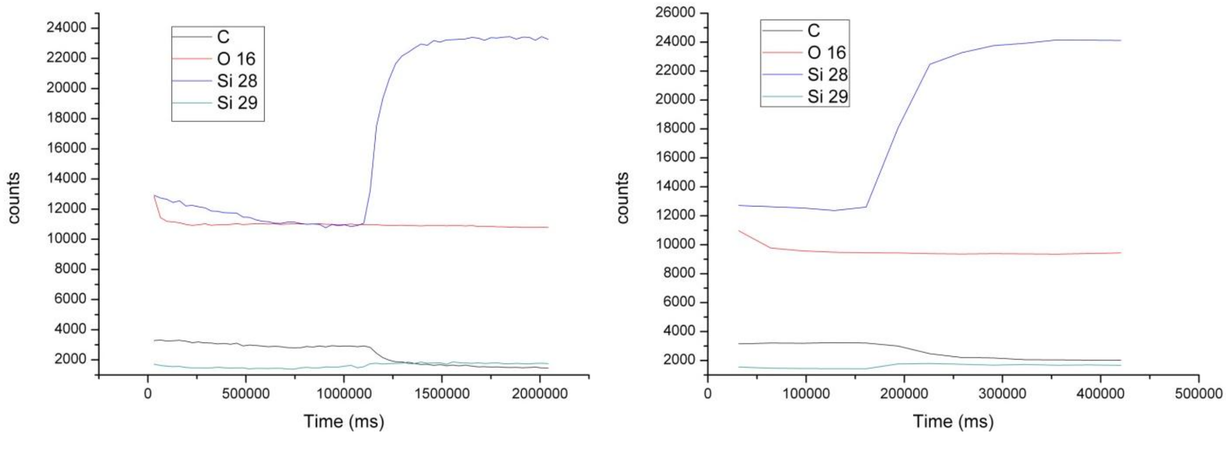

a) b)

Figure 4 - SIMS spectra for a SiC thin film grown by PLD in vacuum at RT and a) 3 J/cm^2 and b) 7 J/cm^2

Increasing the laser fluence to 7 J/cm^2 by diminishing the laser spot leads to the preparation of much thinner (4-6 times) films for the same number of pulses which can be explained by the smaller volume of the target affected by laser pulse. All the other compositional characteristics of the films are kept intact: homogeneity, low oxygen level, sharp interface between the film and the silicon substrate as it can be seen in the figure 4b.

In order to obtain the optical constants (refractive indices and extinction coefficients) spectroellipsometric measurements were performed using a Woollam Variable Angle Spectroscopic Ellipsometer (VASE) system. Measurements were performed in the visible and near-UV region of the spectrum, between 400 and 1700 nm, with a step of 2 nm, at 60°, 65° and 70° angle of incidence.

After measurements, different models were used for fitting the experimental data. In this way two parameters were determined: the refractive index and the films thickness.

For the silicon carbide thin films the initial considered model consists in 4 layers: the silicon substrate (0.5 mm), a native SiO_2 layer (3 nm), the SiC layer and the roughness. The optical constants of the Si substrates and SiO_2 layer are taken from literature [11].

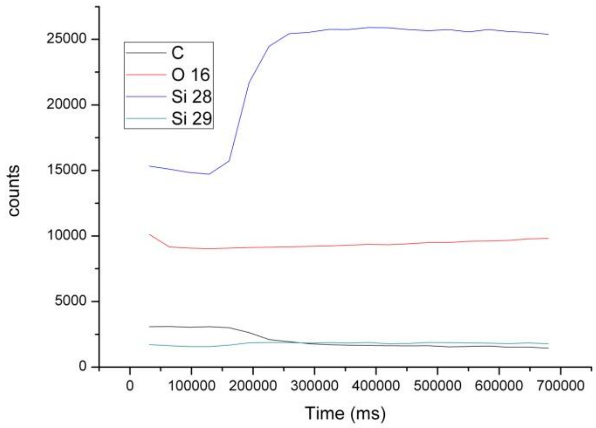

Figure 5 - SIMS spectrum for a SiC thin film grown by PLD in vacuum at 600°C and 7 J/cm^2

For the SiC layer optical constants were calculated from experimental data using Cauchy dispersion with Urbach tail in the spectral range 400-1700 nm. The optical properties of rough layer is extracted from experimental data using B-EMA (Bruggeman effective medium approximation) [12] between Cauchy-Urbach layer and air in proportion 50:50. It was noticed that the proposed model allows a good fit with the experimental data.

The wavelength dependences of the refractive indices and extinction coefficients for the thin films grown in different conditions by PLD or RF-PLD were studied (fig. 6); for the data interpretation the previous described models were used.

Only for SiC thin film grown by PLD in vacuum at a high temperature and high laser fluence, a tendency to become crystalline can be observed. The addition of radio-frequency discharge to the PLD process leads to a smaller value of the refractive index that can be explained by the high roughness (23 nm – see fig. 1) and non-compact aspect of the films.

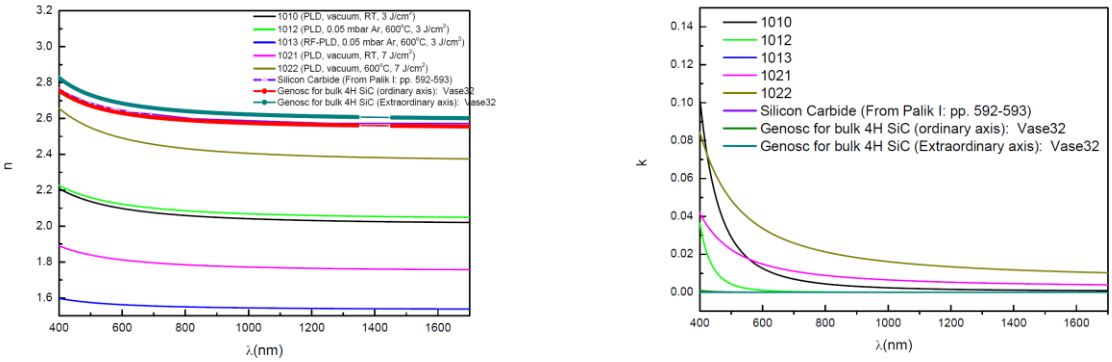

a) b)

Figure 6 - Behaviors of a) refractive and b) extinction indices vs. wavelength of SiC thin films deposited in different conditions

Measurements regarding micro-hardness of SiC thin films deposited on Ti and Si (100) substrates were performed with a Microhardness Tester FM 700 from Ahotec, using a load of 10 g (HV0.01). For a thin film with a thickness of 1.2 microns, grown by PLD in vacuum at RT, the hardness Vickers was determined around the value of 6.3 GPa.

3 Conclusion

Studies performed on thin films obtained in different experimental conditions, showed that crystalline, closed porosity (dense, pores free, roughness below to 2 nm for large area of 20×20 μm^2) layers of silicon carbide were obtained by PLD in vacuum, when the substrate is heated to 600°C and the laser fluence is set at 7 J/cm^2; the roughness on smaller areas (5×5 μm^2) is the angstroms range.

References

[2] M.A. Capano, J. Appl. Phys. 78, (1995) 4790-4792;

[3] Tang Chunhe, Guan Jie, J. Nucl. Mat. 224, Issue 1, (1995) 103-108;

[4] Tomori Tosin, Melkote Shreyes N. and Kotnis Mahesh, Materials and Manufacturing Processes, 18:6, (2003) 943-963;

[5] T. Rajagopalan, X. Wang, B. Lahlouh, and C. Ramkumar, Partha Dutta, S. Gangopadhyay, J. Appl. Phys., 94 (2003) 8;

[6] D. Dietrich, H. Podlesak, G. Marx, B. Wielage, Fresenius J. Anal. Chem. 361, (1998) 568-569;

[7] G. V. Bunton, J. Phys. D: Appl. Phys. 3, (1970) 232-235;

[8] N. Ledermann, J. Baborowski, P. Muralt, N. Xantopoulos, J. -M. Tellenbach, Surface and Coatings Technology, 125, 1-3, (2000) 246-250;

[9] Y. Kamlag, A. Goossens, I. Colbeck, J. Schoonman, Chemical Vapor Deposition 9, Issue 3, (2003) 125–129;

[10] Harvey A. Liu and Kenneth J. Balkus Jr, Materials Letters 63, Issue: 27, (2009) 2361-2364

[11] G. Dinescu et al., Proceedings SPIE 5448, (2004) 136-143

[12] C.M. Herzinger, B. Johs, W.A. McGahan, J.A. Woollam,W. Paulson, J. Appl. Phys. 83 (615) (1998) 3323–3336.

[13] H. Fujiwara, Spectroscopic Ellipsometry Principles and Applications, Maruzen Co. Ltd., Tokyo, Japan, 2007.

MICROSTRUCTURE AND MICROCOMPOSITION CHARACTERIZATION OF W AND WW-ALLOYS BY ANALYTICAL HRTEM (X-EDS, EELS, HAADF), BY SEM/FIB AND BY XRD

Corneliu Sârbu

National Institute for Materials Physics, Măgurele-Bucharest, Romania

Abstract

Microstructure and microcomposition measurements were done on pure W and several W-alloys fabricated by Powder/Metal Injection Moulding (PIM/MIM) technology, in view of developing suitable tungsten grades for application in building of structural and divertor parts of the future DEMO reactor (W-Ta alloy, W+Y2O3 ODS alloys, W+Ta[fibre] composites) and for use as reference material (pure-W). The correlation of micro-structure/composition data with experimentally measured thermal diffusivity and mechanical properties (density, porosity, bending resistance, impact resistance) is important for the choice of fabrication technological parameters.

Papers

[1] D.T.Blagoeva, J.Opschoor, J.G. van der Laan, C.Sârbu, G.Pintsuk, M.Jong, T.Bakker, P. ten Pierick, H.Nolles, *Development of Tungsten Alloys for DEMO Divertor Applications via MIM Technology*, accepted for publication at Journal of Nuclear Materials, 2012 (ICFRM-15 Special Issue)

Conferences

[1] D.T. Blagoeva, J.B.J Hegeman, M. Jong, J. Opschoor and C. Sârbu, *Development and Characterisation of Reference Tungsten / Tungsten alloys and SiC_f/SiC for DEMO Fusion Applications*, 13th PFMC (Plasma Facing Materials and Components for Fusion Applications) Workshop / 1st FEMaS (Fusion Energy Materials Science) Conference, May 9-13, 2011, Rosenheim, Germany

[2] D.T.Blagoeva, J.Opschoor, J.G. van der Laan, C.Sârbu, G.Pintsuk, M.Jong, C.Bakker, P. ten Pierick, H.Nolles, *Development of Tungsten Alloys for DEMO Divertor Applications via MIM Technology*, 15th Int. Conf On Fusion Reactor Materials, October 16-22, 2011, Charleston, South Carolina, USA (presentation 15-390)

[3] N. Baluc, S.M. Gonzalez de Vicente, S.L. Dudarev, M. Rieth, M. Brocq, R. Coppola, M.A. Auger, J. Degmova, B. Fournier, J. Henry, T. Kruml, F. Legendre, M. Lewandowska, R. Lindau, N. Luzginova, M.F. Maday, P. Olier, B. Radiguet, C. Sârbu, P. Trocellier, P. Unifantowicz and T. Vanstaveren, *Overview of the EFDA Work Programme on ODS RAF Steels,* 15th Int. Conf On Fusion Reactor Materials, October 16-22, 2011, Charleston, South Carolina, USA (presentation 15-098)

Detailed Results

Characterization of pure-W made by PIM for use as a reference material

We had in view the purity of the sintered pure-W made by PIM and the atomic structure of its grain boundaries. The final has a very high density (97%-98%), its microstructure is isotropic, homogeneous and very fine grained (of the order of several μm) and is of high purity in what concerns its grains and its grain boundaries. Our microstructure data have proven that the PIM preparation procedure is successful in the achievement of the desired properties. Fig-1 shows the atomic structure of grain boundaries as observed everywhere in the sintered pure-W. No amorphous phase or segregation of impurities could be revealed.

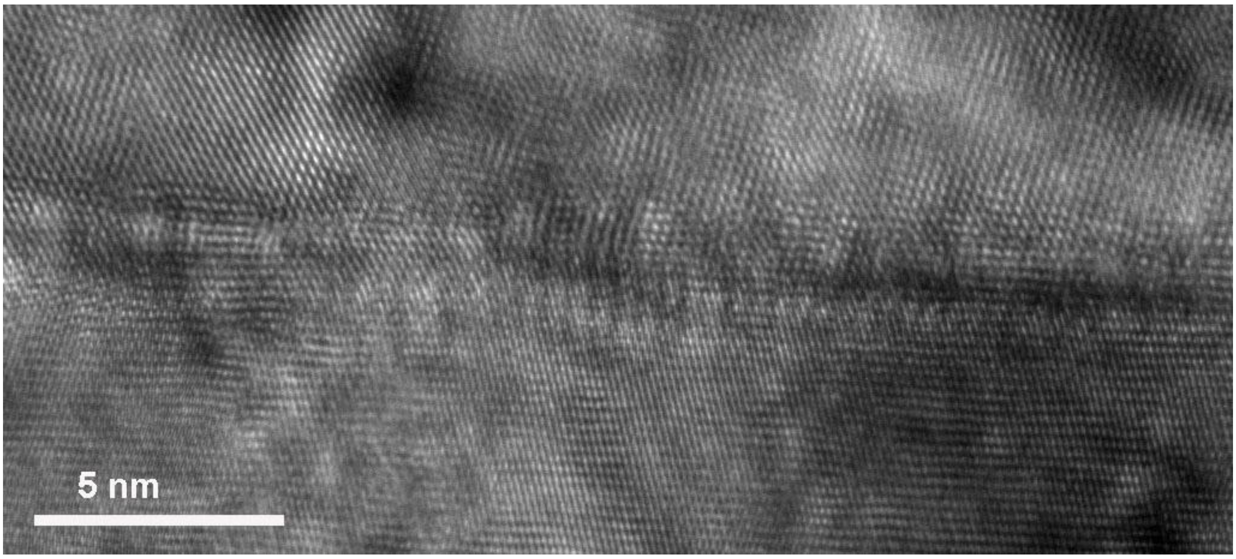

Figure -1

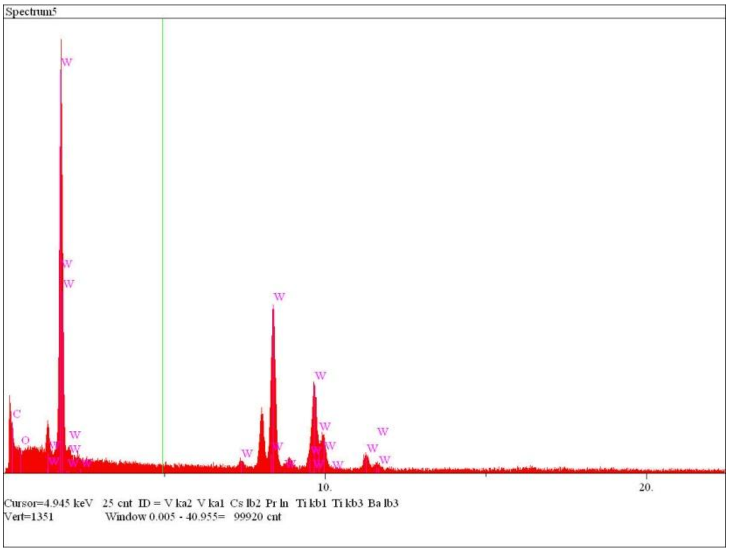

Figure 2

The high purity of the grains in this material was proven by X-EDS measurements done either on different points or by scanning different areas of the sintered material. X-EDS was done in transmission mode, with an analytical TEM working at 200kV by accumulation of a very good statistics of x-ray counting. Practically no impurities were detected by X-EDS analysis. A typical X-EDS spectrum is shown in Fig-2. There is no impurity peaks observed in spectra besides W peaks. C and Cu peaks are always present and are due to the surface contamination of the sample (in case of C) from various sources, mainly during X-EDS spectra accumulation and to the sample contamination during the final operation of ion beam milling (in case of Cu).

Characterization of W+5vol%Ta(powder) alloy made by PIM

The idea of alloying W with 5vol%Ta (which is equivalent to 4.3wt%Ta) was applied in view of improving the mechanical and thermal parameters of the final sintered material, but the expectations were not fulfilled. There was a hope that by alloying W+5vol% the ductility of pure-W can be improved. The experimental measurements done on the final sintered alloy have shown: lower density (up to 92.4%), lowest hardness (303-327 Kg-force/mm^2), lower bending properties (more brittle than pure W under the same conditions) and lower thermal diffusivity (at both RT and high temperatures). It is accepted that this low quality is determined, among others, by the non-homogeneous Ta distribution inside the grains volume and at the interfase surfaces, as revealed by our microanalysis data.

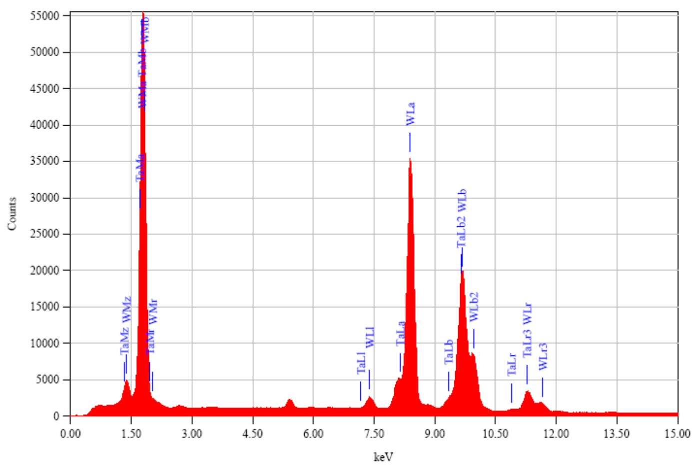

Figure 3 - a typical X-EDS spectrum acquired from many points of the W+5vol%Ta alloy grains.

Table 1

Point of X-EDS spectrum acquisition	Ta(at%)	W(at%)
Point #1	15.66	84.34
#2	28.08	71.93
#3	30.51	69.49
#4	27.65	72.35
#5	27.27	72.73
#6	26.99	73.01
#7	13.72	86.28
#8	19.69	70.61
#9	13.86	86.14

The quantification of X-EDS spectra shows a non-uniform distribution of Ta inside W grains, as can be seen in TABLE-1. The effect on the grain boundaries of the inhomogeneous distribution of Ta in the alloy is confirmed by the HRTEM image shown in Figures 4, where a strong deviation from a perfect arrangement of atoms at the grain boundary becomes obvious by comparison with Fig-1.

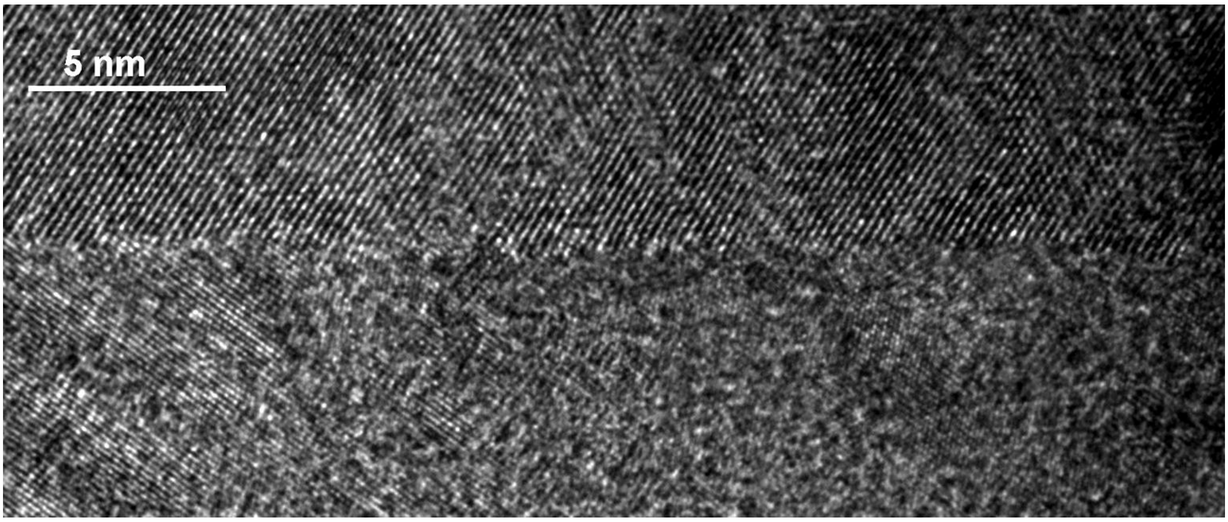

Figure 4

Characterization of the W+10at%Ta(fibre) composite made by SPS at 1.300°C

A previous observation made during cracking tests of the composites W+Ta(fibres) has shown that the presence of fibres has the beneficial effect of stopping the cracks propagation in the W matrix. In that view, it appears to be important the cohesion between the Ta fibre and the W matrix at the contact surface. This is the reason of our investigation of the atomic scale structure of that contact surface. An important result is that shown in Fig-5 and Fig-6 where the presence of an amorphous phase at rectilinear grain boundaries (Fig-5) and at curved grain boundaries (Fig-6).

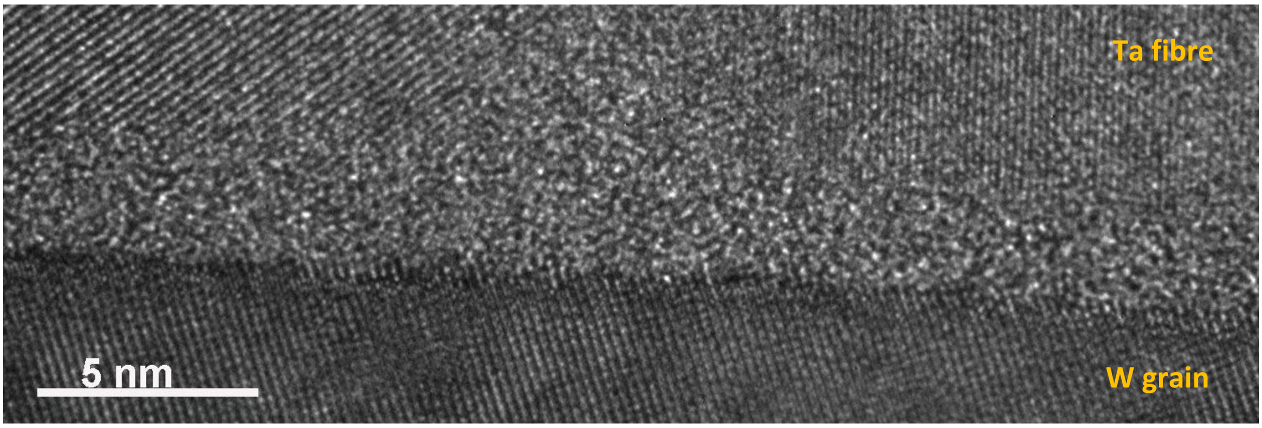

Figure 5

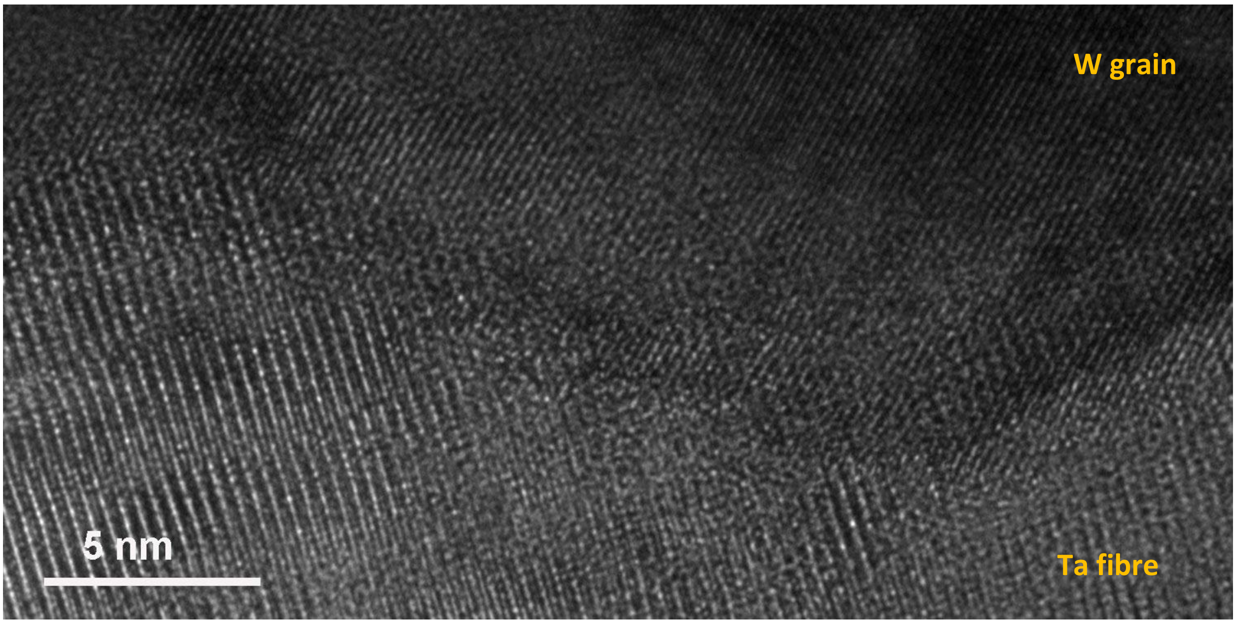

Figure 6

By X-EDS we have measured also the chemical composition of the two components in the W+Ta(fibre) composite and the conclusion was that a massive interdiffusion occurs during sintering between W grains and Ta fibres.

Table 2

Point where measurement was done	at%Ta in W grain	at% W in Ta fibre
point #1 of Ta fibre		30.12
point #2 of Ta fibre		30.85
point #3 of Ta fibre		38.48
point #4 of W grain	0.33	
point #5 of W grain	21.15	
point #6 of W grain	22.66	
point #7 of W grain	22.08	
point #8 of W grain	43.65	

The last observation we made is the existence of amorphous phase in the volume of Ta fibres in the final composite, as shown in Figure-7a, which shows the Ta fibre and the neighbouring W grain, and in Figure-7b, which shows the amorphous phase contained inside the Ta fibre. This amorphous phase could play an important role in determining the mechanical properties of the composite. It is not known whether it is a pre-existing phase in the initial fibers, or it is resulting either from the mechanical alloying process or from the sintering by SPS.

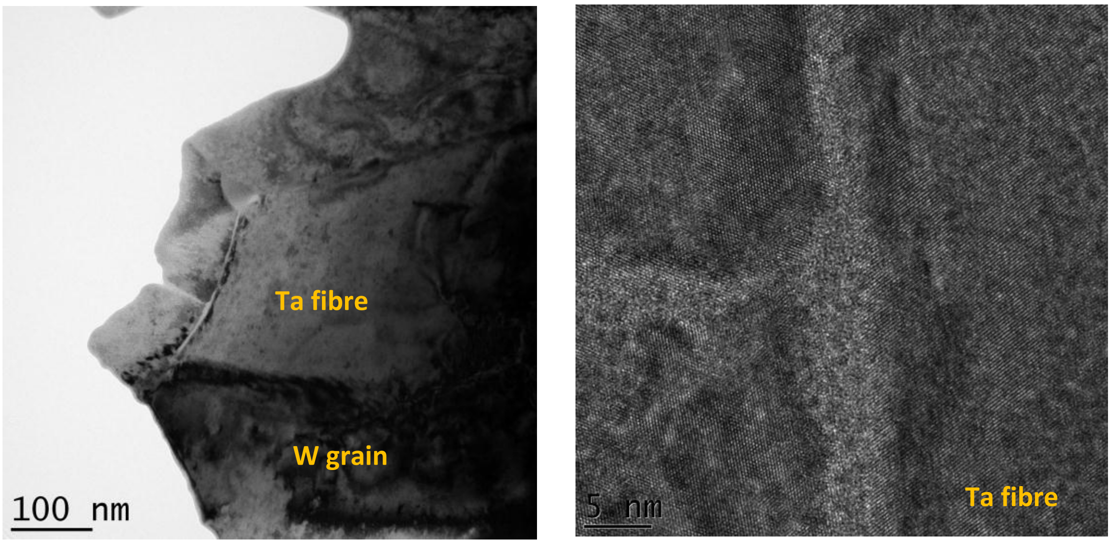

Figure-7

Conclusions

1. The pure W made by PIM has microstructural and microcomposition characteristics which explain the very good properties of the sintered material. It can be recommended for use as a reference. It seems that the only work to be done in the future is for the improvement of density, which is already very high (of 97-98%).
2. The W+5vol%Ta(powder) alloy, made by PIM, has to be abandoned because of its worse properties as compared with pure W. Our microstructural and microcomposition data can partly explain the decline of mechanical and thermal properties.
3. The W+5at%Ta(fibres) composite is a promising material in view of the improvement of the behaviour to cracking, but its microstructural and microcomposition details are revealing the necessity of improvements in what concerns (a) stopping of massive interphase diffusion of Ta and W and (b) hindering the formation of the amorphous phase at the boundaries between Ta(fibre) and W(grains). The existence of an amorphous phase in the volume of Ta fibres is also of concern.

Acknowledgements

The reported work includes contributions from the following people outside the EUATOM-MEdC Association and we acknowledge the very good collaboration with Dr. Darina Blagoeva (EURATOM – NRG Association, FOM, Petten, Holland) and Professor Jose Brito-Correia (EURATOM - IPS Association, Instituto Superior Tecnico, Lisbon, Portugal), who were the producers of the materials whose microstructure is reported here.

Participation at JET Enhancement and Experimental Program

DEUTERIUM AND HELIUM RETENTION IN W COATINGS

C. Ruset, E. Grigore, I. Munteanu, M. Gherendi

National Institute for Laser, Plasma and Radiation Physics, Bucharest, Romania,

Euratom-MEdC Association

Abstract

The W coatings deposited by Combined Magnetron Sputtering and Ion Implantation (CMSII) on CFC and fine grain graphite tiles for JET and ASDEX Upgrade have been extensively investigated from the thermo-mechanically point of view, since the integrity of the coatings during the tokamak operation was the most important aspects for the first wall.

At the same time the new metallic wall should provide a lower fuel retention rate in comparison with the carbon wall. The deuterium retention rate for bulk W is already known, but the ITER-like wall contains about 1300 CFC tiles coated with 10-15 μm and 20-25 μm of tungsten. The D retention rate for W coatings was investigated in this project. MEdC produced a large number of samples (64 Off), made of various materials (CFC, fine grain graphite, eurofer) and coated with different W thicknesses under different conditions.

First experiments carried out at IPP Garching indicated that the D retention of CMSII W coatings is higher that that of bulk W sometimes up to an order of magnitude. This might be associated with the nano-structure of the layer.

<u>Papers:</u>

- B. Zajec, V. Nemanic, C. Ruset, Hydrogen diffusive transport parameters in W coating for fusion applications, Journal of Nuclear Materials 412 (2011) 116-122

- P. Paris, M. Aints, A. Hakola, M. Kiisk, J. Kolehmainen, M. Laan, J. Likonen, C. Ruset, K. Sugiyama, S. Tervakangas, Determination of elemental depth profiles by multi-spot averaging technique of LIBS spectra, Fusion Engineering and Design, (2011), doi: 10.1016/j.fusengdes. 2011.01.117

<u>Reports:</u>

C. Ruset, O. Ogorodnikova, Deuterium and helium retention in W coatings, PWI annual meeeting 28-30 Nov 2012, Garching, Germany

<u>Presentations:</u>

C. Ruset, Deuterium and helium interaction with W coatings used as plasma-facing materials, SEWG meeting on Fuel Retention, 20-22 June 2011, Garching, Germany

1. Background

Combined Magnetron Sputtering and Ion Implantation (CMSII) deposition technology developed at MEdC was used to coat about 2,000 CFC tiles for the ITER-like Wall project at JET and about 1,000 Fine Grain Graphite (FGG) tiles for ASDEX Upgrade. The W coatings have a nano-crystalline structure and a thickness in the range of 10-15 μm or 20-25 μm. Although CMSII technology is applied at industrial scale in the field of PFC (Plasma Facing Components), there is no information so far concerning the deuterium retention for this type of coating. From this point of view an investigation on the influence of the coating structure and thickness on the D retention was necessary. D retention strongly depends on the microstructure of the coating and substrate. Investigation of D retention in different W coatings on carbon-based substrate and on Eurofer substrate helps to understand the influence of substrate, of the coating thickness and its quality on D retention and to minimize the amount of retained D.

On the other hand, He seeding into the D plasma could strongly change the D retention as well as properties of the W coating. This effect needs also to be studied.

The work was carried out in co-operation between two Euratom Associations as follows:

- MEdC: providing the W coatings characterized from the point of view of thickness and impurities.

- IPP: exposure of the W coatings to D plasma and He seeded D plasma and then analysis of the D retention in the coatings exposed to the plasma.

In cooperation with the Slovenian Euratom Association the H penetration through the W coatings produced by CMSII was investigated.

Another fruitful cooperation was with the Estonian Euratom Association (TARTU). They developed a LIBS technique to investigate the depth profiles of the elements across the surface coatings. Initially it was tested on W coatings deposited on carbon and Ti substrates, but the purpose is to be used for depth profiling of deuterium.

2. Objective of the project

Specific objective for MEdC was to provide W coated CFC samples for fuel retention measurements. The samples were characterized in terms of thickness and impurity concentration. The results concerning the D retention were discussed together with the IPP partners.

3. Experimental results

A number of 64 CFC, FGG and Eurofer samples of different dimensions were coated with W/Mo layers of various thicknesses. A detailed specification for these coatings is given in Table 1.

Table 1 The list of W coatings deposited by CMSII on various substrates to be used for D retention studies

No.	Identification	Coating Run	Coating thickness	Substrate / Orientation of the coating
			Lot 1	
1	IU-279-1	IU-279	10.4-12.5 μm	CFC, perpendicular to fibres
2	IU-279-2	IU-279	10.4-12.5 μm	CFC, perpendicular to fibres
3	IU-279-3	IU-279	10.4-12.5 μm	CFC, perpendicular to fibres
4	IU-279-4	IU-279	10.4-12.5 μm	CFC, perpendicular to fibres
5	IU-279-5	IU-279	10.4-12.5 μm	FGG
6	IU-279-6	IU-279	10.4-12.5 μm	FGG
7	IU-279-7	IU-279	10.4-12.5 μm	CFC, parallel to fibres
8	IU-279-8	IU-279	10.4-12.5 μm	CFC, parallel to fibres
9	IU-279-9	IU-279	10.4-12.5 μm	CFC, parallel to fibres
			Lot 2	
10	IU-295-10	IU-295	21.0-21.9 μm	CFC 25x66x5 mm, perpendicular to fibres
11	IU-295-11	IU-295	21.0-21.9 μm	CFC 37x72x2.5 mm, parallel to fibres
12	IU-295-12	IU-295	21.0-21.9 μm	CFC 42x72x2.5 mm, parallel to fibres
13	IU-295-13	IU-295	21.0-21.9 μm	FGG 19x41x2.5 mm
14	IU-295-14	IU-295	21.0-21.9 μm	CFC 25x66x5 mm, perpendicular to fibres
15	IU-295-15	IU-295	21.0-21.9 μm	CFC 25x34x5 mm, perpendicular to fibres
16	IU-295-16	IU-295	21.0-21.9 μm	FGG 19x41x1.2 mm
			Lot 3	
17	IU-313-11	IU-313	10.2-12.5 μm	FGG 14x12x1.0 mm
18	IU-313-12	IU-313	10.2-12.5 μm	FGG 14x12x1.0 mm

19	IU-313-13	IU-313	10.2-12.5 μm	FGG 14x12x1.0 mm
20	IU-313-16	IU-313	10.2-12.5 μm	FGG 14x12x1.0 mm
21	IU-313-17	IU-313	10.2-12.5 μm	FGG 14x12x1.0 mm
22	IU-313-18	IU-313	10.2-12.5 μm	FGG 14x12x1.0 mm
23	IU-313-21	IU-313	10.2-12.5 μm	FGG 14x12x1.0 mm
24	IU-313-22	IU-313	10.2-12.5 μm	FGG 14x12x1.0 mm
25	IU-313-23	IU-313	10.2-12.5 μm	FGG 14x12x1.0 mm
26	IU-313-24	IU-313	10.2-12.5 μm	FGG 14x12x1.0 mm
27	IU-313-5	IU-313	10.2-12.5 μm	Eurofer 14x12x0.5 mm
28	IU-313-6	IU-313	10.2-12.5 μm	Eurofer 14x12x0.5 mm
29	IU-313-7	IU-313	10.2-12.5 μm	Eurofer 14x12x0.5 mm
30	IU-313-8	IU-313	10.2-12.5 μm	Eurofer 14x12x0.5 mm
31	IU-313-9	IU-313	10.2-12.5 μm	Eurofer 14x12x0.5 mm
			Lot 4	
32 33 34	IU-314-5 IU-314-6 IU-314-7	IU-314	5.5-6.5 μm	FGG 14x12x1.0 mm
35 36 37 38	IU-314-8 IU-314-9 IU-314-10 IU-314-11	IU-314	5.5-6.5 μm	FGG 14x12x1.0 mm
39 40 41 42	IU-314-15 IU-314-16 IU-314-18 IU-314-19	IU-314	5.5-6.5 μm	FGG 14x12x1.0 mm

43	IU-314-22	IU-314	5.5-6.5 μm	Eurofer 14x12x0.5 mm
44	IU-314-23			
45	IU-314-24			
46	IU-314-25			
47	IU-315-2	IU-315	36.0-37.2 μm	FGG 14x12x1.0 mm
48	IU-315-3			
49	IU-315-4			
50	IU-315-5			
51	IU-315-15	IU-315	36.0-37.2 μm	FGG 14x12x1.0 mm
52	IU-315-16			
53	IU-315-17			
54	IU-315-18			
55	IU-315-29	IU-315	36.0-37.2 μm	FGG 14x12x1.0 mm
56	IU-315-30			
57	IU-315-24	IU-315	36.0-37.2 μm	Eurofer 15x12x1.0 mm
58	IU-315-26			
59	IU-315-27			
60	IU-315-8	IU-315	36.0-37.2 μm	Eurofer 15x12x1.0 mm
61	IU-315-10			
62	IU-315-11			
63	IU-315-12			
64	IU-315-37	IU-315	36.0-37.2 μm	Eurofer 15x12x1.0 mm

In addition to these samples a number of seven not coated samples of CFC, FGG and Eurofer have been sent to IPP Garching as reference.

Using these samples the D retention can be investigated from the following points of view:

- the influence of W coating thickness

- the influence of substrate (material and thickness)
- the influence of the coating orientation with respect to the carbon fibers (for CFC)
- D retention at the Mo/W interface
- the influence of the He concentration into a D+He plasma

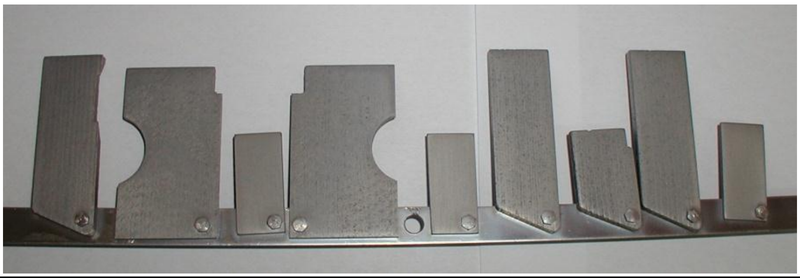
(CFC)

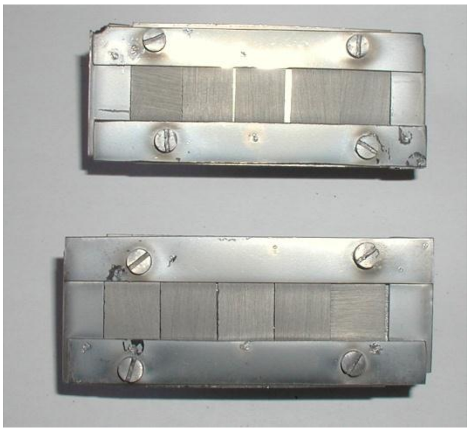
(FGG)

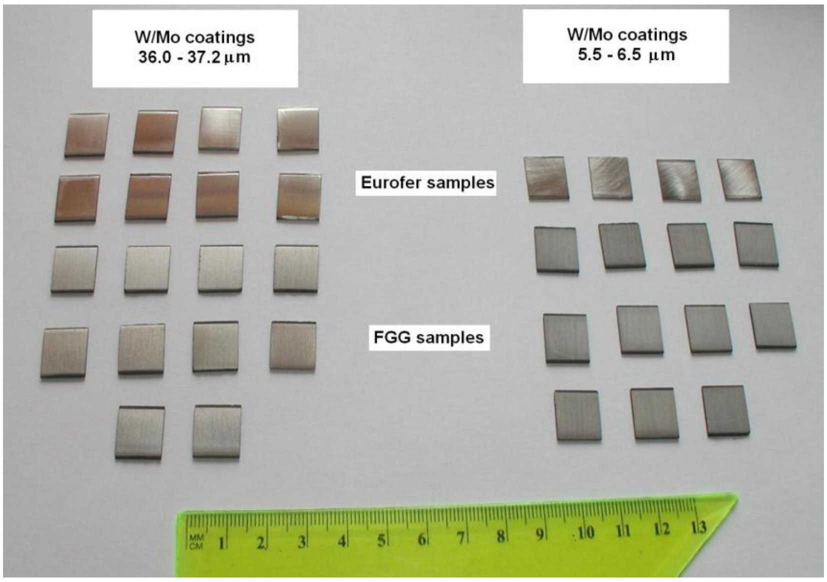

Figure 1 - Tungsten coated samples used for D retention

In order to coat these samples special devices have been manufactured. Special attention was paid to small samples (12 x 14 mm). They have been hold in a frame in such a manner that an area of 12 x

13 mm was coated for each sample. A few samples used for D retention experiments are shown in Fig. 1. The thickness of W coating and Mo interlayer have been determined by GDOS (Glow Discharge Optical Spectrometry) on Ti witness samples coated in the same runs as the carbon and Eurofer samples. Two examples of GDOS profiles for W, Mo, C, O and Ti are can be seen in Fig.2. It is impressive the W coating of 37 µm shown in Fig.3a. The internal stress is quite high. A Ti sample 30 x 25 mm with a thickness of 2.5 mm was bent by this stress with 0.5 mm. This bending can be seen in Fig.3b. It should be noted that the coating was not delaminated.

In the first experiments carried out at IPP Garching the W coatings were exposed to an ECR plasma at a D flux of $2.2\cdot10^{25}$ D/m^2. The D retention was about $3\cdot10^{21}$ D/m^2 while for the bulk polycrystalline W samples exposed in the same conditions the D retention was ~ $3\cdot10^{20}$ D/m^2. It appears that the coating structure is a key factor for the fuel retention. On the other hand this structure is crucial for the very good performance in terms of thermo-mechanical properties. At the moment it is not clear how to reduce the D retention within the W coating preserving its thermo-mechanical properties. More investigations are necessary to be carried out on this subject.

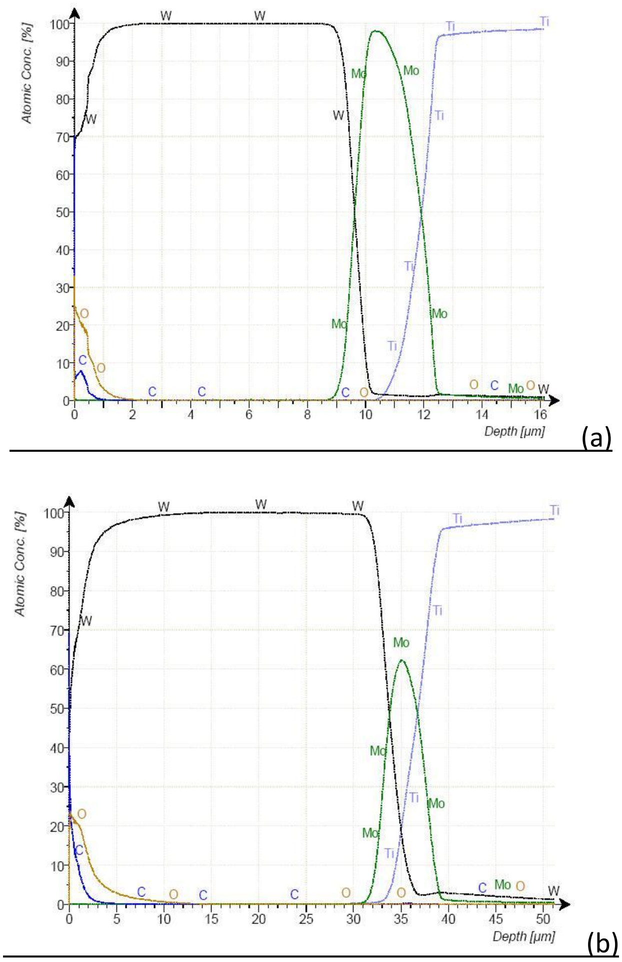

Figure 2 - GDOS depth profiles for W coatings of 12 µm (a) and 37µm (b) deposited by CMSII

The D retention was correlated with the H permeation of the W coatings. The experiments carried out at Jozef Stefan, Institute, Ljubljana, Slovenia proved that the W coating allows penetration of the

H, but significant slower than Eurofer. The results are consistent with those obtained at IPP Garching.

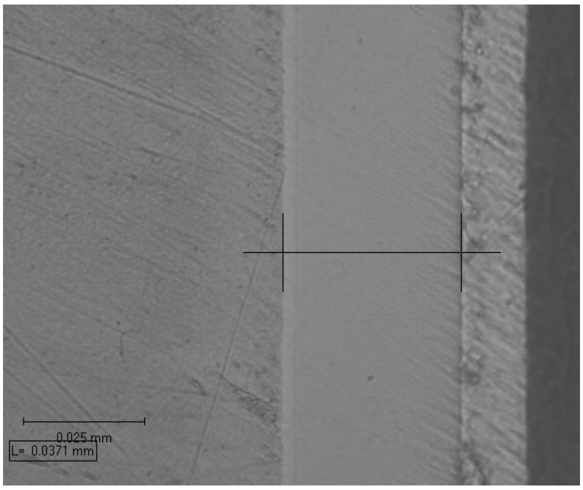

(a)

(b)

Figure 3 - Micrograph of the W coating of 37 μm (a) and of the Ti sample coated with 37 μm (b)

Conclusion

A large number of CFC, FGG and Eurofer samples have been coated with W layers under different experimental conditions and have been sent to IPP for measurement of the D retention.

The first experiments indicated a larger D retention than bulk W.

Acknowledgement

The reported work includes contributions from the following people outside the EUATOM-MEdC Association: Olga Odgorodnikova (Max-Plank Institut für Plasma Physik, Euratom Association, Garching, Germany), Bojan Zajec and Vincenc Nemani (Jozef Stefan, Institute, Ljubljana, Slovenia), Matti Laan (Estonian Euratom Association)

THE LIMITS OF THE W COATINGS DEPOSITED ON CFC TILES FOR THE ITER-LIKE WALL AT JET

C. Ruset, E. Grigore, I. Munteanu, M. Gherendi

National Institute for Laser, Plasma and Radiation Physics, Bucharest, Romania,

Euratom-MEdC Association

Abstract

During the exploitation of the ITER-like wall at JET the W coatings will be subjected to thousands of pulses. In order to evaluate behaviour of the W coatings to a cyclic thermal loading relevant for JET operation, HHF tests have been carried out with a an electron beam facility at peak temperatures of 1,250 °C and 1,450 °C. The power density was about 6 MW/m^2 and the pulse duration 24 s. Coatings with a thickness of 10 μm and 20 μm have been tested up to 3,400 pulses. Optical inspections of the W layer were performed periodically with a stereomicroscope by interrupting the test. At high number of pulses these inspections revealed small delaminations with the size of 50-400 μm. The delaminated area was measured at each inspection and the ratio between this area and the total thermal loaded area was calculated. At the test temperature of 1,250 °C, this ratio was about 1% for 20 μm thickness and only 0.2% for 10 μm thickness at the end of the tests. By increasing the testing temperature to 1,450 °C the percentage of the delaminated area increased to about 6% for 20 μm W coating and 1.2% for 10 μm W coating. The damage of the W coatings deposited on CFC substrate occurs by buckling and it increases gradually with the number of the heating pulses.

The dependence of the delamiantion percentage on the number of pulses can be seen as a degradation curve for each particular W coating. Using these curves the thermo-mechanical properties of the W coatings deposited on carbon based materials can be characterized quantitatively.

Thermal fatigue and mainly carbidization of the tungsten due to the diffusion of the carbon from the substrate have been recognized as mechanisms for degradation of the coatings during the thermal loading at high temperatures.

Papers:

- C. Ruset, E. Grigore, H. Maier, R. Neu, H. Greuner, M. Mayer, G. Matthews, Development of W coatings for fusion applications, Fusion Engineering and Design 86 (2011) 1677–1680

- H. Maier , M. Rasinski , E. Grigore , C. Ruset , H. Greuner , B. Böswirth , G.F. Matthews , M. Balden ,S. Lindig, JET-EFDA, Performance of W coatings on CFC with respect to carbide formation, Journal of Nuclear Materials, 415 (2011), S310-S312

Conferences:

- C. Thomser, S. Brezinsek, J. Coenen, H. Greuner, T. Hirai, J. Linke, G. Matthews, H. Maier, Ph. Mertens, R. Neu, V. Riccardo, A. Schmidt, V. Philipps, M. Rubel, C. Ruset, I.Uytdenhouwen, Materials for the JET ITER-like wall, 15th International Conference on Fusion Reactor Materials, October, 16-22, 2010, Charleston, South Carolina, USA.

Reports:

- The limits of W coatings deposited on CFC tiles for the ITER-like wall at JET, Preliminary report, 02.09.2011.

Presentations:

- C. Ruset, H. Maier, H. The limits of W coatings deposited on CFC tiles for the ITER-like wall at JET, Maier, Task Force FT-1st SAM Meeting, 14-16 June, 2011, JET, Culham, UK

- C. Ruset, E. Grigore, I. Munteanu, M. Gherendi, The limits of W coatings deposited on CFC tiles for the ITER-like wall at JET, Task Force FT-2nd SAM Meeting, 12-14 December, 2011, JET, Culham, UK

1. Background

Combined Magnetron Sputtering and Ion Implantation (CMSII) technology was applied for W coating of about 1,800 CFC tiles for the ITER-like Wall (ILW) project at JET [1, 2, 3]. In the R&D phase of this project, due to the time schedule, only limited tests have been carried out on these coatings. Thermo-mechanical properties were investigated in the ion beam test facility GLADIS at IPP Garching at the following parameters:

- Thermal screening up to 23 MW/m^2 – 1.5 s and
- Cycling thermal fatigue at 10.5 MW/m^2 – 5 s – 300 pulses

The coatings survived these tests without delaminations [4], but the actual limits of the coatings were not investigated. This is extremely important for the exploitation of the new JET wall. A correlation between the coating surface temperature, plasma pulse duration and number of pulses had to be established.

Recently the W carbidization into the coating due to the carbon diffusion from the substrate started to be investigated [5]. This phenomenon might be a significant factor in limiting the W coating lifetime. Thermal fatigue is another factor which could affect the service lifetime of the W coatings. They have been tested up to 300 cycles, but this is less than 10% of the number of the pulses expected to be applied with the new JET wall.

Consequently, an investigation of the phenomena which can determine the W coatings lifetime is necessary. As a result of this investigation, a prediction of their lifetime for various loading conditions is expected to be made.

2. Objective of the project

The goal of the project is to investigate the influence of carbidization and cycling thermal fatigue on the lifetime of the W coatings deposited on CFC. A correlation between the coating surface temperature, pulse duration and number of pulses until failure has to be established.

3. Experimental results

<u>3.1. The method used for W coating testing</u>

W coated samples were heated by an electron beam and cooled down below the ductile to brittle transition temperature (DBTT), which means about 200 °C.

The maximum power of the electron beam is 1.5 kW, but in this experiment only 1.0 ± 0.1 kW was used. The accelerating voltage is ~ 14 kV and the beam current 70-100 mA.

The profile of the electron beam is an ellipse with the big axe 18 mm and the small axe 12 mm. The beam area is ~ 170 mm^2. This profile is determined by the filament geometry and the focusing magnetic field.

3.2. W coated samples and experimental setup

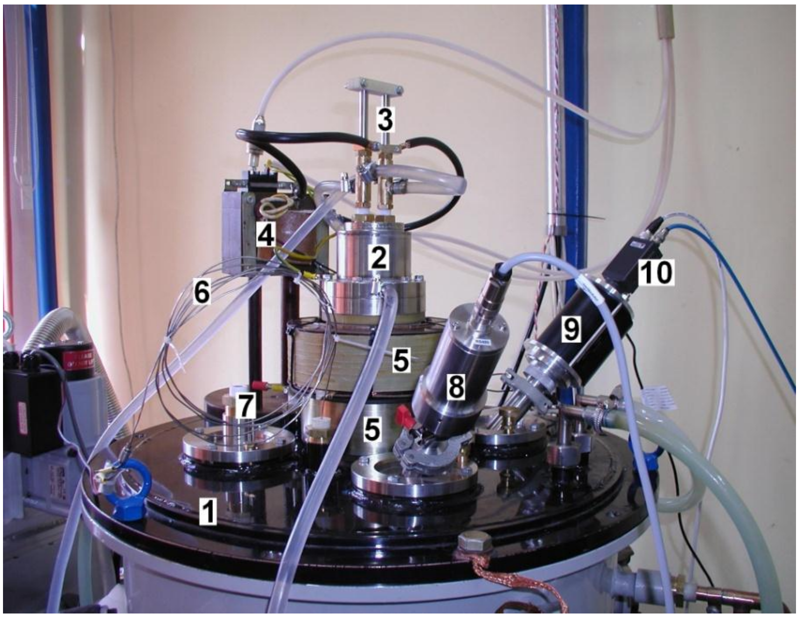

Figure 1 - Top lid of the vacuum chamber of the HTTF; 1. Top lid, 2. Cathode chamber, 3. Filament support; 4. Transformer for filament supply, 5. Focusing magnetic coils, 6. Thermocouple, 7. Sample support, 8. Pyrometer; 9. Motorized lens; 10. IR Hitachi CCD camera

The electron gun, the diagnostics and the support for the sample to be tested are installed on the top lid of the vacuum chamber (Φ540 x 640 mm). An image of the top lid is shown in Fig. 1.

The electron gun contains a double spiral filament made of W with a diameter of 1.3 mm and the accelerating electrodes. The electron beam is focused by a magnetic coil that drives the beam to the testing sample. The samples used for this experiment have the dimensions of 30 x 30 x 6 mm. They are coated on the surface 30 x 30 mm with standard W/Mo layer with the thickness 20-25 µm or 10-15 µm.

The experimental arrangement is shown in Fig. 2. The sample is positioned above a water cooled Cu support by means of a spring system.A very fine graphite powder layer ensures a good thermal contact between CFC sample and Cu support. The water flow rate was ~ 2 l/min. At 2.5 mm below surface a C type thermocouple (W5%Re/W26%Re) is inserted till the middle of the sample. A set of five stainless steel shields are used to protect the thermocouple connector from the heat coming from the sample. The maximum acceptable temperature of the connector is 100 °C. This is to avoid the calibration error of the thermocouple. The sample is centered on the axis of the testing camera. The electron beam is coming from the top lid along the camera axis.

3.3. Diagnostics

The surface temperature is monitored by an IMPAC IGA-5 pyrometer which is sensitive in the wavelength range 1.45…1.8 µm. The temperature was measured approximately in the middle of the W coating as it is shown in Fig.2 by the small red spot produced by the laser incorporated in the pyrometer. A Hitachi KP-M1AP video camera with a bandpass filter of 10 nm centered on 1064 nm was also used to monitor the heated W coating. The temperature in the CFC at 2.5 mm below the surface is monitored with a thermocouple (W5%Re/W26%Re) with a diameter of 1.5 mm and a length of 150 mm.

<u>3.4. Testing parameters</u>

The testing conditions were as follows:

- Minimum temperature: ~ 200 °C

- Maximum surface temperature:

In this phase of the experiments the electron beam power (particularly the beam current) was not very well stabilized.

Consequently the peak temperature of the W coating oscillated in the range of ±50°C.

The experiments have been carried out with W coatings of 10-15 μm and 20-25 μm heated at a maximum temperature of 1250±50°C and 1450-±50°C. The time variation of the temperature was measured by the pyrometer. This variation is shown for 5 successive pulses at 1250°C in Fig. 3.

The average duration when the peak temperature exceeded 1200 °C, calculated for 100 successive pulses was 4.8 s. In Fig. 4 this duration is shown for all 100 pulses. The emissivity used for pyrometer software program was set to 0.5.

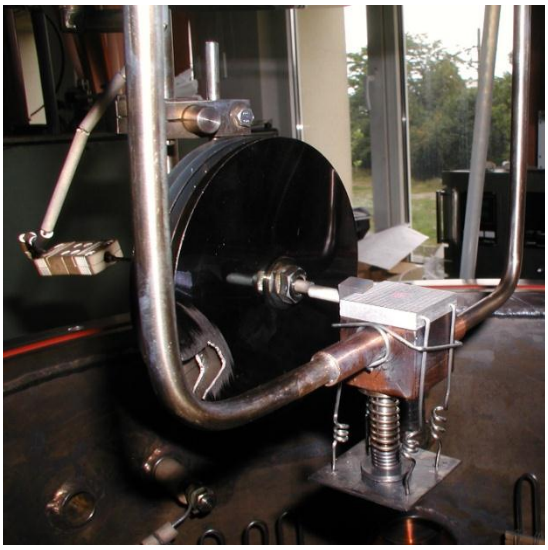

Figure 2 - Experimental setup for testing the W coatings at a large number of pulses

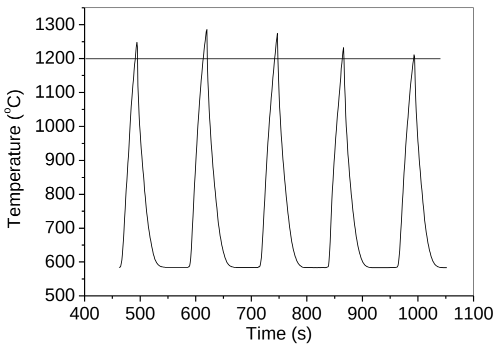

Figure 3 - The time variation of the peak temperature on the W coating during the thermal cycling

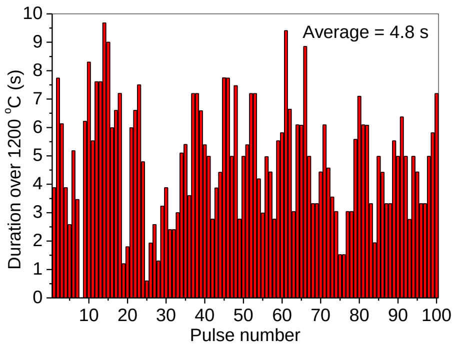

Figure 4 - Duration of the W coating surface temperature over 1,200 °C

This value was calculated from the emissivity measured for W coatings at 1,064 nm in the ACIR Euratom project (0.63) and corrected taking into account the variation of the bulk W emissivity with the wavelength.

The temperature measured with the thermocouple inside the CFC sample was about 1000 °C for the testing temperature of 1250 °C and 1,300 °C for the testing temperature of 1450 °C.

- Estimated electron beam power: ~ 950 - 1050 W

- Accelerating voltage: ~ 14.5 kV

- Estimated beam spot: ellipse with axes 18/12 mm $\Rightarrow$ ~ 170 mm^2

- Estimated power density: ~ 5.8 MW/m^2

- Pulse duration: 24 s;

- Pause between pulses: 60-70 s.

Optical inspections of the W layer were performed periodically with a stereomicroscope by interrupting the test. After each inspection the contact between the Cu cooled support and the back of the sample changes and consequently the cooling conditions change a little bit. The minimum temperature of the sample during the thermal cycling is adjusted by modifying the pause duration.

3.5 Inspection of the W coatings after thermal cycling

The thermal cycling was stopped from time to time and the W coating was inspected with a stereomicroscope with a magnification from 10 to 45. The objective of these inspections was to count the number of the delaminated zones and to estimate their areas. The results are shown in the Table 1. The percent of the delaminated area was calculated by dividing the total estimated damaged area to 170 mm^2 which was estimated to be the electron beam spot area. This can be seen on the sample WCL-02 after 542 pulses or during the heating up period (Figs. 6-7).

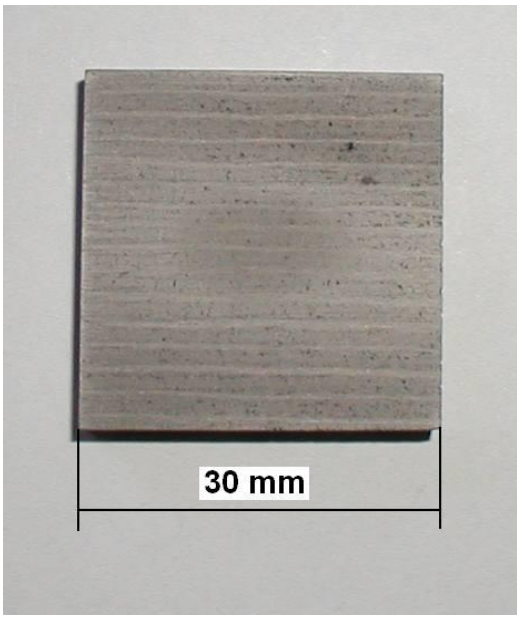

Figure 6 - Electron beam spot image after 542 pulses on W coating of 10 μm

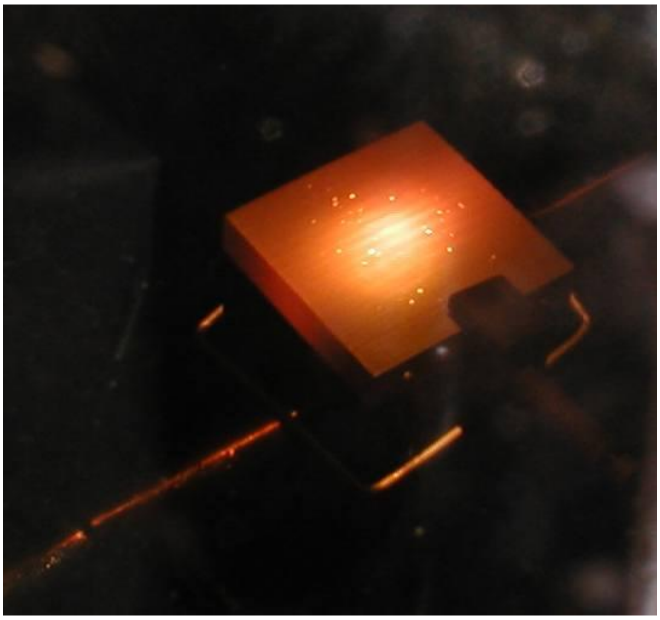

Figure 7 - WCL-02 sample during the heating up period

The graph showing the increase of the damaged area of the W coatings as a result of the thermal cycling tests can be seen in Fig. 8. At the test temperature of 1,250 °C, this ratio was about 1% for 20 μm thickness and only 0.2% for 10 μm thickness at the end of the tests. By increasing the testing temperature to 1,450 °C the percentage of the delaminated area increased to about 6% for 20 μm W coating and 1.2% for 10 μm W coating. The damage of the W coatings deposited on CFC substrate occurs by buckling and it increases gradually with the number of the heating pulses. It is clear that the thinner coatings have a better behavior from the thermo-mechanical point of view than thicker coatings. This might be associated with the heat conduction, through the coating, from the surface to the substrate, but also with the internal stress induced into the coating during its growth. The dependence of the delamiantion percentage on the number of pulses can be seen as a degradation curve for each particular W coating. Using these curves the thermo-mechanical properties of the W coatings deposited on carbon based materials can be characterized quantitatively.

Table 1. W coatings limits for peak temperatures of 1,250 °C and 1,450 °C

Sample / W coating thickness	Number of pulses	Number of delaminated areas	Total estimated delaminated area	
			(mm^2)	Percent of the thermal loaded area
WCL-01 / 20 μm	400	0	0	0 %
T=1250±50	743	4	0.3	0.17 %
	1.423	13	0.63	0.37 %
	2.175	22	1.34	0.79 %

	3.100	56	1.7	1.0 %
WCL-02 / 10 μm	542	0	0	0 %
T=1250±50	1.489	1	0.04	0.023 %
	2.364	5	0.28	0.16 %
	3.380	12	0.34	0.2 %
WCL-03 / 20 μm	495	3	0.41	0.24 %
T=1450±50	1425	39	2.077	1.22 %
	2325	49	3.51	2.0 %
	3230	86	10.33	6.1 %
WCL-03 / 10 μm	510	9	0.265	0.15 %
T=1450±50	1555	15	1.065	0.62 %
	2580	21	1.26	0.74 %
	3300	29	3.07	1.8 %

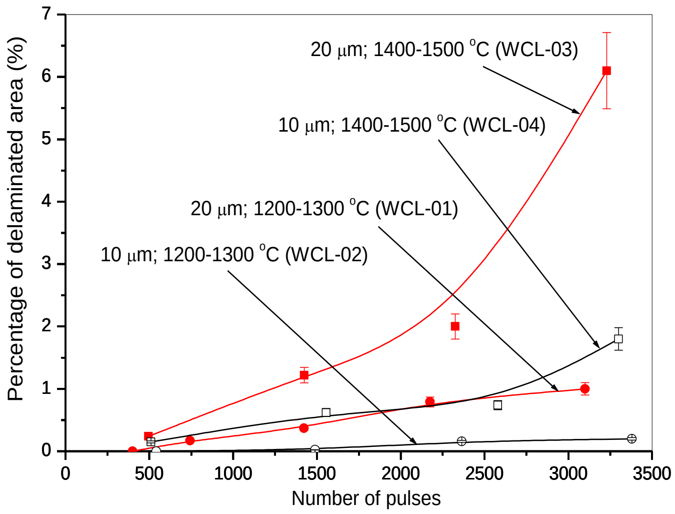

Figure 8 - Damage of the W coatings deposited on CFC by thermal cycling at a peak temperature of 1200-1300 ℃

A few pictures and micrographs of the sample WCL-01 after 3,100 pulses are shown in Figs. 9-10. The delaminations appear as buckling with usual size of 50-400 µm. Sometimes the coating is detached from the CFC and remains under a certain angle with the surface. By loosing the contact with the substrate these small detached coatings become much hotter than the normal coating during the electron pulse, but the melting temperature has not reached yet. It appears that the power density was not enough for melting.

No damage has been detected outside the beam spot area where the temperature is supposed to be by 100 – 200 °C lower. This means that the coating could survive without problems to 3,000 pulses at a temperature below 1,000 °C.

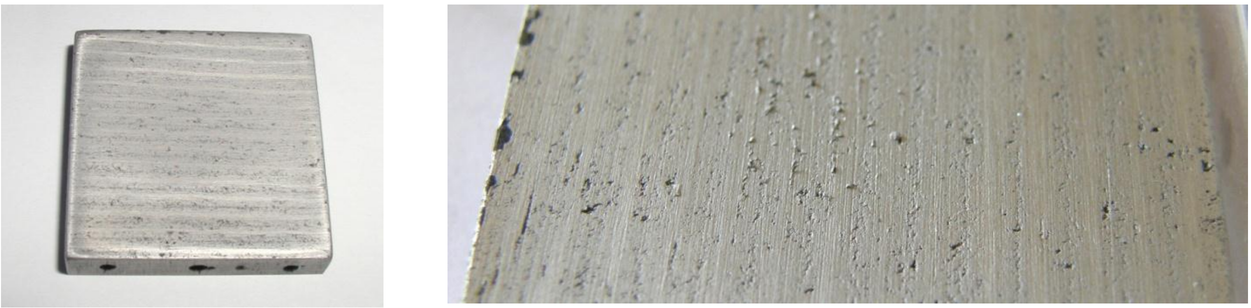

Figure 9 - W coating on sample WCL-01 (20 μm) after 3,100 pulses

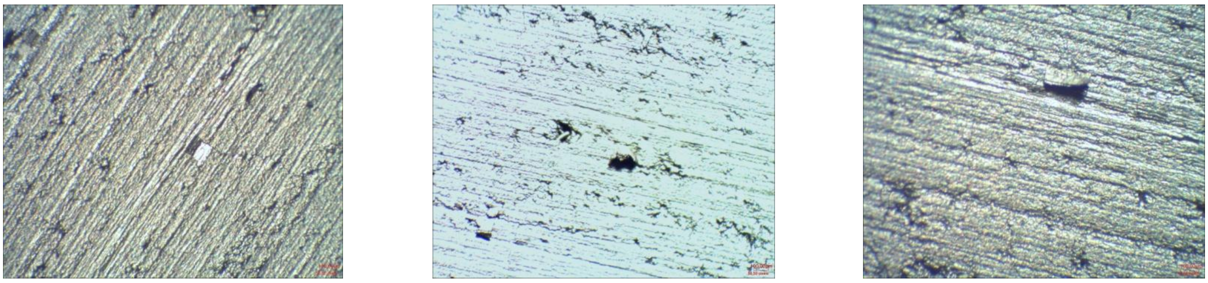

Figure 10 - Typical micrographs of small delaminations produced on W coating (sample WCL-01) after 3,100 pulses

Conclusion

- The damage of the W coatings deposited on CFC substrate occurs gradually with increasing the number of the heating pulses.

- 10 μm and 20 μm W coatings have been tested with 3,380 pulses and 3,100 pulses respectively at a temperature between 1,200 °C and 1,300 °C. The pulse duration was 24 s and the power density ~ 6 MW/m^2. Under these conditions the total delaminated area of the W coating of 20 μm was about 1 % of the thermal loaded area while for coating of 10 μm this percentage was about 0.2 % only. By increasing the testing temperature to 1,400-1,500 °C the percentage of the delaminated area increased to about 6% for 20 μm W coating and 1.2% for 10 μm W coating for a similar number of heating pulses.

- It is clear that the thinner coatings have a better behaviour from the thermo-mechanical point of view than thicker coatings.

- The damage of the W coatings occurs by buckling with the size of delaminated zones in the range of 50-400 μm.

Acknowledgement

The reported work includes contributions from the following people outside the EUATOM-MEdC Association: Hans Maier (Max-Plank Institut für Plasma Physik, Euratom Association, Garching, Germany), G. Matthews (CCFE, Euratom Association, Abingdon, UK)

References

[1] C. Ruset, E. Grigore, I. Munteanu, H. Maier, H. Greuner, C. Hopf, V. Philipps, G. Matthews, JET-EFDA Contributors JET-EFDA, Fusion Engineering and Design **84,** 1662–1665 (2009)

[2] H. Maier, R. Neu, H. Greuner, B. Böswirth, M. Balden, S. Lindig, G. F. Matthews, M. Rasinski, P. Wienhold and A.Wiltner, Phys. Scr. T138 (2009)

[3] C. Ruset, E. Grigore, H. Maier, R. Neu, H. Greuner, M. Mayer, G. Matthews, Fusion Engineering and Design 86 (2011) 1677–1680

[4] H. Maier, Final Report on Test Results of Tungsten Coatings on CFC for the JET ITER-like Wall Project., August 11, 2006, EFDA Task Agreement JW5-TA-EP-BEW-02

[5] H. Maier, M. Rasinski, E. Grigore, C. Ruset, H. Greuner, B. Böswirth, G.F. Matthews, M. Balden, S. Lindig, and JET-EFDA contributors, Journal of Nuclear Materials, 415 (2011), S310-S312

ADVANCED CALIBRATION OF THE PIW IR CAMERAS

C. Ruset, D. Falie, I. Munteanu, M. Gherendi

National Institute for Laser, Plasma and Radiation Physics, Bucharest, Romania,

Euratom-MEdC Association

Abstract

Protection of the ITER-like wall (PIW) at JET is achieved by a special real-time system including twelve Hitachi type KP-M1AP IR cameras, pyrometers and thermocouples. From the IR images provided by the cameras it is possible to deduce the temperature, but the correct value of the surface emissivity must be known. The W coating of the CFC tiles was carried out by Combined Magnetron Sputtering and Ion Implantation technology at MEdC and the emissivity of this coating is not known. The objective of the present project was to measure this emissivity and to calibrate the Hitachi cameras in order to be used for temperature measurement of the W coating during JET operation.

In this phase of the project special CFC samples were coated with 20 μm of W and heated by an electron beam up to 1200°C. The emissivity was measured during the cooling down process using the light intensities (λ=1064 nm) of the coated surface and of a black body generated by a hole in the CFC sample. A value of 0.63$\pm$0.03 was found. No significant dependence of the emissivity on the temperature in the range of 850-1050 °C or on the viewing angle in the range of 0°-60° were detected.

Reports:

- Advanced Calibration of the PIW IR cameras, Task Agreement code JW10-TA-PIW-ACIR-01, Progress Report, 14.09.2011

Presentations:

- C.Ruset_Advanced calibration for PIW IR-Equipment, Technical meeting at JET, 11.05.2011

- D.Falie_Advanced calibration for PIW IR-Measurements, Technical meeting at JET, 11.05.2011

1. Background

Since August 2011 JET operates with the ITER-like Wall (ILW) containing Be in the main chamber, bulk W (divertor-tile 5) and tungsten coated CFC tiles for the main chamber and divertor (tiles G1, G3, G4, G6, G7 and G8). In contrast with the carbon wall the new metallic wall is more sensitive to the temperature. In order to protect the investment a real-time protection system of the ILW (PIW) was developed and implemented at JET. Protection is based on temperature limits (1200 °C for bulk W and W coatings and 900 °C for Be tiles) and involves twelve IR cameras (Hitachi KP-M1), pyrometers and thermocouples. From the IR images provided by the cameras it is possible to deduce the temperature, but the correct value of the surface emissivity must be known.

2. Objective of the project

The main objective of the project was determination of the W coating emissivity and its dependence on the temperature and the viewing angle. Using these experimental values, the Hitachi KP-M1 video camera had to be calibrated and used for temperature measurement.

3. Experimental results

3.1. The method used for measuring the emissivity of the W coatings

The received power by a pixel of the CCD camera from a heated object at the temperature T is given by the Planck relation:

$$I_P(T) = c_{cal} \cdot \frac{2 \cdot h \cdot c^2 \cdot \Delta\lambda}{\lambda^5 \cdot \left(e^{\frac{h \cdot c}{\lambda \cdot k_B \cdot (T+T_0)}} - 1 \right)} = c_{cal} \cdot \frac{c_1}{e^{\frac{c_2}{(T+T_0)}} - 1} \tag{5}$$

where:

c is the speed of light

h - Plank constant

k_B - Boltzmann constant

λ - wavelength of the emitted radiation (ex.0.950µm)

Δλ - wavelength bandwidth of the IR filter (ex.50 nm)

T_0 =273.15K

The calibration constant (c_{cal}) includes the emissivity of the object's surface at the temperature T.

Elements of the camera's geometry are:

$d_f \approx 150$ mm - distance from the centre of the lenses to the chip of the camera

$d_o \approx 250$ mm - distance from the centre of the lenses to the object

D =20 mm - maximum diameter of the diaphragm (lenses)

A_p= 10µ x 10µ - area of a pixel

A_i = area of the pixel's image on the object

$$A_i = A_p \cdot \left(\frac{d_o}{d_f} \right)^2$$

The attenuation produced by the camera geometry is:

$$a_g = \frac{\pi \cdot A_p}{4} \cdot \left(\frac{D_a}{d_f} \right)^2 \cdot \cos^4(\theta) \tag{6}$$

where θ is the angle between the optical axis of the lenses and a line passing through the pixel and the centre of the lenses. From the intensity level (1…256 levels) recorded with the CCD camera the corresponding temperature is computed. A relation between the temperature and the camera reading is plotted in Fig. 1a. A similar curve can be plotted if the number of detected photons is taken into consideration (Fig.1b).

The emissivity of a CFC W coated sample was measured by taking into account the ratio of radiated power by the coated surface in a bandwidth of 10 nm at a central wavelength of 1064 nm to the radiated power of a black body at the same temperature and conditions.

$$\varepsilon_{coat} = \frac{I_{coat}}{I_{bb}} \tag{7}$$

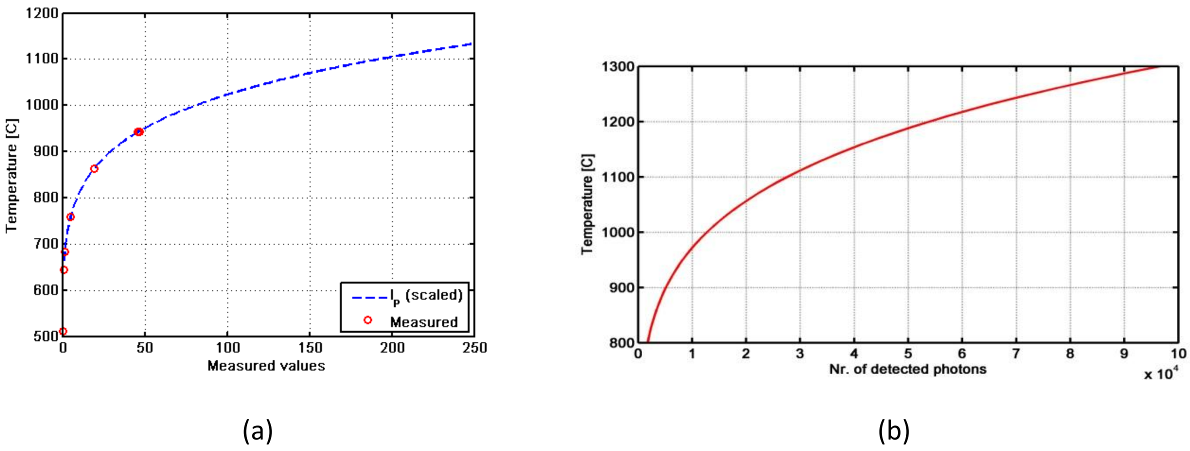

Figure 1 - Computed temperature as a function of camera readings (a) and of number of detected photons (b)

The values of I_{coat} and I_{bb} are computed from the corresponding measured values by subtracting background value I_0 and the scattered light I_s. The background value I_0 is the value recorded by the camera without any light and this can be separately measured. The power radiated by the heated sample accordingly to Eq. (5) is scattered in the vacuum chamber and inside the video camera and a fraction of this radiation (I_s) is detected by each pixel. The value of I_s cannot be directly measured and it will be evaluated from the chamber walls image intensity.

$$I_{coat}=I_{coat\ measured} - I_s - I_0 \quad (4.1)$$

$$I_{bb}=I_{bb\ measured} - I_s - I_0 \quad (4.2)$$

The blackbody was achieved by making a cylindrical cavity in the CFC sample. The emissivity of a cylindrical hole can be computed with Eq. (5) [1-3] where ε_0 is the emissivity of the hole's walls, S_{apert} is the area of the hole aperture and S_{int} is the interior surface of the hole.

$$e_{ref} = \frac{\varepsilon_0}{\varepsilon_0 \cdot \left(1 - \frac{S_{apert}}{S_{\text{int}}}\right) - \frac{S_{apert}}{S_{\text{int}}}} \quad (5)$$

The cylindrical cavity can be considered a black body if its emissivity is higher than 0.99. This happens for a hole drilled in the CFC material if the ratio between the diameter and the depth is higher than 5.

3.2. The samples used for emissivity measurements

One of the samples used for emissivity measurements is shown in Fig. 2. It is a cub with the side of 30 mm. The hole with the diameter of 3 mm can be seen in the centre of the sample. It acts as a black body. On two crossed lines with a width of 3 mm the W coating was removed. A small pin of pure tungsten with a diameter of 6 mm and the length of 6 mm was also inserted in the sample. In this way, on the same surface visualized by the camera there are four different areas: W coating, non-coated CFC, black body and bulk tungsten. The big problem is to get all these areas at the same temperature. This sample is positioned in the centre of the testing camera, rotated at 45°, in such a manner that the Hitachi camera visualizes the testing surface perpendicularly. The thermocouple is introduced in the centre of the sample perpendicularly to the viewing angle. The experimental arrangement is shown in Fig. 3. The sample is heated by an electron beam with a diameter of ~ 15 mm coming from the top, along with the camera axis. During the heating up period it is focused in a certain area of the sample. That zone is significant hotter than other adjacent areas. This regime is not adequate for measurement of emissivity. **The best regime was during the cooling of the sample with the electron beam off.** Due to the high thermal conductivity of the CFC, after about 40 s, the surface temperature of the sample is quite uniform within an error of ± 5°C. The experiments were carried out in the following manner: (i) Heating the sample up to 1,200-1,240 °C (temperature measured with the thermocouple inserted in the middle of the sample) and with the pyrometer. (ii) Keep this temperature for ~ 60 s by reducing the electron beam power. The temperatures measured with the thermocouple and pyrometer are in good agreement. (iii) Switch the electron beam off. The temperature and the image from the camera are recording continuously. The temperature drops to ~ 750 °C in about 200 s from the moment when the electron beam was switched off.

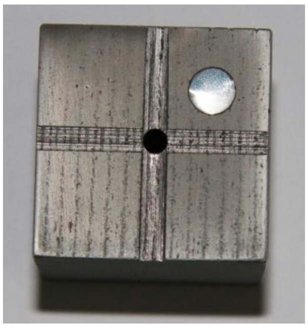

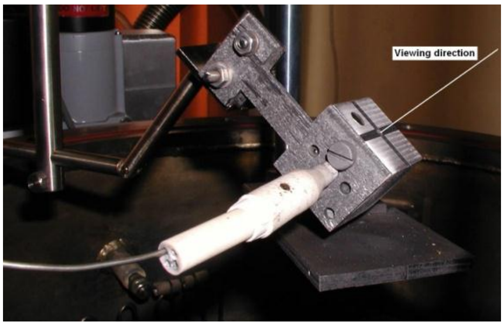

Figure 2 - W coated cub CFC sample

Figure 3 - Experimental arrangement for measurement of surface emissivity

A typical IR image recorded by the Hitachi camera is shown in Fig. 4. The intensity of the image in the selected regions (small squares shown in Fig.4) where used to compute the emissivity of tungsten, CFC and W coated CFC.

In order to investigate the influence of the viewing angle on the W coating emissivity a special CFC sample was designed, manufactured and coated with 20 μm of tungsten. It is shown in Fig.5. The sample is a sort of square pyramid with a base of 30 x 30 mm which exposes to the camera 5 surfaces orientated at 0°, 15°, 30°, 45° and 60° with respect to a surface perpendicular to the viewing angle of the Hitachi camera. In this way the images of the W coatings with various orientations to the camera are recorded simultaneously.

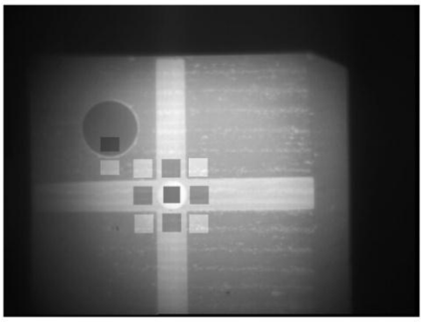

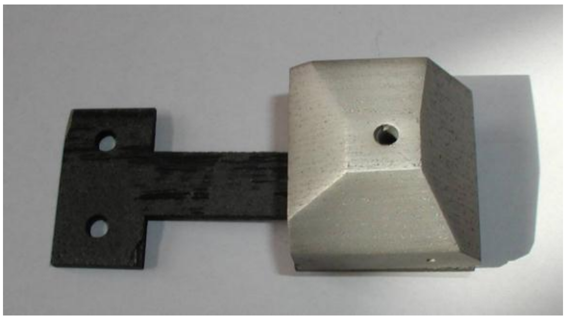

Figure 4 - The sample image recorded with the Hitachi camera

Figure 5 - W coated CFC sample used to investigate the dependence on the emissivity on viewing angle

The emissivity of these coatings was calculated. In the centre of the sample a cylindrical hole with the diameter of 3 mm and the length of 18 mm was performed. The hole has CFC walls and it performs as a black body with an emissivity greater than 0.95. The key factor in these experiments is to have all the surfaces at the same temperature. An image of the heated sample taken with a digital camera is shown in Fig. 6.

Figure 6 - W coated CFC sample heated by the electron beam at 1200 °C

3.3. W coated CFC emissivity

The temperature and the image from the camera are recording continuously. The temperature drops to ~ 750 °C in about 200 s from the moment when the electron beam was switched off. An IR image of the heated sample and the corresponding temperature profiles on horizontal and vertical axes are shown in Fig. 7. As it can be seen the electron beam hits the sample in right up corner.

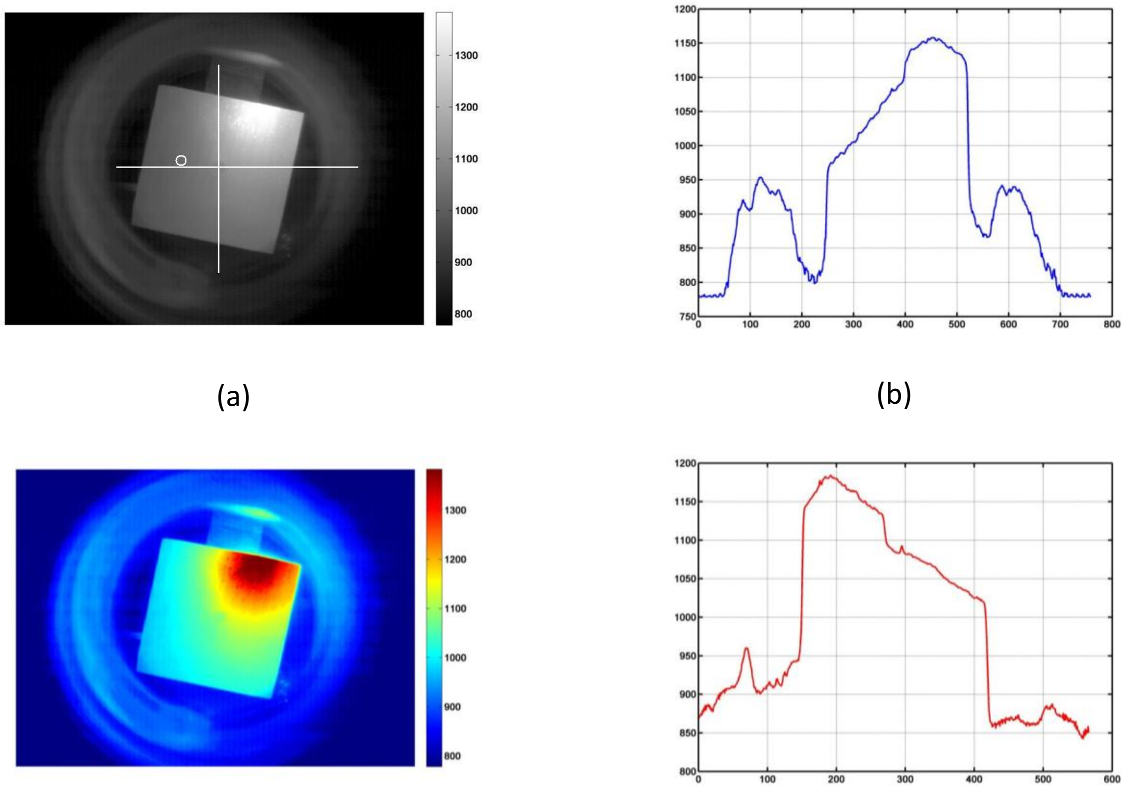

(a) (b) (c) (d)

Figure 7 - The image of the CFC sample during the heating period taken with the Hitachi camera (a), colour converted image (c) and temperature profiles on horizontal (b) and vertical (d) axes.

The temperature difference in horizontal and vertical directions is 150-200 °C, but none of these directions crosses the hot spot. In that area the temperature could be much higher. It is clear that this regime can not be used for emissivity measurements. A better regime is during the cooling down period when after 40-50 s the temperature of the sample surface is much uniform. This can be seen in Fig. 8. The difference in surface temperature is about 20 °C. The edges between the surfaces with different angles with the front surface can not be seen. This means that there is no significant influence of the viewing angle on emissivity in the range 0-60°. The side peaks are due to the reflections of the light on the vacuum connection and they have nothing to do with the real temperature.

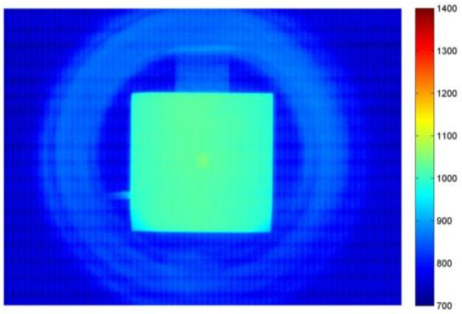

(a)

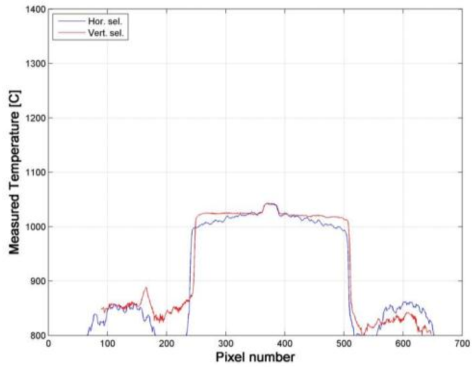

(b)

Fig.8 The colour converted image of the CFC sample during the cooling down period taken with the Hitachi camera (a), and temperature profiles on horizontal and vertical axes (b)

The ratio of the light intensities produced by selected regions highlighted in Fig. 4 and the intensity given by the hole region on the same image was plotted in Fig. 9.

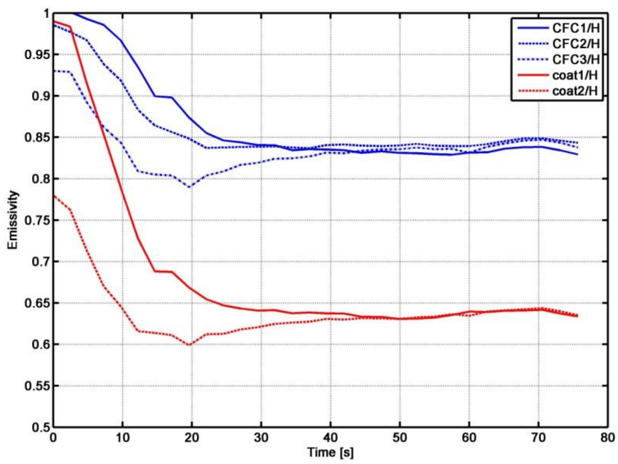

Figure 9 - Ratio of the intensity recorded in some regions coated with tungsten and CFC to the intensity of the hole region

These ratios represent the emissivity when the surface and the hole have the same temperature, which means after about 40 s since the heating was stopped. **The measured emissivity of the tungsten coated surface is 0.63 $\pm$ 0.03 for the wavelength of 1,064 nm.** This is a higher value than that of the bulk W and it might be associated with the high porosity of the W coated CFC surface.

The temperature dependence of ratios between the light intensities produced by selected regions highlighted in Fig. 4 and the intensity given by the hole region are shown in Fig.10.

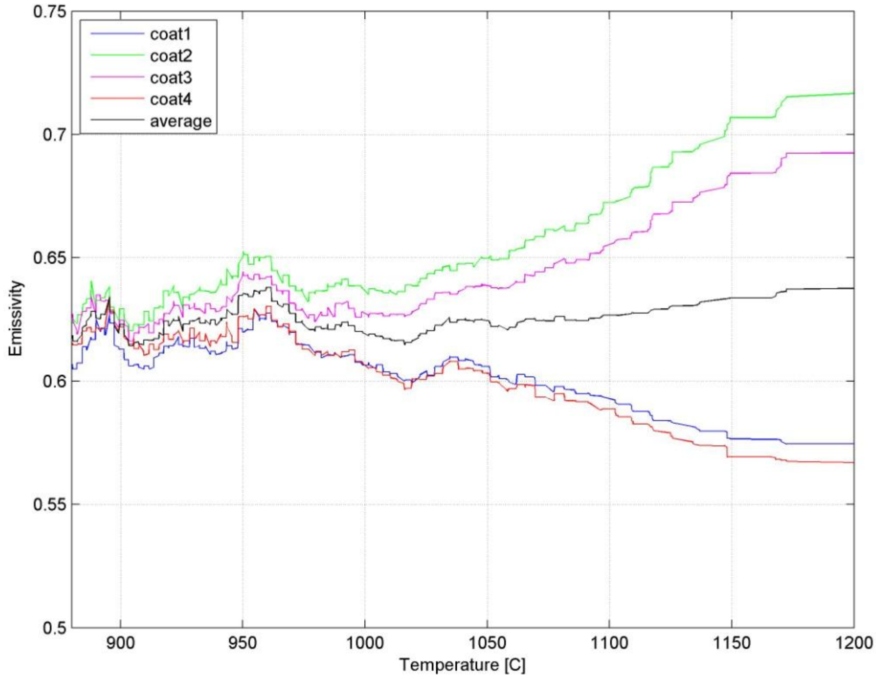

Figure 10 - Temperature dependence of the ratios between light intensities produced by selected W coated areas and that given by the centre hole. The temperature decreases from 1200 ℃.

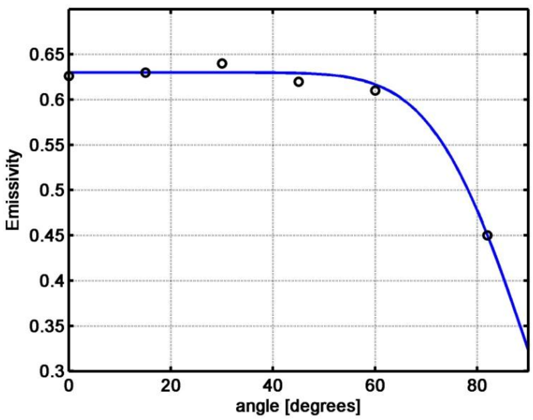

Figure 11 - The influence of the viewing angle on the W coating emisivity

The data were taken during the cooling process from 1200 °C. It can be seen that in the temperature range of 875 °C – 1050 °C the emissivity changes between 0.6 and 0.64. This variation is in the error limit of ± 5%. For higher temperatures the calculated ratios do not represent the emissivity because the coated surface and the hole are not at the same temperature.

The change of emissivity with the viewing angle is shown in Fig. 11. As it can be seen there is no significant influence of the viewing angle in the range of 0° – 60°. The measurement at 80° is not certain.

Conclusion

Hitachi KP-M1AP video camera can be used for temperature monitoring of the W coated CFC tiles from the ITER like Wall at JET. The emissivity of the W coatings with a thickness of 20-25 μm, corresponding to the tiles G1, G6, G7 and G8 of the divertor, was found to be 0.63±0,03 for the wavelength of 1,064 nm. A bandpass filter of 10 nm centred on this wavelength was used. The distance between the hot surface and the camera optics was about 330 nm. Under these conditions the light intensity from the hot surface was enough.

There is no significant influence of the viewing angle in the range 0° – 60° on the coating emissivity.

There is no significant influence of the temperature in the range 850 °C –1,050 °C on the coating emissivity.

Acknowledgement

The reported work includes contributions from the following people outside the EUATOM-MEdC Association: Elena de la Luna (EFDA CSU, Culham, UK), Gilles Arnoux (CCFE, Euratom Association, Abingdon, UK)

References

[1] P. N. Bossart, *Spectral emissivities of tungsten-molybdenum alloys,* Pittsburgh, 1933.

[2] J. C. De Vos, *A new determination of the emissivity of tungsten ribbon*, Physica, Vol. XX, pp. 690-714, 1954

[3] R. D. Larrabee, *The Spectral Emissivity And Optical Properties Of Tungsten*, Massachusetts Institute Of Technology, Cambridge, Massachusetts, Technical Report 328, 1957.

CHARACTERIZATION OF MIXED MATERIALS IN SUPPORT OF THE ITER-LIKE WALL PROJECT

C.P Lungu, C. Porosnicu, I. Jepu, A. M. Lungu, P. Chiru, A. Marcu, C. Luculescu, I. Tiseanu

National Institute for Laser, Plasma and Radiation Physics, Bucharest, Romania,

Euratom-MEdC Association

Abstract

Mixed materials, in combinations similar with those deposited during JET operations were prepared using two TVA simultaneous evaporators. Samples having different relative Be/C/W concentrations were thermal treated in vacuum and characterized using XPS technique. Structural changes had been observed with thermal treatment temperature. Were performed analyses using XPS, SIMS, XRD and X-Ray Fluorescence on specimens taken from the current JET tiles G1B, G3A, G4C, G6D and G6B. As results of XPS measurements of the JET tiles samples were found elements in pure states and oxidized compounds as BeO, WO. W is present in tiny amounts on the surfaces. As results of SIMS measurements was found: (i) the deposits on tiles 1 and 3 have high Be/C ratio similarly as the tiles exposed in 2001-2004 but in contrast to deposits on MkII GB tiles removed in 2001. The duplex nature was attributed to the He-fuelling campaign. (ii) Be/C ratio measured by SIMS technique was found to be lower than on tiles exposed in 2001- 2004. (iii) D/C ratio on inner divertor tiles is lower than on tiles exposed in 1998-2001 and 2001- 2004. The XRD spectra of the received samples in March 2012 (G3, G6) present similar structures and compositions as in the previous lot of samples were the formation of BeO, $WO_{x,}$ Be_2C, NiO compounds as well as pure elements as C, Be, Cr, W, Cu, Ni, Fe were identified. Was highlighted the possible formation of the following alloys: Be_2W (110) hexagonal, Be 20W (51) cubic, Be22W (511) cubic due to the high energetic particles of the plasma during JET operation. By XRF analyses were identified Cr, Fe, Ni, Cu elements, in JET specimens, in good agreement with the XPS and XRD measurements.

Papers

[7] A. Marcu, C.M. Ticoş, C. Grigoriu, I. Jepu, C. Porosnicu, A.M. Lungu, C.P. Lungu, *Simultaneous carbon and tungsten thin film deposition using two thermionic vacuum arcs,* Thin Solid Films, Volume 519, Issue 12, 1 April 2011, Pages 4074-4077

Conferences

[1] C. P. Lungu, J. Likonen, A. Hakola, C. Porosnicu, I. Jepu, A. Anghel, A. M. Lungu, P. Chiru, C. Ticos, Gh. Oncioiu, A. Victor, and JET EFDA Contributors, *XPS and SIMS Analyses of Mixed Deposition Materials*, 13th International Workshop on Plasma-Facing Materials and Components for Fusion Applications / 1st International Conference on Fusion Energy Materials Science, May 09th - 13th, 2011 in Rosenheim, Germany.

Reports

[2] C. P. Lungu, J. Likonen, A. Hakola C. Porosnicu, I. Jepu, A. Anghel, A. M. Lungu, P. Chiru, C. Ticos, Gh. Oncioiu, A. Victor, *Characterisation of mixed materials in support of ILW (JW11-FT-3.66)*, Oral remote presentation at the FT monitoring meeting, 14 - 16 June 2011, Culham, UK.

1. Introduction

The generation of mixed deposition materials has been flagged as a major topic of concern for ITER. JET provides a source of Be-C mixed materials, and in future mixed materials as tungsten carbides and tungsten beryllides are expected to be generated in JET ILW. Compositional information will already be gleaned from continuing analyses programmes using Ion Beam Analysis techniques, SEM and SIMS. However, these methods do not address other film properties such as chemical states, structure and thermal/electrical properties. Further techniques such as XPS/AES and XRD are needed that may add information on film properties, either for predominantly carbon-beryllium films present on current JET tiles, or in preparation for surface films that may be expected from the Be/W wall now being installed.

The mixed materials, in combinations similar with those deposited during JET operations were prepared by the “Beryllium coatings” research group, National Institute for Laser, Plasma and Radiation Physics, the MEdC Association using the original thermionic vacuum arc (TVA) method [1-3].

2. Description of the work :

Be/C/W mixed films were prepared by TVA method and analyzed using, XPS, XRD, SIMS (performed at VTT Finland) and XRF techniques. Were characterized also a set of post-mortem samples of current JET tiles: tile G1B/5, tile G3A/5, tile G4C/7, tile G6D/7, as well as a new set of 8 samples received in March 2012: 14BW G6B Sample 8g (2004-2009),14BW G6B Sample 6g (2004-2009), 14BW G6B Sample 4g (2004-2009), 14BW G6B Sample 1g (2004-2009), 21W G3A Sample 8a (2007-2009), 21W G3A Sample 6a (2007-2009), 21W G3A Sample 4a (2007-2009), 21W G3A Sample 2a (2007-2009)

2.1 Sampling of the tiles

The CFC tiles were sampled at VTT Helsinki, Finland in a glove box using a drill saw to cut cylinders with a diameter of 17 mm. Pieces of about 10 mm high were cut from the core samples. The divertor samples selected for the erosion/deposition analyses are indicated in Figs 1 and 2. Some of the samples were prepared for cross-sectioning and optical microscopy.

Figure 1 - Tile 21WG3A

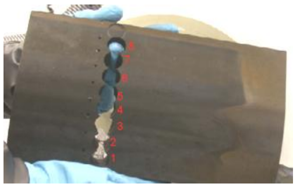

Figure 2 - Tile 21WG3A after cutting

2.2 XPS measurements on mixed films prepared by TVA method

Surface analysis of the samples prepared using the thermionic vacuum arc (TVA) method was carried out on a Quantera SXM equipment, with a base pressure in the analysis chamber of 10^{-7} Pa. The X-ray source was Al K_{α} radiation (1486.6eV, monochromatized) and the overall energy resolution is estimated at 0.75 eV by the full width at half maximum (FWHM) of the $Au4f_{7/2}$ line.

Structural changes of the mixed films containing Be, C and W had been observed with thermal treatment temperature. Oxygen bounds to Be and/or W during thermal treatment result of a possible chemical state change.

The stoichiometric BeO is formed up to 600 ^{o}C while above this temperature the Be1s binding energies increases suggesting the occurrence of some non-stoichiometric oxide BeO_x.

Up to 600 ^{o}C the W remains in its elemental state while above this temperature a combined BeO_x and WO_y are formed with different stoichiometries. The kinetics of oxidation displays that W is slowly oxidized and reaches the WO state only at 800 ^{o}C (Table 1). Another threshold can be noticed at 1000 ^{o}C exhibiting a large difference between the relative concentrations of the Be and W as compared with the previous temperatures. Thus, the W relative concentration suddenly increases at the expense of the decreasing Be relative concentration, the amount of oxygen remaining rather constant. This experimental finding can be explained by a strong tendency of W to segregate from the subsurface region to the top of the surface.

Oxygen was present in all the samples in the same chemical state (O^{2-}) and in roughly the same concentrations. Consequently the elements (Be, C and W) are embedded in the same amount of oxygen.

After Ar cleaning (1keV, 0.5 min) the incorporated C is found as carbides (BeC and/or WC) and C-C bonding as graphitic C. The mentioned carbides are present on the surface up to 600^{o}C (or lower in the range 400-600^{o}C). There is a threshold at 600^{o}C above which we notice no contribution of the carbides on the surface. The only remaining C species is the graphitic one.

In the synthetic Table 1 it can be seen the XPS surface analysis data for the samples BeCW_noT, BeCW_200, BeCW_400, BeCW_600, BeCW_800, BeCW_1000. (noT: non thermal treatment, _200, _400, _800, _1000: thermal treatment at respective temperature in ^{o}C)

Table 1. XPS surface analysis data for the samples BeCW_noT, BeCW_200, BeCW_400 BeCW_600, BeCW_800, BeCW_1000.

Sample	Binding Energies (eV)			
	C1s	O1s	Be1s	W4f
BeCW_noT	283.1 Carbides (28,4%)	531.5 (lattice O^{2-})	113.9 (BeO)	31.5 33.7
BeCW_200	283.4 Carbides (56.8%)	531.8 (lattice O^{2-})	113.8 (BeO)	31.5 33.7
BeCW_400	283.3 Carbides (57.1%)	531.8 (lattice O^{2-})	113.9 (BeO)	31.6 33.8
BeCW_600	284.6	532.2 (lattice O^{2-})	114.6 (BeO_x, x>1)	32.4 34.6
BeCW_800	285.0	532.3 (lattice O^{2-})	114.6 (BeO_x, x>1)	32.4 34.6
BeCW_1000	284.8	532.2 (lattice O^{2-})	114.8 (BeO_x, x>1)	32.8 34.9

2.3. XPS depth profile measurements of the JET samples

The XPS analysis was carried out with a VG model ESCALAB 250 X-ray photoelectron spectroscope (Thermo Electron, USA) using the depth-profiling (DP) regime. Following an Ar ion bombardment for 50 sec the equivalents of 100 atomic layers were removed from the films' surfaces and the subsequent XPS analysis was performed.

The depth profile of the 21WG3A/7 sample was obtained recording each spectrum between the 0 step (as-grown surface) and step "n" (final surface). Fig. 3 shows the obtained results.

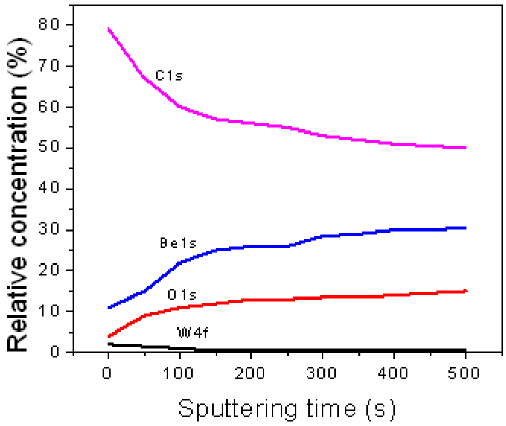

Figure 3 - The XPS depth profile of the 21WG3A/7 sample, obtained by etching using an Ar ion beam.

Due to the Ar ion bombardment, some of chemical bonding could be changed of the original state. We applied the XPS line scanning of an angle-lapped specimen in order to obtain the depth profiling with a very short time ion sputtering of the analyzed surfaces, only to remove the carbon contamination of the analyzed surface. The mixed structure enlarged several times is exposed on an angle-lapped surface, and depth profiling is carried out using the X-ray beam scanning. This method makes it possible to measure the compositional depth profiles of a large depth region that is over several thousand Å within only in several minutes.

The XPS depth profile measurement on the lapped sample 21W G3A/7 is presented in Fig. 4.

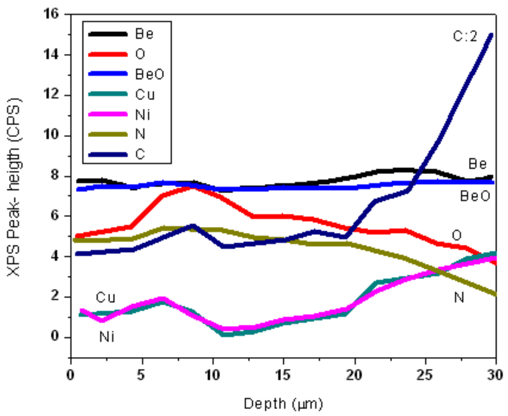

Figure 4 - XPS depth profile analysis on the 21W G3A lapped sample

The XPS depth profile analyses were performed also on the lapped samples G4C/7e, G6D/7e, G3A/5e and G1B/5e, presented in Fig. 5. The co-deposited layer on the JET tiles had a high Be/C ratio and the presence of Ni and Cu was identified, coming from the inconel steel in the JET vessel wall and from internal metal fittings, bolts etc.

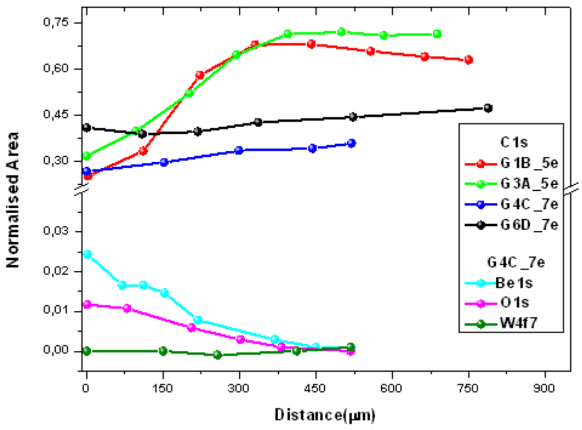

Figure 5 - XPS depth profile analysis on all the samples

XPS dept profiles were obtained also using the "ball cratering" method. The relative concentration of C slightly increase in the samples G4C/7, G6D/7, G1B/5 followed by a slight decrease of the O relative concentration.

Be exhibits the same relative concentration (1.4%) in the samples G4C/7, G6D/7 and an important decrease in the sample G1B/5 (0.7%). Be presents typically its oxide BeO chemical state in the first three samples and additionally a BeO_x bonding (x>1) assigned to a nonstoichiometric compound in the sample G3A/5 (Binding Energy = 114.6 eV)

W is present in tiny amounts on the surfaces of the first 3 samples and cannot be detected in the last one. The sample G3A/5 display a different behaviour: C relative concentration is decreasing abruptly to 50.4% at the expense of the sudden increasing of O relative concentration (30.3%) and the relative Be concentration (19.4%). C shows three chemical bonding in all samples namely: C-C/(CH)n , OH-C-O and C=O respectively.

2.4 SIMS (Secondary Ion Mass Spectrometry) analyses of the samples prepared by TVA

The Be/C/W mixed films prepared by TVA method were analyzed by SIMS at VTT Institute in Helsinki, Finland, using following measurement parameters: VG IX70S double focussing magnetic sector SIMS; O_2^+ (5keV) primary ions, ion current 250nA, Xe^+ (5keV) primary ions, ion current 125nA and 500 nA; Sputtered area 300 x 220 μm2; Sputter rates: 0.56nm/s (Be/W). In Figs 6 and 7 are shown the sputtered zones after SIMS measurements.

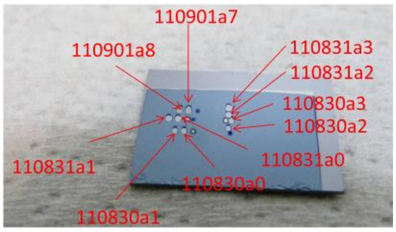

Figure 6 - SIMS sputtered zones of the sample 20110627-02, Be/C/W, thermal treatment: 400 °C, time: 30min

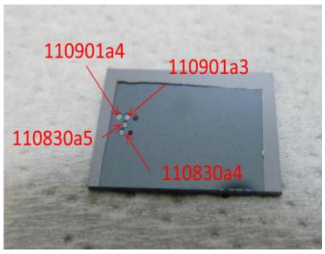

Figure 7 - SIMS sputtered zones of the sample 20110627-07, Be/C/W, thermal treatment: 800 °C, time: 30min

SIMS depth profiles of Be-C-W films using O_2 primary ions are presented in Figs. 8-11.

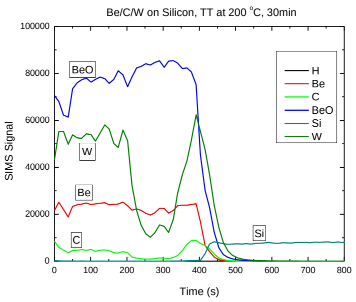

Figure 8 - SIMS depth profiles of Be/C/W films thermal treated at 200 oC for 30 min

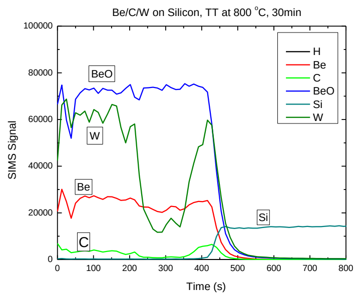

Figure 9 - SIMS depth profiles of Be/C/W films thermal treated at 800 oC for 30 min

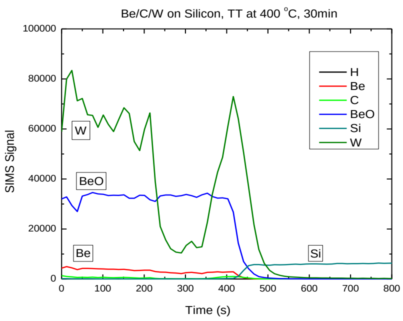

Figure 10 - SIMS depth profiles of Be/C/W films thermal treated at 400 °C for 30 min

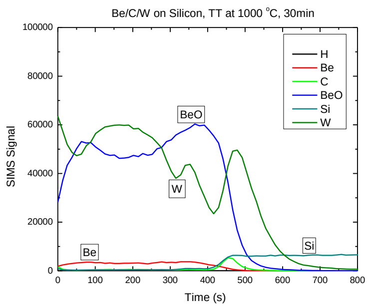

Figure 11 - SIMS depth profiles of Be/C/W films thermal treated at 1000 °C for 30 min

2.5 SIMS analyses of the JET tiles samples

Using the same parameters, the JET tiles samples were analysed, and the dept profile compositions were measured. A depth profile of the Sample3/4 is shown in Fig. 12.

The structure of the co-deposited film on sample 3/4 is similar to that on sample 3/2. The co-deposited film is porous and it consists of globules. The size of the globules is bigger than on sample from same poloidal location exposed in 2001-2004 [4-5].

As results of SIMS measurements was found: (i) the deposits on tiles 1 and 3 have high Be/C ratio similarly as the tiles exposed in 2001-2004 but in contrast to deposits on MkII GB tiles removed in 2001. The duplex nature was attributed to the He-fuelling campaign. (ii) Be/C ratio measured by SIMS technique was found to be lower than on tiles exposed in 2001- 2004. (iii) D/C ratio on inner divertor tiles is lower than on tiles exposed in 1998-2001 and 2001- 2004. Outer divertor tile 8 did not have any marker layer and there is a very thin layer on the surface. This layer is just contamination and the tile has been eroded most likely (results of SIMS measurements).

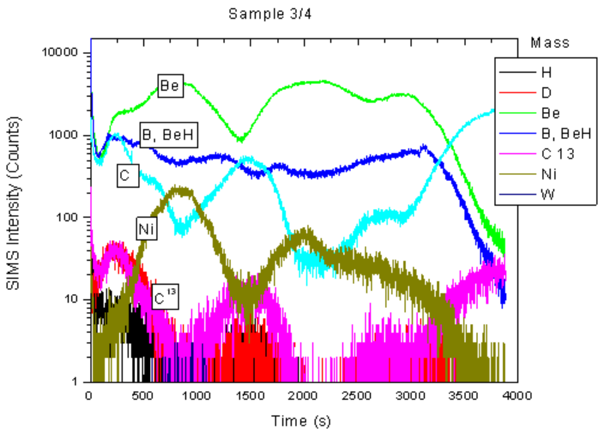

Figure 12 - SIMS depth profile of the sample ¾

3. X-Ray diffraction analyses

The X-ray diffraction analyzes on the JET tiles samples were performed using a X-Ray Rigaku diffractometer using a Cu cathode (Fig. 13). The X-ray of the Cu Kα radiation was filtered by a Ni filter has a wavelength of 1.54178 Å. Diffraction patterns from -3 to 150 degrees in two-theta were recorded.

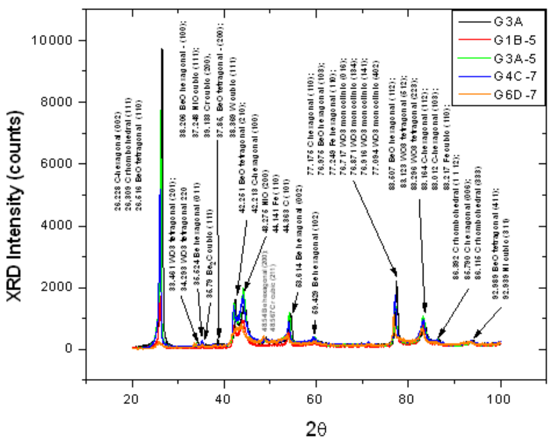

Figure 13 - Superposed XRD spectra of the G3A, G1B-5, G3A-5, G4C-7 and G6D-7 samples

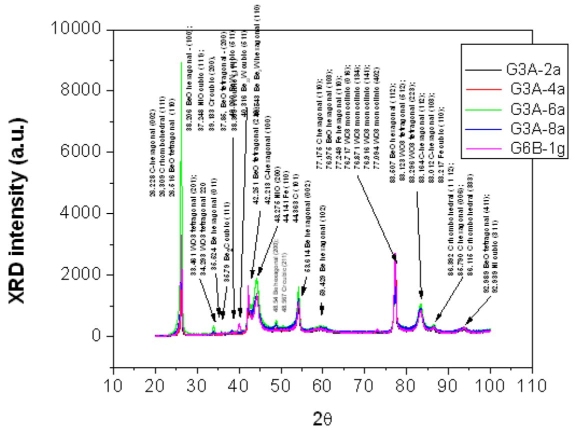

Figure 14 - Superposed XRD spectra of the: 14BW G6B Sample 1g , 21W G3A Sample 8a, 21W G3A Sample 6a, 21W G3A Sample 4a, 21W G3A Sample 2a

A new set of 8 samples were received in March 2012: 14BW G6B Sample 8g (2004-2009),14BW G6B Sample 6g (2004-2009), 14BW G6B Sample 4g (2004-2009), 14BW G6B Sample 1g (2004-2009), 21W G3A Sample 8a (2007-2009), 21W G3A Sample 6a (2007-2009), 21W G3A Sample 4a (2007-2009), 21W G3A Sample 2a (2007-2009)

The XRD spectra of the received samples are presented in Fig. 14. Similar structures and compositions are observed as in the previous lot of samples with the exception of the XRD spectrum of the 14WG6B sample 1g (2004-2009) highlighting the possible formation of the following alloys: Be_2W (110) hexagonal, Be 20W (51) cubic, Be22W (511) cubic.

e have to notice occurrence of the non stoechiometric Be_xW alloy on JET divertor. According to the phase diagram of Be-W the melting temperatures of Be_2W and $Be_{22}W$ alloys are 2250^{o}C and 1289^{o}C respectively. In the JET reactor there are energetic particles and the formation of high temperature alloys is favoured.

4. Measurements using X-ray micro beam fluorescence method

The key element of the XRF component is a policapillary lens which provides a focal spot size in a range from few tens to a few hundreds of micrometers. Thus a significant increase of the X-ray intensity (up to three orders of magnitudes) is obtained. This guaranties higher detection sensitivity and shorter measurement time.

The samples G6D7 and 21WG3A were measured and the obtained results are presented in Fig. 49-51. One can observe that there are slight differences between the two samples. On the XRF spectra were identified Cr, Fe, Ni, Cu elements, in good agreement with the XPS and XRD measurements.

Conclusion

Mixed materials, in combinations similar with those deposited during JET operations were prepared using two TVA simultaneous evaporators. Samples having different relative Be/C/W concentrations, (5/1/1 typically) were thermal treated in vacuum at 200, 400, 600, 800 and 1000 ^{o}C and characterized using XPS technique. Structural changes had been observed with thermal treatment temperature. Oxygen bounds to Be and/or W during thermal treatment result of a chemical state change.

As results of XPS measurements of the JET tiles samples we found that: (a) Be exhibits the same relative concentration (1.4%) in the samples G4C/7, G6D/7 and an important decrease in the sample G1B/5 (0.7%). Be presents typically its oxide BeO chemical state in the first three samples and additionally a BeO_x bonding (x>1) assigned to a nonstoichiometric compound in the sample G3A/5 (Binding Energy = 114.6 eV), (b)W is present in tiny amounts on the surfaces of the first 3 samples and cannot be detected in the last one. (c) The sample G3A/5 display a different behaviour: C is decreasing abruptly to 50.4% at the expanse of the sudden increasing of O (30.3%) and Be (19.4%). C shows three chemical bonding in all samples namely: C-C/(CH)n , OH-C-O and C=O respectively.

As results of SIMS measurements was found: (i) the deposits on tiles 1 and 3 have high Be/C ratio similarly as the tiles exposed in 2001-2004 but in contrast to deposits on MkII GB tiles removed in 2001. The duplex nature was attributed to the He-fuelling campaign. (ii) Be/C ratio measured by SIMS technique was found to be lower than on tiles exposed in 2001- 2004. (iii) D/C ratio on inner divertor tiles is lower than on tiles exposed in 1998-2001 and 2001- 2004. Outer divertor tile 8 did not have any marker layer and there is a very thin layer on the surface. This layer is just contamination and the tile has been eroded most likely (results of SIMS measurements).

The XRD spectra of the received samples in March 2012 present similar structures and compositions as in the previous lot of samples were the formation of BeO, WO_x, Be_2C, NiO compounds as well as pure elements as C, Be, Cr, W, Cu, Ni, Fe were identified. On the XRD spectrum of the 14WG6B sample 1g (2004-2009) was highlighted the possible formation of the following alloys: Be_2W (110) hexagonal, Be 20W (51) cubic, Be22W (511) cubic due to the high energetic particles of the plasma during JET operation.

The key element of the XRF component is a policapillary lens which provides a focal spot size in a range from few tens to a few hundreds of micrometers. Thus a significant increase of the X-ray intensity (up to three orders of magnitudes) is obtained. This guaranties higher detection sensitivity and shorter measurement time. On the XRF spectra were identified Cr, Fe, Ni, Cu elements, in good agreement with the XPS and XRD measurements.

Acknowledgement

The reported work includes contributions from the following people outside the EUATOM-MEdC Association: Jari Liconen and Annti Hakola (EURATOM – TEKES Association, VTT Helsinki, Finland)

References

[12] C. P. Lungu, I. Mustata, V. Zaroschi, A. M. Lungu, A. Anghel, P. Chiru, M. Rubel, P. Coad G. F. Matthews and JET-EFDA contributors, Phys. Scr. T128 (March 2007) 157–161.

[13] C.P. Lungu, C.E.A. Grigorescu, M.I. Rusu, I. Jepu, C. Porosnicu, A.M. Lungu, I.D. Feraru, D. Savastru, Diamond and Related Materials, 20 (July 2011) 1061-1064.

[14] A. Marcu, C.M. Ticoş, C. Grigoriu, I. Jepu, C. Porosnicu, A.M. Lungu, C.P. Lungu, Thin Solid Films, 519 (April 2011) 4074-4077

[15] J. Likonen, J.P. Coad, D.E. Hole, S. Koivuranta, T. Renvall, M. Rubel, E. Vainonen-Ahlgren, A. Widdowson, JET-EFDA Contributors, Journal of Nuclear Materials, Volumes 390–391, 15 June 2009, Pages 631-634

[16] J. Likonen, J.P. Coad, E. Vainonen-Ahlgren, T. Renvall, D.E. Hole, M. Rubel, A. Widdowson, JET-EFDA Contributors, Journal of Nuclear Materials, 363–365 (June 2007) 190-195.

UPGRADE OF GAMMA RAY-CAMERAS: NEUTRON ATTENUATORS

Marian Curuia[1], Mihai Anghel[1], Teddy Craciunescu[2], Mihaela Gherendi[2], Sorin Soare[1], Vasile Zoita[2]

[1] *National Institute for Cryogenics and Isotopic Technologies, Rm. Valcea, Romania*
[2] *National Institute for Laser, Plasma and Radiation Physics, Magurele, Bucharest, Romania*

Abstract

The main objective of the GRC JET Enhancements (EP2) project is the design, construction and testing of neutrons attenuators for the two sub-systems of the KN3 gamma-ray imaging diagnostics: KN3 gamma-ray horizontal camera (KN3-HC-NA) and KN3 gamma-ray vertical camera (KN3-VC-NA). This diagnostics upgrade should make possible gamma-ray imaging measurements in high power deuterium JET pulses, and eventually in deuterium-tritium discharges.

The neutron/gamma-ray attenuating material is demineralised water contained within metal casings. Both KN3-HC-NA and KN3-VC-NA was initially designed to work as a simple pure water container at hydrostatic pressure. The only loads the attenuator structure had to sustain were those generated by the tokamak magnetic field and by their own weight; these loads were evaluated at 200 Nm on vertical axis for the Horizontal Camera Neutron Attenuator.

The material used for the Horizontal Camera Neutron Attenuator was INCONEL 600 sheet 5 mm thick.

At a later stage the attenuating material (demineralised water) source was changed to the JET demineralised water circuit which was supposed to provide a working pressure of 5 bars. The casing material was also changed to INCONEL 600 sheet 3mm thick and the design was changed accordingly (reinforcements were added to withstand the loads evaluated at 112500 N per lateral face). It should be pointed out that the overall attenuator geometry was kept unmodified.

Several severe design and manufacturing issues and a water source pressure of 4.5 bars led to the point of designing and manufacturing of a new KN3-HC-NA casing. The new KN3-HC-NA has been installed at its location on JET and is ready for engineering commissioning. The engineering (non-plasma) commissioning of the KN3-VC-NA system has been successfully done and the system is ready for measurements (physics commissioning).

Papers

[1] Marian Curuia, Mihai Anghel, Nick Balshaw, Patrick Blanchard, Teddy Craciunescu, Trevor Edlington, Mihaela Gherendi, Vasily Kiptily, Klauss Kneupner, Igor Lengar, Andrea Murari, Phil Prior, Steven Sanders, Marek Scholz, Sorin Soare, Ioan Stefanescu, Brian Syme, Vasile Zoita, JET EFDA Contributors, *Implementation and testing of the JET gamma-ray cameras neutron filters pneumatic system,* Fusion Engineering and Design, vol. 86, pp. 1196-1199, ISSN: 0920-3796, doi:10.1016/j.fusengdes.2011.01.125

Reports

[1] M. Curuia, S. Soare, N. Balshaw, P. Blanchard, D. Croft, D. Gear, V. Kiptily, T. Edlington, A. Murari, D. Paton, B. Syme, V. Zoita, Report on design and manufacture of new horizontal camera neutron attenuator casing (Deliverable D-2.4.3), November 2011.

1. New KN3 Horizontal Camera Neutron Attenuator (KN3-HC-NA) casing

The KN3-HC-NA casing geometry resembles a quasi-crescent shape; it is placed between the Octant 1 horizontal main vacuum port (MHVP) and the KN3 horizontal camera shield.

1.1 KN3-HC-NA function

The casing should filter the neutrons during the gamma-ray measurement. The gamma-ray detectors field-of-view should be clear of any material except the attenuator water and the attenuator casing walls. The influence of other materials (used to manufacture the casing) should be kept at a minimum level by either positioning it properly or reducing the quantity of that particular material.

1.2 KN3-HC-NA design

As mentioned before the overall shape and dimensions of the casing are not changed. The modifications are done to the reinforcement geometry and position compared to the manufactured casing. An overall view of the KN3-HC-NA casing is shown in figure 1 and field of views FoV (1, 2,…,10) are shown in figure 2.

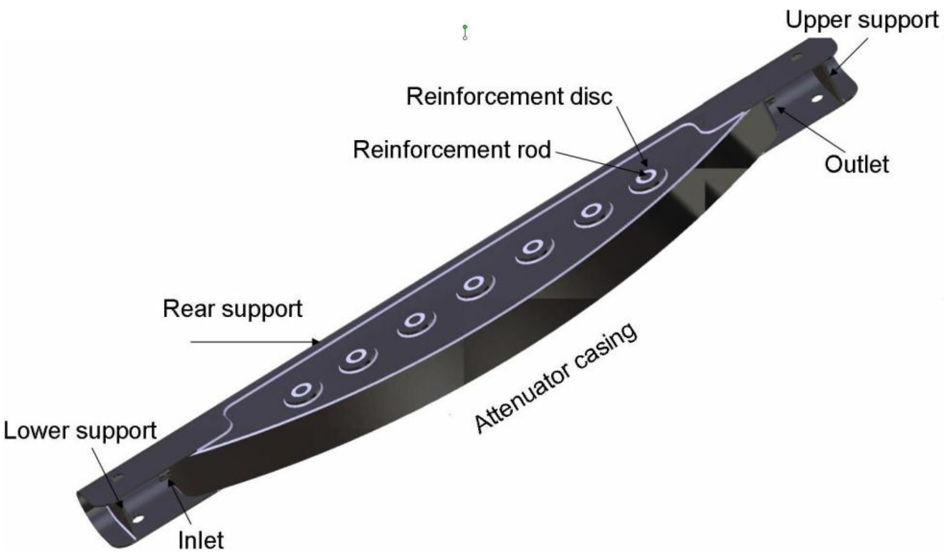

Figure 1 - Overall view of the KN3-HC-NA casing

1.2.1 Casing components and materials

The materials used for manufacturing of new KN3-HC-NA casing were as follows:

- attenuator casing: INCONEL 600, 3mm thick sheet
- rear support: SS316, 3mm thick sheet

- inlet & outlet: SS316
- upper & lower support: SS316 plates, 5mm thick
- internal reinforcements: 7 INCONEL 600 rods, 10 mm diam., 89 mm height;
- external reinforcements: 14 INCONEL600 discs, diam. 60 mm, 5 mm height;

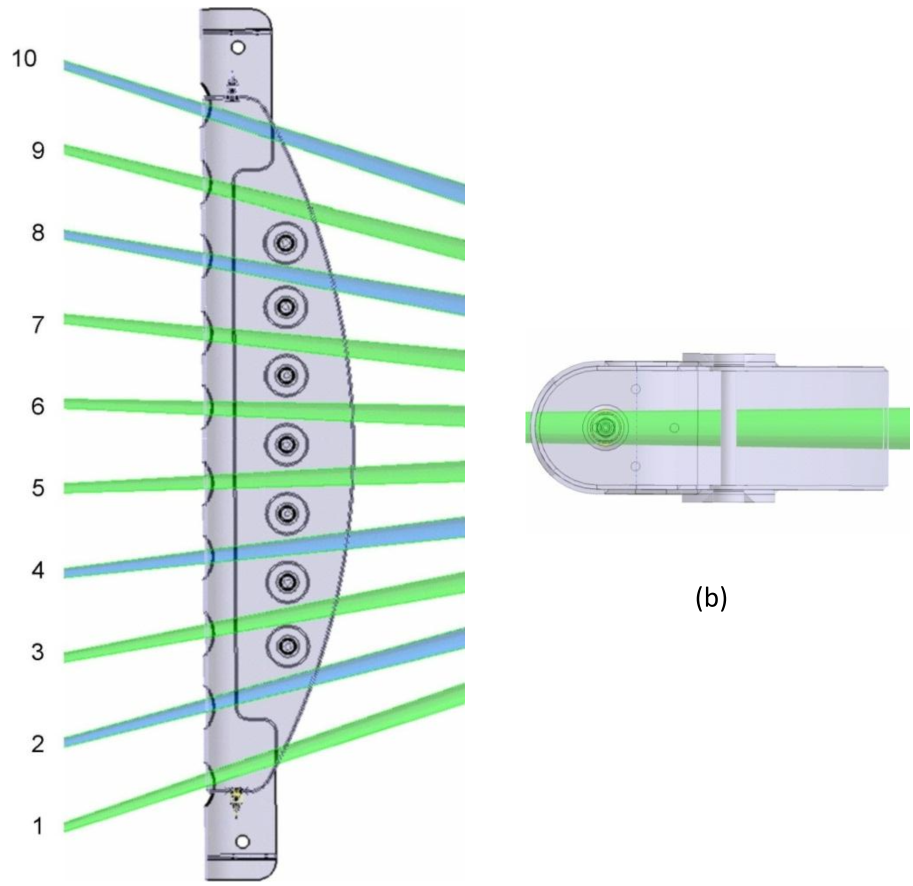

(a)

(b)

Figure 2 - Side (a) & top (b) view of KN3-HC-NA casing with FoV

1.2.2 New KN3-HC-NA casing FEA analysis

The neutron attenuator casing was created using CATIA and exported into FEA software (ANSYS) for mechanical analysis. The casing is an all-welded structure; therefore the model consists of one part only. The material properties attributed to the model are those of the INCONEL 600 (material elastic definition):

- Young's modulus 207 GPa; Poisson's ratio 0.3
- Yield strength 355 MPa (compressive and tensile)

- Ultimate strength 729 MPa (compressive and tensile)

The load is 450.000 Pa on the internal faces and fixed supports on the bolt holes, the mesh was set as [1]:

- relevance centre: fine
- element size: default
- smoothing: medium

'The theories most commonly used are the **von Mises criterion** (also known as the octahedral shear theory or the distortion energy theory) and the **Tresca criterion** (also uknown as the maximum shear stress theory). In fact, many 'Design by Rule' codes make use of the 'maximum stress' criterion but in the 'Design by Analysis' approach a more accurate representation of multiaxial yield is required. Although it is generally accepted that the Mises criterion is more accurate for common pressure vessel steels, the ASME Code uses the Tresca criterion since it is a little more conservative and sometimes easier to apply. British Standard BS 5500 follows the same procedure.

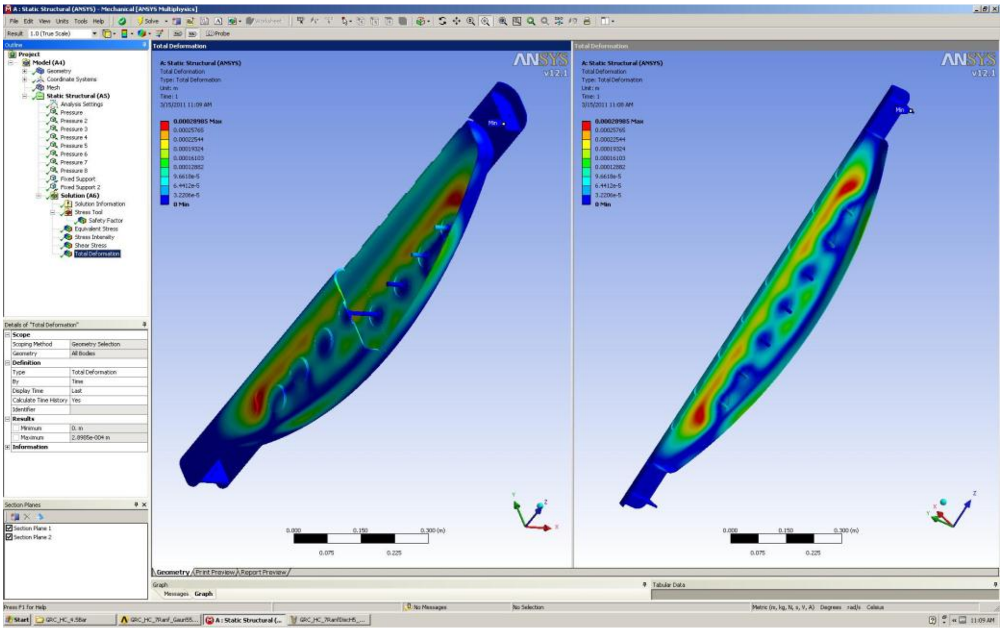

Figure 3 - Total deformations of lateral faces

The results monitored are: total deformation, von Mises stress and the safety factor.

The total deformation, figure 3, is less than 0.2 mm with the maximum localized at the extremities, upper and lower, of the lateral faces. Von Mises stress is shown in figure 4, the maximum level is 178 MPa.

Von Mises stress map shows a fairly low level of stress, the maximum being localized at the outer reinforcements. The distribution of the safety factor on the internal and external surfaces with probe values is shown in figure 5.

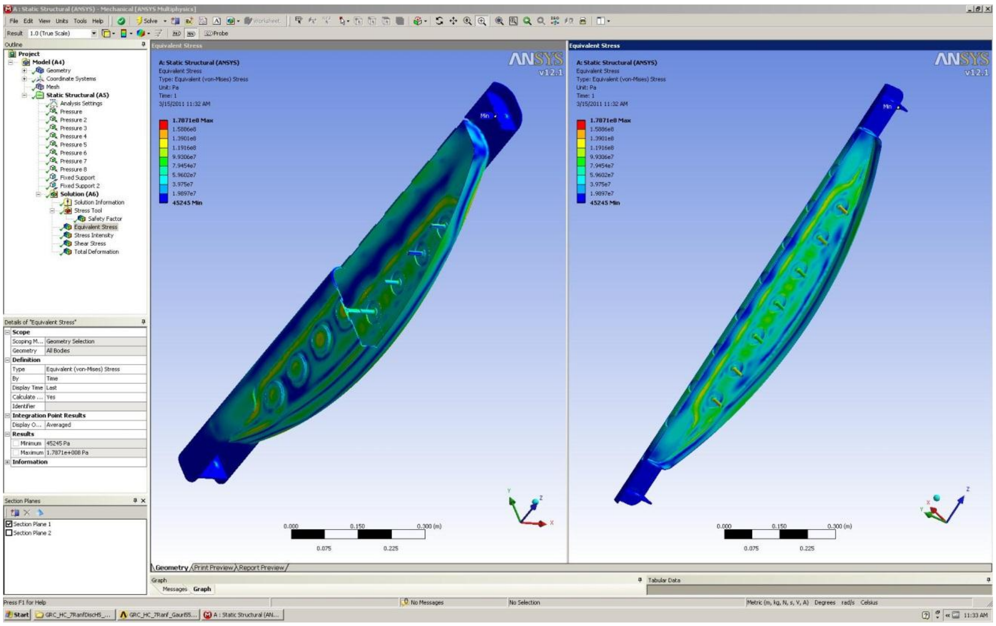

Figure 4 - Von Mises stress

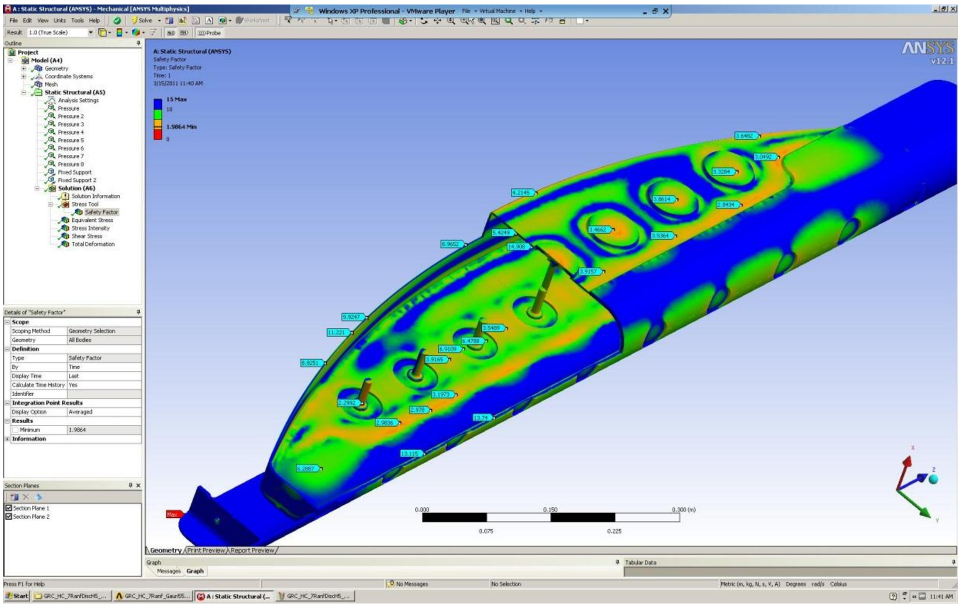

Figure 5 - The safety factor distribution on internal and external surfaces

From the figures showing the von Mises stress and Safety Factor it can be seen that the quasi-crescent face stress levels and safety factor values are well below the critical thresholds:

- von Mises stress: 4e7 Pa (stress map, green to blue regions)
- safety factor: above 5. In the above figure are shown the regions with a safety factor 2.5. These regions are localized at the outer rods surfaces only.

2. Installation on JET of the KN3-NA system

All components of the KN3-NA system were installed, at their locations on JET.

The engineering commissioning for KN3-VC-NA (short version) has been successfully done during August 2011.

The KN3-HC-NA (final version), designed for 4.5 bar internal pressure was installed on its location at JET. All pipes (water and pneumatics) were installed.

Conclusion

The design of new HC-NA casing shows no interference with the detectors FoV and minimizes the amount of material (SS316) in the FoV vicinity. According to the FEA the minimum safety factor is 1.9864.

After fabrication the new HC-NA casing has been tested. All tests stipulated in the Control Plan have been carried out. The results met the design requirements.

The new HC-NA casing has been delivered to JET, on site inspected and installed on the KN3 horizontal camera. The engineering commissioning of KN3-VC-NA has been successfully done and the system is ready for physics measurements.

Acknowledgement

The reported work includes contributions from the following people outside the EURATOM-MEdC Association: P. Blanchard (EFDA/CSU, Culham Science Centre, Abingdon, UK), N. Balshaw, T. Edlington, V. Kiptily, D. Croft, G. Kaveney, D. Paton (Association EURATOM-CCFE/JOC, Culham Science Centre, Abingdon, UK), A. Murari (Association EURATOM-ENEA, RFX, Padova, Italy), I. Lengar, Association EURATOM-MHST (Slovenia).

The authors would like to gratefully acknowledge the continuous support received from their institutes and laboratories.

References

[1] M. Curuia, S. Soare, N. Balshaw, P. Blanchard, D. Croft, D. Gear, V. Kiptily, T. Edlington, A. Murari, D. Paton, B. Syme, V. Zoita-JET Report (deliverable D-2.4.3), November 2011.

UPGRADE OF THE JET TANGENTIAL GAMMA-RAY SPECTOMETER (KM6T)

Sorin SOARE[1], Marian CURUIA[1], Teddy CRACIUNESCU[2], Mihaela GHERENDI[2], Vasile ZOITA[2]

[1]*EURATOM-MEdC Association, Institutul National de Cercetare-Dezvoltare pentru Tehnologii Criogenice si Izotopice - ICSI Rm.Valcea*

[2]*EURATOM-MEdC Association, National Institute for Lasers Plasma and Radiation Physics, Bucharest*

Abstract

The JET KM6T tangential gamma-ray spectrometer has already provided valuable spectral information on the plasma gamma-ray emission from the JET plasmas (e.g., TTE campaign). It is an essential diagnostics for fast particle studies in high performance discharges. The KM6T tangential GRS has been strongly affected following the 2004 JET shutdown (removal of the KJ5 pre-collimator). In order to regain its diagnostics capability and, especially, to extend its operation for high power deuterium and deuterium-tritium discharges a major upgrade is necessary. The main goal of the KM6T Tandem Collimator upgrade is to design and construct a suitable collimation system. The field-of-view of the upgraded KM6T diagnostics is defined by a system of collimators. The proposed KM6T upgrade should produce a significantly better result in terms of the minimum gamma-ray background than the configuration used before the 2004 JET shutdown.

A much simplified KM6T geometry has been evaluated by preliminary MCNP calculations with encouraging results. The analyses and preliminary evaluations carried out during the conceptual design phase of the KM6T diagnostics have led to the following conclusions:

-Replacement of the KJ5 pre-collimator may be more important than replacing the polyethylene neutron attenuators

-Neutron and gamma-ray shielding (may be) more important than neutron attenuation

1. Introduction

Plasma diagnostics based on the gamma-ray emission spectrometry is one of the important techniques used in the JET tokamak for studying fast ions [1-3]. The intense gamma-ray emission is produced in JET plasma when fast ions (ICRF-driven ions, fusion products, NBI-injected ions) react either with fuel ions or with the main plasma impurities such as carbon and beryllium. Gamma-ray energy spectra have been measured in the JET tokamak with three independent spectrometers looking at the plasma along different lines of sight. Two spectrometers look at the plasma in octant 8 along horizontal and vertical lines of sight. A third one has a vertical line of sight in octant 5. The gamma-rays are continuously recorded in all JET discharges over the energy range 1–28MeV, with an energy resolution of about 4% at 10MeV. The project addresses certain components of the horizontal, quasi-tangential gamma-ray spectrometer (the KM6T gamma-ray spectrometer). More precisely, the present enhancement project (TCS, Tandem Collimator System) deals with the first two components of the upgraded diagnostics line-of-sight, the tandem collimator system (KM6T-TC) for the KM6T tangential gamma-ray spectrometer.

A conceptual design was produced for the full line-of-sight of the KM6T Tangential Gamma-Ray Spectrometer [4], with the main design target being the maximisation of the signal-to-background ratio at the spectrometer detector, the ratio being defined in terms of the plasma emitted gamma radiation and the gamma-ray background. The solution is based on a system of collimators and shields for both the neutron and gamma radiations which define the spectrometer field of view. The

main aim of the TCS project consist in providing a proper collimation for the gamma-ray (BGO) detector of the tangential gamma-ray spectrometer, with a well-defined field of view at the plasma end of the diagnostics line-of-sight. The collimation system should at the same time improve the signal-to-background ratio at the detector end of the line-of-sight. MCNP numerical evaluations were performed, during this project, in order to evaluate the KM6T-TC physical performances.
An extended overview concerning the upgrading solutions for this diagnostic system and MCNP evaluations are presented in a previous report [5, 6].
Phase I. During the first part of the year 2011, the final collimation configurations developed for the KM6T tandem collimators have been evaluated. The final configuration developed for deuterium discharges proved to provide shielding factors of about 900 for a parasitic gamma-ray line of 9 MeV. The final configuration developed for tritium discharges proved to produce shielding factors of about 1000 for a parasitic gamma-ray line of 9 MeV. The Front Collimator has been installed during this timespan.
Phase II. During the second part of the year 2011 additional particular effects were evaluated by Monte Carlo transport simulation. The preparation of experimental validation of the KM6T system was accomplished. Also the Rear Collimator has been manufactured and delivered at JET.

2. Detailed Results

During the first half of 2011 the attenuation factor for the collimating system has been evaluated by means of Monte Carlo numerical simulations (MCNP-5 code). A simplified setup consisting of: point photon sources (solid angle irradiation of collimators), collimators and detectors (placed behind the collimators) was used to monitor integrated photon fluxes and spectra at the detectors position. The photon source is represented by a single line of energy 9 MeV corresponding to the most intense nickel neutron capture gamma-ray line expected to be emitted by the INCONEL support of the Inner Wall Guard Limiter (IWGL). Two experimental scenarios were evaluated: for D-D and D-T and compared with a previously investigated configuration (without the pre-collimator).
For the D-D scenario the MCNP model used is shown in figure 1, (CONFIG4-NEW).

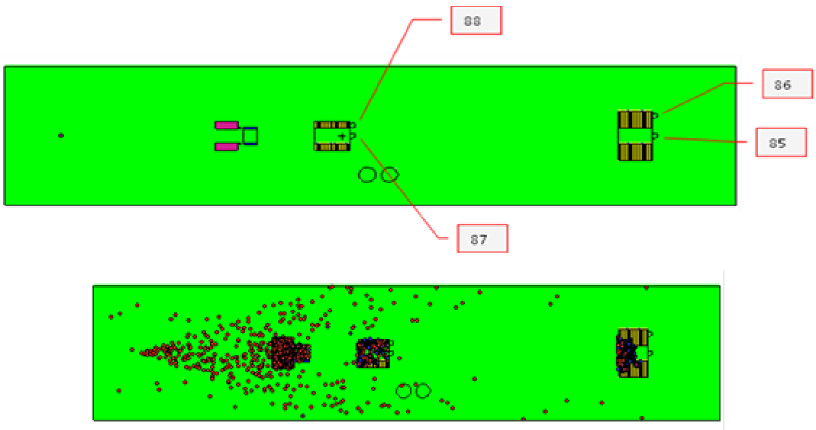

Figure 1 – CONFIG4-NEW MCNP simplified geometry

In this geometry the numerical simulations provided, at the detector positions, the integrated photon fluxes and spectra. The shielding characteristics of the tandem collimators were defined in terms of a shielding factor, which is the ratio of the radiation fluxes in two detectors: one placed on the axis of the system and another placed behind the collimators, at a mid-radius position (cells 88, 87 and 86, 85). The evaluation performed for DD discharges (2.5 MeV neutron emission), using the configuration CONFIG4-NEW is reported in comparison with the evaluation obtained for the previous configuration CONFIG4. The energy distribution of the 9 MeV gamma-ray photons reaching the detectors is calculated in 10 energy bins.

Table 1 – MCNP results obtained for the 9 MeV parasitic gamma-ray line in case of the previous configuration CONFIG4 (right) and new final configuration CONFIG4-NEW (left).

CONFIG4			CONFIG4-NEW		
Rear collimator			**Rear collimator**		
p in 85	(3.03 ± 0.01)E-08	p(85/86) = 464 ± 50	**p in 85**	(4.61 ± 0.01)E-08	p(85/86) = 893 ± 36
p in 86	(6.53 ± 0.70)E-11		**p in 86**	(5.16 ± 0.21)E-11	
Front collimator			**Front collimator**		
p in 87	(0.96 ± 0.01)E-07	p(87/88) = 45 ± 1	**p in 87**	(1.24 ± 0.01)E-07	p(85/86) = 95 ± 1
p in 88	(2.13 ± 0.03)E-09		**p in 88**	(1.30 ± 0.02)E-09	

For the D-T scenario (14 MeV neutron emission) the MCNP model used is shown in figure 2 (CONFIG5-NEW). The front collimator made up of 18 alternating polyethylene (thickness 40 mm) and lead (thickness 10 mm) plates. The rear collimator made up of two sets of 12 alternating polyethylene (thickness 40 mm) and lead (thickness 10 mm) plates. Each set has an additional 10 mm lead plate at the rear face.

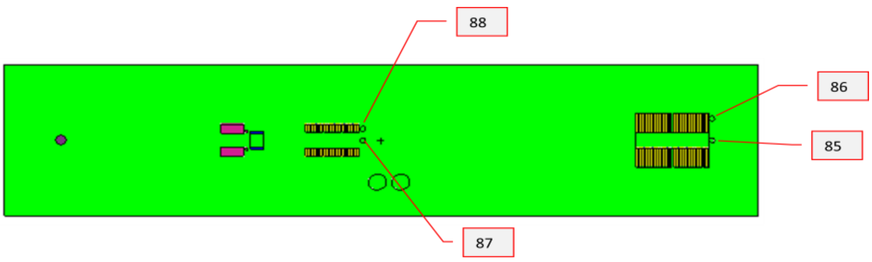

Figure 2 – CONFIG5-NEW MCNP simplified geometry

The evaluation performed for DT discharges (14 MeV neutron emission), using the configuration CONFIG5-NEW is reported in comparison with the evaluation obtained for the previous configuration CONFIG5. The energy distribution of the 9 MeV gamma-ray photons reaching the detectors is presented in Fig. 7. The shielding characteristics of the tandem collimators are listed in Table 2.

Table 2 – MCNP results obtained for the 9 MeV parasitic gamma-ray line in case of the previous configuration CONFIG5 (right) and new final configuration CONFIG5-NEW (left).

CONFIG5			
Rear collimator			
p in 85	(2.40 ± 0.02)E-08	p(85/86) = 795 ± 155	
p in 86	(3.02 ± 0.59)E-11		
Front collimator			
p in 87	(8.79 ± 0.03)E-08	p(87/88) = 54 ± 13	
p in 88	(1.63 ± 0.42)E-09		

CONFIG5-NEW			
Rear collimator			
p in 85	(4.13 ± 0.01)E-08	p(85/86) = 1070 ± 108	
p in 86	(3.86 ± 0.39)E-11		
Front collimator			
p in 87	(1.24 ± 0.01)E-07	p(87/88) = 95 ± 21	
p in 88	(1.30 ± 0.29)E-09		

TCS Front Collimator manufacture & installation

The TCS Front Collimator was manufactured and installed at JET during January 2011. The product arrived partially assembled and no deviations from the drawings were done. It was installed on the former KJ5 platform, with the axis coinciding with that of KX1 flight line. The clearance to the KX1 flight line thermal jacket is considered acceptable. Figure 3 shows the installed Front Collimator:

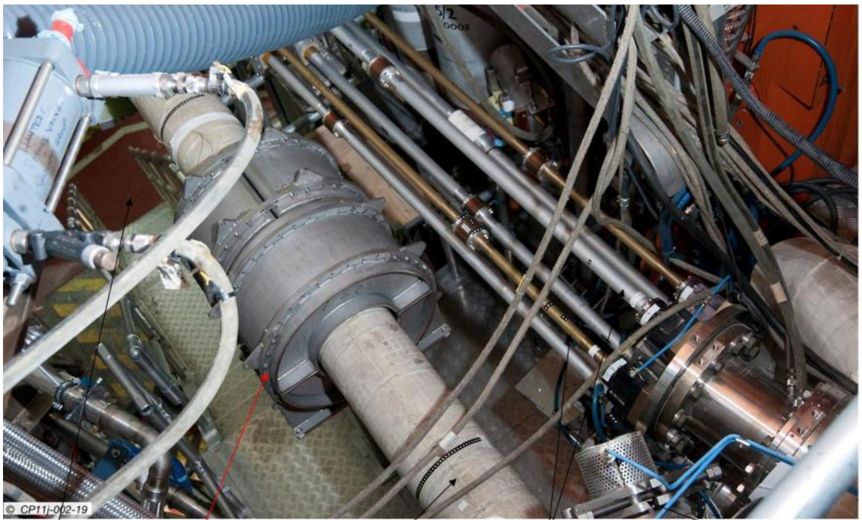

Figure 3 - Front Collimator installed

Phase II. During the second half of 2011 a special configuration of the D-T setup was evaluated. The KM6T will be installed in a very tight packed environment, sharing space with other devices dedicated to plasma diagnostic. Therefore, it appeared the necessity to evaluate the performances of the system in specific configurations. The impact of the removal of one third of the front collimator was evaluated in case of D-T experiments (Fig. 4).

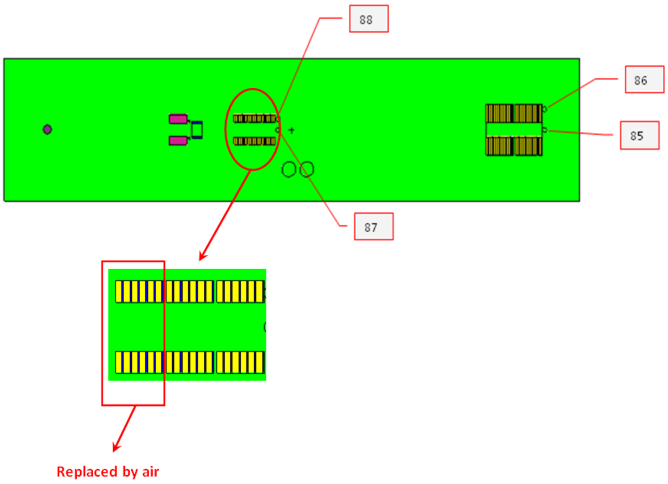

Figure 4 – Modified KM6T geometry for D-T experiments.

The evaluation is based on the same methodology used for previous MCNP calculations. The results are presented in Table 3. It results that it do not exist a significant impact in what it concerns the values of integrated neutron and photon fluxes. The KM6T system will provide efficient shielding factors in the modified geometry but a less tight field of view.

Table 3 – The differences between integrated neutron and photon fluxes obtained in the modified geometry and the original configuration.

14 MeV neutrons and induced gamma ray		**9 MeV photons**	
n in 85	*the difference is below the uncertainty range*	**p in 85**	*the difference is below the uncertainty range*
n in 86	*the difference is below the uncertainty range*	**p in 86**	*the difference is below the uncertainty range*
p in 85	*the difference is below the uncertainty range*	**p in 87**	*the difference is below the uncertainty range*
p in 86	*the difference is below the uncertainty range*	**p in 88**	+30%
n in 87	+50%		
n in 88	+345%		
p in 87	+390%		
p in 88	+250%		

Preparations of the experiments were performed during parasitic experiment Px-3.3.6. The parasitic experiments were dedicated to diagnose confined and lost fast-ions. The plasma scenarios, which were available for the parasitic observation, were not fast ion friendly, nevertheless, in the first time that confined and lost fast ions in the MeV-energy range were measured in JET plasmas with ILW.

From the point of view of the validation of the KM6T system, in the performed discharges, the gamma-ray flux was not sufficiently high for measurements able to clearly prove the improvement of the signal to background ration for the quasi-tangential BGO-spectrometer, figure 5. This will be possible in the discharges with a high ICRH power at central resonance: $B_T \sim 2.7\,T$ and $P_{ICRH} > 3\,MW$ which are scheduled for the year 2012. However useful results were obtained recording Gamma-ray spectra in low density plasma discharges.

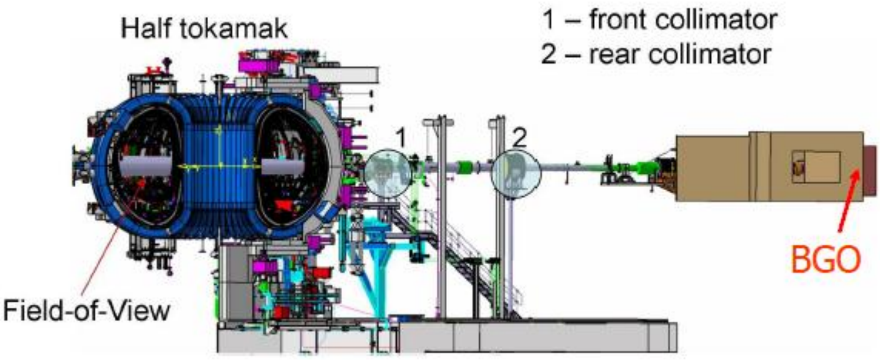

Figure 5 – Geometry of the experiment

TCS Rear Collimator manufacture & installation

The TCS Rear Collimator was manufactured and installed at JET during January 2011. The product arrived partially assembled. It was installed at the foot of the fast cameras access platform spanning a floor penetration, with the axis coinciding with that of KX1 flight line. The clearance to the KX1 flight line thermal jacket is considered acceptable. Below is a picture of the front & rear collimator, figure 6:

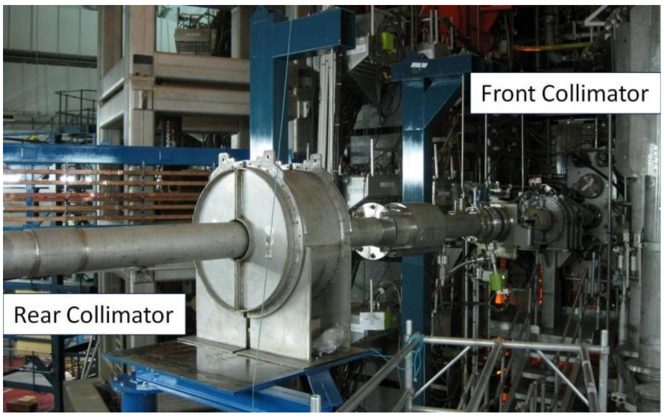

Figure 6 - Installed Front & Rear Collimators

Conclusions

The final collimation configurations developed for the KM6T tandem collimators have been evaluated by Monte Carlo transport simulations using the MCNP numerical code. The final configuration developed for deuterium discharges (CONFIG4-NEW) provides shielding factors of about 900 for a parasitic gamma-ray line of 9 MeV. The final configuration developed for tritium discharges (CONFIG5-NEW) produce shielding factors of about 1000 for a parasitic gamma-ray line of 9 MeV. MCNP evaluation of a modified geometry of the front collimator, needed for specific experiments proved that the system will still provide efficient shielding factors. Preparations of the experiments were performed during parasitic experiment Px-3.3.6. The next step of the project consists in for the final validation and commissioning of the KN3-NA system consists in complex experiments performed in the JET environment. The experiments are scheduled for the first part of the year 2012.

Both the collimators have been successfully installed. Validation and commissioning shall be done during 2012.

Acknowledgement

This work was partly supported by the European Commission under Contract of Association between EURATOM and the MEdC Association. It was carried out within the framework of the European Fusion Development Agreement. The views and opinions expressed herein do not necessarily reflect those of the European Commission.

The reported work includes contributions from V. Kiptily, (Association EURATOM-CCFE, Culham Science Centre, Abingdon, UK), who leaded the experiment Px-3.3.6.

References

[1] G. I. Sadler *et al.*, Fusion Technol. 18(1990)556.

[2] V. G. Kiptily *et al.*, Nucl. Fusion 42(2002)999.

[3] V. G. Kiptily *et al*., Rev.Sci, Instrum. 74(2003)1753.

[4] V.L. Zoita *et al "Conceptual Design Report, Tangential Gamma-Ray Spectrometer, (KM6T TGRS)"*, JET, Culham, Nov. 2008

[5] T. Craciunescu, *et al*., Evaluation of the Radiation Parameters of the Tandem Collimator System For The Km6t Tangential Gamma-Ray Spectrometer, JET, Culham, Dec. 2009.

AMS AND FCM MEASUREMENTS OF TRITIUM IN LASER CLEANED TILES AND TRITIUM DEPTH PROFILES IN JET DIVERTOR TILES

Catalin Stan-Sion[1], Mihaela Enachescu[1], Marius Dogaru[1], Alexandru Petre[1], Gunta Kizane[2], Larisa Baumane[2], Jevgenijs Gabruesnoks[2], Mihails Halitovs[2], Liga Avotina[2], Arturs Zarins[2], Jari Likonen[3], Seppo Koivuranta[3], Madis Kiisk[4]

[1] *Horia Hulubei National Institute for Physics and Nuclear Engineering, Bucharest, Romania, Association Euratom - MEdC*

[2] *Institute of Chemical Physics, University of Latvia, Association Euratom - AEUL*

[3] *VTT Technical Research Centre of Finland, Association Euratom-Tekes, Finland*

[4] *Institute of Physics, University of Tartu, Estonia*

Abstract

Deuterium and tritium are necessary fuels for the fusion experiments. For safety and protection reasons, their retention inside of the Tokamak protection walls must be avoided. Initially, the JET vessel was lined up with carbon tiles. During the last major shutdown, performed during 2009-2011, JET has been equipped with beryllium and tungsten materials covering the carbon substrate (ITER like wall). From this moment, due to plasma wall erosion, the retention of hydrogen isotopes was accompanied by co-depositions of W and Be. It has the consequence of modifying the surface structure of the protection tiles.

With the aim of investigating such effects and to study the fuel removal by means of Laser ablation, the analyzing methods Accelerator Mass Spectrometry (AMS) and Full Combustion flowed by scintillator Counting (FCM) were applied.

AMS, analyzes atom concentrations (e.g. T or D), by detecting and counting individually the atoms that are sputtered continuously form the sample material. In this way it provides a continuous measurement of the fuel retention profile in the depth of the protection tile. The resolution of the depth profiling can be varied according to the research goal.

The second one, the FCM, measures the averaged concentration of tritium in a defied volume that is obtained by full combustion of the sample material. It complements the microscopic AMS analyses.

By both these methods, the following striking results were obtained: 1) unexpected fuel retention and migration of tritium in protection tiles, 2) first microscopic investigation of fuel removal by laser ablation. Research work was performed under contract JW11-FT- 1.19.

Reports

C. Stan-Sion, AMS and FCM measurements of tritium in laser cleaned tiles and tritium depth profiles in jet divertor tiles, Annual Meeting, Culham, December 2011.

1. Introduction.

In order to withstand extreme heat fluxes the Joint European Torus (JET) and most current tokamaks use carbon fiber composite (CFC) tiles for the First Wall. Interaction of plasma with the inner wall material of the vessel causes erosion and formation of deposited/co-deposited layers, mixed materials and spatially non uniform tritium retention. Mechanisms of fuel retention and desorption is not completely clarified.

An accumulation of tritium in materials of the vacuum vessel creates problems for operation of fusion devices both as from view of a safety and economy.

The amount of tritium retention depends of on the materials of a fusion device and of on the plasmas operation conditions. The larger amount of tritium will be co-deposited with carbon based materials. Therefore, it is important to determine the tritium retention in the bulk of those tiles and to estimate the conditions that have an effect on that accumulation.

Since JET's D-T experiments have shown that carbon composites are not suitable for the tritium operation due to high carbon migration leading to tritium deposition in walls, the ITER design comprises a beryllium-clad First Wall in the main chamber, while use of carbon tiles is limited to the region where the edge plasma is deflected on to the divertor wall ("strike points") and tungsten tiles are to be used elsewhere on the divertor. During the functioning of ITER it is highly probable that Be will be eroded from its First Wall and being immediately ionized by the plasma it will be re-deposited on the divertor tiles leading to the formation of mixed material films and modifying the original properties. This will also occur at JET with the new ITER-like wall. For future researches is of importance to simulate such an effect and to evaluate the consequences. This can be done in the laboratory by depositions on carbon (CFC) substrates of Be and W performed simultaneously with exposure to D and T low energy fluxes.

Since 2008 the measurement of tritium retention in plasma facing components has been investigated with two different methods:

- The Full Combustion Measuring (FCM) technique which has been used to analyse tritium bulk content in small samples drilled from the protection tiles and to compare the distribution of tritium in the divertors of different designs: (SRP, 2001-2004); (MkII HD, 2005-2009).

- SIMS (Secondary Ion Mass Spectrometry) technique which is a surface sensitive analytical technique in which an energetic Oxygen dimer ion beam sputters a sample surface and secondary ions are formed and collected into magnetic sector (in our case) mass spectrometer. The technique is noted for exceptional sensitivity (0.1 ppm), depth profiling capability and mass range from Hydrogen (H) to Uranium (U) and lateral resolution down to micrometers. This technique has been used in the analyses of JET wall and divertor tiles allowing precise mapping on trace elements from H and D species to carbon isotopes as well as beryllium, nickel and tungsten and useful in the 13C puffing experiments and post mortem analyses of the co-deposited layers.

- The Accelerator Mass Spectrometry (AMS) which is the most sensitive analyzing method known today and the only one capable of measuring tritium concentration depth profile up to a depth of few hundred microns. Its sensitivity is 10^{-15} for the ratio: isotope/element. With a depth analysis up to hundreds of µm, this method is suitable for measurements of the depth profiles of T on the surface of samples and in the bulk and to assess the efficiency of the detritiation processes. It is also suitable to obtain the T-depth distribution in the divertor tiles and to investigate the result of simulations (material deposition and D and T gas enclosures) of the ITER Wall-like processes. AMS has already been applied since 2009.

2. Experimental work

Samples from divertor tiles were cut as cylinder disks (diameter 16mm), with special care to avoid damage of the sample surface. Complete distributions of the T content and depth distribution were measured by AMS in the depth of samples cut from the divertor protection tiles. Below, in Figure 1, the location of sample (14ING3B) in the Jet divertor it is shown. On the right side, the photo shows how cylinder cores will be drilled and extracted and then cut to thin slices, of about 3mm thickness.

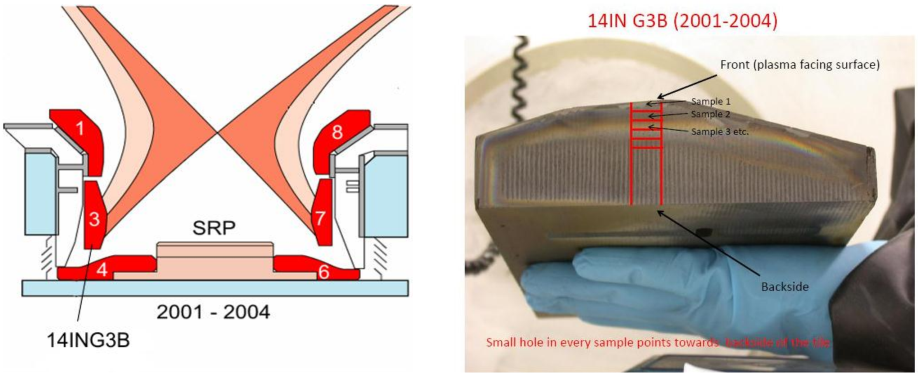

Figure 1 - Position of the analysed sample in the JET divertor and the drilling scheme for obtaining samples for analyse.

We have to emphasise from the begging that tile 14ING3B was detritiated by LASER ablation on a half of its surface and the other half remained unchanged regarding the initial T concentration. The feature will also be studied in this research project.

For the AMS data calibration new standard samples T/C were previously prepared, measured, and inter-compared with old standards. The procedure of determining the absolute values of the standard T samples is as follows: Each standard sample (having a given value) is measured for 10 times and up to about 4000 counts (for each of the 10 measurements). The background value of a blank sample is measured immediately after each sample measurement and is subtracted form the first value, producing the individual final value. Then the statistic error of this block of data is calculated. It has to be emphasised that due to the high concentration of the standards, adequate to the concentrations of the samples from JET, we have to consider the memory effect of the ion source. That is the background value after each such a measurement. These values fluctuate. Thus, the error will contain this background correction that is also fluctuating and increasing the error correspondingly. The above procedure was repeated for each of the 3 standard samples (3 different values). From each measured mean value, for a given concentration (standard value), the other two values will be calculated. In this way we will obtain 3 x 3 sets of values for the 3 standard concentrations. Then, the standard deviation is calculated for each of the 3 statistical assembles.

Table 1 below gives the obtained values for the standard samples measured by both FCM and AMS.

Table 1 – T/C standard samples.

Standard no.	Value (Bq/g)	
	AMS	FCM+SD
1	48±5	52±7
2	103±11	110±12
3	197±15	218±14

New standard samples are required by AMS since the sample material is destroyed in time by the sputtering with the ^{133}Cs beam. Long time before their destruction or radioactive decay large craters will develop in their structure. The rim effect of the produced crater is altering the extraction yield of the negative ions and consequently the measured absolute value of the concentration.

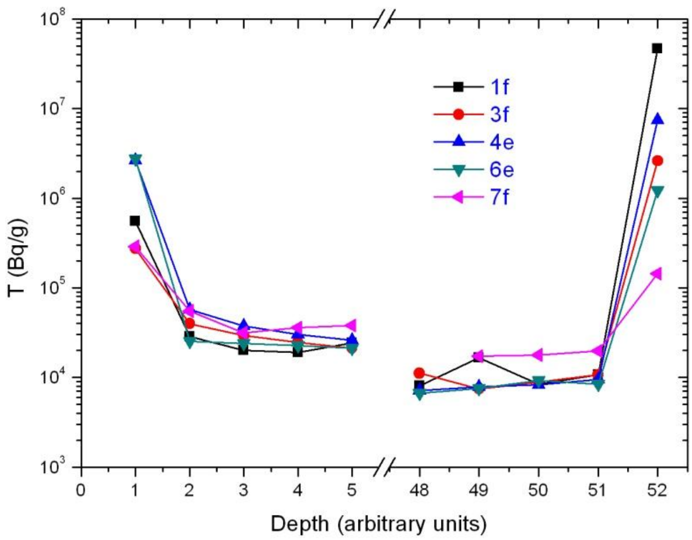

Figure 2 - Tritium retention in a protection tile of the Jet divertor. The depth scale is in arbitrary units however, this can be well approximated with a scale in mm.

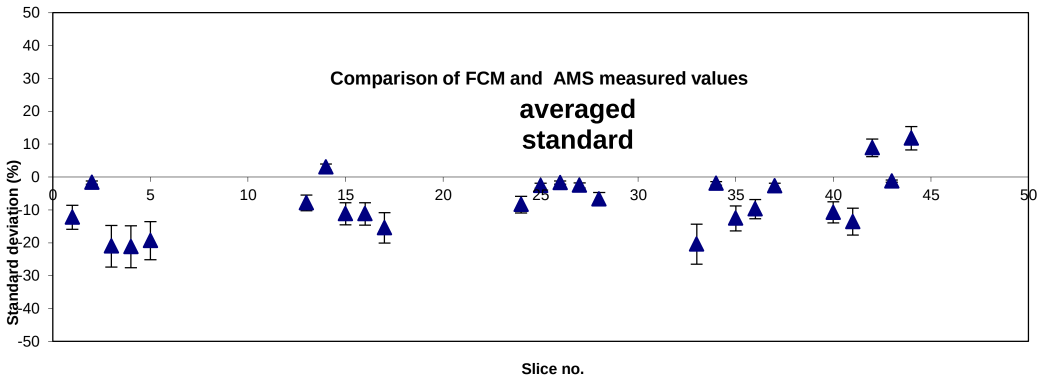

Figure 3 - Inter-comparison of T retention measurements performed by AMS and FCM.

AMS and FCM spectra were measured in different positions of the 14ING3B tile but for the entire thickness of the tile. Figure 2 below shows the integrated results of the AMS concentration depth profile averaged with the results obtained by FCM.

During the measurements performed on many tiles a comparison study of the results obtained by the AMS and FCM was also performed. Of course, the AMS being a microscopic method and FCM a macroscopic method some correction had to be added to this comparison.

As shown by Figure 3 the overall agreement is good. The differences between the values delivered by the two methods do not exceed 10%. This makes it possible that FCM can be used complementary to the AMS analyse whenever a steady and constant concentration is expected over a large volume.

AS mentioned before, the tile under investigation was also subject of a LASER detritiation procedure. For the assessment of the Laser detritiation efficiency a set of samples were be cut from the inner divertor tile 14IN G3B that was exposed in 2001-2004. Samples were cut from both the un-treated and the cleaned areas, representing a set with presumably low T concentration and, another set, with higher T concentration. The results obtained with AMS and FCM techniques were cross compared. Figure 4 presents the depth profile spectra measured by AMS from a detritiated and non detritated sample.

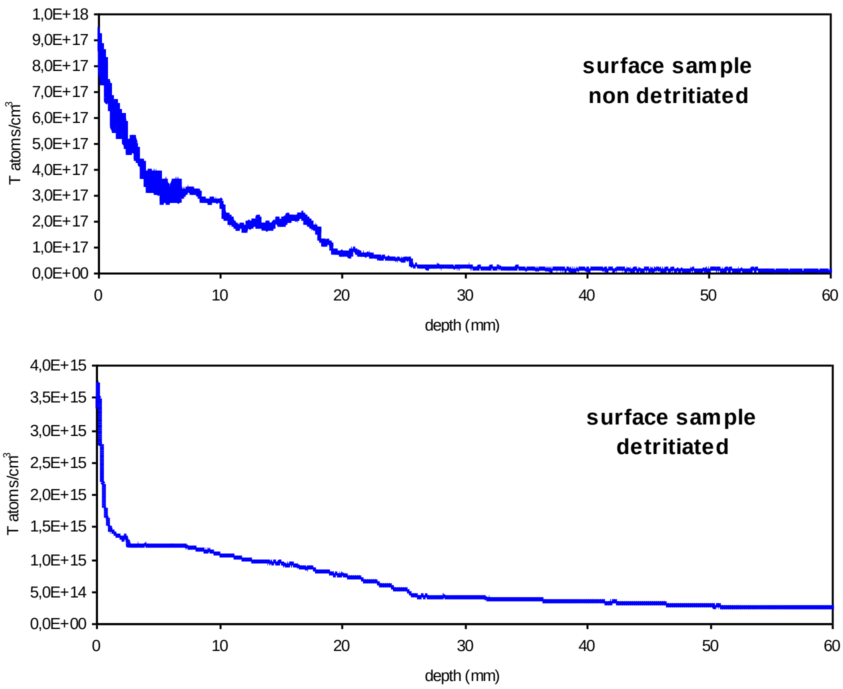

Figure 4 - AMS concentration depth profiles of tritium retention in CFC tiles before and after LASER ablation.

The integrated concentration depth profiles over a depth interval of 15 μm reveal the linearity of the LASER effect on T removal. This effect is to be seen in Figure 5.

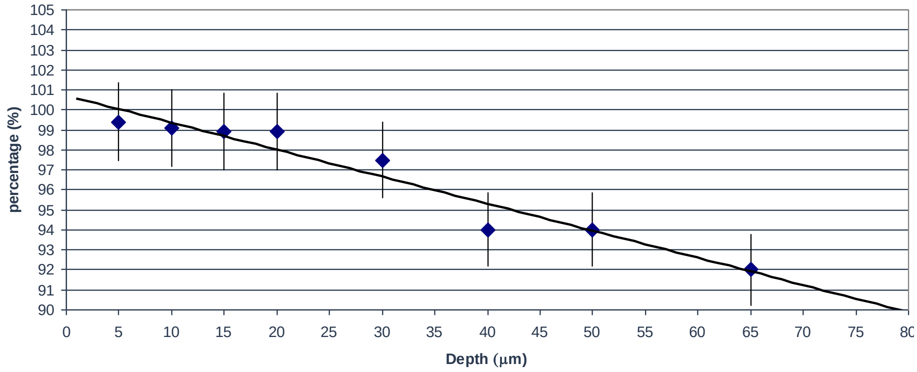

Figure 5 - Detritiation efficiency by Laser ablation. The points in the plot represent the ratio of integrated values over intervals of 15 μm, obtained from the two spectra presented above.

If we decrease the length of the integrated interval of the concentration analyse, which corresponds to a better depth resolution, a stinking effect of non-linearity at the edge of the LASER penetration length occurs. This is to be seen in Figure 6.

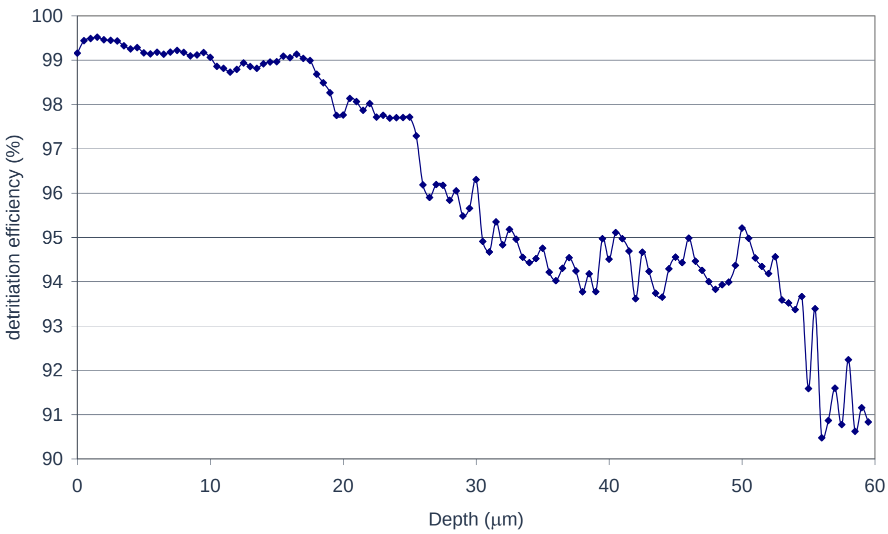

Figure 6 - Detritiation by Laser ablation measured with a 500 nm depth resolution by AMS

The Laser power should allow a penetration depth in carbon of 50 μm. However, as one can see from Figure 6, starting with a depth of only 20 μm the ablation starts decreasing and more than this, at 40 μm it starts fluctuating.

3. Conclusions.

More then twenty years ago it was recognized that AMS is the only analyzing method capable to perform sensitive measurements of tritium. At that time applications were performed for medicine.

More recently, this method has been motivated by the increasing interest for the construction a fusion reactor and AMS was applied to the analysis of hydrogen isotopes and to the depth profiling of their concentrations.

In the last decade the rapid progress in fusion technology opened a large area of new applications that required inherently an evolution and upgrading of the AMS-DP experiments together with the FCM method. As shown in this paper, AMS and FCM are now able to perform many applications for determining the tritium retention or detritiation of the fusion facilities and also for simulation of material transport, fuel retention and deposition in the Tokamak .

Such experiments will continue to provide interesting results of the poloidal distribution of tritium retention in the divertor of JET as well as to determine the material transport in the tokamak.

Since the Fusion Technology team at JET has investigated various methods to recover and analyze tritium in a variety of samples the two motioned methods will have a lot to do in the future.

During the last major shutdown performed during 2009-2011, JET has been completely equipped with beryllium and tungsten materials. The new lining is called the “ITER-Like Wall” because the materials are the same as the ones chosen for ITER. Therefore, experiments have study the migration of beryllium and to measure the amount of fuel retained on the new tiles and AMS and FCM can efficiently participate.

MOTION ESTIMATION WITHIN THE MPEG VIDEO COMPRESSED DOMAIN FOR THE DETERMINATION OF PELLETS EXTRUSION VELOCITY

Teddy CRACIUNESCU[1], Andrea MURARI[2], Ion TISEANU[1], Peter LANG[3]

JET-EFDA CulhamScienceCentre,Abingdon,OX143DB,UK

[1]EURATOM-MEdC Association, National Institute for Lasers ,Plasma and Radiation Physics, Bucharest, Romania

[2]Consorzio RFX,AssociazioneEURATOM-ENEAperlaFusione,Padova,Italy

[3]Association EURATOM-IPP,Max-Planck-Institut für Plasmaphysik, Garching, Germany

Abstract

Injection of solid, cryogenic hydrogen isotope pellets in tokamaks is used for particle fuelling as well as for ELM control (triggering and mitigation). The method has been demonstrated to open access to operational regimes not reachable by gas puffing. A controlled high fuelling efficiency is needed as otherwise the beneficial effects are spoiled by the increase of neutral pressure from fuel losses. Also the pellets can be used for the control of edge localized modes (ELMs). ELM triggering by pellets has been recognized as a potentially useful tool to mitigate type-I ELMs in large fusion experiments. ELM triggering and the variation of the ELMs dynamics depend on technical control variables such as pellet size, velocity, frequency and poloidal launch position. The efficiency depends on technical control variables such as pellet size, velocity, frequency and poloidal launch position. A recently developed optical flow image processing method has been improved and adapted in order to evaluate one of these key parameters, namely the ice extrusion velocity, based on the image sequences provided by a CCD camera viewing the ice at the exit of the nozzles of the extrusion cryostat. The optical flow method allows, under certain assumptions, deriving information about the velocity of video objects, associated with different physical phenomena. The implemented method is robust under noise and yield dense flow fields. The method was further developed taking advantage of the fact that video streams are usually compressed for storage. MPEG-2 compressed domain information is processed to obtain real time and reasonably accurate 2-D motion estimation of the deuterium ice extrusion velocity.

Publications

[1] T. Craciunescu, A. Murari, I. Tiseanu, P. Lang, *Motion estimation within the MPEG video compressed domain for JET plasma diagnostics*, Nuclear Instruments and Methods in Physics Research, Section A: Accelerators, Spectrometers, Detectors and Associated Equipment, 659-1(2011) 467-476.

[2] T. Craciunescu, P. Lang , A. Murari, T. Szepesi, S. Kálvin., G. Kocsis, A. Alonso, I. Tiseanu, V. Zoita, *Determination of the pellet parameters by image processing methods. Fusion Engineering and Design*, 86(2011)1186-1190.

1. Introduction

Injection of solid, cryogenic hydrogen isotope pellets in tokamaks is used for particle fuelling as well as for ELM control (triggering and mitigation). The method has been demonstrated to open access to operational regimes not reachable by gas puffing [1]. Pellet fuelling in the high confinement (H-mode) regime is characterized by the curvature induced drift of the high pressure plasmoid forming around the ablating pellet [3]. This can be exploited in order to improve the fuelling efficiency by launching pellets from the magnetic high field side (HFS) [4]. Also the pellets can be used for the control of edge localised modes (ELMs) [4]. ELM triggering by pellets has been recognised as a potentially useful tool to mitigate type-I ELMs in large fusion experiments [5]. However, a controlled high fuelling efficiency is needed as otherwise the beneficial effects are spoiled by the increase of neutral pressure from fuel losses. ELM triggering and the variation of the ELMs dynamics depend on technical control variables such as pellet size, velocity, frequency and poloidal launch position.

A recently developed optical flow method [6] was adapted in order to evaluate the ice extrusion velocity based on the image sequences provided by a CCD camera viewing the ice at the exit of the nozzles of the extrusion cryostat [7]. The method which combines the advantages of local methods (robust under noise) and global techniques (which yield dense flow fields). The real-time determination of the deuterium ice extrusion velocity become is an extremely difficult task, as the events revealed by the video sequences have time constants ranging around 20 ms. However, videos are stored in some kind of compressed format, for further analysis. Therefore it would be more efficient to retrieve the information, needed for physical studies, in the compressed domain. In case of MPEG compression format, widely accepted as a video compression standard, a kind of motion estimation is performed for compression purposes. It exploits the redundancy between consecutive or temporally close video images. This MPEG motion field (MPEG-MF) estimation is a crude approximation to the optical flow although it is heavily corrupted by the sudden occurrence of lack of correlation between estimated motion vectors and real motion in the video scene. However, this information can be exploited, as presented here, for separating the video sequence into multiple spatio-temporal regions corresponding to different rigid-body motion. Part of the rigid-body moving objects can be associated with different relevant physical phenomena. In this case the motion segmentation is further used for fast accurate optical flow estimation.

The main advantage derives from the fact that only partial decoding of the compressed video is needed to extract the useful information. This allows, for specific cases, a calculation speed which is compatible with on-line evaluation of the motion parameters. In this case the algorithms for motion segmentation and optical flow estimation can be implemented inside the MPEG compressing code, allowing the evaluation and storage of the physical parameters together with the storage of the video sequence.

2. Methods

Video sequences contain a significant amount of data similarity within and between frames. These statistical redundancies in both temporal and spatial directions are exploited for moving picture compression in MPEG-2 standard [8]. Although alternatives exist (H.261, H.263, MPEG-1, MPEG-4), this standard keeps a high level of popularity and is widely used in DVD and digital TV. The bit-rate reduction for storage and transmission is achieved by using the *discrete cosine transform* (DCT) to reduce the spatial redundancy, and a motion-*compensation* (MC) scheme based on a block matching method to exploit the temporal redundancies. A Huffman entropy encoder is used afterwards to obtain a compact bit stream.

The basic assumptions of the MPEG encoding process are the existence of an inter-pixel correlation and of a simple translatory motion between consecutive frames. Then the magnitude of a particular image pixel can be predicted from nearby pixels within the same frame (intra-frame coding) or from pixels of a nearby frame (inter-frame coding).

MPEG encoding is implemented using macroblocks (MB16) which consist of 16 x16 pixels. For intra-frame coding each MB16 is further divided into 8 x 8 pixel blocks (MB8). In case of a 4:2:0 chroma sub-sampling this results in 6 MB8 for a MB16.

MPEG stream consists of three types of pictures: I, P and B. Intra (I) frames are coded using only information present in the picture itself by the DCT. Each MB8 block of the I frame is processed independently with an 8 x 8 DCT. The distribution of the DCT coefficients is non-uniform. The DCT concentrates the energy into the low-frequency coefficients and many of the other coefficients are near zero. This is a result of the spatial redundancy present in the original image block. Consequently a bit rate reduction is obtained by neglecting the low value coefficients. Afterwards *quantization* is used to reduce the number of possible values to be transmitted. High-frequency coefficients are more coarsely quantized than the low-frequency coefficients. Quantization makes the coding/decoding processes 'lossy' due to the irreversible noise introduced. The result is similar to JPEG compression.

The high degree of compression specific to MPEG is achieved by means of the inter-frame coding. Inter-frame coding uses the correlation between the current frame and a past or future frame to achieve compression. P (*predicted*) frames are coded with *forward* motion compensation, using the nearest previous reference (of type I or P) images. *Bi-directional* (B) pictures are also motion compensated, this time with respect to both past and future reference frames. The parts of the image that do not change significantly are simply copied from other areas or other frames. In case of the other parts, for each MB16, the best matching block is searched in the reference frame(s). Residuals are then encoded, in a similar manner to I frame coding. A trade-off must be found between the accuracy in predicting complex motion in the image and the expense of transmitting the motion vectors (MV). Therefore only one MV is estimated for each MB16. The motion vectors are directly entropy coded without transformation and quantization.

Summarizing, the MPEG stream carries both intensity and motion information of the underlying scene. Intensity is represented by a set of DCT coefficients while motion is represented by a field of MV vectors. The motion between frames is described by a limited number of parameters (i.e. MV translation vectors). MPEG video stream may be of different types, i.e. I-, P or B-, and can occur in a variety of GOP (Group Of Pictures) patterns. 2-D motion estimation of a video scene within the MPEG compressed domain is presented in certain details in the following paragraph.

In order to transform the MV field in a smooth motion field, Coimbra [9] introduced a regularization set of rules that do not rely on future images (in case of B-frames). Therefore they are appropriate for real-time application. Assuming that consecutive images are strongly correlated, in case of I-frames, which have no motion, the MV field is supposed to be the same as for the previous image. In case of B-frames, for which two sets of MV exists, the one pointing backward is reversed and averaged with the one pointing forward. Applying these rules creates a motion field with one MV per macroblock.

A confidence measure can be introduced to ensure that the MV field is meaningful. Starting from the assumption that areas with strong edges exhibit better correlation with real motion than textureless ones, the DCT coefficients AC(1) and AC(8) (see Fig. 1) can be used to measure the edge strength in the horizontal and vertical directions within the MB8 block. In Ref. 25 it is shown that these coefficients can be interpreted as weighted averages of the image gradients f_x and f_y. Shen et al. [10] proved that the AC(1) and AC(8) coefficients outperform the Sobel edge detector.

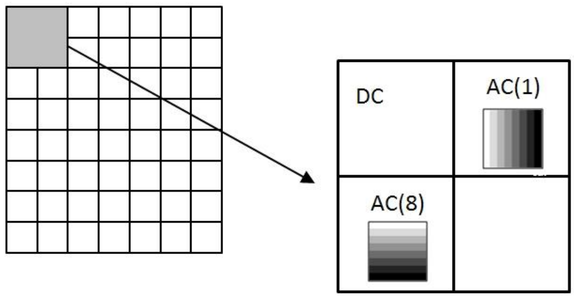

Figure 1 - AC[1] and AC[8] in the MB8 DCT block. The top left coefficient is referred to as DC, which is the first DCT coefficient of each block and it is eight times the average intensity of the respective block.

A confidence measure for the optical flow can be introduced by mean of the following algorithm:

$$v = -M^{-1}\left(\textstyle\sum_i b_i\right) \tag{6}$$

where:

$$M = \begin{pmatrix} f_x^2 & f_x f_y \\ f_x f_y & f_y^2 \end{pmatrix} = \frac{\pi^2}{2}\,[-AC(1) \quad -AC(8)]\begin{bmatrix} -AC(1) \\ -AC(8) \end{bmatrix} \qquad \text{and} \qquad b = \begin{pmatrix} f_x & f_t \\ f_y & f_t \end{pmatrix} \tag{7}$$

The confidence of the optical flow estimate is determined by the matrix M. An eigenvalue decomposition of the matrix M can be performed. The size of the eigenvalues (λ_1, λ_2) is a measure of uncertainty in the direction of the corresponding eigenvector. The first eigenvalue $\lambda_1$alone provides a good confidence measure for the optical flow field. The eigenvalue λ_1 can be calculated using the following relation:

$$\lambda_1 = \frac{\pi^2}{2}[AC(1)^2 + AC(8)^2] \tag{8}$$

A different approach consists in using the MV field only as a crude initial estimation for optical flow recovery which can be performed using the classical framework, outside the compressed domain [see e.g. Ref. 11]. The intensity information for the optical flow algorithm can be provided by the DC coefficients. The use of the (DC + 2AC) image, instead of just the DC image, is adequate to provide more intensity information for the estimation of the compressed domain optical flow field and ensures improved results [12]. The (DC + 2AC) image is a reconstructed image from the DC and two lowest-order AC coefficients (AC(1) and AC(8)) of each block.

3. Implementation and Results

A significant reduction of the computation time in case of the evaluation of the ice extrusion velocity can be obtained if the optical flow calculation is performed only for the image region which overlaps the ribbons of ice. But as the ribbons of ice are floating in the image, the ROI must be determined dynamically, for each pair of images in the sequence (Fig. 3).

Figure 3 – Three different frames from the image sequence showing the extruded deuterium ice in case of JET pulse #76379. ROI is represented on the images (dashed contour).

Segmentation techniques can be used in order to shrink the optical flow calculation to the image region where motion activity occurs.

The MPEG MV field obtained is obtained after applying the above described Coimbra's regularization rules. The regularization procedure removes the dependence on specific MPEG-2 characteristics such as picture and macroblock type and creates a motion field with one vector per macroblock with standardized magnitude.

The MV field, affected by irregular random patterns, cannot be used as an initial guess for the optical flow problem. However, this information can be exploited for object detection and tracking. A reasonable assumption is to consider that just a few moving objects exist within a frame, with a size larger than the noise. Therefore a 3x3 spatial median filter is then applied to the motion field, removing isolated vectors that have a low probability of reflecting the real movement in the image. The median filtering and also the further morphological image processing steps are very fast since they are performed on images with a very low size, representing the MV field. A pair of dilation and erosion operators is used to reveal "large" features of the image, using a structuring element which takes into account the first order vertical and horizontal neighbours. A labelling operation is further applied in order to detect the connected components in the image and select the ROI with the biggest area.

A block-based manipulation can be performed to obtain a stretched enclosure of the ROI. A moving object can be theoretically identified as a group of pixels in which the motion vectors are consistent with each other. A block grouping criterion for grouping neighboring pixels may be performed by using a consistency model [13]. However, in case of images characterised by strong noise and saturationthe identification of each moving object in the image (i.e. each ice pellet) may increase significantly the image processing time. Therefore it is more efficient to reformulate the objective of the segmentation procedure. A tight enough region which encompasses the whole motion activity can be determined in two fast steps: applying the regularization rules for the MV field and median filtering. The segmented region, illustrated in Fig. 4 can be used further for optical flow calculations. The average value of the ratio R_{OF} between the segmented area and the total image area is below 8%.

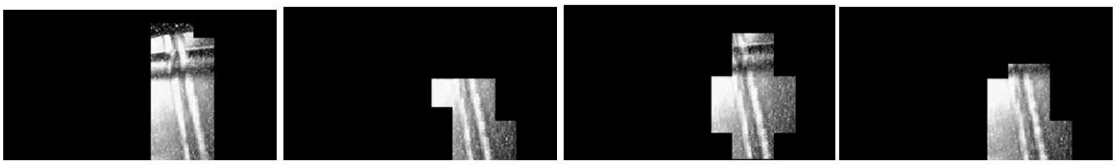

Figure 4 - Illustration of the motion activity segmentation.

The computation time is accounted in Table 1. It summarize the computation time needed for segmentation and for optical flow calculations. For details about the optical flow algorithm steps please see Ref. 8.

Table 1 – Time needed for ice extrusion velocity estimation.

Image processing step	**Time (ms)**
Segmentation using information from MPEG video compressed domain	
Applying the regularization rules for the MV field	0.6
Median filtering	0.8
Optical flow calculation performed on the segmented image region	
Image derivatives	1.8
SOR iteration	4.1
Median filtering	0.3

As can be seen in Table 1, the segmentation time is ~1.4 ms and the optical flow computation time, for three iterations, is ~ 13.2 ms (the image derivatives are calculated only at the beginning of the iterative process while the median filtering is performed after each SOR iteration – for details about the optical flow algorithm implementation see Ref. 14). The total optical flow computation time is ~16.4 ms. As the image acquisition framing rate is 50 Hz, it results that, in principle, the optical flow calculations can be performed on-line. The optical flow can be estimated together with the storage of the video sequence.

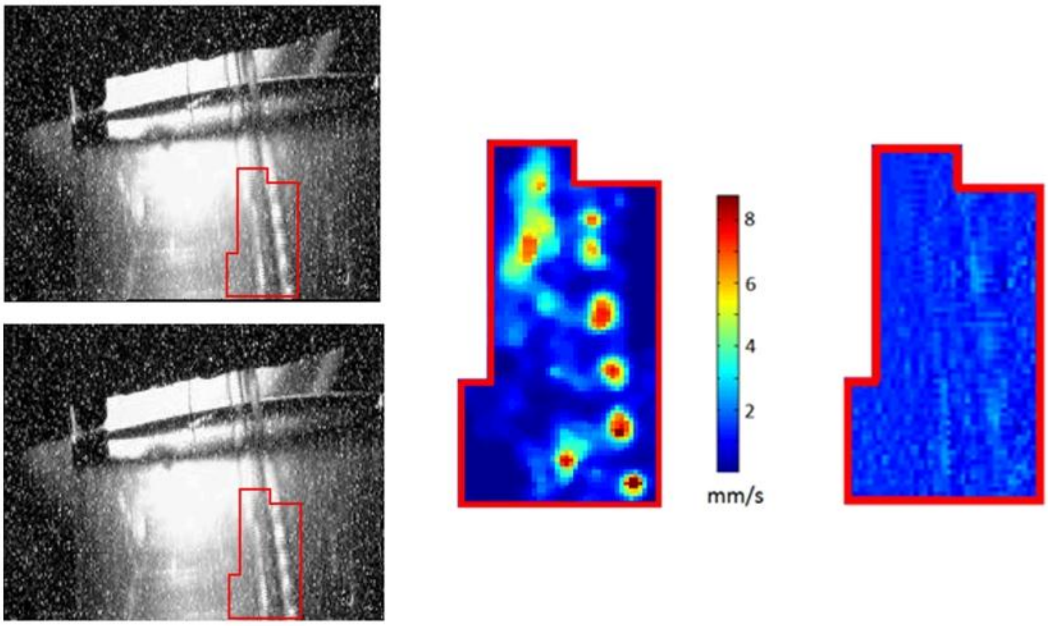

Figure 5 - Illustration of the optical flow estimation. Two successive images from the video sequence corresponding to the JET pulse #76379 are presented together with the region of interest (ROI) determined by the segmentation procedure (left). The velocity field (middle) and the image difference I_{diff} *(right) are calculated only inside ROI.*

High speed and good accuracy optical flow estimation are obtained. A representative result is reported in Fig. 5. The difference between the speeds of the different pellets in the ribbon structure, calculated using the optical flow, is below 12.5%. This factor can provide an estimate of the error associated with the optical flow calculation. It was evaluated for more than 300 image pairs in the video sequence corresponding to the JET pulse #76379. Its value is always below 16%.

Another criterion to discern between correct and wrong calculated flow fields can be based on the difference between one image of the image pair and its reconstruction obtained using the other image and the estimated optical flow:

$$I_{diff} = (I_2 - I_2^{rec}),\ where\!:\ I_2^{rec} = I_1 + OF \qquad (8)$$

(I_1, I_2) is the image pair and OF is the optical flow calculated using I_1 and I_2. I_{diff} is presented also in Fig. 5. The peak-signal-to-noise (PSNR) ratio, calculated for I_{diff}, can also be used as a confidence criterion to determine the validity of the results. PSNR is defined as the ration between the maximum possible power of a signal and the power of the corrupting noise that affects the fidelity of the representation:

$$PSNR = 10 \times log \frac{128^2 \times N}{\sum_{i=1}^{M} \sum_{j=1}^{N} \left(I_{2,ij} - I_{2,ij}^{rec}\right)^2} \tag{9}$$

where N is the total number of pixels in the ROI and the images which are represented on 128 gray-levels. A higher PSNR indicates a higher quality of the reconstruction. For the image difference in Fig. 5 PSNR has a value of 19 dB. For the video corresponding to the JET pulse #76379, PSNR has always a value above 14 dB. The main limitation on the accuracy of the optical flow estimate is determined by the poor quality of the input images which are affected mainly by strong noise and saturation.

4. Conclusion

A recently developed optical flow image processing method has been improved and adapted in order to evaluate the pellets extrusion velocity, based on the image sequences provided by a CCD camera viewing the ice at the exit of the nozzles of the extrusion cryostat. Motion estimation within the MPEG video compressed domain was used to reach the computation time performances that allow real-time determination of the deuterium ice extrusion velocity. The video sequences of images are stored in a compressed format for further analysis. In the case of the MPEG-2 format, crude motion estimation is performed for compression purposes. A set of methods, which exploit this information, has been adapted to the specific JET specific requirements. The methods achieve efficient motion segmentation. Motion segmentation is used as a key contrivance to allow very fast optical flow estimation for the determination of the deuterium ice extrusion velocity of JET pellet injector. Experimental validation is performed on significant JET video data. The methods can be engrafted in the MPEG compressing routines. The time performances achieved may allow real-time determination of the deuterium ice extrusion velocity, an important parameter for pellet injection.

References

[1] S.L. Milora, W.A. Houlberg, L.L. Lengyel, V. Mertens, Nucl. Fusion 35 (1995) 657.

[2] H.W.Muller, K. Büchl, M. Kaufmann, P.T. Lang, R.S. Lang, A. Lorenz, et al., Phys. Rev. Lett. 83 (1999) 2199.

[3] P.T. Lang, K.Büchl, M. Kaufmann, R.S. Lang,V. Mertens,H.W. Müller, et al., Phys. Rev. Lett. 79 (1997) 1487.

[4] P.T. Lang, H. Zohm, K. B¨uchl, J.C. Fuchs, O. Gehre, O. Gruber, et al., Nucl. Fusion 36 (1996) 1531 (Corrigendum in Nucl. Fusion 36 (1996) 153).

[5] P.T. Lang, P. Cierpka, J. Harhausen, M. Kaufmann, J. Neuhauser, C. Wittmann, G. Kocsis, J. Sarkozb, T. Szepesi, C. Dorner, G. Kauke, Fus. Eng. Des. 82 (2007) 1073–1080

[6] T. Craciunescu, A Murari, A,Alonso, P.T. Lang, G. Kocsis, I. Tiseanu, V. Zoita, J. . Nucl. Mater. 400 (2010) 205–212.

[7] A. Geraud M. Dentan, A. Whitehead, P. Butcher, D. Communal, F. Faisse, J. Gedney, G. Gros, D. Guillaume, L. Hackett, V. Hennion, D. Homfray, R. Lucock, J. McKivitt, M. Sibbald, C. Portafaix, J.P. Perin, M. Reade, D. Sands, A. Saille, I. Symonds, M.Watson, L. Worth, I. Vinyar, Fus. Eng. Des. 82 (2007) 2183–2188

[8] ISO/IEC CD 13818-2 . ITU-T H.262 (MPEG-2 Video), Information technology. Generic coding of moving pictures and associated audio information: Video, 1995.
[9] M.T. Coimbra, M.Davies, Approximating optical flow within the MPEG-2 compressed domain. IEEE Trans. Circuit Syst. Video Tech. 15 (2005) 103–107.
[10] B. Shen and K. Sethi, Direct feature extraction from compressed images, Proc. SPIE Storage and Retrieval for Image and Video Databases IV, vol. 2670, pp. 404–414, 1996.
[11] K.E. Rapantzikos, Dense Estimation of optical flow in the compressed domain using robust techniques, PhD Thesis, 2002, *http://www.image.ece.ntua.gr/*rap/*.
[12] G. Yang, W. Chen, Q. Zhou, Z. Zhang, Optical flow approximation based motion object extraction for MPEG-2 video stream, J Real-Time Image Proc. 4 (2009) 303–316.
[13] R.H. Chung, F.Y. Chin, K.Y. Wong, K.P. Chow, T. Luo, H.S. Fung, Efficient block-based motion segmentation method using motion vector consistency, in: Proceedings of IAPR Conference on Machine Vision Applications MVA-2005, May 16-18, 2005, Tsukuba Science City, JAPAN, pp. 550–553.
[14] T. Craciunescu, A. Murari, I. Tiseanu, P. Lang, Motion estimation within the MPEG video compressed domain for JET plasma diagnostics, Nuclear Instruments and Methods in Physics Research, Section A: Accelerators, Spectrometers, Detectors and Associated Equipment, 659-1(2011) 467-476.